Modulated Ultrasound-enabled Particle and Cell Separation in Surface Acoustic Wave Microfluidic Devices

Gergely Simon

School of Engineering and Physical Sciences

Heriot-Watt University

A thesis submitted for the degree of

Doctor of Philosophy

March 2019

The copyright in this thesis is owned by the author. Any quotation from the thesis or use of any of the information contained in it must acknowledge this thesis as the source of the quotation or information

Abstract

In recent years considerable amount of research focussed on development of the so-called lab-on-a-chip (LoC) devices that feature complex laboratory sample preparation functions (such as sample washing, sorting, detection or drug delivery) on the microscale. These devices offer lower manufacturing costs, reagent use and the required sample size can be as small as a few microlitres. In this thesis, particle and cell separation is investigated utilising the primary acoustic radiation force in a surface acoustic wave device. After providing review of similar techniques, various phase and frequency modulation methods are proposed for achieving target separation based on size, density or compressibility difference. A special form of primary acoustic radiation force is presented for surface wave devices and is used to obtain particle trajectories in modulated fields for fast analytical comparison of the proposed methods. Experiments for size-based particle separation reveal 95% efficiency and >85% purity for particle size ratio as small as 1.45. Physical property-based separation of iron-oxide and polystyrene microparticles shows even higher figures of merit: >95% efficiency and >90% purity illustrating the versatility of the method. Biological cell separation is performed on human red blood cells and white blood cells, displaying 94% efficiency and >84% purity. Bandpass sorting of particles and cells is also proposed and validated by experiments. Various numerical models are developed for flow and acoustic field simulation, including investigation of secondary acoustic radiation force, and finally a Monte-Carlo study is carried out to verify the superiority of modulated acoustic sorting methods compared to static acoustic field separation techniques.

Acknowledgements

Firstly I would like to thank my mother and my family for their continuous support and for the patience for answering all my *why?* questions since I was wee. It helped me to better understand the universe. I am thankful for my father for suggesting me the electrical engineering career, it was a spot-on decision that makes me happy every day.

I am grateful to my primary and high school maths teachers—Ms Isza Sándorné and Mr György Hajzer—for sacrificing their free time just to further my education and to improve my problem solving skills to a level where no problem during PhD could really be a problem, but more of a challenge to solve.

During the course of the PhD many people have helped me with their suggestions and discussions. I thank my primary supervisor, Dr Anne Bernassau, for her availability on short notices, and the weekly meetings we had. Preparing the summary slides for those meetings was daunting, but helped me greatly in writing this thesis, and locating certain experiments in time.

As my knowledge on biology—especially the experimental part—was severely limited, I needed great deal of help keeping my cells happy and designing the experiments. For this a great deal of appreciation goes to Dr Mathis Riehle, Mrs Carol-Anne Smith and Ms Caroline Busch. Thank you for being patient hearing out my daft questions.

In the early stage of my PhD, the struggles caused by device fabrication were greatly alleviated by Dr Julien Reboud, who not only spent his valuable time training me, but shared all his small tricks.

I am happy to have Dr Marco Andrade as a collaborator, and I believe the long distances were never a problem to have a fruitful brainstorming together and take steps towards answering all those tricky questions the reviewers imposed on us.

Although officially Professor Marc Desmulliez was no supervisor to me, he was always available for my questions and happily worked on my papers to improve their quality.

Finally a big thanks to all the friends I have in Edinburgh and around the world,

especially the ones from taekwondo for letting me release some steam after a long day. And last but not least I am eternally grateful to Asia for giving me support on the stressful days (virtually every day).

Thank you all!

Contents

List of Figures v

List of Publications x

List of Symbols xii

1 Introduction 1

1.1 Motivation and aim . . . 1

1.2 Objectives . . . 1

1.3 Organisation of thesis . . . 2

2 Literature review on sorting 5

2.1 General sorting strategies . . . 7

2.1.1 Passive methods . . . 7

2.1.1.1 Microsieves, membrane filters and cross-flow filtration 7

2.1.1.2 Deterministic lateral displacement . . . 9

2.1.1.3 Pinched flow fractionation and hydrodynamic filtration 11

2.1.1.4 Inertial (Dean) flow . . . 12

2.1.1.5 Biomimetic . . . 14

2.1.2 Active label free . . . 14

2.1.2.1 (Di)electrophoresis . . . 15

2.1.2.2 Magnetophoresis . . . 17

2.1.3 Active labelled (bead-based) . . . 18

2.1.4 Fluorescence-activated cell sorting . . . 19

2.2 Acoustic manipulation and sorting . . . 20

2.2.1 Static acoustic sorting methods . . . 23

2.2.2 Dynamic acoustic sorting methods . . . 27

2.3 Chapter summary . . . 30

3 Theory of fluid flow, acoustic manipulation and piezoelectricity 32

3.1 The Navier–Stokes equation as a basis of fluid flow and acoustic wave propagation . . . 32

3.2 Microfluidic flow profile in a rectangular microchannel . . . 33

3.3 Piezoelectricity . . . 34

3.4 Acoustic variables and wave propagation . . . 35

3.4.1 Acoustic radiation force calculation methods . . . 38

3.4.2 Primary acoustic radiation force in surface wave devices . . . 40

3.4.3 Secondary acoustic radiation force . . . 45

3.4.4 Acoustic streaming . . . 47

3.5 Chapter summary . . . 48

4 Dynamic waveforms for sorting 49

4.1 Phase modulated particle separation . . . 49

4.1.1 Particle trajectories . . . 50

4.1.2 Optimum time parameters and scaling laws for particle sorting 52

4.1.3 Effect of initial phase modulation angle on particle sorting . . 54

4.2 Frequency modulation . . . 58

4.3 Changing the directivity of sorting . . . 61

4.4 Bandpass sorting . . . 62

4.5 Chapter summary . . . 62

5 Device design, fabrication, characterization and experimental setup 64

5.1 Design of IDTs and microchannel . . . 64

5.2 Fabrication procedure . . . 67

5.2.1 Interdigitated transducer fabrication . . . 68

5.2.2 PDMS microchannel fabrication . . . 71

5.2.3 Bonding of the substrate and the channel . . . 73

5.3 Experimental setup . . . 75

5.3.1 LabView optimization and porting . . . 75

5.4 Device characterization . . . 76

5.4.1 Butterworth–van Dyke model of transducers . . . 76

5.4.2 Force measurement methodology 81
5.5 Chapter summary 84

6 Simulation models **87**
6.1 For fluid flow and particle focusing 87
6.2 Full piezoelectric/pressure acoustics simulation 90
6.3 Simplified models for particle trajectory generation 91
6.3.1 Neglecting streaming effects 92
6.3.2 Incorporating streaming effects 93
6.4 Secondary radiation force modelling 99
6.4.1 Simplified 2D model 100
6.4.2 Full 3D model with re-scattering events 101
6.4.3 Results of secondary radiation force simulations 102
6.5 Chapter summary 107

7 Experimental results with synthetic particles **109**
7.1 Comparison of sorting methods 110
7.2 Frequency modulated sorting 113
7.3 Bandpass sorting 120
7.4 Chapter summary 126

8 Experimental results with biological cells **128**
8.1 Jurkat cell culturing 129
8.1.1 Cell preparation protocol 129
8.1.2 Counting cells and doubling time 129
8.2 Planned experiments with biological cells 132
8.2.1 Size-based separation of RBCs and WBCs 132
8.2.2 Size-based separation of Jurkat cells at different stages of the cell cycle 132
8.2.3 Compressibility-based separation of dead and live Jurkat cells 133
8.3 Jurkat cell phenotyping 134
8.3.1 Methodology using reference particles 134
8.3.2 Live Jurkat cell contrast factor measurements 135

8.3.3 Dead Jurkat cell contrast factor measurements 136
8.3.4 Acoustic contrast factor of colchicine treated cells 137
8.4 Cell viability of RBCs and Jurkat cells 138
8.4.1 Viability of RBCs 138
8.4.2 Viability of Jurkat cells 138
8.5 Size-based separation of particles and cells 140
8.5.1 Separation trajectory of 5 micron PS particles and Jurkat cells 140
8.5.2 Separation experiments of RBCs and Jurkat cells 141
8.6 Bandpass separation of cells 142
8.7 Chapter summary 143

9 Sensitivity analysis and Monte-Carlo simulation 144
9.1 The need for numerical sensitivity simulation 144
9.1.1 Random initial time 144
9.1.2 Random particle position at inlet region 145
9.2 Sensitivity of continuous and jump modulation methods 148
9.3 Comparison of sensitivity of phase modulated and time-of-flight techniques 150
9.3.1 Intrinsic parameters 150
9.3.2 Extrinsic parameters 151
9.3.3 Analytical sensitivity of the time-of-flight method 151
9.3.4 Simulation setup and parameters 153
9.3.5 Results for the time-of-flight method 154
9.3.6 Results for the phase modulated method 156
9.4 Chapter summary 156

10 Summary and future work 158

A Calculation of secondary radiation force potential 162

B Radial and tangential components of the secondary radiation force 166
B.1 Radial direction 166
B.2 Tangential direction 169

Bibliography 171

List of Figures

2.1 Passive microfluidic filtration and sorting methods 7
2.2 Active microfluidic filtration and sorting methods 15
2.3 Fluorescence activated cell sorting 20
2.4 The acoustic pressure and the resulting acoustic radiation force . . . 21
2.5 The most commonly used types of acoustic manipulation and sorting devices in microfluidics 22
2.6 The most common static acoustic sorting methods 24
2.7 The tilted transducer sorting method 26
2.8 Some of the available dynamic acoustic sorting methods 27

3.1 Representative variables in acoustics and the equations linking them . 35
3.2 Schematic of a surface acoustic wave microfluidic device with the PDMS microchannel bonded on top 40
3.3 Primary radiation force acting on polystyrene (PS) and iron-oxide particles 45

4.1 Illustration of the phase modulated sorting method 50
4.2 Analytical separation trajectories of particles based on size and density difference 52
4.3 Graphical investigation of phase modulated sorting of particles 54
4.4 Comparison of the continuous and jump phase modulation techniques 57
4.5 Illustration of the sorting principle with focus on the notation of the two transducers 58
4.6 The sorting principle of the frequency modulated method, including the two excitation signals 60
4.7 The directivity of the sorting can be reversed by adjusting the inflow rates and negating the excitation signal 61

4.8 Coupling two modulation cycles directly allows for performing bandpass sorting of the middle size particles of a three particle mixture 62
4.9 Analytical particle trajectories of bandpass separation 63

5.1 Overview of the most common inderdigitated transducer designs for surface acoustic wave actuation or sensing 65
5.2 The fabricated microfluidic device, with the gold IDTs on the lithium niobate substrate and the PDMS microchannel bonded on top. To better visualize the inlets, microchannel, and outlets, blue dye is used to fill up the channels 67
5.3 Steps during fabrication of IDTs for SAW devices 69
5.4 Example images seen with the white light interferometer emphasising the pattern inversion between the images corresponding to before metal evaporation and after lift-off 71
5.5 The experimental setup, comprising the microfluidic device, syringe pumps, signal generator and power amplifiers. The particle motion is observed through a regular microscope with bright field configuration, both the light source and camera are above the specimen 75
5.6 Comparison of particle trajectories with the direct phase modulation and internal phase modulation approaches of signal generator control 77
5.7 Butterworth–van Dyke lumped model of a transducer 77
5.8 Measurement results of the transducers with the fitted curves using the lumped element BVD model 78
5.9 Plot of transducer response for various designs with changing temperature 81
5.10 Various BVD model parameter dependence on temperature of a fixed frequency and a chirped IDT design 82
5.11 Resonance and antiresonance frequency dependence of a fixed frequency and a chirped IDT design on temperature 82
5.12 Comparison of acoustic energy density approximation methods 85
5.13 Acoustic energy density vs input peak-to-peak transducer voltage . . 85

6.1 Schematic of the device with dashed green and blue lines indicating the locations for flow speed investigation in Fig. 6.2 87
6.2 Velocity distributions at the inlets and in the main channel and particle distributions in the main channel 89

6.3 The full piezoelectric, acoustic, structural mechanic finite element model 90
6.4 The simple 2D COMSOL model with the pressure distribution within the microchannel 93
6.5 Trajectories obtained by the analytical trajectory equation and the COMSOL simulation 93
6.6 Mesh convergence analysis 96
6.7 Pressure distribution within the microchannel for different phase differences between the two transducers 97
6.8 Analysis of the effect of particle size on trapping efficiency and identification of critical particle diameter 98
6.9 Illustration of trapping of a polystyrene particle within the microchannel for various phase difference values between the two transducers 99
6.10 Analytical and numerical particle trajectories for separation of polystyrene particles 99
6.11 Illustration of the anechoic corner or shadow zone 100
6.12 Two small particles in a plane standing wave field 101
6.13 Simulation results for a polystyrene particle in air, when the nodal line aligns with the scatterer position 103
6.14 Simulation results for a polystyrene particle in air, when the antinodal line aligns with the scatterer position 103
6.15 Simulation results for a polystyrene particle in water, when the nodal line aligns with the scatterer position 105
6.16 Simulation results for a polystyrene particle in water, when the antinodal line aligns with the scatterer position 106

7.1 Recap of the available single direction sorting methods 111
7.2 Upwards sorting of 10 and 14.5 micron PS particles 112
7.3 Downwards sorting of 10 and 14.5 micron PS particles 113
7.4 Trajectories of upwards particle sorting experiments and analytical fit 114
7.5 Trajectories of downwards particle sorting experiments and analytical fit 115
7.6 Experimental and theoretical average particle speed for various frequency difference values between transducers 116
7.7 Overlay images of experimental size-based and density/compressibility-based sorting 118

7.8 Comparison of experimental and theoretical limit for sorting 119
7.9 Recap of the available bidirectional bandpass sorting methods 121
7.10 Upwards bandpass sorting of 6, 10 and 14.5 micron PS particles . . . 122
7.11 Downwards bandpass sorting of 6, 10 and 14.5 micron PS particles . . 123
7.12 Trajectories of upwards bandpass sorting 124
7.13 Trajectories of downwards bandpass sorting 124
7.14 Experimental bandpass sorting of 6, 10 and 14.5 micron PS particles 125
7.15 Figures of merit of bandpass sorting of 6, 10 and 14.5 micron PS particles 125

8.1 Schematics of the Neubauer cell counting chamber 130
8.2 Cell counts versus incubation time 131
8.3 Visual investigation of drug treated Jurkat cell samples 132
8.4 Dose test of colchicine treatment 133
8.5 Acoustic contrast factor of live Jurkat cells versus diameter 135
8.6 Acoustic contrast factor of live and dead Jurkat cells versus diameter 136
8.7 Acoustic contrast factor of live and formaldehyde fixed Jurkat cells versus diameter 137
8.8 Acoustic contrast factor of live and colchicine treated Jurkat cells versus diameter 138
8.9 The effect of ultrasound on the viability of the red blood cells 139
8.10 Visual investigation of viability of Jurkat cell samples 139
8.11 Separation results of a 5 micron PS particle and a Jurkat cell 140
8.12 Separation of RBCs and Jurkats 141
8.13 Bandpass separation of 1 micron PS particles, RBCs and Jurkat cells 142

9.1 Particle trajectories for 10 and 14.5 micron PS particles with various start times with respect to the start of the ramping period 146
9.2 Particle trajectories for 10 and 14.5 micron PS particles with various initial y particle positions 146
9.3 Particle trajectories for 10 and 14.5 micron PS particles resulting in the largest negative displacement of the large particles 146
9.4 Particle trajectories for 10 and 14.5 micron PS particles resulting in the small particles locate closest to the antinode 147

9.5 Efficiency and purity values of continuous and jump modulation sorting schemes for various ramping time and particle sets 148
9.6 Sensitivity of the sorting efficiency and purity with variation of different extrinsic and intrinsic sorting parameters, for the time-of-fight and phase modulated techniques 155

List of Publications

The results of the thesis have been published in various journal papers and conference proceedings. They are referred to in the text using the special format provided below to allow for easier identification.

Peer-reviewed journal papers

[**Simon2019LOC**] G. Simon, M.A.B. Andrade, M.P.Y. Desmulliez, M.O. Riehle, A.L. Bernassau, "Single transducer pair acoustic bandpass sorting of heterogeneous cell samples", manuscript in preparation.

[**Simon2019PP2**] G. Simon, G.B. Hantos, M.A.B. Andrade, M.P.Y. Desmulliez, M.O. Riehle, A.L. Bernassau, "Monte-Carlo based sensitivity analysis of acoustic sorting methods", *Periodica Polytechnica Electrical Engineering and Computer Science*, 63(2), pp. 68-76, 2019.

[**Simon2019PP1**] G. Simon, M.A.B. Andrade, M.P.Y. Desmulliez, M.O. Riehle, A.L. Bernassau, "Theoretical framework of radiation force in surface acoustic waves for modulated particle sorting", *Periodica Polytechnica Electrical Engineering and Computer Science*, 63(2), pp. 77-84, 2019.

[**Simon2018MM**] G. Simon, M.A.B. Andrade, M.P.Y. Desmulliez, M.O. Riehle, and A.L. Bernassau, "Numerical determination of the secondary acoustic radiation force on a small sphere in a plane standing wave field", *Micromachines*, 10(7), 431, 2019.

[**Simon2018APL**] G. Simon, Y. Pailhas, M.A.B. Andrade, J. Reboud, J. Marques-Hueso, M.P.Y. Desmulliez, J.M. Cooper, M.O. Riehle, and A.L. Bernassau, "Particle separation in surface acoustic wave microfluidic devices using reprogrammable, pseudo-standing waves", *Applied Physics Letters*, vol. 113, no. 4, 2018.

[**Simon2017Bio**] G. Simon, M.A.B. Andrade, J. Reboud, J. Marques-Hueso, M.P.Y. Desmulliez, J.M.Cooper, M.O. Riehle, and A.L. Bernassau, "Particle separation by phase modulated surface acoustic waves", *Biomicrofluidics*, vol. 11, no. 5, p. 054115, 2017.

Conference proceedings

[**Simon2018IUS**] G. Simon, M.A.B. Andrade, M.P.Y. Desmulliez, M.O. Riehle, A.L. Bernassau, "Numerical Simulation of Particle Motion in a Phase Modulated Surface Acoustic Wave Microfluidic Device", *IEEE International Ultrasonics Symposium*, Kobe, Japan, 2018.

[**Simon2017ICSV**] G. Simon, J. Marques-Hueso, M.P.Y. Desmulliez, A.L. Bernassau, D. Roolvink, G. Burns, P.A.G. Cormack, M.A.B. Andrade, J. Reboud, J.M. Cooper, M.O. Riehle, "Reconfigurable particle separation by dynamic acoustic fields in microfluidic devices", *24th International Congress on Sound and Vibration, ICSV 2017*, London, United Kingdom, 2017.

[**Simon2016IUS**] G. Simon, M.A.B. Andrade, D. Roolvink, P.A.G. Cormack, M.O. Riehle, A.L. Bernassau, "A deterministic method for particle sorting by dynamic acoustic fields", *IEEE International Ultrasonics Symposium*, Tours, France, 2016.

Further unpublished talks were given at the Acoustofluidics 2018 Meeting in Lille, France and at the Acoustofluidics Special Interest Group Meeting at Edinburgh in 2018.

List of Symbols

α	Auxiliary variable used in derivations to denote $k_y y + k_z z$
β	Notation used for compressibility of particles or media in some literature
γ	Auxiliary variable for $2k_y c_{\text{ac}}/c_{\text{visc}}$
ψ	Auxiliary variable used in derivations to denote $-k_y y + k_z z$
$\widetilde{\delta}$	Viscous boundary layer thickness, $\widetilde{\delta} = \sqrt{2\nu/\omega}$
η	Dynamic viscosity of the medium
θ_R	Rayleigh angle of wave propagation
κ	Compressibility of the particles or media
λ	Wavelength of the harmonic signal, $\lambda = c_{\text{sub}}/f$
μ	Notation used for dynamic viscosity in some of the literature
ν	Kinematic viscosity of the medium, $\nu = \eta/\rho$
ρ	Density of fluid or particles
$\phi(t)$	Phase modulation signal
φ	Acoustic velocity potential
Φ_{ac}	Acoustic contrast factor
ω	Angular frequency, $\omega = 2\pi f$
a	Particle radius
c_{ac}	Primary radiation force parameters, $c_{\text{ac}} = V_p E_0 k_y \Phi_{\text{ac}}$
c_{sub}	Surface acoustic wave speed on the top of the substrate
c_{visc}	Hydrodynamic drag force parameters, $c_{\text{visc}} = 6\eta\pi a$

f	Frequency of the harmonic excitation
f_1	Monopole scattering coefficient
f_2	Dipole scattering coefficient
i	Imaginary unit
k_0	Wavenumber in the medium
k_y	Wavenumber along the y axis
k_z	Wavenumber along the z axis
p	Acoustic pressure
Q	Volumetric flow rate
s	Linear phase modulation speed
t	Time
$\mathbf{u}$	Acoustic particle velocity
Z	Auxiliary variable for $\sqrt{s^2 - \gamma^2}$

Chapter 1

Introduction

1.1 Motivation and aim

Cell separation and sorting are crucial for many biomedical applications including diagnostics, therapeutics and cell biology. Increasing the purity of samples (and therefore the sensitivity of detection) is critical for diagnostic tests. For example, almost any constituent of blood can be used for diagnostic purposes: for early cancer detection, cell-free plasma is necessary; nucleated red blood cells in blood can indicate anaemia or bone marrow cancer; white blood cells for deoxyribonucleic acid (DNA) sequencing for assessing genetic diseases or circulating tumour cells (CTCs) can help with tailored treatments and prognoses. For therapeutic use, stem cells can be extracted for tissue engineering; purified blood platelets can be used for transfusion during surgery; CTCs can be filtered out to prevent cancer spread.

Acoustic techniques are potential alternative approaches for cell separation as discussed in the literature review in the next chapter. The aim of the thesis was to propose and investigate modulated acoustic methods and assess their performance for synthetic particle and blood cell separation based on theoretical considerations, experiments and numerical simulations.

1.2 Objectives

The work addresses the following main objectives:

- Propose acoustic separation techniques where the principle of operation is based on modulated ultrasound signals.

- Investigate these techniques theoretically, especially focussing on particle motion and limitations.
- Carry out experiments to obtain real purity and efficiency values.
- Develop simulation models for fluid flow and acoustic processes to be able to validate experimental and theoretical findings.
- Investigate the secondary interparticle radiation force with the aid of finite element simulation models.
- Compare the proposed techniques with commonly used time-of-flight methods.

1.3 Organisation of thesis

While organising the thesis, I tried to maintain coherent units without the need for repetition and avoiding many cross-references. Therefore, the results are not always organised in separate chapters but are embedded into the bodies of work—this felt more natural at the time of writing. To aid the reader, the skeleton is presented here, *italicizing* the author's new results (if applicable) for each chapter. Chapters 6 through 9 mainly contain novel contributions in their entirety.

Chapter 2 places the research in the literature by providing an overview of the various microfluidic sorting methods along with their advantages and disadvantages. The summary underlines the rationale behind investigating acoustic methods as a good alternative for other separation techniques.

In Chapter 3 the basic concepts of fluid flow, piezoelectricity and acoustic wave propagation are introduced for the specific case of surface acoustic wave acoustofluidics in the microfluidic domain. The primary acoustic radiation force is presented as arises in bulk devices, and *a new equation describing primary acoustic radiation force in surface wave devices is proposed and validated numerically.* Scattering from particles results in the interparticle secondary radiation force as discussed in Chapter 3. Finally, the (usually) unwanted effect of acoustic streaming finishes the chapter.

Chapter 4 discusses the available modulation techniques that allow acoustic sorting. *Analytical equations of particle trajectories* are derived and *validated using numerical ODE solvers.* The theoretically *fastest modulation technique is found* and its *limitations* are investigated along with *scaling laws.* The *frequency stepping*

technique is shown to be equivalent to phase modulation when small modulation frequencies/slow phase modulation are considered. *Changing the directivity of the sorting* and thus *achieving bandpass separation* using a single transducer pair is possible.

In Chapter 5 the general design of surface acoustic wave (SAW) devices and polydimethylsiloxane (PDMS) microchannels are overviewed and applied for the phase modulated methods to obtain a suitable device after fabrication. The standard cleanroom procedure for device manufacturing is discussed next, emphasizing the challenges and *an alternative method for plasma bonding is presented*. The experimental setup is introduced afterwards, focussing on the implementation of the control software and using internal modulation on the signal generator for all methods. Finally, the devices are characterized using a Butterworth–van Dyke model to reveal negative temperature dependence of the resonant frequency and the effect of interdigitated transducer (IDT) geometry on device sensitivity. Finally a *fast and robust primary acoustic radiation force approximation technique is introduced* and used to obtain the relationship between input voltage and acoustic pressure amplitude.

In Chapter 6 all the different simulation models are discussed: (i) for fluid flow and mixing (ii) for simulating full piezoelectric surface wave propagation and pressure distribution inside the channel (iii) simplified models for particle trajectory generation (iv) for numerical modelling of secondary radiation force.

Chapter 7 focusses on experimental results with synthetic particles. First, the proposed modulated sorting methods are compared, followed by an in-depth investigation of the frequency skipping technique, revealing efficiency and purity values for different particle sizes and different material particles. The chapter finishes by investigating the bandpass sorting method, where a medium-size particle is separated from smaller and larger entities.

In Chapter 8 the experimental results for biological cells are presented. The choice behind Jurkat cells and red blood cells as experimental targets is justified and the culturing protocol is discussed. A simple method for cell phenotyping is introduced and used for characterising live, dead and drug treated cells. These results are used to analyse feasibility of certain planned separation experiments for cells. Size-based bidirectional separation of RBCs and Jurkat cells is presented along with bandpass sorting of red blood cells (RBCs) from Jurkat cells and synthetic particles. The viability of cells after the experiments is also validated.

Chapter 9 investigates the sorting method in a numerical fashion using Monte-Carlo simulations. Efficiency and purity values are calculated for the modulated sorting method and the widely used time-of-flight method for changing parameter values, such as acoustic pressure amplitude, flow rate, particle properties to reveal sensitivities of the two approaches regarding these intrinsic or extrinsic properties.

In the final chapter, the work is summarized and future plans are outlined that can form a continuation of the thesis.

Chapter 2

Literature review on sorting

In this chapter the main microfluidic sorting methods with their advantages and disadvantages are presented, focusing on cell sorting applications. The main parameters allowing for comparison of the methods are flow rate, achieved efficiency, purity, and recovery, collectively referred to as figures of merit (FoM).

Continuous flow microfluidic devices have multiple outlets. The target outlet is where the desired particles or cells exit. Similarly, in no-flow devices, the target region is an area in the device where the target entities agglomerate. Target region is the middle outlet in Fig. 2.1b or the top half in Fig. 2.1c or in Fig. 2.1f.

Indicating the number of target particles in the target region by $N_{\mathrm{T@T}}$, the number of target particles outside of target region by $N_{\mathrm{T@nonT}}$, the non-target particles in the target region by $N_{\mathrm{nonT@T}}$ and non-target particles outside of target region by $N_{\mathrm{nonT@nonT}}$, the FoMs can be defined. Efficiency indicates how well the target particles are transported to the target region:

$$\text{efficiency} = \frac{N_{\mathrm{T@T}}}{N_{\mathrm{T@T}} + N_{\mathrm{T@nonT}}} \tag{2.1}$$

This number alone can be misleading: a method, where the inflow is directed towards the target region without any processing has 100% efficiency. Therefore efficiency should always be accompanied by purity, indicating how free the target region is from non-target particles:

$$\text{purity} = \frac{N_{\mathrm{T@T}}}{N_{\mathrm{T@T}} + N_{\mathrm{nonT@T}}} \tag{2.2}$$

As in many cases the number of target and non-target particles in the sample is different, a normalized purity is useful to define, allowing for direct comparison of

different methods:

$$\text{normalized purity} = \frac{N_{\text{T@T}}/N_{\text{T}}}{N_{\text{T@T}}/N_{\text{T}} + N_{\text{nonT@T}}/N_{\text{nonT}}} \tag{2.3}$$

where N_{T} is the total number of target particles, N_{nonT} is the total number of non-target particles. This definition of purity indicates the ratio of the target particles in the target region to the total number of particles in the target region, assuming a 1:1 ratio of these particles at the inlet. Finally, recovery is used by some authors interchangeably with efficiency [1, 2].

As the literature normally uses the phrases switching, fractionation, separation and sorting interchangeably, I define these as they are most commonly referred to. When particles are separated or enriched from the carrier fluid medium, but no distinction between the particles themselves occurs, is referred to as fractionation. When the aim of the method is to achieve grouping of particles on the basis of difference in a physical property, is called sorting. Finally by switching I mean the steering of particles to different outlets, based on a one-by-one decision. The term separation is generally used.

For this literature review the available methods are grouped according to the following taxonomy: passive methods, labelled active methods, label-free active methods and fluorescence-activated cell sorting (FACS). Since the latter three rely on an external field of some kind, I start with describing these fields, which include (di)electrophoresis [3, 4], magnetophoresis [5], acoustophoresis [6, 7]. Electrophoresis is the phenomena when an applied DC electric field moves the suspended particles towards the electrodes depending on the surface charge of these particles. Dielectrophoresis relies on the polarizability of particles and utilizes a non-uniform AC field, due to an asymmetric electrode arrangement. Magnetophoresis (similarly to electrophoresis) implies particle movement induced by an external magnetic field due to the magnetizability properties of beads. All of these external fields can be used in any of the three configurations (active label-free, active labelled or FACS) as described above.

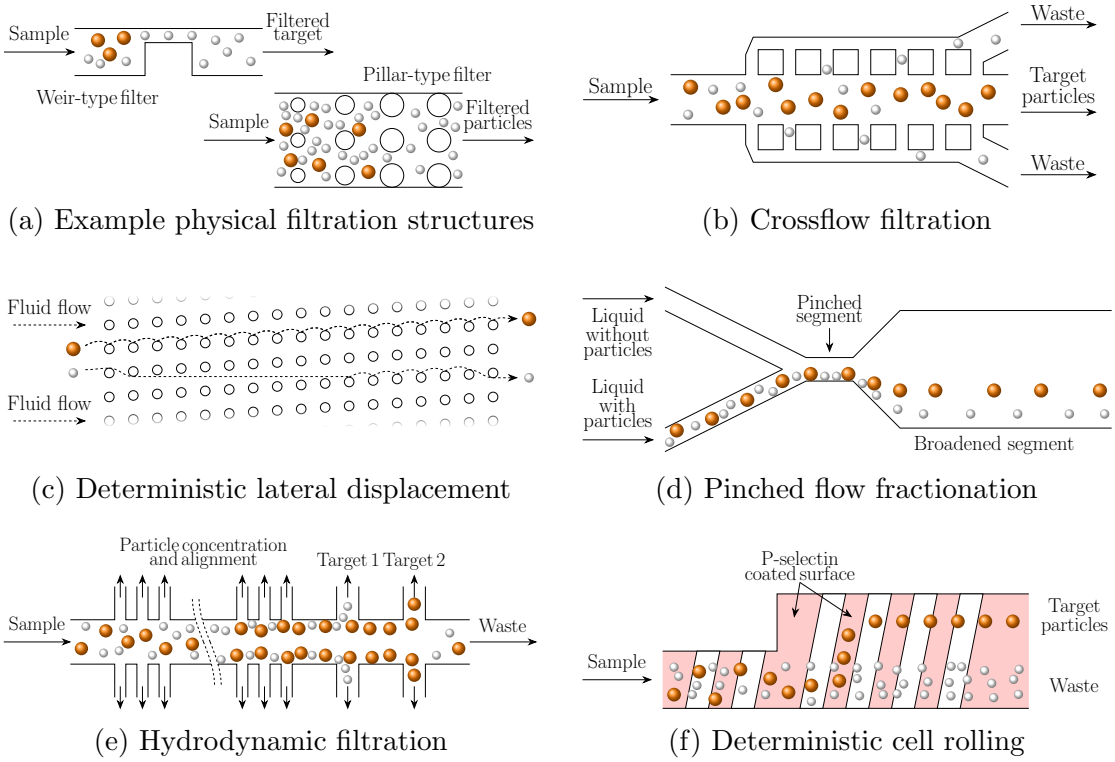

(a) Example physical filtration structures

(b) Crossflow filtration

(c) Deterministic lateral displacement

(d) Pinched flow fractionation

(e) Hydrodynamic filtration

(f) Deterministic cell rolling

Figure 2.1: Passive microfluidic filtration and sorting methods

2.1 General sorting strategies

2.1.1 Passive methods

Passive methods include any technique that uses a device without an external field to achieve particle and cell separation. The separation is achieved either by structural elements in the channel or by relying on microfluidic flow phenomena. With these devices, discrimination of particles is enabled by differences in size, shape and deformability, with some examples utilising density difference.

2.1.1.1 Microsieves, membrane filters and cross-flow filtration

The most straightforward size and deformability-based separation can be performed by microsieves. In these devices, pillars, blocks or constrictions are placed in the channel, allowing only the smaller or more deformable particles to pass through the device [8]. Weir-type devices (Fig. 2.1a) can be used for filtration of cell-free blood plasma, but the processed volume is limited to few nanoliters [9, 10] as the device is prone to clogging, since particles are trapped in the direction of the flow. The same exclusion-based filtration can be achieved by placing pillars of increasing diameter in the microchannel (Fig. 2.1a). Fetal nucleated red blood cells can be separated

from maternal cells taking advantage of their deformability compared to white blood cells with $0.35\,\mu l\,h^{-1}$ flow rate [11]. Similarly to Weir-type filtration, this method is also exposed to blocking. To successfully enrich blood plasma, Son *et al.* used an inverted membrane filter, where the flow exits on top of the device [12]. Gravity makes trapped red blood cells (RBCs) and white blood cells (WBCs) to sediment in the channel, thus allowing for continuous operation with 2.4 µl throughput in 20 min increasing plasma volume 4-fold. A similar membrane type device is used for whole blood processing to extract WBCs [13], with 72.1% WBCs recovery (over 232-fold enrichment ratio) at a throughput as high as $37.5\,\mu l\,min^{-1}$, meanwhile, more than 99.7% RBCs were removed. In this case separation is not continuous flow but processing a given volume using valves and pumps. Due to low abundance of CTCs in blood, microsieves can be used for removal without risk of clogging as demonstrated by Huang *et al.* [14] in a massively parallel 86 channel device using $0.4\,ml\,h^{-1}$ flow rate and achieving recovery better than 92%. High retention rate isolation of CTCs without the need for massive parallelization can be carried out using a combined micropore-surface treated device. By adding surface functionalization, efficiency increased to 96%, using flow rates as high as $3\,ml\,min^{-1}$ [15].

Cross-flow filtration (Fig. 2.1b) utilizes the same sieving principle, but as the filter structure is placed perpendicular to the flow direction, the otherwise trapped particles can be removed and a continuous flow operation is achieved, similarly to the sieving mechanism in fish [16]. An evaluative study on structure-based passive methods revealed best performance for white/red blood cell separation using cross-flow filtration [8]. Straightforward application of cross-flow filtration is blood plasma separation as shown by VanDelinder *et al.* [17] from 20% diluted blood, extracting 8% of blood volume as plasma, with an average flow rate of $0.65\,\mu l\,min^{-1}$. Further adjusting obstacle geometry and introducing spiral channels allows for even higher flow-rates at the expense of need for dilution [18, 19]. The devices uses diluted blood samples of 20:1 and 12:1, at flow rate $10\,\mu l\,min^{-1}$, with the plasma volume accounting for 49.6% of the total output volume. The maximum filtration efficiency can be improved with a zigzagging design to 99.9%, with a plasma collection rate of $0.67\,\mu l\,min^{-1}$ for an input blood flow rate of $12.5\,\mu l\,min^{-1}$ [20]. The group of VanDelinder *et al.* also demonstrated WBC extraction from whole blood [21], reducing RBCs by a factor of 4000, while retaining 98% of WBCs at inflow of $0.06\,\mu l\,h^{-1}$. Design optimization allows larger blood volumes of hundreds of microliters to be

processed at higher flow-rates using Weir-type cross-flow filtration devices, such as white blood cell removal from whole blood [22] at $2.5\,\mu l\,min^{-1}$. A membrane-like cross-flow device was proposed by Li *et al.* [23] with a sample throughput of $1\,ml\,h^{-1}$, for recovery of 27.4% WBCs with purity of 93.5%. Three-step processing—cell separation, cell lysis and DNA purification—is performed in a combined cross-flow device for DNA extraction from WBCs [24]. Both pillar-type and Weir-type tested at $5\,\mu l\,min^{-1}$ flow rate revealing superiority of the Weir-type both in RBC removal (91.2% vs 82.3%) and WBC retention (28.3% vs 9.2%). Cross-flow devices were also successfully used for more specific sorting scenarios, such as promegapoietin enrichment [25]. These therapeutic proteins are produced in *Escherichia coli*, and were separated from protein inclusion bodies for further pharmaceutical processing at flow rate $1\,ml/\,min$. Furthermore, direct *Escherichia coli* bacteria separation from undiluted whole blood was presented with 70 to $130\,\mu l\,min^{-1}$ flow rate, removes 97% of RBCs while retaining 30% of the bacteria [26].

More special device designs or operation mechanisms can also be found in the literature. Microfabricated porous polymer monoliths (PPMs) can aid enrichment of extracellular vesicles (which play important roles in intercellular communication). Separation of vesicles from whole blood and ribonucleic acid (RNA) extraction was demonstrated at 0.1 to $1\,\mu l\,min^{-1}$ flow rate [27]. A CTC capturing device with an operating principle similar to cross-flow method was presented with capture efficiency 95% and purity 99% [28] at flow rate $1\,ml\,h^{-1}$ with the drawback that the cells are trapped in the device. Plasma separation in clinical environment during cardiac surgery with continuous 15% pure plasma volume extraction at flow rate of $80\,\mu l\,min^{-1}$ was also demonstrated [29].

2.1.1.2 Deterministic lateral displacement

In microchannels, the small device dimensions and low flow rates lead to a small Reynolds-number [30], resulting in laminar flow. The streamlines are parallel, and velocity increases from zero at the channel walls to a maximum value at the midddle of the channel, following a parabolic profile. Obstacles within the microchannel disturb the laminar flow and an asymmetric bifurcation can be used for particle separation [31]. Pillar structures or other shapes with gaps larger than the maximum particle size can therefore be employed for size-based sorting, using deterministic

lateral displacement (DLD) [32] as illustrated in Fig. 2.1c. The array of pillars is uniformly spaced both perpendicular and along the flow direction, but each column is shifted with respect to the previous one. The pillar size, gap distance and shift amount gives a critical particle size: above this size, particles are more affected by the relative displacement of the pillars and shift to the side of the channel; while smaller particles follow more straight paths. As in this device the gap size allows all particles to pass through, continuous operation without clogging is achieved. The method has extremely good size resolution: as small as 10 nm difference can be resolved as shown experimentally [31] and by simulations [33].

Prenatal diagnosis and monitoring of the fetus through analysis of nucleated red blood cells offer a good non-invasive alternative to traditional methods and was presented at $0.45\,\mathrm{ml\,min^{-1}}$ flow rate with 99.99% elimination rate using a DLD device [34]. The method was validated for pathogen sorting by extracting *Trypanosoma brucei* parasites (causing sleeping sickness) from whole blood at flow velocities of $600\,\mu\mathrm{m\,s^{-1}}$ [35]. Experiments with a different, I-shaped pillar array allowed for separation of non-spherical RBCs from blood with 100% efficiency and 0.4 µl/ min flow rate [36]. Further investigations revealed that smaller channel height or high shear rates can lead to successful separation based on other modalities such as shape and deformability of the cells similar to the I-shaped pillars. Soft, disc-shaped RBCs change their effective critical diameter with orientation aligning vertically or horizontally, and also by exhibiting various shear stresses due to their compressibility [37]. Although this research was only a proof-of-concept it showed successful separation of RBCs from similar size cells in a 4.27 µm high microchannel with flow velocities between $30\,\mu\mathrm{m\,s^{-1}}$ and $18\,\mathrm{cm\,s^{-1}}$. An exhaustive study on stiffness-based separation using a DLD device was reported by Holmes *et al.* [38]. Red blood cells were artificially prepared using different concentrations of glutaraldehyde to increase membrane stiffness. The difference between lateral displacement for cells with different stiffness was larger than 1500 µm, and as the stiffness of malaria (*Plasmodium falciparum*) infected RBCs is similar to the chemically induced ones they analysed, the DLD method can be potentially used for isolation of infected cells and malaria detection. Behaviour of rigid and deformable particles in DLD devices with various post shapes was investigated numerically shortly afterwards [39] to validate previous experimental works [36–38] and propose improvements in device design.

Enrichment of CTCs from whole mouse blood has also been reported recently with $7\,\mu l\,min^{-1}$ specimen flow rate and $190\,\mu L\,min^{-1}$ buffer flow rate [40]. Before sorting, the tested blood fraction contained no CTCs among 3 million other cells, while after sorting, the CTCs contributed to 0.05% (which would correspond to 1500 CTCs in 3 million cells). Numerical simulations contributed to better understanding of separation of CTCs from blood using DLD devices [41]. In another therapeutic application DLD was utilised to separate microvesicles from prepared blood sample containing RBCs and peripheral blood mononuclear cells (PBMCs) suspended in RPMI media [42]. The tested flow rate of $1\,\mu l\,h^{-1}$ shows 100 to 160 µm displacement for cells, while the microvesicles experienced no displacement. The authors claim the method can be successfully applied for whole blood processing of tumour-derived vesicles for diagnostics and personalized therapy. To aid regenerative medicine, separation of viable and non-viable Jurkat cells (immortalized human T lymphocytes) was also demonstrated with 89% sorting efficiency and 50% sorting purity with $1.2\,ml\,h^{-1}$ flow rate [43].

2.1.1.3 Pinched flow fractionation and hydrodynamic filtration

The specific laminar flow field in microfluidics allows for hydrodynamic filtration and pinched flow fractionation (PFF), as the centre of different sized particles follow different streamlines. With pinched flow fractionation (Fig. 2.1d) the particle mixture enters at one outlet and are pushed to one side of the channel by using another sheath inflow without particles. The centre of larger particles are located further away from the wall, and as downstream the channel suddenly widens, the particles are spread as they follow the different streamlines. The broadened segment than can be partitioned into many outlets, allowing collection or post-processing of the size differentiated entities. The concept was introduced by Yamada *et al.* with particles only (15 and 30 µm diameter, poly(styrene-co-divinylbenzene)) [44]. They achieved 99% small and 91.6% large particle efficiency with 70 to $560\,\mu l\,h^{-1}$ total flow rate, with 16% accounting for the particle inflow.

The method has been used to enrich red blood cells from 0.3% diluted blood samples at $20\,\mu l\,h^{-1}$ flow rate with 80% efficiency [45]. A modified pinched flow device with double sheath and inertial effects achieved 300-fold enrichment of *Escherichia coli* bacteria in 10% (v/v) blood sample with flow rate $18\,\mu l\,min^{-1}$ [46]. The group of

Nho *et al.* experimented with tilted sidewalls and achieved separation resolution of synthetic particles increased by 11.6-fold compared to a conventional PFF device with vertical walls at $60\,\mu l\,h^{-1}$ sample flow rate [47]. They observed the same enhancement (but only by 2.6-fold) for separation of platelets and red blood cells from 10% diluted blood for flow rates between 100 and $350\,\mu l\,h^{-1}$ [48]. By further improving the device design and fabrication they managed to achieve resolution increase as high as 9.5-fold [49] for the same flow rate. Successful separation of cancer cells from WBCs with recovery of 96.0% and a 93.6% removal of WBCs at $10\,\mu l\,h^{-1}$ was also demonstrated [50]. Numerical simulations of the effect of different geometries can be used for adjusting for enhanced device operation [51].

A similar method to pinched flow fractionation is hydrodynamic filtration (Fig. 2.1e), but in this case there is only one inflow and the particles are pinched at the sidewalls using outlets perpendicular to the main flow direction. After alignment, the smaller particles, located closer to the wall and therefore having slower velocities, exit at an earlier outlet. Larger particles, due to their higher speed, are allowed to travel further down the channel, facilitating size-based separation [52].

This technique was applied to separate liver cells (hepatocytes and nonparenchymal cells) with $50\,\mu l\,min^{-1}$ flow rate [52]. The method has also been applied for twin particles and yeast cells, where two spherical entities attach to each other forming a peanut shape [53]. The applied 1 to $3\,\mu l\,min^{-1}$ flow rate allowed at least 80% of the single and twin yeast cells to be separated to different outlets. By reducing the focusing channel width, margination mechanisms ensure RBC depleted regions at the channel side [54]. Enhancement of *Escherichia coli* and *Saccharomyces cerevisiae* bacteria removal (up to 80% and 90% removal efficiency) is possible by margination using $6\,ml\,h^{-1}$ maximum processing flow rate.

2.1.1.4 Inertial (Dean) flow

In microchannels with higher flow rates the Reynolds number can reach 100, leading to a significant increase in inertial effects. The particles experience additional lift forces, perpendicular to the main flow direction, that arrange them in circular patterns in pipes, or in the middle of the four faces in rectangular cross sections [55]. Additionally, in curves channels due to the different flow speeds in the vicinity of the inner and outer walls, secondary Dean drag forces arise.

These focusing effects can be used to enrich particles or cells suspended in liquid medium: H1650 lung cancer cells from 0.5-5% diluted blood have been focused with as high as 80 nm accuracy [56]. Further improvement of the method by the same group allowed for a factor of 100 enrichment of platelets from diluted blood (2% whole blood in phosphate buffered saline, PBS) with $0.9\,\mathrm{ml\,min^{-1}}$ flow rate [57]. Separation of more specific entities such as SH-SY5Y neuroblastoma (cancer in nerve tissue) and C6 glioma cells (tumour originating in the neuron support cells in the brain or the spine) is also demonstrated [58]. These cells that can be used to study Parkinson's disease were separated with efficiency >80% from 0.05% volume fraction dilution, corresponding to 10^6 cells/s processing speed. *Cryptosporidium* is a highly resistant protozoa in water with low abundance therefore concentration methods with high recovery are required for detection. An inertial Dean-flow device was developed to achieve 100% separation efficiency at $500\,\mathrm{\mu l\,min^{-1}}$ throughput [59].

Depending on channel geometry and flow rate, particles with different sizes can be focused at different positions in the channel, achieving sorting of various entities. A massively parallel inertial system for >80% removal of *Escherichia coli* bacteria from 0.5% (v/v) diluted blood was presented with $8\,\mathrm{ml\,min^{-1}}$ total throughput while enriching RBC concentration 4-fold [60]. The method was applied for separation of cancer cells from red blood cells with flow rate $565\,\mathrm{\mu l\,min^{-1}}$ [61]. The group achieved 120-fold increase in CTC count with 85% efficiency, with the hematocrit concentration initially being diluted to 1% in the sample.

As the inertial method offers highly repeatable and reliable focusing of particles and cells it is also commonly employed as part of a multi-stage sorting system. Inertial focusing was used as part of microscopy system for final optical evaluation, validated by yeast and breast cancer cells at as high rates as 100,000 cells/s [62]. A combined hydrodynamic–inertial focussing–magnetic activation method was applied for whole blood: the first stage removes RBCs and platelets, the second stage focuses remaining WBCs and CTCs (using Dean flow), and finally magnetic activation removes CTCs at 10^7 cells/s total processing rate [63]. The flow rate used in this combined device was 50 to $150\,\mathrm{\mu l\,min^{-1}}$ demonstrating >90% recovery rate for four of the five tested cell lines, with the lowest being 78%.

2.1.1.5 Biomimetic

One example to show the possibility of borrowing ideas from nature and thus creating devices that mimic behaviour of biological systems was already mentioned at crossflow filtration and the sieving mechanism of fish. These devices can serve various microfluidic purposes [64]. For sorting, the most researched such bioinspired phenomenon is the Zweifach–Fung effect stating in a bifurcated channel the higher flow rate carries higher volume fraction of the particles or cells, as observed for red blood cells in blood vessels. Although the physical mechanism behind the effect is not fully understood, yet it can be successfully utilised in microfluidic systems for cell sorting. Blood plasma separation up to 100% efficiency with filtered plasma volume of 15 to 25% of original sample volume was presented at 3 to 4 $\mu l\,min^{-1}$ flow rate [65]. Another example for biomimetic operation uses the principle that leukocytes have a tendency to migrate towards channel walls (known as margination) and therefore can be removed from the main channel through a narrow branch. Achieving 34-fold increase of leukocyte to erythrocyte ratio with flow rate at outflow of 16 $pl\,s^{-1}$ (approx 1 $nl\,min^{-1}$) is demonstrated [66]. Numerical simulations predicted that a cilia-like behaviour could lead to successful capturing of cells with size-based exclusion, similarly to the feeding mechanism of marine suspension feeders [67, 68] and were used to propose a sorting device design [69]. Successful trapping and release of lymphoblast cancer cells using aptamer that binds to protein tyrosine kinase-7 also demonstrated [70].

2.1.2 Active label free

In the active label free sorting methods, the distinction between particles or cells is based on some inherent physical property. These include surface charge, polarizability, magnetizability, difference in size, density, compressibility. The only group of methods not included in this subsection is the group of acoustic techniques: since this thesis is focused on acoustic separation, a whole separate section is dedicated to these methods with a more detailed theoretical overview. A common device configuration for active label free (or labelled) methods is shown in Fig. 2.2a, where the external field force selectively displaces the target particles or cells to be collected at the bottom target outlet.

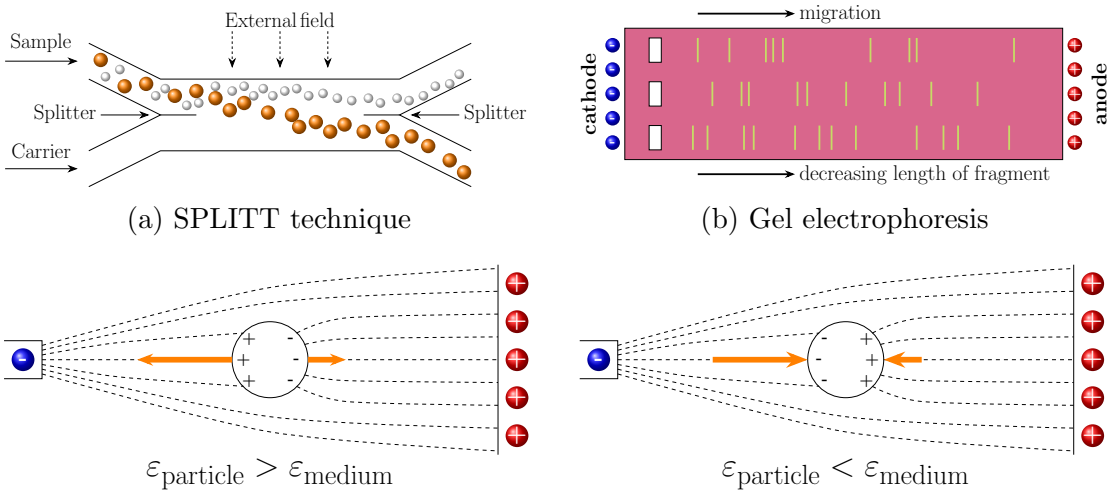

(a) SPLITT technique

(b) Gel electrophoresis

(c) Positive dielectrophoresis

(d) Negative dielectrophoresis

Figure 2.2: Active microfluidic filtration and sorting methods

2.1.2.1 (Di)electrophoresis

An applied external electric field has different magnitude of electrostatic force on microobjects with different surface charge densities, which can be employed for electrophoretic separation. As illustrated in Fig. 2.2b, an electric potential difference is applied across a gel matrix, that has openings towards the cathode for sample insertion. As most biological molecule fragments are negatively charged, they migrate towards the anode, at different speeds, depending on the interplay of the electrical and drag forces [71]. As the obtained electrostatic force is small, the method is mainly applicable for protein or biomolecule separation, and is used for RNA/DNA sequencing [71].

The method was also applied for continuous free flow biomolecule separation, such as human serum albumin (HSA, protein in blood plasma that can be used to detect liver failure), bradykinin (inflammatory mediator peptide, blood pressure indicator) and ribonuclease A (an enzyme, low abundance points to pancreatic problems) enrichment at flow rate 10 to 30 µl min^{-1} [72]. Separation of cytosolic proteins can help analysing metabolic activity, as demonstrated by Hoffmann *et al.* with 1.4 ml min^{-1} flow rate [73]. Electrostatic actuation is also one of the most straightforward actuation mechanisms for fluorescence-activated cell sorting (FACS) as shown below but usually require high voltages due to the small electrostatic forces [3].

Unlike electrophoresis, where the particles have to carry an electric charge, dielectrophoresis (DEP) relies on the polarizability of particles or cells for separation

[74]. As shown in Figs. 2.2c and 2.2d, an applied electric field polarises the particle, with a dipole moment direction based on the permittivity of the particle and the medium. In a uniform electric field, the particle would experience no net force, however due to the asymmetric configuration of the electrodes, a non-uniform field is generated and the particle moves towards the stronger field with positive dielectrophoresis (Fig. 2.2c, $\varepsilon_{\text{particle}} > \varepsilon_{\text{medium}}$) and away from it for negative dielectrophoresis (Fig. 2.2d, $\varepsilon_{\text{particle}} < \varepsilon_{\text{medium}}$). Important to mention that with reversed electrodes both the field and the dipole direction reverses, resulting in the same direction of the total force. Therefore dielectrophoresis can be used with AC fields as well [75]. As the permittivity of the medium and the particle are frequency dependent, the behaviour of the cell depends on the frequency used, with respect to the so-called crossover frequency, where the positive and negative dielectrophoresis changes. The dielectrophoretic force also depends on the volume of the particle or cell: therefore separation based on size and permittivity difference is possible within dielectrophoretic devices.

The first application for CTC isolation from blood using DEP offered 1000 cells/s processing rate with 100% efficiency and 5 to 10 µl min^{-1} flow rate [76]. The flow rate was doubled [77] and quadrupled [78] with optimised designs to reach 20 to 50 µm s^{-1} in a wireless dielectroproretic device using capacitive coupling. Slightly different approach to capture CTCs using a microwell array of 300,000 elements was presented recently with 70-90% capture efficiency depending on the specific cell type and a total processing time of 3 min [79]. Computational analysis revealed that significant improvement in capture efficiency and flow speed can be achieved by a combined magnetophoretic–DEP device [80].

The method is also ideal for blood plasma separation as demonstrated in a capillary device to extract 300 nl plasma from 5 µl blood (yield 6%) with 97% cell removal rate [81]. The processing flow rate shortly reached 10 µl min^{-1} keeping the purity similarly high with 94.2% and the yield increased to 16.5% [82]. Processing whole blood with extremely low voltages (< 1 V) was presented by Chen *et al.* for 69.8% volume separation and an 89.4% removal rate of red blood cells at 5 to 130 µm s^{-1} flow rate and total processing time 5 to 2000 s depending on the flow speed. A capillary driven whole blood plasma extraction device with 15 min maximum processing time producing 33 nl cell free plasma was also demonstrated [83]. Very recently a plasma separation device with moderate flow rates (0.1 to 2 µl min^{-1})

but excellent cell retention capabilities was presented (>95%) [84].

Similarly to the above sorting methods, blood can be separated into other components. A field flow device (a direct implementation of the schematic in Fig. 2.2a) was used for platelet separation from blood with 98.8% efficiency and 2% loss between 130 to 850 µm s^{-1} flow rate [85]. Preliminary results for leukaemia cell separation from blood also shows the versatility of the technique [86].

2.1.2.2 Magnetophoresis

Erythrocytes from blood can be separated using their inherent iron content and magnetizability [87]. Based on the oxygenation level, red blood cells show diamagnetic or paramagnetic properties while the WBCs always exhibit diamagnetic behaviour. Such isolation of red blood cells from other blood components (plasma, white blood cells and platelets) using magnetic field was first demonstrated by Melville *et al.* [88]. Doped PDMS or microwires can form local maxima in magnetic field, enhancing separation in a microchannel [89]. Using 5 µl h^{-1} flow rate 93.5% of the RBCs and 97.4% WBCs were successfully separated. Numerical simulations verified tens of seconds simulation times for RBC extraction from whole blood [90].

Although most type of other cells do not exhibit significant difference in magnetic properties to be utilised for separation, adjustments of the fluid properties or magnetic field can aid separation of other biological entities. Ferrofluids can be used for shape-based magnetic type of sorting when no labelling or inherent magnetic properties are available [91]. With a 6 µl h^{-1} sample flow, equal-volumed round and peanut-shaped particles were successfully separated and findings supported by theoretical considerations. Similar method was applied for *Escherichia coli* and *Saccharomyces cerevisiae* bacteria sorting with 1.5 µl min^{-1} sample flow rate and 98.8% efficiency [92]. A multi-magnet device developed by Zeng *et al.* was used with 0.6 mm s^{-1} flow speed to focus and sort yeast cells from 10 µm polystyrene particles [93]. By mixing paramagnetic ions with the medium size-based separation of cells is possible and was validated U937 lymphoma cells and RBCs by Shen *et al.* using 0.32 µl min^{-1} achieving >90% purity.

2.1.3 Active labelled (bead-based)

To enhance response of target cells to external fields, biomarkers exhibiting electric or magnetic properties can be used to increase applied forces on cells to be sorted. Two approaches are applied for cell labelling: the biomarkers can be attached to the surface of the cells using surface binding properties [94] or the different uptake of nanopartices by cells can be harvested [95].

The first magnetic sorter was presented by Miltenyi *et al.* for sorting 10^9 cells per 15 min with enrichment rates of more than 100-fold and depletion rates several 1000-fold [94, 96]. Using simultaneous fluorescent tagging allows for direct optical analysis of sorted cells after magnetic separation. The group used magnetic labelling and sorting for CD20 positive B lymphocyte separation with enrichment up to 97% [96]. These cells can be used in diagnosis of non-Hodgkin lymphoma [97]. Ferritin-labeled lymphocyte enrichment with $0.28\,\mathrm{mm\,s^{-1}}$ average flow speed was also presented with almost complete depletion of non-target cells (>99%) [98]. The group further improved sorting by using quadrupole magnetic sorting with $4\,\mathrm{ml\,min^{-1}}$ total flow (of which 3% was the sample inflow) for separating CD45 lymphocytes with 28-fold enrichment [99]. Labelling of human T-cells was expanded for CD4+, CD45RA+ and CD34+ surface expressions by Thiel *et al.* processing up to 10^{11} cells in 30 min [100]. Separation of leukocytes from whole human blood at $180\,\mathrm{\mu m\,s^{-1}}$ with a narrow 10 µm wide region containing more than 60% of the leukocytes downstream [101]. As white blood cells (leukocytes) are nucleated, they can be used for DNA analysis as well (ref Dutch). Doubling of capture efficiency for DNA analysis can be achieved with flow rate up to $3\,\mathrm{\mu l\,min^{-1}}$ for T cells, at the cost of reducing cell count to 10 to $150\,\mathrm{ml^{-1}}$ [102]. The authors verified the efficacy of the method by polymerase chain reaction (PCR) of the extracted DNA fragments. As T-cell count is an important surrogate marker for the clinical course of Human Immunodeficiency Virus (HIV) infection, Darabi *et al.* carried out CD4+ lymphocyte separation from 50% diluted blood, with purity >95% and flow speed $50\,\mathrm{ml\,h^{-1}}$ [103].

Separation of fetal nucleated erythrocytes from maternal circulation allows for non-invasive diagnosis [104]. In this research CD45 and CD32 antibody specific beads were utilised to deplete the sample from non-nucleated cells at $1.5\,\mathrm{ml\,min^{-1}}$ and $3.5\,\mathrm{ml\,min^{-1}}$ flow rate. Two stage processing is required to achieve 18 to 184-fold final enrichment ratio, which is dependent on initial cell count. A similar study was

presented for fetal cell isolation using multistage sorting with anti-CD71 binding magnetic beads [105].

Magnetic bead aided sorting was also applied for separation of *Escherichia coli* bacteria from red blood cell suspension with 25 to 40 µl min^{-1} flow rate at efficiency >70% [106]. The method was expanded by Adams *et al.* with different tags to achieve multitarget separation [5]. Three strains of *Escherichia coli* MC1061 cells (anti-T7, streptavidin-binding peptide and no surface marker) were directed to three different outlets with 245 to 523-fold enrichment and 5 ml h^{-1} and 42 ml h^{-1} sample and sheath flow rates, respectively.

Labelling of circulating tumour cells is a challenge, since they observe an epithelial–mesenchymal transition as the cancer goes metastatic, which changes surface properties [107, 108]. However, some progress has been made by labelling the cells with antibodies with epithelial adhesion molecules to allow isolation with 2.5 to 10 ml h^{-1} flow rate and capture rate >53% for various cell concentrations [109]. The same group carried out simulations to improve device design and doubled capture rate with inverted structure with 5 to 10 ml h^{-1} flow rate [110]. Further improvement can be made using micromagnets within the channel to achieve 98% capture rate of a human colon cancer cell line at 2.5 ml h^{-1} flow speed [111]. A different device design with pockets for magnetic CTC collection from PBS suspended RBCs with a single inlet was demonstrated with 90% efficiency and >90% viability at 20 µl min^{-1} flow rate [112]. Combined device with DLD, inertial focusing and magnetic stages allows for fast, label-free separation of CTCs at 10^7 cells s^{-1} [63, 113].

Different endocytosis (uptake) of magnetic nanoparticles of biological entities can also be utilized for sorting [95], monocytes and machrophages are separated with purity >88%, efficacy >60%, throughput 10 to 100 cells s^{-1}.

Kashan *et al.* developed various simulation tools to analyse magnetic sorters for 1 to 10 µl s^{-1} flow rate with beads [114], or how to improve magnetic field by embedded soft elements [115] or to validate scalability [116]. Magnetic particles do not influence the viability and function of cells as investigated by Berger *et al.* [117].

2.1.4 Fluorescence-activated cell sorting

The gold standard method for cell separation is fluorescence activated cell sorting [118, 119]. The target cells are rendered fluorescent using specific surface binding antigens

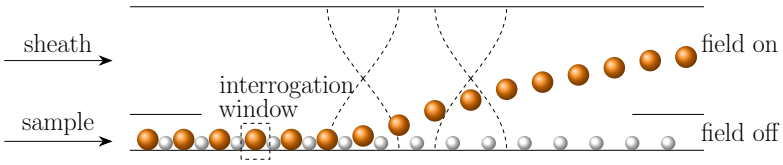

Figure 2.3: Fluorescence activated cell sorting. The external field is denoted by the dashed waves. Arrows indicate the direction of flow

or chemical groups and passed through the device. Series optical interrogation of the cells in a one-by-one manner determines a target by its fluorescence level and activates an actuation mechanism to steer the particle towards the target region as illustrated in Fig. 2.3. The external force can be arbitrary.

HeLa cells were sorted at a few events per second rate with flow rate of $0.55\,\mathrm{mm\,s^{-1}}$ using electric activation as high as 600 V [120], that was later reduced to a few V range [3]. A device with modified electrode and channel geometry allowed for separation of different strains of *E. coli* with increased event rate of a few kHz, however, requiring as high voltages as 1.8 kV [121]. Acoustic actuation by as low as 8 $V_{\mathrm{p-p}}$ was utilised for pancreatic β cell separation with 27 cells/s rate [6]. The event count was shortly increased to 1000 cells/s while maintaining the same voltage range with an acoustic FACS [122]. CTC isolation with as high as 100% efficiency is possible by optically induced dielectrophoresis with 1 to $5\,\mathrm{\mu l\,min^{-1}}$ flow rate [123].

A few other FACS research are discussed in the acoustic section, where more details of mechanism behind acoustics is required.

2.2 Acoustic manipulation and sorting

A brief overview on the principle of acoustic radiation force is given here to facilitate understanding of the various sorting methods in this section, however a more detailed discussion is provided in Section 3.4.

Microparticles introduced in an acoustic field act as scatterers. The incident and scattered acoustic fields result in a second-order time-averaged primary radiation force [124–128]. The analysis of the acoustic radiation force dates back to the work of King [124] where the treatment of both standing and travelling acoustic fields was carried out on incompressible spheres, much smaller in size than the wavelength of the field, at the Rayleigh scattering limit ($a_{\mathrm{p}} \ll \lambda$). Yosioka and Kawasima [125] extended this discussion by introducing compressibility of the spheres. These results

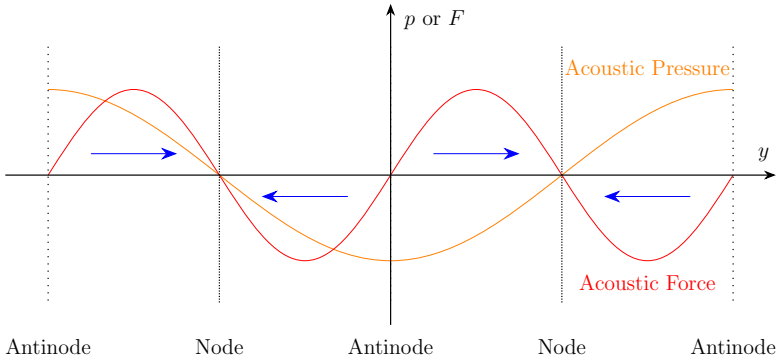

Figure 2.4: The acoustic pressure and the resulting acoustic radiation force; the particles considered to have positive acoustophoretic contrast factor therefore the force moves them towards nodes, for negative contrast factor, *vice versa*

were summarized and reformulated by Gorkov [126] and a compact equation for the acoustic radiation force in standing wave fields was provided as a gradient of the acoustic potential. Recently, Settnes and Bruus [127] included viscosity of the surrounding media in the analytical treatment and found this contributed significantly to the magnitude of forces arising from travelling waves.

Using Gorkov's approach, the primary acoustic radiation force in a standing wave can be given as the gradient of a potential as

$$U_{\mathrm{ac}}(\mathbf{r}_{\mathrm{p}}) = \frac{4a_{\mathrm{p}}^3\pi}{3}\left[\frac{f_{1,\mathrm{p}}}{2}\kappa_0\langle p_{\mathrm{in}}(\mathbf{r}_{\mathrm{p}})^2\rangle - \frac{3f_{2,\mathrm{p}}}{4}\rho_0\langle \mathbf{u}_{\mathrm{in}}(\mathbf{r}_{\mathrm{p}})\cdot\mathbf{u}_{\mathrm{in}}(\mathbf{r}_{\mathrm{p}})\rangle\right] \tag{2.4a}$$

$$\mathbf{F}_{ac} = -\boldsymbol{\nabla}U_{\mathrm{ac}} \tag{2.4b}$$

$$f_{1,\mathrm{p}} = 1 - \kappa_i/\kappa_0 \tag{2.4c}$$

$$f_{2,\mathrm{p}} = \frac{2\left(\rho_{\mathrm{p}}/\rho_0 - 1\right)}{2\rho_{\mathrm{p}}/\rho_0 + 1} \tag{2.4d}$$

where a_{p} is the particle radius, κ and ρ are compressibility and density, with index 0 and index i denoting a fluid and particle property, respectively. The total incident acoustic field is given by the pressure p_{in} and velocity field $\mathbf{u}_{\mathrm{in}}$ and finally f_1 and f_2 are called the monopole and dipole scattering coefficients, respectively. The resulting primary acoustic radiation force in a bulk one-dimensional standing wave is

$$\begin{aligned}\mathbf{F}_{\mathrm{ac}} &= \frac{4\pi a^3}{3}\frac{u_0^2\rho_0}{4}k\left[f_1 + \frac{3}{2}f_2\right]\sin(2ky)\hat{\mathbf{y}} \\ &= V_{\mathrm{p}}E_{\mathrm{ac}}k\Phi_{\mathrm{AC}}\sin(2ky)\hat{\mathbf{y}} = c_{\mathrm{ac}}\sin(2ky)\hat{\mathbf{y}}\end{aligned} \tag{2.5a}$$

$$\Phi_{\mathrm{AC}} = f_1 + \frac{3}{2}f_2 \tag{2.5b}$$

with energy density given as $E_{\mathrm{ac}} = p_0^2\kappa_0/4 = u_0^2\rho_0/4$. Some terms are collected to volume, V_{p}, and acoustic contrast factor, Φ_{AC}. Particles generally have positive

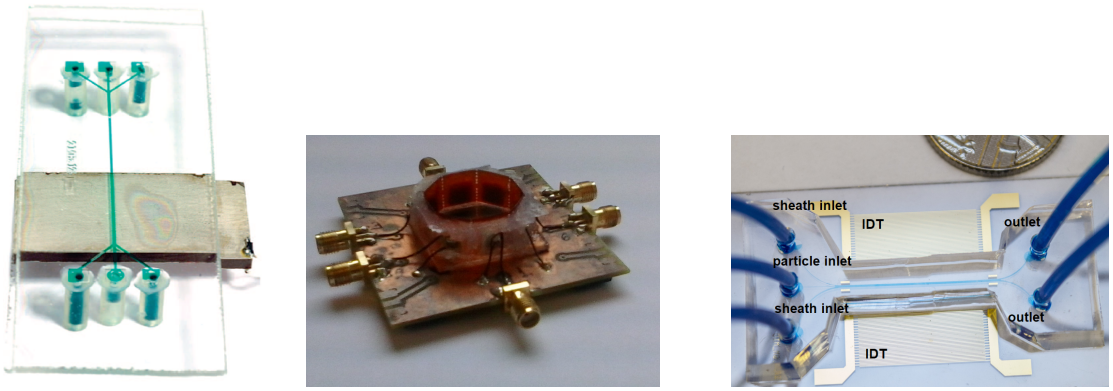

(a) (b) (c)

Figure 2.5: The most commonly used types of acoustic manipulation and sorting devices in microfluidics (a) a BAW resonator device with transducer mounted on the bottom, reproduced from [132] (b) a BAW non-resonant device with transducers on the sides (c) a surface wave device

acoustic contrast factor, and therefore, when subjected to an acoustic standing wave, they experience a force that steers them towards the pressure node [127–129]. The pressure and force distribution in a bulk acoustic wave is illustrated in Fig. 2.4. Some materials such as air bubbles and lipid vesicles have density and compressibility values that result in a negative contrast factor, which means that these objects agglomerate at the pressure antinodes [130]. Thus, a separation occurs if particles with acoustic contrast factors of different signs are present, termed binary acoustophoresis [130,131]. The currently used acoustic manipulation and separation devices are usually grouped by the type of wave propagation used (Fig. 2.5): in bulk acoustic wave (BAW) devices, the wave propagates in the whole of the solid and liquid media [130], whereas for surface acoustic wave [129] devices the wave propagation is confined to the top of the substrate material. However, as a substantial portion of BAW devices work in resonant mode [130–132], supporting only acoustic standing waves of fundamental frequencies, in this thesis only the non-resonant devices are named simply BAW devices to avoid confusion. These devices are usually have special structures, materials or excitation signals to overcome resonance condition [133–135]. The resonant devices are explicitly referred to as *resonant* BAW devices.

The acoustic vibrations in these devices are excited using piezoelectric materials, which convert applied electrical field to mechanical strain and *vice versa*. An applied sinusoidal voltage results in periodic deformation of the material, giving rise to acoustic waves. The most commonly used acoustic manipulation devices use either a single transducer and utilize a travelling wave or resonant mode of the device, or

have more electrodes to generate more complex fields.

In most acoustofluidic devices, the only force counteracting the acoustic radiation force is the viscous drag force

$$\mathbf{F}_{\text{drag}} = -6\eta\pi a_{\text{p}}\dot{y} = -c_{\text{visc}}\dot{y} \tag{2.6}$$

where η is the fluid viscosity, and all constants can be grouped in c_{visc}. Newton's second law can be written for the force balance, and by neglecting inertial effects [128, 136] the particle trajectories in acoustic standing waves can be obtained in the form of

$$y(t) = \frac{1}{k}\tan^{-1}\left[\tan(ky_0)\exp\left(\frac{2kc_{\text{ac}}}{c_{\text{visc}}}t\right)\right] \tag{2.7}$$

where y_0 is the initial particle position in the microchannel. This equation predicts three modalities of sorting: size, density and compressibility. As particles that differ in any of these properties exhibit different trajectories (given by Eq. 2.7) devices can be developed collecting the target and non-target particles at their respective final position. These acoustic sorting methods are usually referred to as free flow acoustophoresis.

As the main goal of this thesis to develop and expand knowledge on dynamic acoustic sorting methods I separate the literature review into two groups, static techniques and dynamic approaches. The definition I use for static devices is that they have a spatially dependent, but temporally invariant time-averaged acoustic radiation force, i.e.

$$\langle\mathbf{F}_{\text{ac,static}}\rangle = \mathbf{F}(\mathbf{r}_{\text{p}}) \tag{2.8}$$

whereas in dynamic devices the time-averaged field might have a temporal dependence as well

$$\langle\mathbf{F}_{\text{ac,dynamic}}\rangle = \mathbf{F}(\mathbf{r}_{\text{p}}, t) \tag{2.9}$$

where the scale of temporal dependence must be much greater than the oscillation period to allow for the time-averaging over a period.

2.2.1 Static acoustic sorting methods

Sorting by static acoustic sorting methods is usually achieved by time-of-flight difference of various particles or cells when subjected to an acoustic field as outlined

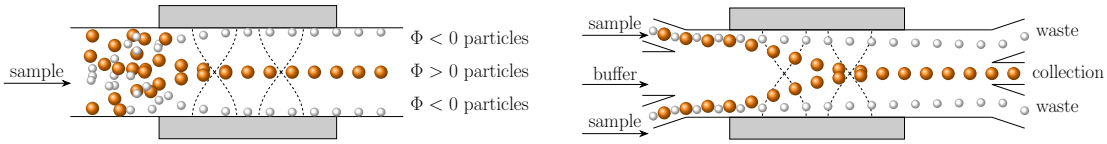

(a) Binary acustophoresis (b) Principle of free flow fractionation

Figure 2.6: The most common static acoustic sorting methods. In all figures the grey rectangles represent the acoustic transducers, arrows indicate flow direction

above. Most commonly methods employ an acoustic standing wave [129–131,137,138], travelling wave [139–141] or a combination of the two [142, 143].

The simplest binary separation (Fig. 2.6a) based on different sign of contrast factor was presented by Petersson *et al.* in a resonant BAW device for lipid particles and RBCs [130]. The 0.3 ml min^{-1} flow rate and 2 MHz operating frequency resulted in separation efficiencies >70% for processing diluted blood of 1%–5%. Extracellular vesicles prepared with different phospholipid bilayer exhibit a temperature dependent acoustic contrast factor: at a certain temperature the two populations show a sign difference, allowing for separation [144]. Separation was achieved after 30 s within the 1.4 MHz resonant cavity. However, most cells or blood components inherently exhibit positive acoustic contrast factor, limiting the applicability of the binary sorting strategy [128, 130]. To overcome this issue, Cushing *et al.* developed crosslinked silicone particles that exhibit negative contrast factor in water, serum or blood [145]. Therefore, achieving the same deterministic sorting based on the difference in final trapping location is possible after surface functionalization of the spheres. The drawback of the technique as mentioned for general labelled techniques is the long processing time and the need for specific antigens or surface groups to be available.

The Laurell group applied the standing wave method for continuous flow separation of cells that have the same sign of acoustic contrast factor, but different magnitudes due to their size or physical properties [131]. This research on free-flow separation (Fig. 2.6b) of blood components (platelets, leukocytes and RBCs) was carried out with 2 MHz frequency resonant device at a lower flow rate 0.1 ml min^{-1}. Although moderate separation efficiencies were achieved overall (>40%) most of the platelets (>80%) were steered to one outlet. Blood separation was also demonstrated in a cheap thermoplastic resonator device using 1.71 MHz frequency and 50 µl min^{-1} flow rate, achieving efficiency close to 90% [146]. The flow rate for platelet enrichment was significantly increased to 10 ml min^{-1} using a 230 kHz resonant cavity while

maintaining high platelet recovery (>85%) and RBC/WBC removal (>80%) [147]. Cancer cell separation with 94.8% efficiency and 97.8% purity was presented in a 2 MHz silicon resonator device operating at 100 µl min^{-1} flow rate [108]. Platelet rich plasma was generated on macroscale in a 20 ml syringe by sonication at 4.5 MHz for 10 min [148].

Time-of-flight sorting of blood components was investigated with a standing surface acoustic wave (SSAW) device as well [149]. The device utilised a 7.54 MHz frequency standing wave and at 0.25 µl min^{-1} flow rate 99.9% of the unwanted cells (RBCs and WBCs) were removed while retaining 74.1% of platelets at the target outlet. As high shear rates might result in platelet activation during sorting, an extensive study on the effect of ultrasound on platelets was carried out recently [150].

Yet the very same principle and device design was applied for *E. coli* bacteria separation from peripheral blood mononuclear cells in a 13 MHz standing surface wave device [151]. Using 0.5 µl min^{-1} flow rate the authors could separate the pathogens with 95.65% purity. Density-based sorting in SSAW device was presented by Nam *et al.* by preparing alginate beads containing different number of cells, thus altering the density [152]. The 3.94 MHz frequency device achieved 97% recovery and 99% purity processing 2300 beads per second. Microvesicles were also successfully enriched using a SSAW device at 38.5 MHz with 2.8 mm s^{-1} flow speed to achieve efficiency and recovery both >90% [153]. Acoustofluidic separation of prostate specific DNA fragments was carried out at 1.99 MHz with a flow rate of 500 µl min^{-1}, with the drawback of need for specific antigen coated particles [154]. The results for surface wave devices were recently investigated using numerical simulations accounting for attenuation within the channel [155, 156]. A coupled finite element piezoelectric and acoustic numerical simulation method was also used to gain further insight to SSAW sorting [157].

Acoustic radiation forces in travelling acoustic waves scale with the sixth power of particle radius [126–128]. Although this provides a higher sensitivity to particle size compared to standing waves, at the same time the magnitude of the force is smaller [127]. This was only overcome recently using a focused surface wave transducer to achieve CTC sorting from diluted blood [158]. The device used two-stage acoustic processing: a 29.78 MHz SSAW for pre-focusing and a 38.74 MHz travelling surface acoustic wave (TSAW) for sorting with a flow rate of 0.3 µl min^{-1} to achieve 90% separation efficiency. A two-stage travelling surface wave device

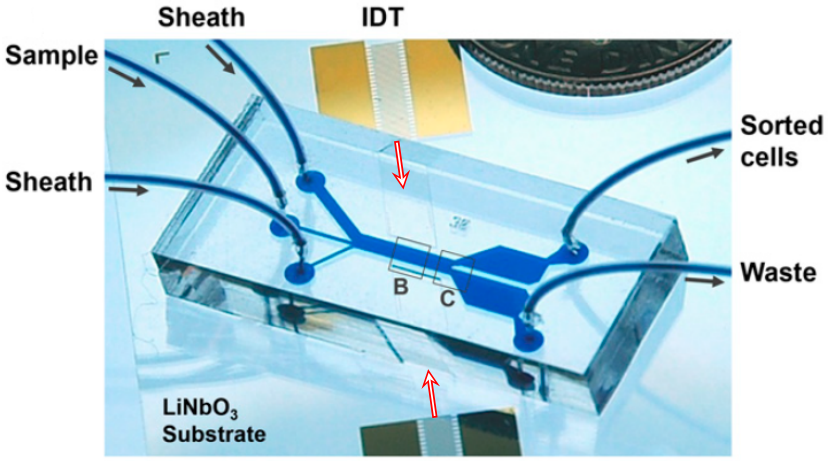

Figure 2.7: The tilted transducer sorting method. Although the principle is similar to free-flow acoustic sorting techniques, the tilted pressure nodes alleviate the $\lambda/4$ separation distance of particles. Red arrows indicate the waves emitted from the transducers. Reproduced from [162]

was used to demonstrate bandpass sorting of medium-sized particles from a sample mixture [159], but similar technique for cell sorting has not been performed yet. Above the Rayleigh limit ($a_\mathrm{p} \gg \lambda$) particles have frequency dependent contrast factor subjected to travelling waves [160], that can lead to sub-micron size difference separation [140].

The standard time-of-flight sorting can be improved by either grooves at the top of the microchannel [161] or by tilting the transducers with respect to the channel axis [162, 163]. Although the groove method was only presented for an acoustic FACS-type sorting it shows great potential in extending the separation distance between target and non-target particles [161].

The tilted transducer approach (Fig. 2.7) was investigated and applied for various target cells by the Huang group [162]. The main advantage of the method is that the separation distance between target and non-target particles is no longer limited to $\lambda/4$, but can be arbitrary as the trapped particles follow the slanted pressure nodes across the channel. MCF-7 breast cancer cells were separated from leukocytes with $9\,\mu\mathrm{l\,min^{-1}}$ flow rate and 20 MHz operating frequency to achieve 71% recovery rate and 84% purity. Numerical simulations also revealed the optimum inclination angle of 30°. The group applied the method to separate CTCs of low concentration (100 cells per ml) with recovery rates better than 83% while increasing the flow rate to $20\,\mu\mathrm{l\,min^{-1}}$ [163]. The technique was also successfully used for *E. coli* bacteria separation from red blood cells using $1\,\mu\mathrm{l\,min^{-1}}$ flow rate and 19.54 MHz

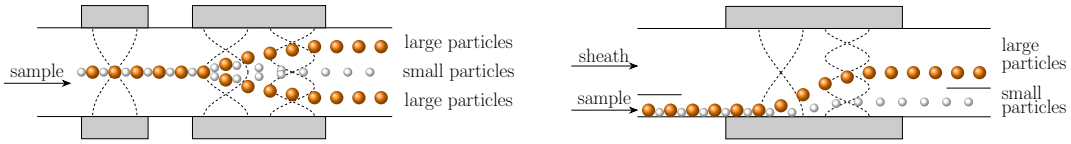

(a) $2f_0$–$3f_0$ switching with acoustic pre-focusing

(b) f_0–$3f_0$ frequency switching with sheath flow

Figure 2.8: Some of the available dynamic acoustic sorting methods. In all figures the gray rectangles represent the acoustic transducers. Arrows indicate the direction of flow

frequency with purities of the bacteria outlet and RBC outlet both around 96% [164]. Furthermore, isolation of exosomes from an extracellular vesicle mixture with a purity of 98.4% was achieved using the tilted surface wave approach at 39.4 MHz with flow rate $4\,\mu l\,min^{-1}$ [165]. Finally the method can also be used for inflammatory cell extraction from sputum sample [166], cell washing and medium exchange [167] and for coating particles or HeLa cells [168]. The Neild group demonstrated filtration of particles using the tilted transducer approach, where the high frequency beam essentially blocks the large particles to pass through the channel and allow the smaller particles to exit only [169].

Finally a method using travelling waves was presented to achieve bidirectional sorting: the target particles can exit at either outlet by changing the frequency [170]. However, the separated particle size is constrained with this method and it has not been applied to cells yet. This limitation has been alleviated within the research of this thesis [**Simon2018APL**].

2.2.2 Dynamic acoustic sorting methods

Although a recent review paper [171] on dynamic acoustic particle manipulation methods lists numerous different approaches, most of these are only used for particle trapping and positioning. The grouping of techniques suggested by Drinkwater is therefore slightly modified to allow more focus on the actual particle or cell sorting and separation methods.

The simplest approach to achieve reconfigurability and dynamic radiation force is to use on-off switching, preferably with multiple transducers. This was presented for 3D fibre printing using two sets of orthogonally aligned transducer pairs where the active transducer pair was switched during the process allowing for various

fibre patterns to be achieved [172]. By definition, any FACS method using acoustic actuation can be viewed as a dynamic technique: the particles are focused at a certain position along the microchannel length and exit at a certain outlet, experiencing zero acoustic radiation force. When target particles are detected, these can be individually steered using travelling [173], or standing waves [1] of different types as validated by microparticles. A highly focused travelling wave (actuation width $\approx 50\,\mu m$) was applied for SYTO 9 fluorescent dye stained MCF-7 cancer cells with higher than 86% recovery from diluted blood with kHz rate [2]. Focused standing waves can increase the throughput of the sorting to as high as 13800 events per second as shown for HeLa cells by the Huang group [7, 174]. An actuation mechanism for steering HaCaT cells (human keratinocytes), fibroblasts from mice and MV3 melanoma cells was presented using tapered surface wave IDTs (of frequencies between 140 and 150 MHz) for several kHz actuation rate [175, 176].

As Drinkwater suggests [171], another possibility—that is especially handy for resonant devices—is to move from the first resonance frequency to higher harmonics or switching between different harmonics rapidly. This idea was used first to concentrate particles in a cylindrical tube (with a transducer at the bottom and reflector on the top) by cycling through higher order harmonics from f_n to f_m [177]. As a result, the pressure nodes at the bottom and the top of the tube follow deterministic spatial shift and concentrate particle clumps at the edges. Relatively low frequencies (685 to 715 kHz) and large 200 µm duroplast particles were used in the research. The idea was utilized by Oberti *et al.* to achieve trapping at locations not directly defined by the resonance frequencies [178]. By applying the rapid switching between different modes, the particles obtain positions not directly defined by either frequency.

In surface wave devices the channel is of soft material and no resonances occur within the cavity. Therefore frequency switching has to be viewed differently, but nevertheless has been applied successfully for sorting purposes. Wideband chirped transducers allow for various excitation frequencies where the trapping locations are different. Therefore, switching of target cells to various outlets is possible [179]. Combining the method with a detection stage, FACS separation of HL-60 human promyelocytic leukemia cells is presented up to 222 events per second [180].

The direct application of frequency mode-switching for particle separation was presented by the Hill group [181, 182]. The second harmonic frequency produces two pressure nodes off the centreline of the channel, while the third mode results

in three pressure nodes, the middle one aligned with the channel centreline (Fig. 2.8a). Particles are initially focused at the centre. By rapidly switching between these two modes, the large and small particles experience the trapping pull from the side modes differently, and eventually the large particles will be separated out from the heterogeneous mixture. The idea was further developed (Fig. 2.8b) for particle sorting up to 100% efficiency (with diameter ratio of 2) and 90% purity [183]. This method has not been applied for cells yet.

The final group of techniques all use approaches where the resonant behaviour of the device is suppressed by various material layers or changes in geometry, allowing for phase modulation or frequency modulation. Furthermore, by looking at a phase modulated sinusoidal signal

$$\sin(\omega t + \varphi(t)) = \sin\left[\left(\omega + \frac{\varphi(t)}{t}\right) t\right] \tag{2.10}$$

it can be rearranged as a frequency modulation. This correspondence will be used in the following discussion as well.

Using a slightly different frequency on two opposing transducers, a quasi-standing wave is produced, which traps particles at the nodes while the pressure pattern shifts laterally [184, 185]. The detailed theoretical discussion and validation is given in Chapter 4. This method was applied to harvest 9 µm particles around 3 MHz frequency with 20 Hz frequency difference [186]. Translation of clumps formed from human erithrocytes and *Saccharomyces cerevisiae* (yeast) bacteria [187] or *E coli* bacteria [188] were also presented as applications of the technique. Kozuka *et al.* investigated precise translation of particles using tetrahedral transducer arrangements combined with frequency hopping [189,190]. Peterson *et al.* define a critical movement speed for various particles and based on this envisage an actual sorting method, where different sized cell components can be sorted [191]. This sorting method was only presented three decades later for microfluidics for HaCaT cell and 2 µm polystyrene particle separation with 83% efficiency [192]. One result of this thesis is improvement of this method using non-continuous quasi-standing waves to achieve higher efficiency while reducing the ratio of size of the sorted entities [**Simon2018APL**].

As mentioned before, a similar actuation is achieved using phase modulation. However—possibly due to lack of precise phase control of dual channel instruments—these techniques were only presented recently. Bernassau *et al.* used a matching layer between the transducer and the fluid chamber in their bulk acoustic wave

device to suppress reflections and resonant behaviour [193]. The octagonal shaped chamber with 8 transducers mounted on the sides allowed for various 2D trapping patterns [133,194] or arbitrary translation [134]. They also utilised a phase modulation pattern to be able to sort microparticles or dorsal root ganglion cells from debris within the non-resonant bulk acoustic wave device (Fig. 2.5c) [195]. Another main contribution of the thesis is to develop a theoretical model for the phase modulated sorting and successfully apply it for continuous flow sorting [**Simon2017Bio**].

More complex separation methods were also presented for surface wave devices such as combination of standing and travelling waves with frequency sweep in the absence of flow [142] however, no assessment for cell sorting is available.

2.3 Chapter summary

In this chapter the main groups of cell separation techniques in microfluidics have been reviewed. A selection of the state of the art devices representative for the taxonomy of the chapter is listed with advantages, disadvantages and figures of merit in Table 2.1. The passive methods generally show high flow rates (reaching $\mathrm{ml\,min^{-1}}$) and excellent specificity (efficiency and purity both >99%) with small discrimination differences, but they lack reconfigurability and therefore their applicability in a general bench-top setup is limited. Labelled techniques can provide similar high flow rates and efficiencies, however, require an additional preprocessing step and the specific surface binding is not available for all cell types. Fluorescence activated cell sorting methods have been recently shrunk in size, but still require many off-chip components, such as fluorescence microscope or control system for sorting, and are inherently serial processing. Active label-free methods offer a good alternative to other techniques with reconfigurability while possibility of small device size. Of these methods, acoustic techniques are especially versatile, for their sorting capabilities based on size, density or compressibility difference.

Device group	Device type	Sorting parameters	Advantages	Disadvantages
Passive	Cross-flow filtration [8]	$20\,\mu l\,min^{-1}$, pass RBC >60%, trap WBC >70%	Non-clogging, continuous operation can be achieved	Limited to size-based separation, no reconfigurability
Passive	Deterministic lat. displacement [31]	$400\,\mu m\,s^{-1}$ flow, up to 100% efficiency, 10 nm resolution	Extremely fine size discrimination in continuous flow	No reconfigurability, only for size-based separation
Passive	Pinched flow fractionation [50]	Flow rate $10\,\mu l\,h^{-1}$, 96% efficiency, 93.6% purity	Adjustable for various target size intervals	Requires focussing flow; non-spherical entities pose a challenge
Passive	Hydrodynamic filtration [52]	$50\,\mu l\,min^{-1}$ flow rate with up to 96% efficiency	Single inflow required; multiple target groups can be extracted	Complex device design, limited maximum size and resolution
Active l. free	Electrophoresis [85]	98.8% efficiency, maximum flow rate $850\,\mu m\,s^{-1}$	High specificity, effect of size variations is low; no labelling	Difference of electrical properties needs to be characterised
Active l. free	Magnetophoresis [94]	93.5% efficiency, 97.4% purity, $5\,\mu l\,h^{-1}$ flow rate	High specificity, effect of size variations is low; no labelling	Inherent difference of magnetic properties is required
Active l. free	Acoustic [149]	$0.25\,\mu l\,min^{-1}$, 99.9% purity, 74.1% efficiency	No labelling, large forces, reconfigurable	Complex device design, moderate cost
Active l. free	Acoustic [152]	97% recovery, 99% purity, $8\,\mu l\,min^{-1}$	No labelling, large forces, reconfigurable, density-based	Complex device design, moderate cost
Active labelled	Magnetic labelled [111]	$2.5\,ml\,h^{-1}$, 98% capture rate	Very high specificity	Extra processing step; no general labelling; changes cell behaviour
FACS	FACS [123]	up to 100% efficiency, $5\,\mu l\,min^{-1}$	Can be used on otherwise challenging to separate cells	Serial processing, labelling is extra processing time, bulky and expensive equipment

Table 2.1: Overview of microfluidic sorting methods

Chapter 3

Theory of fluid flow, acoustic manipulation and piezoelectricity

3.1 The Navier–Stokes equation as a basis of fluid flow and acoustic wave propagation

Fluid flow, acoustic wave propagation, fluid mixing and generally any physical process involving fluids can be described by the Navier–Stokes equation or one of its special simplified forms [30, 196]. The compressible form of the Navier–Stokes equation in Eulerian (fixed) reference frame is given as

$$\rho\left[\frac{\partial}{\partial t}\mathbf{u}+(\mathbf{u}\cdot\boldsymbol{\nabla})\mathbf{u}\right]=-\boldsymbol{\nabla}p+\eta\nabla^2\mathbf{u}+\left(\frac{1}{3}\eta+\zeta\right)\boldsymbol{\nabla}(\boldsymbol{\nabla}\cdot\mathbf{u})+\rho\mathbf{g}+\rho_{\mathrm{el}}\mathbf{E} \qquad (3.1)$$

where the terms from left to right correspond to variation of inertia, convection of inertia, pressure gradient, diffusion, compressibility, gravitational field and electric field (or other external field due to a body force). The variables ρ, $\mathbf{u}$, p, η, ζ, ρ_{el} correspond to density of the fluid, fluid particle velocity, pressure, dynamic viscosity of the fluid, second (or bulk or volume) viscosity of the fluid, and electric charge density, respectively. The second viscosity is sometimes reformulated as $\zeta=\beta+\frac{2}{3}\eta$ with β being the second viscosity coefficient. In the following sections the appropriate simplifications are applied to this equation to arrive at laws describing acoustic wave propagation or fluid flow in microchannels.

3.2 Microfluidic flow profile in a rectangular microchannel

It is well known that the Navier–Stokes equation is generally notoriously difficult to solve. However, for some special fluid flow, the equation can be solved analytically or numerically efficiently with small error. One special case is the Hagen–Poiseuille flow, a pressure-driven, steady-state flow, which is of utmost importance for microfluidic processes [30]. In the case of the Hagen–Poiseuille flow the channel (directed along x) is assumed to be rigid, straight and much longer than its cross-sectional dimensions and the pressure difference is applied between the two ends. As the channel is straight and have constant cross section, the problem is spatially invariant in the x direction. Moreover, the gravitational field can be assumed to be balanced by hydrodynamic forces, and therefore no forces act in the yz plane. The two conditions result in a velocity field only dependent on the y and z position and directed along the x axis: $\mathbf{u} = u_x(y,z)\hat{\mathbf{x}}$. Now referring to the original version of the Navier–Stokes equation, significant simplifications can be made: the flow is assumed to be steady-state, therefore $\frac{\partial \mathbf{u}}{\partial t} = 0$; the convection term is $(u_x(y,z)\hat{\mathbf{x}} \cdot \boldsymbol{\nabla})u_x(y,z)\hat{\mathbf{x}} = u_x(y,z)\frac{\partial}{\partial x}u_x(y,z)\hat{\mathbf{x}} = 0$ since it is independent of x; the fluid is assumed to be incompressible, therefore the third term on the right hand side is neglected; and finally we neglect or balance any external field. The substantially simplified equation [30] reads

$$0 = -\boldsymbol{\nabla} p + \eta \nabla^2 \mathbf{u} \tag{3.2a}$$

$$\eta \left[\frac{\partial^2}{\partial x^2} + \frac{\partial^2}{\partial y^2} \right] u_x(y,z) = \frac{\partial p}{\partial x} \tag{3.2b}$$

which combined with the no-slip boundary condition ($\mathbf{u} = 0$) at the microchannel walls can be used to obtain the velocity profile for any cross-sectional area either theoretically or numerically. Although the rectangular cross-section is highly symmetric, no analytical closed-form equation has been provided yet, but the solution is written as an infinite sum of Fourier series solution:

$$\mathbf{u}_x(y,z) = \frac{4h^2 \Delta p}{\pi^3 \eta L} \sum_{n,\text{odd}}^{\infty} \frac{1}{n^3} \left[1 - \frac{\cosh\left(\frac{n\pi y}{h}\right)}{\cosh\left(\frac{n\pi w}{2h}\right)} \right] \sin\left(\frac{n\pi z}{h}\right) \tag{3.3a}$$

$$Q = \frac{4h^2 \Delta p}{\pi^3 \eta L} \sum_{n,\text{odd}}^{\infty} \frac{1}{n^3} \frac{2h}{n\pi} \left[w - \frac{2h}{n\pi} \tanh\left(\frac{n\pi w}{2h}\right) \right] = Q_{\text{const}} S \tag{3.3b}$$

$$Q_{\text{const}} = \frac{4h^2 \Delta p}{\pi^3 \eta L} \tag{3.3c}$$

$$S = \sum_{n,\text{odd}}^{\infty} \frac{1}{n^3} \frac{2h}{n\pi} \left[w - \frac{2h}{n\pi} \tanh\left(\frac{n\pi w}{2h} \right) \right] \tag{3.3d}$$

where w, h are the width and height of the channel and Q denotes volumetric flow rate. The separation of the constant term Q_{const} and the sum S allows for linking the volumetric flow rate and velocity profile without any knowledge of the channel length L or pressure gradient Δp. The flow follows a parabolic profile: it is maximal in the middle of the channel and zero at the channel walls. Equations 3.3 are used for device design and simulation in Chapter 5 and 6.

3.3 Piezoelectricity

Piezoelectricity is the coupling effect between electrical and mechanical states within a crystalline material [197]. The generation of an electrical field due to applied mechanical stress is termed the direct piezoelectric effect, while the reverse process is termed the inverse piezoelectric effect. Piezoelectricity is useful for simple generation of acoustic waves [198] and various sensing and actuation purposes [199] [200]. The effect can be described by matrix equations, the two most commonly used being the so-called strain-charge and stress-charge form, the difference is between the material property matrices due to the different assumption of the zero state. The strain-charge form is given as

$$\mathbf{S} = \mathbf{s_E} \cdot \mathbf{T} + \mathbf{d}^{\mathrm{T}} \cdot \mathbf{E} \tag{3.4a}$$

$$\mathbf{D} = \mathbf{d} \cdot \mathbf{T} + \boldsymbol{\epsilon_T} \cdot \mathbf{E} \tag{3.4b}$$

where $\mathbf{S}$, $\mathbf{s_E}$, $\mathbf{T}$, $\mathbf{d}$, $\mathbf{E}$, $\mathbf{D}$, $\boldsymbol{\epsilon_T}$ are the strain, compliance, direct piezoelectric effect matrix, electric field, electric charge density displacement, and permittivity, respectively, and superscript T denotes matrix transposition [197]. The subscript $\mathbf{E}$ and $\mathbf{T}$ denote constant fields when measuring the material parameter matrices — this would be different for the stress-charge form of equations.

The dipole domains within the crystal are aligned using a strong external electric field to obtain a highly polarized crystal with large electromechanic coupling coefficient during a poling process. The strong coupling generally allows for thickness mode or shear thickness mode operation to fabricate piezoelectric transducers: the applied

electric field is either parallel [201] or perpendicular [202] to the poling direction. Thus bulk acoustic wave transducers for sensing and actuation purposes are readily available [200].

The analysis of surface acoustic wave piezoelectric devices is more complex due to the nature of the applied electric field relative to the poling direction. In these devices the electrodes are formed on the top of the substrate material and therefore the applied potential results in curved electrical fields that give rise to a combined acoustic wave field. Depending on the electrode geometry and substrate thickness, the resulting wave can be a Rayleigh wave, Lamb wave or Love wave [203]. Assuming substrate thickness and electrode apertures larger than the wavelength, mainly Rayleigh waves are excited. These are characterized by the combination of a longitudinal and a vertical shear component, and is usually confined to a few wavelength depth of the surface of the substrate [203]. The waves are also termed as elliptical waves as a fixed point of the substrate undergoes elliptical motion, which is either clockwise or counter-clockwise depending on the depth. This brief discussion of surface waves underlines its a complex phenomenon, but with simplifications of its nature it can be comfortably applied to design and simulate microfluidic manipulation devices as described in Section 5.1 and Chapter 6.

3.4 Acoustic variables and wave propagation

In the following the basic measures of acoustic wave propagation will be described along with the primary acoustic radiation forces that are used to manipulate microparticles subjected to an acoustic field following two textbooks [205] [204]. The wave propagation, which is an oscillation in space and time $y(x,t)$, can be characterized by its (temporal or spatial) frequency, period, wavelength, wave number, and speed of sound. The period of oscillation T is the shortest time

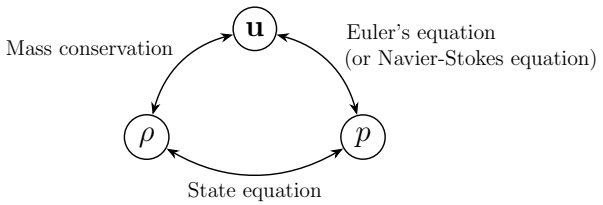

Figure 3.1: Representative variables in acoustics and the equations linking them. Reproduced from [204]

such that $y(x,t) = y(x,t+T)$ for any given x. Its reciprocal, the temporal frequency ($f = 1/T$) represents the speed of oscillation in time. The rate of phase change with respect to time, the angular frequency ω, can be obtained from the frequency as $\omega = 2\pi f$ since the phase is changed by 2π during a period of time T. Similar arguments can be made for spatial oscillation: the wavelength λ describes the shortest distance such that $y(x,t) = y(x+\lambda,t)$ and its reciprocal is (the rarely used) spatial frequency $\xi = 1/\lambda$. The speed of phase change with respect to space, the wave number k is given as $k = 2\pi/\lambda$ since again a total 2π phase change is obtained moving x by λ. When the media is considered to be non-dispersive, the relation between spatial and temporal parameters is linear, and correspond to the longitudinal speed of sound propagation c:

$$c = \lambda f = \frac{\lambda}{2\pi} 2\pi f = \frac{\omega}{k} = \frac{f}{\xi} \tag{3.5}$$

In the following discussion the subscript 0 will be used for parameters of a media, such as c_0 or κ_0 and subscript 1 or p corresponds to parameters of the particles suspended in the fluid. Furthermore, as linear acoustics are considered, the frequency of oscillation (f or ω) is considered to be constant throughout the whole domain of sound propagation.

In acoustics the three representative variables that are used to describe the field are the pressure, particle velocity and density. These can be linked by the mass conservation law, Euler's equation (or the Navier–Stokes equation) and the state equation (Fig. 3.1).

The mass conservation law states the continuity of mass for any differential volume of the liquid and links density and fluid particle speed. The mass flux through the surface of this volume can be expressed as

$$\int_S (\rho \mathbf{u}) \cdot \mathrm{d}\mathbf{n} = \int_V \boldsymbol{\nabla} \cdot (\rho \mathbf{u}) \mathrm{d}V \tag{3.6}$$

where Gauss' theorem has been used to convert the surface integral to a volume integral. The mass change inside the volume must be balanced by the mass flux through the surface, since mass cannot appear nor disappear:

$$\frac{\partial}{\partial t} \int_V \rho \mathrm{d}V = \int_V \frac{\partial}{\partial t} \rho \mathrm{d}V = -\int_V \boldsymbol{\nabla} \cdot (\rho \mathbf{u}) \mathrm{d}V \tag{3.7}$$

where the volume is fixed therefore the order of integration and differentiation can be exchanged. The minus sign denotes that an outward flux (positive divergence)

results in a decrease of the mass inside the volume. Since the above equation should hold for any arbitrary (but fixed) volume, the integrands must be the same, resulting in the differential form of the mass conservation law:

$$\frac{\partial}{\partial t}\rho = -\boldsymbol{\nabla}\cdot(\rho\mathbf{u}) \tag{3.8}$$

A similar derivation can be used to obtain Euler's equation and link the pressure and velocity. Since a force acting on a surface normal to x of a differential volume is $p\mathrm{d}S_x$, the total force in the x direction due to pressure difference can be expressed as

$$p\mathrm{d}S_x - \left(p\mathrm{d}S_x + \frac{\partial}{\partial x}(p\mathrm{d}S_x)\mathrm{d}x\right) = -\frac{\partial}{\partial x}(p\mathrm{d}S_x)\mathrm{d}x \tag{3.9}$$

where Taylor expansion has been used. This force difference must be balanced by mass times acceleration in accordance with Newton's second law:

$$\begin{aligned} -\frac{\partial}{\partial x}(p\mathrm{d}S_x)\mathrm{d}x = \rho\mathrm{d}x\mathrm{d}S_x\frac{\mathrm{d}u_x(x,t)}{\mathrm{d}t} &= \rho\mathrm{d}x\mathrm{d}S_x\left(\frac{\partial}{\partial t}u_x + \frac{\partial}{\partial x}u_x\frac{\mathrm{d}x}{\mathrm{d}t}\right) \\ &= \rho\mathrm{d}x\mathrm{d}S_x\left(\frac{\partial}{\partial t}u_x + u_x\frac{\partial}{\partial x}u_x\right) \end{aligned} \tag{3.10}$$

where care must be taken performing the derivation, since an Eulerian description of velocity field is given instead a Lagrangian one. Again since the differential volume is fixed

$$-\frac{\partial}{\partial x}p = \rho\left(\frac{\partial}{\partial t}u_x + u_x\frac{\partial}{\partial x}u_x\right) \tag{3.11}$$

The above one-dimensional expression can easily be extended to three dimension using the same arguments for y and z directions and collecting the three equations using vector calculus:

$$-\boldsymbol{\nabla}p = \rho\left[\frac{\partial}{\partial t}\mathbf{u} + (\mathbf{u}\cdot\boldsymbol{\nabla})\mathbf{u}\right] \tag{3.12}$$

Here the second term of the RHS corresponds to convection, and is usually omitted in microfluidics due to the low flow speeds [30, 204]. The same equation can be derived from the Navier–Stokes equation neglecting viscous effects (second and third term of RHS of Eq. 3.1) and external field contributions (last two terms of RHS of Eq. 3.1).

The third equation (the state equation) that connects pressure and density stems from thermodynamic considerations. Assuming fast processes in acoustics, an isentropic approximation can be made and for the isentropic derivative of the

pressure

$$\frac{\partial p}{\partial \rho} = \frac{B}{\rho} = c_0^2 \tag{3.13}$$

holds. Here B is the bulk modulus of the fluid, which is the inverse of the compressibility ($B = 1/\kappa$). This relationship $\kappa = 1/(\rho c^2)$ is used extensively for acoustic radiation force calculations.

Using the above three equations and neglecting convection, the linearised wave equation for a fluid can be written as

$$c_0^2 \nabla^2 p = \partial_t p \quad \text{or} \quad c_0^2 \nabla^2 \rho = \partial_t \rho \tag{3.14}$$

In the following the linearised Euler equation (Eq. 3.12) will be used when determining the primary acoustic radiation force for a standing wave field; the state equation (Eq. 3.14) to calculate compressibility from material properties and any standing wave acoustic pressure field can be verified by direct substitution into the wave equation. In acoustic wave propagation, the steady ambient pressure is omitted and only the pressure variation is considered (which is referred to as acoustic pressure). This notation is followed here as well, and in the following p simply refers to the acoustic pressure. Assuming a separable solution with harmonic time dependence, a velocity potential $\phi(\mathbf{r})e^{-i\omega t}$ can be defined such that

$$\mathbf{u}(\mathbf{r}) = \boldsymbol{\nabla}\phi(\mathbf{r}) \tag{3.15a}$$

$$p(\mathbf{r}) = i\omega\rho_0\phi(\mathbf{r}) \tag{3.15b}$$

$$\rho(\mathbf{r}) = \frac{i\omega\rho_0}{c_0^2}\phi(\mathbf{r}) \tag{3.15c}$$

where $p(\mathbf{r})$ follows from the Euler equation (Eq. 3.12), and $\rho(\mathbf{r})$ from the state equation (Eq. 3.14). These relationships are used extensively during derivation of any acoustic radiation force in Section 3.4.2. Finally, I note that as the actual fields are taken as the real part of $\mathbf{u}(\mathbf{r})e^{-i\omega t}$, it would not matter if the harmonic time dependence was given as $e^{-i\omega t}$ or $e^{i\omega t}$. However, the acoustic radiation force is a non-linear phenomenon; most authors [124, 126, 127, 206] use $e^{-i\omega t}$ and therefore obtain results corresponding to this reference frame.

3.4.1 Acoustic radiation force calculation methods

Since the seminal work of King on primary acoustic radiation force [124], various equations were presented to obtain the acoustic radiation force for different approxi-

mations of particle or fluid properties [125–127, 207]. The most general such equation incorporating viscous effects states the radiation force on a spherical particle within the Rayleigh limit ($a \ll \lambda$) including monopole and dipole scattering contributions is given as

$$\mathbf{F}_{\mathrm{ac}} = -\pi a^3 \left[\frac{2\kappa_0}{3} \mathrm{Re}\left\{ f_1 p_{\mathrm{in}}^* \nabla p_{\mathrm{in}} \right\} - \rho_0 \mathrm{Re}\left\{ f_2^* \mathbf{u}_{\mathrm{in}}^* \cdot \boldsymbol{\nabla} \mathbf{u}_{\mathrm{in}} \right\} \right] \tag{3.16}$$

where a is the particle radius, κ_0 and ρ_0 the fluid compressibility and density. The total acoustic field is given by the pressure p_{in} and velocity field $\mathbf{u}_{\mathrm{in}}$, and star denotes complex conjugate [127]. The two scattering parameters, f_i, are defined by the following set of equations:

$$f_1\left(\kappa_i\right) = 1 - \kappa_i/\kappa_0 \tag{3.17a}$$

$$f_2\left(\widetilde{\rho}, \widetilde{\delta}\right) = \frac{2\left[1 - \gamma\left(\widetilde{\delta}\right)\right]\left(\widetilde{\rho} - 1\right)}{2\widetilde{\rho} + 1 - 3\gamma\left(\widetilde{\delta}\right)} \tag{3.17b}$$

$$\gamma\left(\widetilde{\delta}\right) = -\frac{3}{2}\left[1 + i\left[1 + \widetilde{\delta}\right]\right]\widetilde{\delta} \tag{3.17c}$$

$$\widetilde{\delta} = \sqrt{2\nu/\omega}/a \tag{3.17d}$$

The force equation can also be reformulated as the gradient of a potential, as proposed by Gorkov [126] and adapted by Silva and Bruus [206]. Here the method is not applicable to pure travelling waves, as viscous effects are neglected by considering only the real part of f_2. The potential form of the force equation is

$$U_{\mathrm{ac}}(\mathbf{r}_{\mathrm{p}}) = a_{\mathrm{p}}^3 k^2 \pi \rho_0 \left[\frac{f_{1,\mathrm{p}}}{3} \left|\phi_{\mathrm{in}}(\mathbf{r}_{\mathrm{p}})\right|^2 - \frac{f_{2,\mathrm{p}}}{2} \left| \frac{1}{k} \boldsymbol{\nabla} \phi_{\mathrm{in}}(\mathbf{r}_{\mathrm{p}}) \right|^2 \right] \tag{3.18a}$$

$$\mathbf{F}_{ac} = -\boldsymbol{\nabla} U_{\mathrm{ac}} \tag{3.18b}$$

Finally, to be able to calculate the radiation force on an arbitrary shaped object of arbitrary size (not limited by the Rayleigh limit) a surface integral can be employed as proposed by Yosioka and Kawasima [125] and applied numerically by Glynne-Jones *et al.* [208]:

$$\mathbf{F}_{\mathrm{ac}} = -\int_{S_0} \left\{ \left[\frac{\langle p^2 \rangle}{2\rho_0 c_0^2} - \frac{\rho_0 \left\langle |\mathbf{u}|^2 \right\rangle}{2} \right] \mathbf{n} + \rho_0 \left\langle (\mathbf{n} \cdot \mathbf{u})\, \mathbf{u} \right\rangle \right\} dS \tag{3.19a}$$

The three methods can be applied for different force calculations, for example in

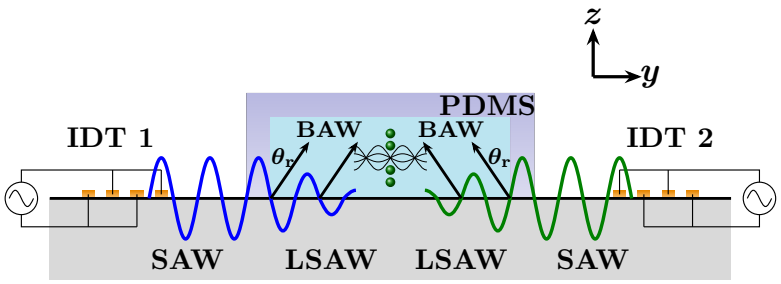

Figure 3.2: Schematic of a surface acoustic wave microfluidic device with the PDMS microchannel bonded on top. The IDTs launch surface waves, which are converted to leaky surface waves at the water/lithium niobate interface, radiating two travelling bulk acoustic waves into the fluid. The boundary condition for the apparent wave numbers at the surface gives the radiation angle, θ_R. The combination of the two travelling waves forms a standing wave, that traps particles at the pressure nodes

a bulk standing acoustic wave the first method offers the quickest solution:

$$\phi_{in}(y) = \frac{u_0}{k}\cos(ky) \tag{3.20a}$$

$$p_{in}(y) = \frac{i\omega\rho_0 u_0}{k}\cos(ky) = -p^*_{in}(y) \tag{3.20b}$$

$$\mathbf{u}_{in}(y) = \mathbf{u}^*_{in}(y) = -u_0\sin(ky)\hat{\mathbf{y}} \tag{3.20c}$$

$$p^*_{in}(y)\cdot\boldsymbol{\nabla}p_{in}(y) = -\frac{\omega^2\rho_0^2u_0^2}{k}\sin(ky)\cos(ky)\hat{\mathbf{y}} \tag{3.20d}$$

$$\mathbf{u}^*_{in}(y)\cdot\boldsymbol{\nabla}\mathbf{u}_{in}(y) = ku_0^2\sin(ky)\cos(ky)\hat{\mathbf{y}} \tag{3.20e}$$

$$\begin{aligned}\mathbf{F}_{ac} &= \frac{4\pi a^3}{3}\frac{u_0^2\rho_0}{4}k\left[f_1+\frac{3}{2}f_2\right]\sin(2ky)\hat{\mathbf{y}}\\ &= V_p E_{ac} k\Phi_{AC}\sin(2ky)\hat{\mathbf{y}}\end{aligned} \tag{3.20f}$$

as seen in Chapter 2. The energy density is given as $E_{ac} = p_0^2\kappa_0/4 = u_0^2\rho_0/4$.

For the secondary radiation force between particles, the first method (Eq. 3.16) would be tedious to use, and therefore the potential is calculated by the second method (Eq. 3.18). Finally, the third method can be used to evaluate the primary and secondary radiation force in finite element numerical simulations.

3.4.2 Primary acoustic radiation force in surface wave devices

Although the principle of particle trapping in a surface acoustic wave device is similar to the bulk acoustic wave devices, and most research groups use the same equation to describe the radiation force, this force has a slightly different form in surface acoustic wave (SAW) devices. The theoretical considerations are presented in this

subsection and these are validated by a simple numerical model.

A surface acoustic wave microfluidic device comprises a piezoelectric substrate and a polydimethylsiloxane (PDMS) microchannel as shown in Fig. 3.2. The harmonic electrical excitation signal applied on the interdigitated transducers (IDTs) launch mechanical vibrations in the form of surface acoustic waves along the surface of the substrate. As they reach the water within the microchannel, they partially travel further along the surface as leaky surface waves and partially radiate into the liquid as slanted bulk acoustic waves 3.2. The angle of propagation (the Rayleigh angle, θ_R) is given by the continuity boundary condition of the wave number at the water/substrate interface: the projection of the wave vector of the bulk acoustic wave (BAW) must equal the wave number of the surface wave: $k_y = k_\mathrm{surface} = 2\pi f/c_\mathrm{sub}$ and therefore $\theta_\mathrm{R} = \sin^{-1}(c_0/c_\mathrm{sub})$, where c_0 and c_sub are the wave speeds in the fluid and on the surface of the substrate, respectively. Consequently, $k_y = k_0 \sin(\theta_\mathrm{R})$ and $k_z = k_0 \cos(\theta_\mathrm{R})$ with $k_0 = 2\pi f/c_0$.

The two slanted travelling BAW waves within the PDMS microchannel of a SAW device can be characterised by their velocity potential

$$\phi_1 = \frac{u_0}{k_0} \exp\left(i\left(-\omega t + k_y y + k_z z\right)\right) = \frac{u_0}{k_0} \exp\left(-i\omega t\right) \exp\left(i\alpha\right) \tag{3.21a}$$

$$\phi_2 = \frac{u_0}{k_0} \exp\left(i\left(-\omega t - k_y y + k_z z\right)\right) = \frac{u_0}{k_0} \exp\left(-i\omega t\right) \exp\left(i\psi\right) \tag{3.21b}$$

where index 1 denotes the rightward, and index 2 the leftward propagating wave, respectively. The wave numbers along the y and z direction are denoted by k_y and k_z, u_0 is the velocity amplitude and ω the angular frequency. The wave number in water (along the propagation direction) is denoted by k_0, and α and ψ are introduced for shorthand notation. In the following, the harmonic time dependence is omitted for simplicity.

In order to obtain the primary radiation force for the acoustic field, the complex conjugate and gradient of the pressure and velocity field has to be calculated. First, from the velocity potential the pressure-related terms can be obtained:

$$p_1 = -\rho_0 \frac{\partial \phi_1}{\partial t} = i\rho_0\omega \frac{u_0}{k_0} \exp\left(-i\omega t\right) \exp\left(i\alpha\right) = ip_0 \exp\left(-i\omega t\right) \exp\left(i\alpha\right) \tag{3.22a}$$

$$p_2 = -\rho_0 \frac{\partial \phi_2}{\partial t} = i\rho_0\omega \frac{u_0}{k_0} \exp\left(-i\omega t\right) \exp\left(i\psi\right) = ip_0 \exp\left(-i\omega t\right) \exp\left(i\psi\right) \tag{3.22b}$$

with $p_0 = \rho_0 \omega u_0/k_0$. Neglecting temporal dependence in the following, we directly

have

$$p_{\text{in}} = p_1 + p_2 = ip_0 \exp(i\alpha) + ip_0 \exp(i\psi) = ip_0 [\exp(i\alpha) + \exp(i\psi)] \tag{3.23a}$$

$$p_{\text{in}}^* = -ip_0 [\exp(-i\alpha) + \exp(-i\psi)] \tag{3.23b}$$

since to obtain complex conjugate, all i has to be replaced by $-i$. The gradient of the total pressure field can also be directly obtained by taking the spatial partial derivatives of Eq. 3.23a:

$$\nabla p_{\text{in}} = -k_y p_0 [\exp(i\alpha) - \exp(i\psi)] \hat{\mathbf{y}} - k_z p_0 [\exp(i\alpha) + \exp(i\psi)] \hat{\mathbf{z}} \tag{3.24}$$

and the dot product of the complex conjugate of the pressure and its gradient will take the form of

$$p_{\text{in}}^* \nabla p_{\text{in}} = -2k_y p_0^2 \sin(2k_y y) \hat{\mathbf{y}} + 2ik_z p_0^2 [1 + \cos(2k_y y)] \hat{\mathbf{z}} \tag{3.25}$$

Now focussing on the velocity field, similar steps can be followed to reach the $\mathbf{u}_{\text{in}}^* \cdot \nabla \mathbf{u}_{\text{in}}$ term. First obtaining the velocity field itself

$$\mathbf{u}_1 = \nabla \phi_1 = ik_y \frac{u_0}{k_0} \exp(-i\omega t) \exp(i\alpha) \hat{\mathbf{y}} + ik_z \frac{u_0}{k_0} \exp(-i\omega t) \exp(i\alpha) \hat{\mathbf{z}} \tag{3.26a}$$

$$\mathbf{u}_2 = \nabla \phi_2 = -ik_y \frac{u_0}{k_0} \exp(-i\omega t) \exp(i\psi) \hat{\mathbf{y}} + ik_z \frac{u_0}{k_0} \exp(-i\omega t) \exp(i\psi) \hat{\mathbf{z}} \tag{3.26b}$$

$$\mathbf{u}_{\text{in}} = \mathbf{u}_1 + \mathbf{u}_2 = ik_y [\exp(i\alpha) - \exp(i\psi)] \hat{\mathbf{y}} + ik_z [\exp(i\alpha) + \exp(i\psi)] \hat{\mathbf{z}} \tag{3.26c}$$

$$\begin{aligned} \mathbf{u}_{\text{in}}^* &= \mathbf{u}_1^* + \mathbf{u}_2^* \\ &= -ik_y [\exp(-i\alpha) - \exp(-i\psi)] \hat{\mathbf{y}} - ik_z [\exp(-i\alpha) + \exp(-i\psi)] \hat{\mathbf{z}} \end{aligned} \tag{3.26d}$$

and its partial derivatives

$$\frac{\partial \mathbf{u}_{\text{in},y}}{\partial y} = -k_y^2 \frac{u_0}{k_0} [\exp(i\alpha) + \exp(i\psi)] \tag{3.27a}$$

$$\frac{\partial \mathbf{u}_{\text{in},y}}{\partial z} = \frac{\partial \mathbf{u}_{\text{in},z}}{\partial y} = -k_y k_z \frac{u_0}{k_0} [\exp(i\alpha) - \exp(i\psi)] \tag{3.27b}$$

$$\frac{\partial \mathbf{u}_{\text{in},z}}{\partial z} = -k_z^2 \frac{u_0}{k_0} [\exp(i\alpha) + \exp(i\psi)] \tag{3.27c}$$

and therefore the inner product of the complex conjugate of the vector field and its gradient can be readily obtained as

$$\begin{aligned} (\mathbf{u}_{\text{in}}^* \cdot \nabla \mathbf{u}_{\text{in}})_y &= \mathbf{u}_{\text{in},y}^* \frac{\partial \mathbf{u}_{\text{in},y}}{\partial y} + \mathbf{u}_{\text{in},z}^* \frac{\partial \mathbf{u}_{\text{in},y}}{\partial z} \\ &= 2k_y \frac{u_0^2}{k_0^2} \left(k_y^2 - k_z^2\right) \sin(2k_y y) \end{aligned} \tag{3.28a}$$

$$(\mathbf{u}_{\text{in}}^* \cdot \nabla \mathbf{u}_{\text{in}})_z = \mathbf{u}_{\text{in},y}^* \frac{\partial \mathbf{u}_{\text{in},z}}{\partial y} + \mathbf{u}_{\text{in},z}^* \frac{\partial \mathbf{u}_{\text{in},z}}{\partial z}$$

$$= 2ik_y^2 k_z \frac{u_0^2}{k_0^2}\left[1-\cos\left(2k_y y\right)\right] + 2ik_z^3\frac{u_0^2}{k_0^2}\left[1+\cos\left(2k_y y\right)\right] \tag{3.28b}$$

As a last step, these results given by Eqs. 3.25 and 3.28 has to be substituted into Eq. 3.16 to finally arrive at the primary acoustic radiation force in a surface wave device. First focussing on the horizontal force in the y direction, as the y component of both $p_{\text{in}}^* \nabla p_{\text{in}}$ and $\mathbf{u}_{\text{in}}^* \cdot \nabla \mathbf{u}_{\text{in}}$ are pure real, we have

$$\begin{aligned}
\mathbf{F}_{\text{ac},y} &= -\pi a^3 \left[-\frac{2\kappa_0}{3} f_1 2k_y p_0^2 \sin\left(2k_y y\right) - \rho_0 \text{Re}\left\{f_2\right\} 2k_y \frac{u_0^2}{k_0^2}\left(k_y^2 - k_z^2\right)\sin\left(2k_y y\right)\right] \\
&= \frac{4\pi a^3}{3}\frac{p_0^2}{\rho_0 c_0^2} k_y \left[f_1 + \frac{3}{2}\text{Re}\left\{f_2\right\}\frac{k_y^2 - k_z^2}{k_0^2}\right]\sin\left(2k_y y\right) \\
&= V_{\text{p}} E_0 k_y \left[f_1 - \frac{3}{2}\text{Re}\left\{f_2\right\}\cos\left(2\theta_R\right)\right]\sin\left(2k_y y\right)\hat{\mathbf{y}}
\end{aligned} \tag{3.29a}$$

where in the last equation θ_R is the Rayleigh angle. The above form of primary acoustic radiation force is very similar to the BAW radiation force (Eq. 2.5), the slight difference arising in the acoustic contrast factor term (square brackets). However, two special cases can be investigated: when two counter-propagating travelling waves are considered (as in a pure BAW device), the Rayleigh angle is 90° and $\cos(2\theta_R) = -1$, resulting in the usual contrast factor for BAW devices, $f_1 + 3/2\text{Re}\{f_2\}$. When the Rayleigh angle is taken as zero, which is the case for two upward propagating travelling waves, $k_y = 0$ and the acoustic radiation force in the horizontal direction is trivially zero, as expected.

Similarly for the vertical z direction, but now as the pressure term is purely imaginary and f_1 purely real, the first term disappears. Moreover, as the velocity term is pure imaginary as well, only the imaginary part of f_2 will play a role:

$$\begin{aligned}
\mathbf{F}_{\text{ac},z} &= \pi a^3 \rho_0 \text{Re}\left\{f_2^* \left(2ik_y^2 k_z \frac{u_0^2}{k_0^2}\left[1-\cos\left(2k_y y\right)\right] + 2ik_z^3\frac{u_0^2}{k_0^2}\left[1+\cos\left(2k_y y\right)\right]\right)\right\} \\
&= 2\pi a^3 k_z u_0^2 \rho_0 \text{Im}\left\{f_2\right\}\left[1 - \frac{k_y^2 - k_z^2}{k_0^2}\cos\left(2k_y y\right)\right] \\
&= 2\pi a^3 k_z u_0^2 \rho_0 \text{Im}\left\{f_2\right\}\left[1 + \cos\left(2\theta_R\right)\cos\left(2k_y y\right)\right]\hat{\mathbf{z}}
\end{aligned} \tag{3.30a}$$

Here again the two special cases can be investigated: when the two travelling waves are directed towards each other along the y direction, $k_z = 0$ and therefore the vertical force is zero, as expected; when the travelling waves are vertically upwards along the z direction, $k_y = 0$ and $\theta_R = 0°$, implying that $\mathbf{F}_{\text{ac},z} = 4\pi a^3 k_z u_0^2 \rho_0 \text{Im}\left\{f_2\right\}$ which is identical to the acoustic radiation force due to two travelling waves [206]. These results already show that the proposed acoustic radiation force equation reduces to

the previously known special cases well, as a further validation a simple COMSOL model has been utilised with the Gorkov potential approach for the acoustic force calculation. The model comprised a simple 2D rectangular fluid domain, with perfectly matched layer (PML) domains at all edges. The acoustic pressure fields are supplied as background pressure fields, with their magnitude being p_0 and their wave numbers $k_y/k_0\hat{\mathbf{y}} + k_z/k_0\hat{\mathbf{z}}$ and $-k_y/k_0\hat{\mathbf{y}} + k_z/k_0\hat{\mathbf{z}}$. Performing a frequency domain simulation, the finite element modelling tool was used to calculate the velocity fields; the primary acoustic radiation force neglecting viscous effects acting on a small spherical particle at any point can be obtained from the acoustic pressure and velocity fields as

$$U_{\mathrm{ac}} = \frac{4\pi a^3}{3}\left[f_1\frac{1}{2}\kappa_0\left\langle p_{\mathrm{in}}^2\right\rangle - f_2\frac{3}{4}\rho_0\left\langle \mathbf{u}_{\mathrm{in}}\cdot\mathbf{u}_{\mathrm{in}}\right\rangle\right] \tag{3.31a}$$

$$f_1 = 1 - \frac{\kappa_p}{\kappa_0} \tag{3.31b}$$

$$f_2 = \frac{2\rho_p/\rho_0 - 2}{2\rho_p/\rho_0 + 1} \tag{3.31c}$$

$$\mathbf{F}_{ac} = -\boldsymbol{\nabla}U_{\mathrm{ac}} \tag{3.31d}$$

and as the acoustic pressure and velocity fields have harmonic time dependence, their average for one cycle is half of the amplitude squared and for the velocity the RMS value is directly accessible within COMSOL. The equation had to be borrowed from Eq. 2.4 due to no access to velocity potential in COMSOL. The corresponding line in COMSOL syntax reads as

```
Vp*(f1_sc*kappa_m*abs(acpr.p_t)^2/4-3/4*f2_sc*rho_m*acpr2.v_rms^2)
```

Note here the different definition of the dipole scattering coefficient f_2. For the frequency and particle sizes used in this work, the boundary layer thickness is much smaller than the particle characteristic size ($\widetilde{\delta} \ll a$) and therefore the imaginary part of the f_2 scattering parameter is negligible compared to its magnitude. Therefore, the Gorkov potential approach can be applied to calculate the horizontal acoustic radiation force, but not the vertical one, as this is proportional to the imaginary part of f_2, which is neglected in the model.

The results of this investigation can be seen in Fig. 3.3. Excellent agreement between the theoretical prediction and the Gorkov potential approach can be seen for both particles. The difference between the BAW and SAW forces are more pronounced for the iron-oxide particle as the dipole scattering coefficient f_2 affects

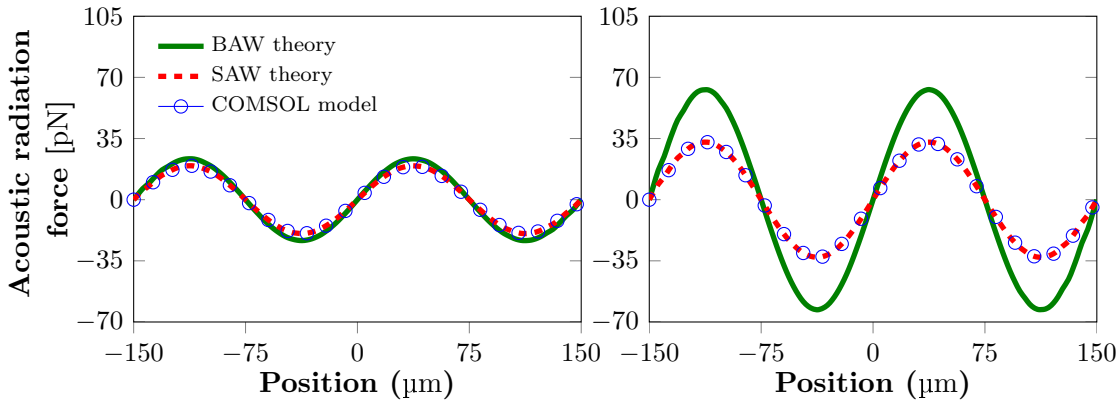

(a) PS particle in water (b) Iron-oxide filled PS particle in water

Figure 3.3: Primary radiation force acting on polystyrene (PS) and iron-oxide particles. The graphs include the widely used BAW equation, the predicted SAW equation and the Gorkov simulation results

the contrast factor difference and for the iron-oxide particle f_2 is larger due to it being more dense. The SAW contrast factor is 83% and 52% of the BAW contrast factor for polystyrene and iron-oxide particles, respectively [**Simon2019PP1**].

Finally, the primary acoustic radiation force in phase modulated surface wave devices takes a straightforward form by directly applying the phase pattern in the argument of the force assuming that this is much lower than the angular frequency of the signal. Having an excitation signal proportional to $\sin(\omega t + \varphi(t))$, where $\varphi(t)$ is the phase modulation, in the above derivation, the only difference in such fields would be the amplitude of the acoustic pressure, being proportional to $\omega(t) + \varphi(t)$ due to the temporal partial differentiation. However, in usual scenarios $f = \omega/2\pi$ is in the order of MHz, while the modulation speed is a few Hz, justifying that $\varphi(t) \ll \omega$ and therefore the primary acoustic radiation force being

$$\begin{aligned} \mathbf{F}_{\mathrm{ac},y} &= V_\mathrm{p} E_0 k_y \left[f_1 - \frac{3}{2} \mathrm{Re}\{f_2\} \cos(2\theta_R) \right] \sin(2k_y y + \varphi(t)) \\ &= V_\mathrm{p} E_0 k_y \Phi_{\mathrm{ac,SAW}} \sin(2k_y y + \varphi(t)) \end{aligned} \tag{3.32}$$

For a detailed derivation and proof refer to the ESI of [**Simon2017Bio**].

3.4.3 Secondary acoustic radiation force

Considering multiple particles in a fluid medium, the scattering events between these particles give rise to interparticle forces (also called secondary radiation force or Bjerknes force), which can result in particle clump formation, adversely affecting device performance [209]. Desired arrangement of particles in layers [210] or chains

[207] is also suspected to occur due to the secondary radiation force [211]. Special cases of this force were investigated thoroughly: the seminal work by Bjerknes [212] on bubble-bubble interactions was followed by other theoretical studies [213–216] and validated experimentally [217]. Theoretical rigid-rigid particle interactions were developed both for short range (separation distance much shorter than wavelength [207]) and long range interactions (separation distance much greater than wavelength [218]), and validated by experiments with elastic latex solid particles in water medium [219]. A general theoretical model both for compressible and rigid particles, with no restriction on interparticle distance was presented by Silva and Bruus recently [206]. They followed a monopole-dipole description of the secondary acoustic radiation force potential; this analytical formula being valid for particle sizes much smaller than the wavelength. To alleviate this restriction, numerical approaches have been developed for determining interparticle forces. Doinikov used a multipole series expansion technique for calculating the interaction force between two air bubbles in water [220]. In 2015, a weighted residue method was combined with the multipole expansion series for calculating the interparticle forces between spherical particles in an ideal fluid [221]. Recently, a boundary element method was applied for calculating the interparticle force between spheroidal particles [222]. Although different numerical methods have been developed, they are complex to use and require a laborious implementation, restricting its use to few research groups. Analytical methods, in contrast are limited to small particle sizes and objects of simple geometry.

To obtain the secondary acoustic radiation force theoretically, first the scattered velocity potential has to be obtained as

$$\begin{aligned}\phi_{\mathrm{sc}}(\mathbf{r}_{\mathrm{p}}|\mathbf{r}_{\mathrm{s}}) =& i f_{1,\mathrm{s}} \frac{a_{\mathrm{s}}^3 \omega}{3\rho_0} \frac{\rho_{\mathrm{in}}(\mathbf{r}_{\mathrm{s}}) e^{ikR_{\mathrm{ps}}}}{R_{\mathrm{ps}}} \\ &- f_{2,\mathrm{s}} \frac{a_{\mathrm{s}}^3}{2} \boldsymbol{\nabla}_{\mathrm{p}} \cdot \left[\frac{\mathbf{u}_{\mathrm{in}}(\mathbf{r}_{\mathrm{s}}) e^{ikR_{\mathrm{ps}}}}{R_{\mathrm{ps}}} \right] + O\left[\frac{(ka_{\mathrm{s}})^5}{(kR_{\mathrm{ps}})^3} \right] \end{aligned} \tag{3.33a}$$

Then the total acoustic velocity potential (incident field and scattered field) is substituted into Eq. 3.16 from the previous section, neglecting any cross-terms that come from the interaction of the incident field with the self scattered field of the particle (this would be the primary radiation force). Although this work has been done by Silva and Bruus before [206], their secondary radiation force potential formula contains a typo and therefore the full derivation is provided as Appendix A

to this thesis. The final formula reads:

$$
\begin{aligned}
U_{\mathrm{sec}}(r,\theta) =& \pi E_0 k^3 a_{\mathrm{p}}^3 a_{\mathrm{s}}^3 \Bigg(\cos\left[k(r\cos\theta - h_{\mathrm{n}})\right] \frac{f_{2,\mathrm{p}}}{2} \Bigg\{ f_{1,\mathrm{s}} \cos(kh_{\mathrm{n}})(1+3\cos 2\theta) \frac{\cos kr}{(kr)^3} \\
&+ \left[\frac{4}{3} f_{1,\mathrm{s}} \sin(kh_{\mathrm{n}}) \cos\theta \cos kr + f_{2,\mathrm{s}} \cos(kh_{\mathrm{n}})(1+3\cos 2\theta) \sin kr \right] \frac{1}{(kr)^2} \\
&- \left[f_{2,\mathrm{s}} \cos(kh_{\mathrm{n}})(1+\cos 2\theta) \cos kr - \frac{4}{3} f_{1,\mathrm{s}} \sin(kh_{\mathrm{n}}) \cos\theta \sin kr \right] \frac{1}{kr} \Bigg\} \\
&+ \sin\left[k(r\cos\theta - h_{\mathrm{n}})\right] \frac{2 f_{1,\mathrm{p}}}{3} \Bigg\{ f_{2,\mathrm{s}} \cos(kh_{\mathrm{n}}) \cos\theta \frac{\cos kr}{(kr)^2} \\
&+ \left[\frac{2}{3} f_{1,\mathrm{s}} \sin(kh_{\mathrm{n}}) \cos kr + f_{2,\mathrm{s}} \cos(kh_{\mathrm{n}}) \cos\theta \sin kr \right] \frac{1}{kr} \Bigg\} \Bigg)
\end{aligned}
\tag{3.34}
$$

with $E_0 = \rho_0 u_0^2/2$. The gradient of this potential gives the acoustic interaction force and is given in Appendix B, along with forms of the force equation for special cases, near-field and far-field approximations.

3.4.4 Acoustic streaming

Acoustic streaming is the net fluid flow generated by the gradient of the time-averaged acoustic momentum flux [223] which can be caused by either the attenuation of high amplitude acoustic waves or the friction between the fluid medium and channel walls [224]. The former (also termed Eckhart streaming or Quartz wind) can be minimised by reducing the resonator size [135, 225]. Absorption in the viscous boundary layer at the walls causes Schlichting and Rayleigh streaming, which differ in their characteristic sizes, the Schlichting streaming confined at the wall, while the Rayleigh streaming propagating into the fluid domain, with characteristic length scale of $\lambda/4$ [226]. Although streaming can be used for fluid mixing and stirring [227] as well as manipulation [228–230] and sorting [231]. In our case streaming would be considered a negative effect for precise manipulation and sorting of particles as it can take over the primary radiation force. Therefore it is inevitable to investigate the critical particle size (below which acoustic streaming dominates primary radiation force) as proposed by Nama *et al.* or Devendran *et al.* [232] [233]. The numerical model to obtain acoustic streaming fields and simulation results are presented in Chapter 6.

3.5 Chapter summary

In this chapter an overview of fluid flow in microchannels, the piezoelectric effect and the basic descriptive variables of an acoustic field has been presented. Three methods for calculating the acoustic radiation force were discussed and a new analytical equation for the primary acoustic radiation force in surface acoustic wave microfluidic devices was presented and validated by numerical modelling. Detrimental effects such as secondary radiation force and acoustic streaming were introduced and the correct analytical equation for secondary acoustic force potential was presented, directing the reader to Appendix B for the complete list of secondary radiation force equations and to Appendix A a detailed derivation of the secondary potential.

Chapter 4

Dynamic waveforms for sorting

4.1 Phase modulated particle separation

The interplay between the primary acoustic radiation force and the hydrodynamic viscous force can also be utilized in more complex acoustic fields to achieve particle separation in contrast to the time-of-flight particle sorters [138, 195]. As the phase modulated method was already published for a bulk device (inside a large acoustic chamber) [195], within this section the focus is on new theoretical results and the method's applicability for continuous flow microfluidic devices.

The illustration of the sorting method can be seen in Fig. 4.1. Particles or cells are initially focused by a trifurcated inlet configuration to trap at the bottom acoustic pressure node (closer to the viewer) inside the channel, where they naturally collect due to their positive contrast factor (left of Fig. 4.1c). The utilized phase pattern is shown in Fig. 4.1a. First, the phase is ramped linearly from 0° to 360° at a rate that displaces the small and large particles at different speeds, such that they are located on different sides of the pressure antinode after the ramping time t_{ramp} (Fig. 4.1(c) middle graph). As the primary radiation force makes them relax towards the nearest pressure node during the resting period, t_{rest}, where the phase is kept constant, they locate at a different spatial location, and separation can be achieved (Fig. 4.1(c) right graph). As the primary acoustic radiation force (see around Eq. 2.5 and in Section 3.4.1) is also density-dependent, particles with different density can be separated as well [138].

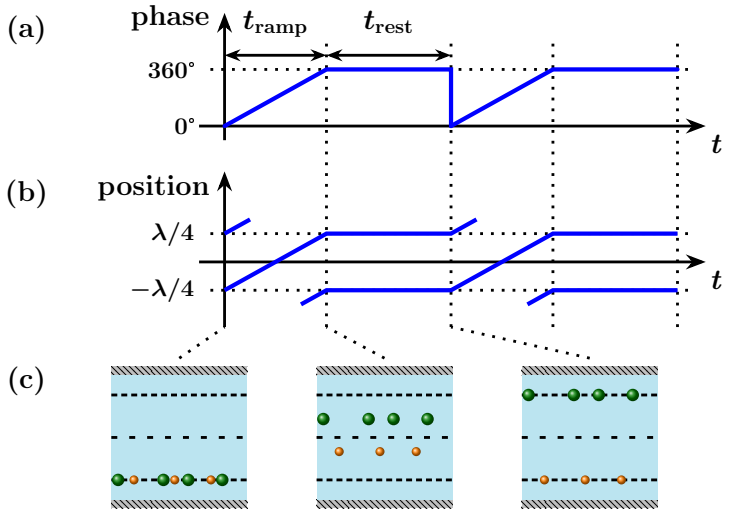

Figure 4.1: Illustration of the phase modulated sorting method. (a) the phase pattern used on the second transducer (b) the resulting movement of the nodes (c) the particle distribution in the microchannel at different time instants

4.1.1 Particle trajectories

In the horizontal direction within the microchannel, the two forces acting on a particle are the primary acoustic radiation force and the hydrodynamic drag force

$$F_{\text{ac},y} = V_{\text{p}} E_0 k_y \Phi_{\text{ac,SAW}} \sin\left(2k_y y + \varphi(t)\right) = c_{\text{ac}} \sin\left(2k_y y + \varphi(t)\right) \tag{4.1a}$$

$$F_{\text{visc},y} = -6\eta\pi a\dot{y} = -c_{\text{visc}}\dot{y} \tag{4.1b}$$

where all constants are collected in c_{ac} and c_{visc}. Due to the small particle sizes, they cannot carry inertia and the inertial approximation can be utilised, stating that $m\ddot{y}$ is zero on the particles [136]. Therefore Newton's second law becomes a force balance:

$$F_{\text{ac},y} + F_{\text{visc},y} = 0 \tag{4.2a}$$

$$c_{\text{ac}} \sin\left(2k_y y + \varphi(t)\right) = c_{\text{visc}}\dot{y} \tag{4.2b}$$

now assuming a linear phase modulation $\varphi(t) = -s(t - t_s)$, where t_s is the start of the phase shift, substitutional integration can be carried out to obtain the closed form of the equation describing particle trajectories. The negative sign corresponds to the force pattern to move towards the positive y direction as time elapses. If there is a complete 360° phase modulation during t_{ramp}, consequently $s = 2\pi/t_{\text{ramp}}$. Denote the argument of the sin function by u, so

$$u = 2k_y y - s(t - t_s) \tag{4.3a}$$

$$\frac{du}{dt} = 2k_y\dot{y} - s \implies \dot{y} = \frac{du/dt + s}{2k_y} \tag{4.3b}$$

reducing Eq. 4.2b in the form of

$$c_{\text{ac}} \sin(u) = \frac{c_{\text{visc}}}{2k_y} (du/dt + s) \tag{4.4}$$

for which separation of variables can be applied

$$dt = \frac{du}{\gamma \sin(u) - s} \tag{4.5}$$

with $\gamma = 2k_y c_{\text{ac}}/c_{\text{visc}}$ as a simplification. From [234] the indefinite integral of the right hand side can be given as

$$\int \frac{1}{\gamma \sin(u) - s} du = \frac{2 \tan^{-1}\left(\frac{\gamma - \tan(u/2)}{Z}\right)}{Z} \qquad Z = \sqrt{s^2 - \gamma^2} \tag{4.6}$$

and from Eq. 4.6 we have

$$t + c_1 = \frac{2 \tan^{-1}\left(\frac{\gamma - \tan(u/2)}{Z}\right)}{Z} \tag{4.7}$$

in which $u(t) = 2k_y y - s(t - t_s)$ can be substituted back and $y(t)$ expressed:

$$y(t) = \frac{s\,(t - t_s)}{2k_y} + \frac{1}{k_y} \tan^{-1}\left[\frac{\gamma - Z \tan\left(\frac{tZ + c_1 Z}{2}\right)}{s}\right] \tag{4.8}$$

where c_1 is used to satisfy the initial particle position. When $y(0) = -\lambda/4$, this constant evaluates to $c_1 = \pi/Z$. Note that in this resulting equation both Z and c_1 are generally allowed to be complex to capture all cases ($s < \gamma$ and $s > \gamma$) in a single equation. Moreover, the tan() function must be taken to be monotonic on the solution range [**Simon2017Bio**]. Example separation trajectories are plotted in Fig. 4.2 for size-based separation of polystyrene particles (with density $\rho = 1.05\,\text{g/cm}^3$, compressibility $\kappa = 249\,\text{TPa}^{-1}$) and density-based separation of polystyrene and iron-oxide particles (with density $\rho = 1.5\,\text{g/cm}^3$, compressibility assumed negligible). The acoustic pressure amplitude was 96 kPa, the ramping and rest times 1.5 and 1 s, respectively. To aid the reader, the pressure antinode and the end of the ramping period are indicated by dashed lines. It can be seen that for both cases the particles separate and locate on different sides of the pressure antinode after the ramping period ($t = 1.5$ s). Finally, the trajectory equation was compared with the numerical solution of the differential equation of motion developed previously [195, 235]. For a time step of 1 ns, the difference between the numerical and analytical trajectories was less than 0.1 nm at any time point, resulting in an R^2 value higher than 0.9999.

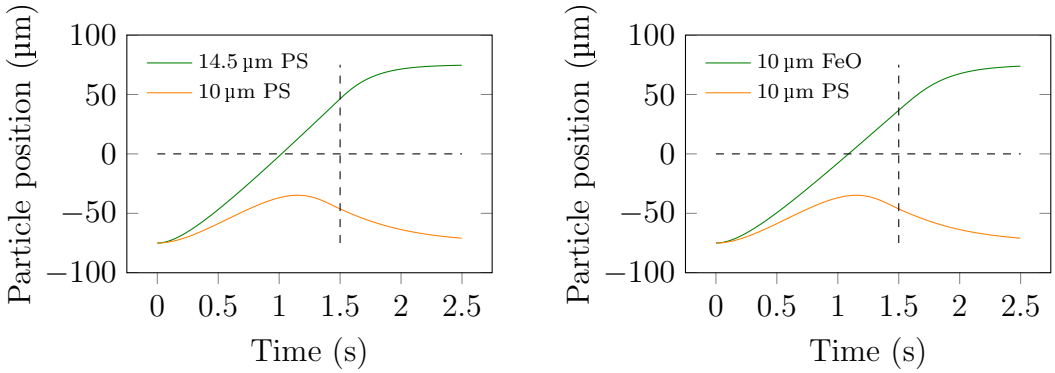

(a) Size-based separation trajectories of 10 and 14.5 µm polystyrene particles

(b) Density-based separation trajectories of 10 µm polystyrene and iron-oxide particles

Figure 4.2: Analytical separation trajectories of particles based on (a) size and (b) density difference. The horizontal and vertical dashed lines indicate the acoustic pressure antinode and the end of the ramping period, respectively

However, the computational time for the direct numerical method is of the order of tens of seconds; the analytical solution provides a fast and robust alternative for simulation of particle trajectories.

4.1.2 Optimum time parameters and scaling laws for particle sorting

Analysis of the phase modulated method by obtaining limiting values of parameters using the standard tools such as direct solution of the trajectory equation or investigation of its partial derivatives is elaborate due to the complex form of Eq. 4.8. Therefore an alternative approach had to be developed.

The limiting case for sorting is when a particle locates exactly at the pressure antinode after the ramping cycle (Fig. 4.1(c)). On substitution of $y(t_{\text{ramp}}) = 0$ into Eq. 4.8 and assuming $t_{\text{s}} = 0$ without the loss of generality, on rearranging we get

$$\gamma = Z \tan\left[\frac{\pi}{2} + \frac{Z}{2} t_{\text{ramp}}\right] \tag{4.9}$$

which is a transcendental equation in t_{ramp} (note that both γ and Z depend on t_{ramp}). However, on expanding the variables and rearranging

$$\left[\left(\frac{2\pi}{\gamma t_{\text{ramp}}}\right)^2 - 1\right]^{-1/2} = \tan\left[\frac{\pi}{2} + \frac{\sqrt{(2\pi)^2 - (\gamma t_{\text{ramp}})^2}}{2}\right] \tag{4.10}$$

the resulting equation can be solved numerically for the product

$$\gamma t_{\text{ramp}} \approx 4.2503 \tag{4.11}$$

Three conclusions can be drawn: for known input parameters, the limiting t_{ramp} can be obtained by simply substituting into Eq. 4.11 for both particle sets. The adequate t_{ramp} to achieve sorting would lie between these two limiting values. Consider a sorting scenario with two types of particles. The small particles are expected to travel no further than the midpoint at $y = 0$ and the large particles have to travel further than this midpoint. Therefore the ideal ramping time must be clearly between the bounds given by

$$\frac{4.2503}{\gamma_{large}} < t_{\text{ramp}} < \frac{4.2503}{\gamma_{small}} \tag{4.12}$$

following the above derivation.

Secondly, the scaling laws for sorting are known as all parameters are collected in γ and its product with t_{ramp} is a constant. For example, γ scales with the square of particle radius, and therefore t_{ramp} must be scaled by raising it to the power of -2. Similarly, as the pressure is proportional to the applied voltage, and γ is proportional to the square of the pressure, again, an inverse-square dependence of the ramping time with input voltage is expected. This is validated experimentally in Section 7.2. Adjusting sorting parameters for different particle populations is straightforward and does not require any knowledge of parameters such as acoustic energy density or contrast factor as long as they are kept constant.

Finally, as illustrated in Fig. 4.3, for any type and size particle the sorting can be investigated graphically. As in a sorting scenario, the energy density, viscosity, frequency, wave number are all constant, γ is proportional to

$$\gamma = \frac{2k_y c_{\text{ac}}}{c_{\text{visc}}} = \frac{2k_y V_{\text{p}} E_0 k_y \Phi_{\text{ac,SAW}}}{6\eta\pi a} \propto a^2 \Phi_{\text{ac,SAW}} \tag{4.13}$$

Furthermore, γt_{ramp} is constant (Eq. 4.11), and therefore the particles represented on a diameter versus contrast factor graph are have to be separated by a $\Phi_{\text{ac,SAW}} \propto a^{-2}$ style graph for successful sorting. This is indicated by a dashed line in Fig. 4.3 that would either separate polystyrene (PS) particles in size (10 and 14.5 µm) or particles by density (10 µm PS and iron-oxide). In conclusion, the limiting t_{ramp} equation 4.11 can be used to choose an operating point: the limit for both particles can be calculated, and using a t_{ramp} value in between the two values ensures the

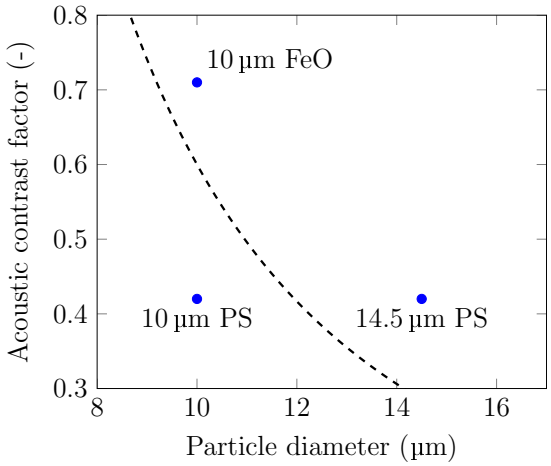

Figure 4.3: Graphical investigation of phase modulated sorting of particles. The particle sets on the acoustic contrast factor vs diameter graph must be separable by an inverse-square style curve

large particles are displaced more than the antinode, while the small particles stay below the antinode. This property is used in Section 8.3.3 to analyse the feasibility of certain cell sorting scenarios.

The resting time has much smaller effect on the sorting. The key to sorting is the ramping time that makes the particles to be separated lie to different sides of the pressure antinode after the ramping stage. The resting time only allows particles to relax at the respective pressure nodes. A numerical study for bulk devices has been carried out in the beginning of this research, however, due to different physical device dimensions it is omitted here and the reader is directed to [**Simon2016IUS**]. Nevertheless, resting times of same length as ramping times generally are adequate to stabilise particles at the nodes and longer periods are not necessary.

4.1.3 Effect of initial phase modulation angle on particle sorting

The linear phase modulation from 0° to 360° provides a simple method for particle separation as shown in the previous section. However, the initial movement of the particles is slow, due to the small radiation force around the nodes, limiting separation speed. In this section, a modified phase modulation method is proposed to achieve the fastest possible movement of the target particles. The peculiar sinusoidal spatial distribution of the primary acoustic radiation force (see around Eq. 2.5 and in Section 3.4.1) allows for maximum force acting on the particle and therefore it

travelling with maximum speed when the particle lags the force pattern by $\lambda/8$. This can also be obtained analytically referring to the force balance

$$c_{\text{ac}} \sin\left(2k_y y - s\left(t - t_s\right)\right) = c_{\text{visc}} \dot{y} \tag{4.14a}$$

$$\dot{y} = \frac{c_{\text{ac}}}{c_{\text{visc}}} \sin\left(2k_y y - s\left(t - t_s\right)\right) \tag{4.14b}$$

If a constant (maximum) speed of a particle is desired, it follows that

1. This maximum speed is $v_{max} = c_{\text{rad}}/c_{\text{visc}}$
2. The argument of the sin function must be $\pi/2$ at all times during the ramping to ensure a positive and maximal speed (corresponding to $\lambda/8$ distance)

Differentiation of the argument with respect to time t directly gives the slope parameter, s, as

$$\frac{d}{dt}\left[2k_y y - s\left(t - t_s\right)\right] = 2k_y \dot{y} - s = 0 \tag{4.15}$$

since the argument must be constant. Rearranging for s yields

$$s = 2k_y \frac{c_{rad}}{c_{visc}} = \gamma \tag{4.16}$$

Note that this can also be reformulated similarly to the continuous phase modulation case to have a time parameter for the slope

$$s = \frac{2\pi}{t_{\text{slope}}} \rightarrow t_{\text{slope}} = \frac{2\pi}{s} \tag{4.17}$$

which means that the phase is modulated at a rate that a complete 0° to 360° shift would occur during t_{slope}. The t_{s} can be expressed using the second condition,

$$2k_y y - s\left(t - t_s\right) = \frac{\pi}{2} \tag{4.18}$$

noting that the particle starts at $y(0) = -\lambda/4$, when $t = 0$, substitution of s and rearranging yields

$$t_{\text{s}} = \frac{1}{s}\left(\frac{\pi}{2} + 2\frac{2\pi}{\lambda}\frac{\lambda}{4}\right) = \frac{3}{4} t_{\text{slope}} \tag{4.19}$$

which is equivalent to $t_{\text{s}} = -\frac{t_{\text{slope}}}{4}$ due to the periodicity of the sin() and is probably more meaningful physically.

It is interesting to mention that since $s = \gamma$ and therefore $Z = \sqrt{s^2 - \gamma^2} = 0$ in this case, the equation for particle trajectory reduces to

$$y(t) = \frac{s\left(t - t_s\right)}{2k} - \frac{1}{k} \tan^{-1}\left[\frac{\gamma}{s}\right] \tag{4.20}$$

$$= \frac{st}{2k} - \frac{st_{\text{slope}}}{8k} + \frac{\pi}{4k} \tag{4.21}$$

$$= \frac{st}{2k} = \frac{c_{\text{ac}}}{c_{\text{visc}}} t \tag{4.22}$$

as expected of a particle that moves with speed $c_{\text{ac}}/c_{\text{visc}}$.

The start phase of the modulation pattern is obtained by $st_{\text{s}} = (2\pi/t_{\text{slope}}) \cdot (-t_{\text{slope}}/4) = -\pi/2$, and therefore in the following this method is collectively referred to as jump phase modulation. However, for the end of the phase shift various values can be investigated as shown in Fig. 4.4. For 180° total phase difference (Fig. 4.4b), the large particles only shift until the pressure antinode, so this is definitely a lower bound for sorting. For 270° total phase difference (Fig. 4.4c), the small particles are well confined compared to the continuous modulation case (Fig. 4.4a). Finally, a total of 360° phase difference moves the large particles linearly with maximum speed to the next node, however, the small particles exhibit less confined movement (Fig. 4.4d). The same simulation parameters are used as before, $\gamma = 4.39$ for the large particle, resulting in $t_{\text{slope}} = 1.43$ s. For the good balance between well-confined movement of small particles and fast shifting of large particles, the -90° to 180° phase modulation method is used in the following.

Although this modified method seems promising, there is a theoretical limit of small particle size that cannot be separated from the larger ones. For the trajectory of the small particle we have the limit as it should not exceed the antinode at zero

$$0 > y(t_{\text{ramp}})_{\text{small}} \tag{4.23}$$

In this case, we know that $s = \gamma_{\text{large}}$ so we can define the size ratio $r = a_{\text{small}}/a_{\text{big}}$ and then $\gamma_{\text{small}} = r^2 \gamma_{\text{big}}$. Furthermore, $t_{\text{ramp}} = 3t_{\text{slope}}/4$, $t_s = -t_{\text{slope}}/4$, and $st_{\text{slope}} = 2\pi$ so first we can obtain the constant in the trajectory equation

$$c_1 = -\frac{2}{\gamma_{\text{big}}\sqrt{1-r^4}} \tan^{-1}\left[-\sqrt{\frac{1-r^2}{1+r^2}}\right] \tag{4.24}$$

for the small particle and then the condition for separation

$$0 > y(t_{\text{ramp}})_{\text{small}} = \frac{s\,(t_{\text{ramp}} - t_s)}{2k_y} + \frac{1}{k_y} \tan^{-1}\left[\frac{\gamma - Z\tan\left(\frac{t_{\text{ramp}} Z + c_1 Z}{2}\right)}{s}\right] \tag{4.25}$$

$$0 > \frac{2\pi}{4k_y} + \frac{1}{k_y} \tan^{-1}\left[\frac{\gamma - Z\tan\left(\frac{t_{\text{ramp}} Z + c_1 Z}{2}\right)}{s}\right] \tag{4.26}$$

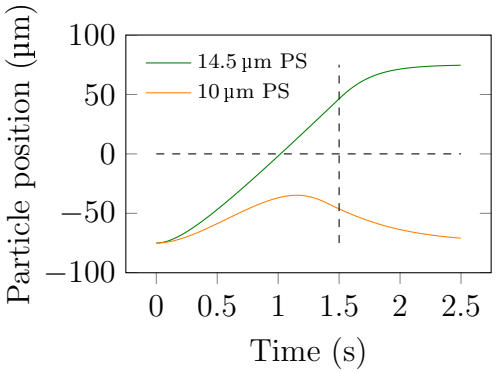

(a) Continuous phase modulation separation trajectories of 10 and 14.5 µm polystyrene particles

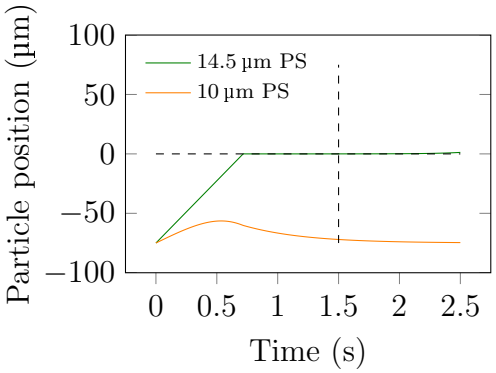

(b) -90° to 90° phase modulation (total phase difference of 180°) separation trajectories of 10 and 14.5 µm polystyrene particles

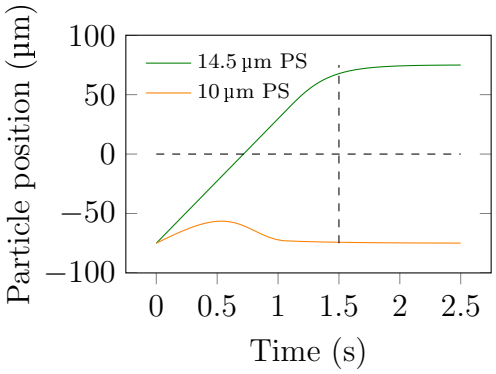

(c) -90° to 180° phase modulation (total phase difference of 270°) separation trajectories of 10 and 14.5 µm polystyrene particles

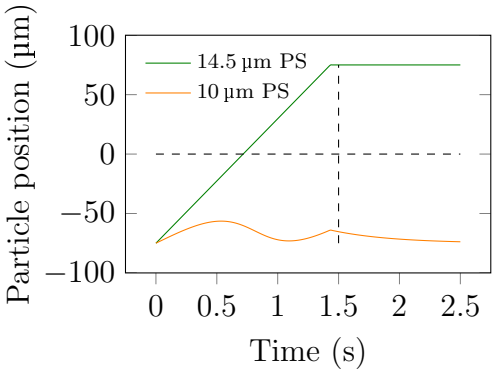

(d) -90° to 270° phase modulation (total phase difference of 360°) separation trajectories of 10 and 14.5 µm polystyrene particles

Figure 4.4: Comparison of the continuous and jump phase modulation techniques

or consequently

$$-\frac{\pi}{2} > \frac{1}{k_y}\tan^{-1}\left[\frac{\gamma - Z\tan\left(\frac{t_{\text{ramp}}Z+c_1Z}{2}\right)}{s}\right] \tag{4.27}$$

which is seemingly impossible to satisfy, but as in the trajectory equation the tan() is not always normalized on $-\pi/2$ to $\pi/2$, but taken to be monotonic on the solution range, the above equality can indeed be true. Solving for the equality limit:

$$-\infty = \frac{\gamma - Z\tan\left(\frac{t_{\text{ramp}}Z+c_1Z}{2}\right)}{s} \tag{4.28}$$

and since all parameters are finite and non-zero

$$\frac{\pi}{2} = \frac{t_{\text{ramp}}Z + c_1Z}{2} \tag{4.29}$$

and from rearranging

$$Z^2 = \gamma_{\text{big}}^2 - \gamma_{\text{small}}^2 = \left(\frac{\pi}{t_{\text{ramp}} + c_1}\right)^2 \tag{4.30}$$

which combined with the equation for c_1 leads again to a transcendental equation:

$$\frac{1}{\sqrt{1-r^4}} = \frac{3}{2} - \frac{2}{\pi\sqrt{1-r^4}} \tan^{-1}\left[-\sqrt{\frac{1-r^2}{1+r^2}}\right] \tag{4.31}$$

with solutions $r \approx \pm 0.915845$, from which the positive is the meaningful one in this case. Its reciprocal $1/r \approx 1.0919$ probably expresses better the relationship of the two particle sizes for sorting, which is limited to about 10% relative size difference. Note that although the continuous phase modulation does not pose such limitation on sortable particle size ratio, variation of particle properties and sorting parameters lower the figures of merit. This is discussed in Chapter 9 in detail.

4.2 Frequency modulation

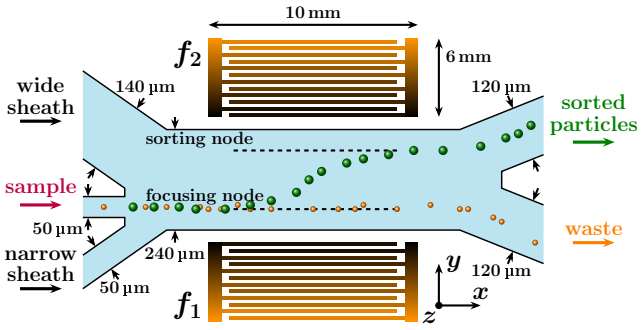

Figure 4.5: Illustration of the sorting principle with focus on the notation of the two transducers. The bottom transducer and its parameters are denoted by index 1

Phase modulation of one excitation signal to achieve moving standing waves is a straightforward method, however, requires one cycle of the phase modulation signal to be uploaded to the function generator, as detailed in the forthcoming Section 5.3.1. A similar quasi-standing wave can be achieved by two counter-propagating travelling waves with slightly different frequencies, but implementation of this setup is substantially simpler than the phase modulation pattern. To verify the method, assume the sum of two counter propagating travelling pressure waves with the same amplitude but different frequency and wave number:

$$p_1(y,t) = p_0 \cos(k_{y,1} y - \omega_1 t) \tag{4.32a}$$

$$p_2(y,t) = p_0 \cos(k_{y,2} y + \omega_2 t) \tag{4.32b}$$

$$p(y,t) = p_1(y,t) + p_2(y,t) = p_0\left[\cos(k_{y,1}y - \omega_1 t) + \cos(k_{y,2}y + \omega_2 t)\right] \tag{4.32c}$$

$$p(y,t) = 2p_0 \cos\left[\left(k_{y,1} + k_{y,2}\right) y/2 - \Delta\omega t/2\right] \cdot \cos\left[\left(\omega_1 + \omega_2\right) t/2 - \Delta k y/2\right] \tag{4.32d}$$

where index 1 denotes the bottom transducer and the acoustic wave travelling away towards $+y$, while index 2 denotes the top transducer, with acoustic wave travelling towards $-y$ (refer to Fig. 4.5). The latter equation is obtained after using the trigonometric identity $\cos(\alpha) + \cos(\beta) = 2\cos((\alpha+\beta)/2)\cos((\alpha-\beta)/2)$. The difference of angular frequencies and wave numbers are given as $\Delta\omega = \omega_1 - \omega_2$ and $\Delta k = k_{y,1} - k_{y,2}$. In Eq. 4.32d, it is apparent that the first cosine has a strong spatial dependence, while the second cosine has a more pronounced temporal dependence, as $\Delta\omega \ll \omega$ and $\Delta k \ll k$. The spatial positions of the nodes, where the pressure field is zero, are therefore provided from the condition

$$\pm\pi/2 = \left(k_{y,1} + k_{y,2}\right) y/2 - \Delta\omega t/2 \tag{4.33}$$

and differentiation with respect to time directly gives the movement speed of the pressure field:

$$\begin{aligned} v_\mathrm{p} &= \frac{\Delta\omega}{(k_{y,1} + k_{y,2})} = \frac{2\pi\Delta f}{2\pi/\lambda_{y,1} + 2\pi/\lambda_{y,2}} = \frac{\Delta f}{1/\lambda_{y,1} + 1/\lambda_{y,2}} \\ &\approx 150\Delta f \quad \text{in µm/ sec} \end{aligned} \tag{4.34}$$

since we can assume $\lambda_{y,1} \approx \lambda_{y,2} \approx \lambda = \omega/c_\mathrm{sub} = 300\,\mu\mathrm{m}$ where $c_\mathrm{sub} = 3990\,\mathrm{m/sec}$ the surface wave speed on the lithium niobate substrate, and the typical frequency is 13.3 MHz. Comparing this with the notation of transducer 1 and transducer 2 (Fig. 4.5), it can be seen that the pressure nodes and therefore the particles are always displaced away from the higher frequency transducer. It can be shown [**Simon2018APL**]that the primary acoustic radiation force has the frequency difference directly in its argument as for the phase modulated case:

$$F_{\mathrm{ac},y} = c_\mathrm{ac} \sin\left(2k_y y - \Delta\omega t\right) \tag{4.35}$$

and therefore the frequency modulated method is essentially analogous to the continuous phase modulated method, when we take $\Delta\omega = s$, i.e. $\Delta f = 1/t_\mathrm{ramp}$. Both the trajectory equation and the force balance predict a limit for the linear translation of particles. The maximum particle speed, is obtained from the maximum primary acoustic radiation force

$$v_\mathrm{max} = (\dot{y})_\mathrm{max} = c_\mathrm{ac}/c_\mathrm{visc} \tag{4.36}$$

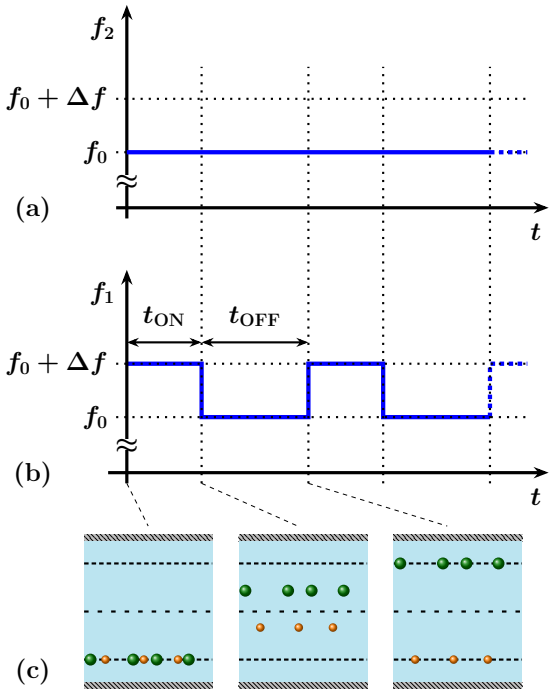

Figure 4.6: The sorting principle of the frequency modulated method, including the two excitation signals

Any frequency difference that causes a nodal translational speed v_p less than v_{max}, forces the particles to move linearly with a constant speed. For the illustration of this type of sorting, refer to Fig. 4.6. The frequency difference, Δf, is switched on for a period of time t_{ON}, followed by an off period, t_{OFF}. During the OFF period particles can relax at the nearest node before being translated again. Note that the transducers are on for the entire sorting process and only the frequency modulation switches periodically. The on period has a length of $t_{ON} = 1/\Delta f$ guaranteeing that the pressure nodes move half a wavelength, as illustrated in Fig. 4.6c. The off period allows the particles to reach an equilibrium position at the focusing node (small particles) or at the sorting node close to the target outlet (large particles) as shown in Fig. 4.6c. This on-off switching approach makes the sorting technique more reliable, as the oscillating small particles are forced to a fixed position periodically at the acoustic pressure nodes.

However, if the nodal speed is greater than the maximum speed ($v_p > v_{max}$) the particles oscillate and shift at the same time, in a less deterministic manner.

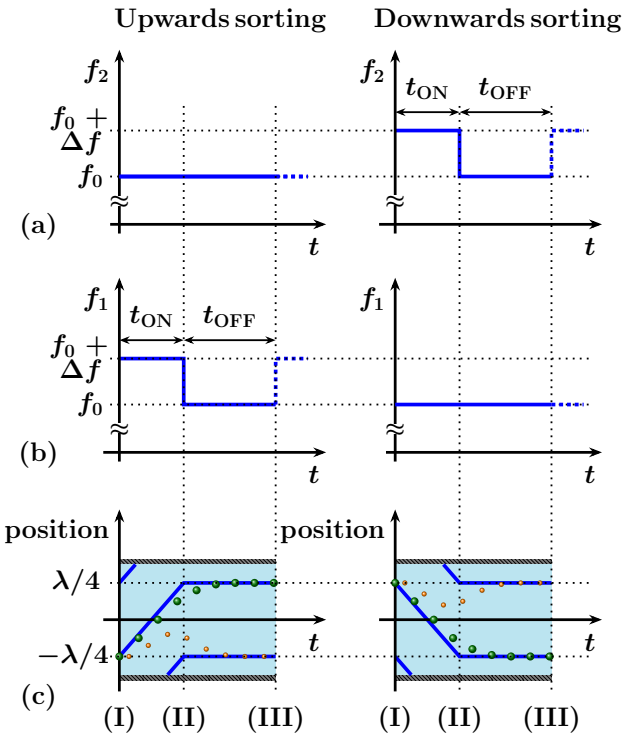

Figure 4.7: The directivity of the sorting can be reversed by adjusting the inflow rates and negating the excitation signal to achieve either upwards (target exits at the top outlet) or downwards (target exits at the bottom outlet) sorting. These directions are defined looking at the device top down, i.e. in reality sorting is performed towards the back and front faces in the horizontal direction and not in the vertical direction. The illustration shows frequency modulation due to its simple nature, but phase modulation could be used as well

4.3 Changing the directivity of sorting

The particle sorting can be also performed in the reverse direction by adjusting the flow rates at the input and the sign of the electrical excitation signal. In the following, the upwards and downwards directions are defined looking at the device top down (Fig. 4.7 and its caption). Using relative flow rates such that the particles trap at the top node initially, and allowing the pressure nodes to move towards $-y$, the sorting is performed towards the bottom node. The sorting with the target particles exiting at the upper outlet is referred to as upwards sorting, while the reverse scenario is called downwards sorting. Although this two-way sorting can be performed using any of the phase modulated methods (PM) or the frequency modulation (FM), in Fig. 4.7 it is illustrated with the frequency modulation due to its simplicity. This technique was investigated to analyse the effect of the asymmetric inlet sorting device (see Fig. 4.5). Furthermore, it allows for bandpass sorting to be carried out as discussed in the next section.

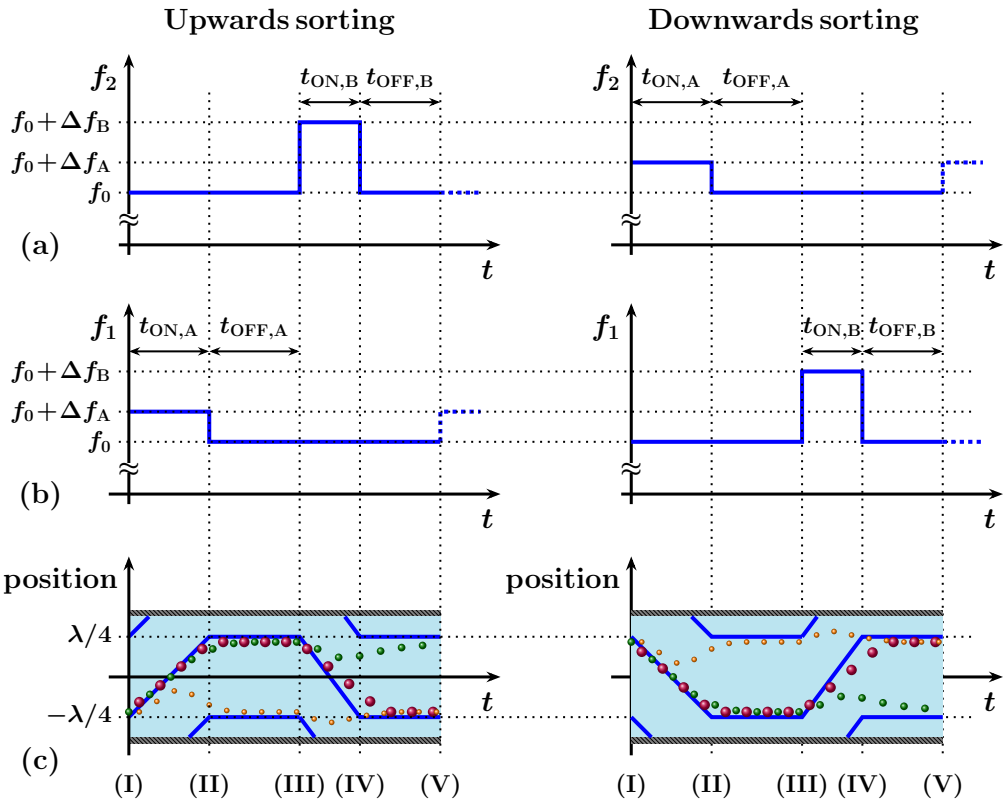

Figure 4.8: Coupling two modulation cycles directly allows for performing bandpass sorting of the middle size particles of a three particle mixture

4.4 Bandpass sorting

The previous section allows separation of particles towards either of the two outlets using excitation signal with opposite sign. This can also be utilised in a combined sorting pattern to achieve bandpass sorting and selection of the middle-sized particle from a three particle size mixture. This method can be used with either PM or FM, but again, for simplicity the illustration (Fig. 4.8) is given for the FM case. The initial setup is the same: the particles are focused at one of the nodes and trapped there. During the first stage, the two larger sized particles are displaced and relax at the other pressure node (sorting node). During the second stage, by adjusting the frequency difference, only the largest particles are moved back towards the original trapping node, leaving the middle sized particles at the sorting node. Typical trajectories are also plotted in Fig. 4.9.

4.5 Chapter summary

In this chapter various dynamic acoustic waveforms were introduced that can be applied for particle separation. These are either based on phase or frequency

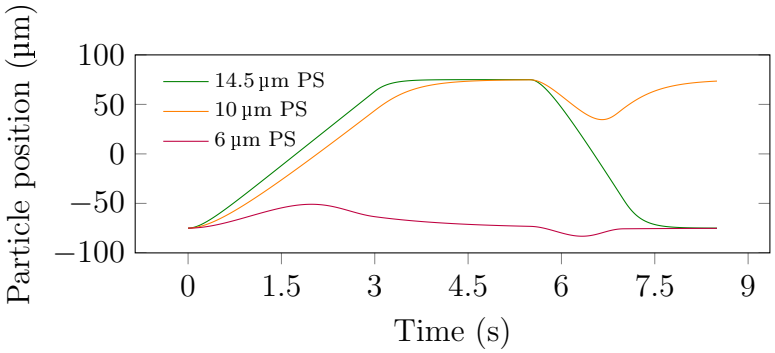

(a) Upwards bandpass separation trajectories of 6, 10 and 14.5 µm polystyrene particles in diameter

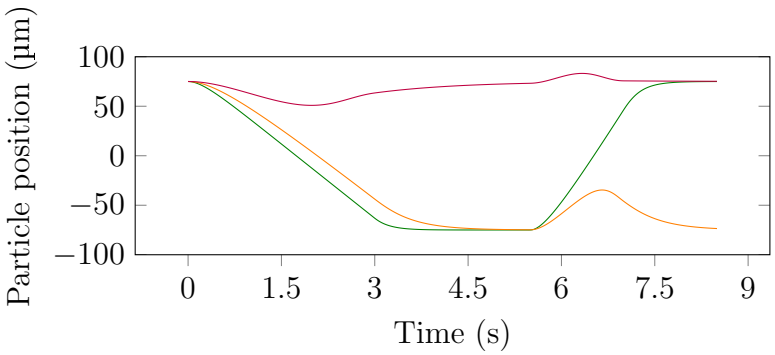

(b) Downwards bandpass separation trajectories of 6, 10 and 14.5 µm polystyrene particles in diameter

Figure 4.9: Analytical particle trajectories of bandpass separation of 10 µm polysytrene particles from 6 and 14.5 µm ones.

modulation of the excitation signal of the transducers. Although the frequency modulation was shown to be analogous to the continuous phase modulation, it offers simpler implementation. The analytical equation for particle trajectories within phase modulated fields was given and used to assess the optimum timing parameters for sorting and the scaling laws for various experimental parameters such as voltage or particle size. A linear phase modulation with an initial phase jump was proposed for faster sorting and compared against the continuous phase modulation. Although this method confines the smaller particles better, it inherently has a limiting size ratio that can be successfully separated. All sorting methods are proven to be bidirectional by adjusting the inflow rates and the sign of the excitation signal. Finally combining two opposite directed sorting periods with adequate timing parameters a bandpass-type separation of particles is feasible.

Chapter 5

Device design, fabrication, characterization and experimental setup

5.1 Design of IDTs and microchannel

Some of the most commonly used designs of interdigitated electrodes to achieve surface wave actuation are shown in Fig. 5.1. These are all periodic structures, with periodicity

$$\lambda = \frac{c_{\text{sub}}}{f_0} \tag{5.1}$$

where the typical surface wave velocity on the substrate is c_{sub} and the resonant (centre) frequency of the transducer is f_0. At this frequency f_0, the best electromechanical coupling can be observed, i.e. the highest surface wave displacement amplitude for a given transducer voltage. The various designs that result in different directionality and bandwidth of the surface wave excited are discussed in the following.

The simplest design (Fig. 5.1a) uses a metallization ratio of 0.5, meaning the electrode fingers and the gap between them all equal to each other and $\lambda/4$. Due to the symmetry of this structure, a surface wave, which is narrow band with high resonance peaks, is launched in both the forward and backward direction [203]. As the backwards travelling wave carries away half of the energy and in most cases have no use, changes to the structure are desired to make the wave propagation unidirectional. This can be achieved by either reflectors or making the structure asymmetric. The

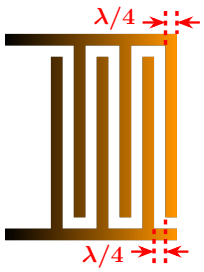

(a) The simplest transducer design, with all finger widths and separation gaps equal to $\lambda/4$

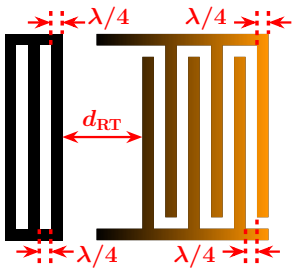

(b) The simple transducer complemented with a reflector bank at the back side to ensure wave propagation in the forward direction only

(c) Split finger transducer design that suppresses reflections. All metal strips and gaps are $\lambda/8$ wide

(d) SPUDT unidirectional transducer utilising asymmetric design. All unmarked (larger) gap widths are $3\lambda/16$

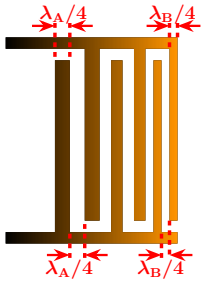

(e) Chirped transducer, where the finger widths gradually change from quarter λ_A to λ_B thus resulting in a wideband operation

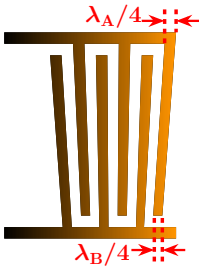

(f) Slanted-tapered transducer design, where the two sides correspond to simple designs with λ_A and λ_B characteristic wavelength

Figure 5.1: Overview of the most common inderdigitated transducer designs for surface acoustic wave actuation or sensing

straightforward implementation of a reflector-based structure is to place additional metal strips behind the transducer (Fig. 5.1b), where the backwards travelling wave is reflected [236, 237]. To have constructive interference from the reflected and forward travelling waves, a phase difference of 2π must be ensured. Although the design at higher frequencies ($> 100\,\mathrm{MHz}$) is quite complex [238] at lower frequencies simpler considerations can be made. As the reflection itself introduces a reflection phase change of π [203], a path difference of $\lambda/2$ odd integer multiple is required for the wave travelling from the IDT, getting reflected and arriving at the IDT again (distance d_{RT} in Fig. 5.1b). Moreover, this path is double the distance between the IDT and the reflector, as a conclusion, $\lambda/4$ odd integer multiple difference between the IDT and the reflector is needed. Most devices directly have as small distances as either $\lambda/4$ [239, 240] or $3\lambda/4$ [236, 237]. In acoustofluidic applications even arbitrary

distances are successfully used [241]. A similar approach is a split electrode design (Fig. 5.1c). Here the distance between the centreline of two split fingers is $\lambda/4$, making sure the path difference is $\lambda/2$ leading to a phase difference between the two reflected waves of π, and therefore destructive interference and successful suppressing of reflected waves. However, this comes at the cost of reducing the minimal feature size by half and requiring stricter fabrication [242, 243].

Making the IDTs asymmetric (Fig. 5.1d), the surface waves are only allowed to propagate in the forward direction and the backward propagation is suppressed via destructive interference, resulting in a single-phase uni-directional transducer (SPUDT). The minimal feature size with this device is again half as of the traditional approach [242, 244].

The individual IDT finger pairs do not need to have the same $\lambda/4$ width throughout the whole transducer, but it can vary between two quarter wavelength values, resulting in chirped IDTs (Fig. 5.1e). These transducers behave similarly to the simple design as they launch bidirectional surface waves, but the bandwidth of the transducer is broader and consequently the resonance frequency peak lower [245].

An interesting approach is to make the fingers slanted and tapered towards one side, creating slanted-finger interdigital transducers (SFITs), where the lateral sections of the transducer function as the simple transducer design, but the wavelength changes spatially across the width (Fig. 5.1f). This IDT can be used to achieve a peculiar version of particle trapping, where the trapping distance varies along the microchannel [246, 247].

Finally, it is important to mention that none of these transducers launch a perfect plane surface wave, meaning the edge effects are quite significant and diffraction patterns are observed at the two edges of the transducers [248, 249]. Although to review the design to suppress this detrimental effect is out of the scope of the thesis, interesting to mention that as simple structures as cuts across the electrode fingers can help to overcome these effects, thus creating apodized IDTs [203].

Attenuation coefficients up to 5 dB/cm are reported for lithium-niobate substrates at tens of MHz operating frequencies [250]. In most microfluidic applications the round-trip length from transducer to the edge of the substrate and to the channel is usually a few cm, allowing 5-10% of the reflected signal to interfere within the channel. Consequently, the bidirectionality of a transducer usually does not cause problems [233, 251]. Therefore, the simplest design (Fig. 5.1a) was used initially, and

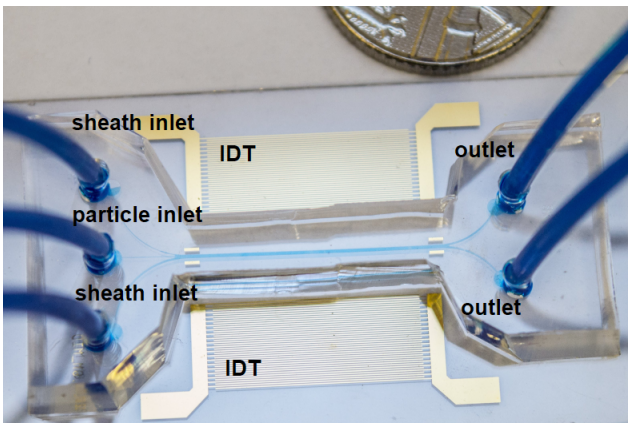

Figure 5.2: The fabricated microfluidic device, with the gold IDTs on the lithium niobate substrate and the PDMS microchannel bonded on top. To better visualize the inlets, microchannel, and outlets, blue dye is used to fill up the channels

later on replaced by the chirped design (Fig. 5.1e) which is justified in this Chapter. In experiments, no performance difference was seen when absorbing materials were placed behind the transducer, further validating the negligible effect of edge-reflected waves. The operating wavelength was chosen to be 300 µm for handling objects of 5 to 20 µm and staying well below the Rayleigh limit [128], while still minimising device size. This corresponds to a centre frequency of 13.3 MHz on the lithium niobate 128°-Y cut wafer with $c_{\text{sub}} = 3990\,\text{m}\,\text{s}^{-1}$ [232, 233].

For the microfluidic channel design less stringent requirements are to be followed. The height of the channel must be large enough to accommodate the largest particles or cells without the risk of clogging, however, too high channel (around and above 80 µm) puts stringent requirements on the photoresist and leads to long fabrication process (see next Section). For these reasons, a channel of 50 µm offers a good trade-off. To obtain a suitable width, two pressure nodes must fit within the device ($\lambda/2 = 150\,\mu\text{m}$), and on both sides a safety margin needs to be left for the anechoic corner (see Section 6.3.2). For the given height, this results in 30 µm on both sides, resulting in a total minimum of 210 µm width. With additional safety margin for manufacturing uncertainties, 240 µm is selected as the channel width.

5.2 Fabrication procedure

The standard fabrication process used by the acoustofluidic community [251, 252] was applied with appropriate parameter modifications as a result of differences in instruments (such as UV output power, plasma power etc.). The device comprised of

three separate fabrication steps: the IDTs need to be patterned on the piezoelectric substrate, the PDMS microchannel needs to be moulded and the two components bonded using O_2 plasma.

5.2.1 Interdigitated transducer fabrication

An overview of the IDT fabrication in shown in Fig. 5.3. Refer also to Fig. 5.2 for a photo of a final device. The fabrication is based on a lift-off process with five main steps. Before fabrication, the 3-inch wafer (500 µm thick) is cut into smaller pieces, to be able to manufacture more devices on one wafer and thus being resourceful. An automated wafer dicing saw with diamond blade was used (Disco DAD 3220, Disco Corporation, Japan) with cutting speed of $1.5\,\mathrm{mm\,s^{-1}}$ to avoid overheating of the wafer. The machine parameters during dicing were the following: spindle revolution $25\,000\,\mathrm{min^{-1}}$, current at spindle 0.9 to 1.1 A. To reduce mechanical stress during the dicing process, a two-run dicing was used, resulting in a total processing time of 7 min for 3 pieces and 8 cuts on a wafer.

The pieces are cleaned using acetone and isopropanol (IPA). In the first step, the photoresist (AZ2070 negative lift-off resist, MicroChemicals GmbH, Germany) is dispensed and spin-coated onto the substrate (Fig. 5.3a). To avoid the rectangular-shaped wafer pieces falling off the chuck during spin-coating, double sided tape was used to secure the piece. As this resist only acts as a sacrificial layer and no exact thickness is required for post-processing, no characterisation of thickness versus the spin speed was carried out. Instead, the spin ramp parameter was used as suggested by the datasheet ($500\,\mathrm{min^{-1}\,s^{-1}}$), but the terminal rotational frequency was reduced from $4000\,\mathrm{min^{-1}}$ to $3600\,\mathrm{min^{-1}}$, again to make sure the piece is in a stable position during coating. The edge bead formed by the spin-coating process did not affect further manufacturing and therefore was not removed.

A pre-exposure bake is required to evaporate solvents from the photoresist. Since lithium niobate is a pyroelectric material [253, 254], meaning that heat causes surface charges and sparkles to form, which can crack the device, extra care is taken, and the temperatures are gradually increased and decreased to avoid any such effect. In this specific case, the sample is placed on a hotplate for 65℃, 95℃ and 65℃ for 1 min, 2 min and 1 min, respectively. Two separate hotplates are used to allow precise control of the required temperatures.

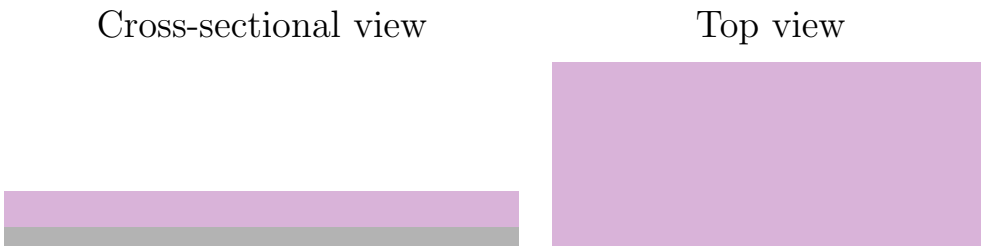

(a) The lithium niobate substrate is coated with AZ2070 negative liftoff resist

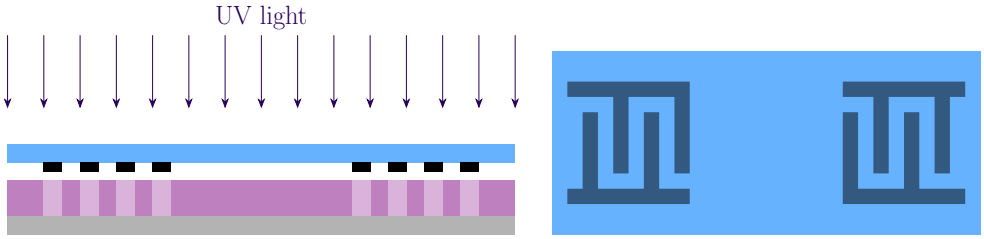

(b) UV exposure through a positive mask. Exposed areas crosslink

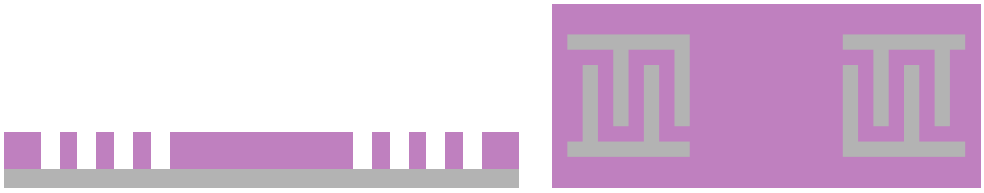

(c) The unexposed areas develop away leaving a negative pattern of the IDT design

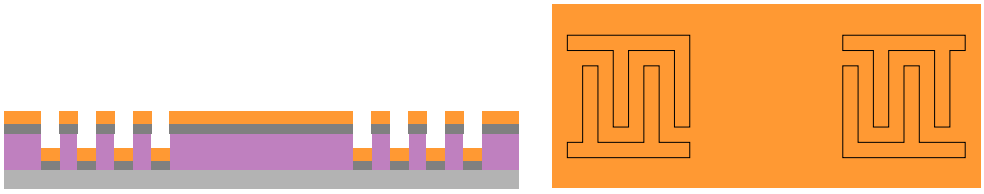

(d) Chrome (or titanium) and gold are deposited onto the substrate

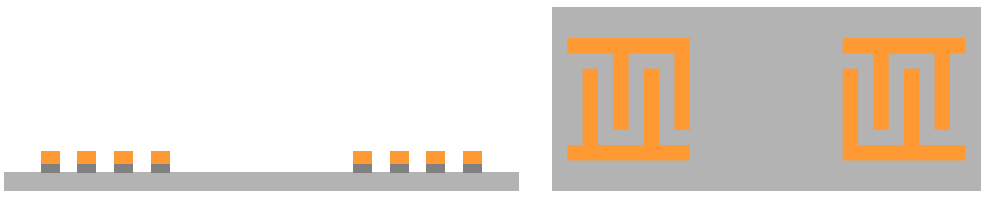

(e) After liftoff the desired IDT patterns are formed on the substrate

Figure 5.3: Steps during fabrication of IDTs for SAW devices. The materials used are: lithium niobate ■, unexposed resist ■, exposed (crosslinked) resist ■, chrome (or titanium) ■, gold ■, glass ■

Based on the tone of the resist, a suitable mask pattern should be selected. As now a negative resist is used, but the lift-off process inherently causes an inversion of the pattern, a positive mask should be applied (i.e. with black areas of the shape of the desired metal pattern). A low-cost polymer film mask (Micro Lithography Services, UK) was used that could fit various designs to allow for prototyping and tests. A dose test was carried out to characterise the UV lamp output power and its effect on the resist. The mask was placed onto the coated wafer, and masking tape used to cover three quarters of the mask initially, exposing the resist for 6 s, uncovering another quarter and repeating to finally arrive at a sample where the quarters were exposed to UV light for 6, 12, 18 and 24 s. For this resist and exposure times, no difference between the patterns was visible that would indicate a severe under- or overexposure, and a mean value of 15 s was used later.

After UV exposure (Fig. 5.3b) a post-process bake ensures the cross-linking of the polymer. Here the exact same ramped heating/cooling of the resist is applied as for the pre-bake. The recommended developer for this photoresist is either AZ726 or AZ826, but as the AZ326 was stocked in the cleanroom, it was tried and used after a successful development (Fig. 5.3c). Usual development times range from 60 to 180 s and can be monitored visually. The developed sample is rinsed with distilled (RO) water. With the above parameters, the resist thickness was $5\,\mu m \pm 10\%$ throughout the whole piece. In case of fabrication problems, the exposed or unexposed resist can be removed by acetone and the process can be repeated on the same piece.

Metal deposition follows the resist development stage (Fig. 5.3d). First a thin layer (10 nm) of chrome or titanium is deposited to facilitate adhesion of gold onto the substrate, and then the gold of 50 nm is evaporated on top. Unfortunately the quartz thickness monitor in the metal deposition chamber was out of order during the evaporation, and therefore the thickness obtained are much larger than the intended values. However, this did not affect the overall performance of the device critically, only lowered the quality factor (Section 5.4 for device characterisation).

Finally the remaining cross-linked photoresist (which acts as a sacrificial layer) with the undesirable metal on top is dissolved in acetone and the final IDT patterns reveal (Fig. 5.3e). Successful lift-off occurs within tens of seconds, longer required exposure to acetone usually indicates manufacturing errors, such as metal stiction onto the substrate.

Some example fabricated transducers investigated with Zygo interferometer

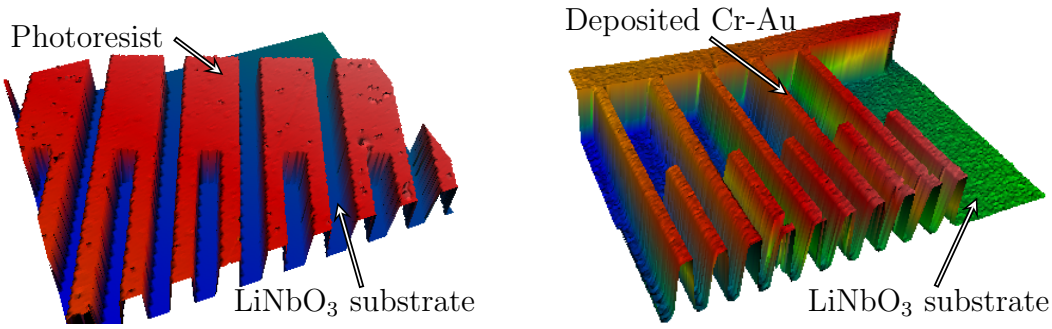

(a) Recording after resist development, the transducer finger areas are not covered with resist

(b) Recording after lift-off, the transducer pattern is covered with metal

Figure 5.4: Example images seen with the white light interferometer emphasising the pattern inversion between the images corresponding to before metal evaporation and after lift-off

(NewView 5000, Zygo Corporation, USA) are shown in Fig. 5.4, after development and after lift-off to show the inherent pattern inversion of the process.

5.2.2 PDMS microchannel fabrication

The PDMS microchannel can be seen as a blue dye filled rubber-like material on top of the device shown in Fig. 5.2. As for the polydymethylsiloxane (PDMS) the wafer only acts as a carrier of the pattern during fabrication, there were no limitations (orientation, doping, thickness) on wafer parameters apart from being silicon. A 3-inch single sided 500 µm thick wafer was used and as the cut can be performed with a diamond pen in this case this process step is faster.

The preparation steps in this case include substrate clean with acetone/IPA followed by a dehydration bake in oven at 180℃, 5 min and finally O_2 plasma treatment for 30 s at 100 W.

The channel master is fabricated using SU8 photoresist due to its high chemical and physical stability [255]. The specific SU8 3050 (MicroChem Corp., USA) type has nominal thickness of 50 µm ideal for the channel.

The resist thickness directly determines the channel height, therefore precise control of thickness is desired. Therefore for spin coating various terminal frequencies were tested and compared with the datasheet values [255]. The initial ramp speed was reduced to $100\,\mathrm{min^{-1}\,s^{-1}}$ to ensure the substrate is in a stable position on the spin coater chuck. A total time of 45 s was used for all terminal frequency values, the results are tabulated in Table 5.1. The results are in good agreement with the

Terminal frequency (rpm)	Datasheet thickness value (µm)	Measured average thickness value (µm)
1000	102	115
2000	68	75
3000	50	51
4000	44	40

Table 5.1: Datasheet and experimental thickness values for SU8 3050 photoresist

datasheet values (less than 13%), especially around the required 50 µm thickness. The precise process control of SU8 is especially important since the removal of cross-linked photoresist is only possible with Technistrip (NI555, MicroChemicals GmbH, Germany) and requires days to process.

Due to the thick resist, pre-exposure bake in this case takes 1.5 h and carried out at 100℃ on a hotplate. The wafer is afterwards let to to cool down for 1 h on room temperature, making this step the most time-consuming of the entire fabrication process.

As the SU8 is a negative tone resist, a negative mask of the channel is required for the fabrication process. In the case of the SU8, various doses of UV exposure result in significant pattern distortions. To better assess the dose test, instead of channel designs, the transducers design was used, which has symmetric and periodic structures. Exposure times between 20 and 80 s were tested and for 80 s the original 1-to-1 ratio of finger areas to gap areas turned into 2:1 ratio of those areas due to overexposure. The reflection of UV light from the substrate top and diffraction at pattern edges combined with longer exposure time makes a larger SU8 surface to be exposed and cross-linked. Best features observed for 20 s which is used for following exposures.

The cross-linking process of the polymer can be sped up by heat treatment. Therefore, post-exposure bake was carried out on a hotplate at 100℃ for 3 min, then the sample was left to cool down at room temperature for 10 min.

The commonly used developer of SU8 is termed EC solvent (chemical name PGMEA or PGMA or 1-methoxy-2-propanol acetate), for the resist thickness used here typical development time varied between 5 to 8 min. The developed sample is rinsed in IPA.

A mechanical cure follows to ensure good stability of the channel master. First the sample is O_2 plasma treated for 30 s at 100 W, followed by a 2 h long heat treatment

at 120℃.

As the SU8 on the silicon substrate is used as a master for the PDMS channel and the PDMS needs to peel off of the master without any stiction, a hydrophobic surface treatment must follow. The samples are placed in a mixture of 30 µl silane (Trichloro(1H,1H,2H,2H-perfluorooctyl)silane, Sigma-Aldrich, UK) and 50 ml heptane (Sigma-Aldrich, UK), covered for 10 min and finally rinsed in DI water.

The preparation of PDMS (Sylgard 184 kit, Sigma-Aldrich, UK) was done by mixing the polymer and curing agent in 10:1 ratio. The mixture was placed under vacuum for 30 to 45 min to remove air bubbles. This time is short compared to the full curing time (24 h) of the PDMS. The smooth mixture can be poured onto the surface treated SU8 master (placed in a Petri dish) and cured either on room temperature overnight or in an oven (30 to 60 °C) to speed up the process. The oven curing has to be done at relatively low temperatures: at 60 °C shrinkage and warping of the PDMS is observed. The fastest curing (about 1 to 2 h in total, depending on PDMS thickness) without any adverse effects was carried out at 40℃. The channels can be cut out using a scalpel (No. 11, Sigma-Aldrich, UK) or any general purpose blade, inlets and outlets punched with a biopsy punch (outer diameter 2 mm, Thermo Fisher Scientific, UK).

5.2.3 Bonding of the substrate and the channel

Bonding the PDMS channel to the lithium niobate substrate has proven itself the most challenging fabrication step. Precise parameter control and sample preparation is required along with good dexterity to achieve a high quality final device.

First the lithium niobate samples are cleaned in acetone in ultrasonic bath, followed by methanol cleaning of both the PDMS channels and the substrate samples. The pieces are dried and placed with the sides to-be bonded facing up in a reactive ion etch (RIE) machine at 100 mTorr pressure and 50 sccm oxygen inflow. After activation, a drop of methanol is applied on the substrate to allow positioning of the PDMS channel [245] under an optical microscope. Finally, the aligned samples are placed on a hotplate at 65℃ for 15 minutes. Various power and time values of the RIE were investigated for effectiveness on bonding, however, the quality or strength of bond is difficult to characterise and usually visual and manual tests were performed. These observations are summarised in Tables 5.2 and 5.3 after placing

	10 s	24 s
60 W	Bonding initiates at the sides slowly (0.5 to 1 mm s^{-1} propagation speed) some voids can be observed even after 5 minutes on hotplate (due to the start of bonding at the sides). After 15 minutes on hotplate it appears to be 90% bonded.	Bonding again initiates at the sides (now 1 to 2 mm s^{-1}), a half void is formed at one edge. Void stays even after hotplate treatment (20% of total surface area). Pressing down on void does not help forming a bond.
100 W	Very rapid bonding (2 to 3 mm s^{-1}) again from edges. Around the channel and inlets bonding stops, possibly due to an uneven edge cut. However, it continues to bond on a hotplate. After the heating the bonding seems to be fully developed.	Bonding does not initiate. Placing under vacuum does not help. Pressing down on the PDMS helps to initiate bonding, continues on hotplate. Large variance in coverage between samples, around the channels it seems to be not bonded.

Table 5.2: Observations of PDMS and substrate bonding quality for various power and oxygen plasma activation time

	10 s	24 s
60 W	Unbonded area is 5% of total 750 mm^2. After peeling off, three sides perfect, at the void side it increases to 10%. Still holds well.	Unbonded area is 15% of total 570 mm^2. After peeling off, three sides perfect, the void propagates inwards an extra 70-80% of original size (to 25%) and only the channel stops it.
100 W	Debonded area is only 2.5% of original 800 mm^2. Peeling off moves void inwards by 2.5x, and another void is formed at the corner. Total voids now 7%.	One piece 3.5% of 600 mm^2, other 12% of 550 mm^2. After peeling off first goes up to 10%, second to 35%. Significant delamination. Problem of bonding around channels.

Table 5.3: Observations of bonding quality during manual pull test

the samples on the hotplate and after a manual pull test is performed on the bonded samples, respectively. From these values, 100 W power and 10 s activation time were used afterwards. It is suspected that longer times result in lower quality bonding due to 'burning' of the PDMS: instead of creating free radicals, the surface is treated for too long and everything is removed.

Worth mentioning that newer types of RIE machines with a constantly depressurised chamber usually have a small opening allowing for the samples to enter, which would not fit the PDMS mould. In these cases, a hand-held corona discharge gun can be used to activate the PDMS surface [256] and was successfully utilised in the last month of this project for the same reason. The output power of the corona gun

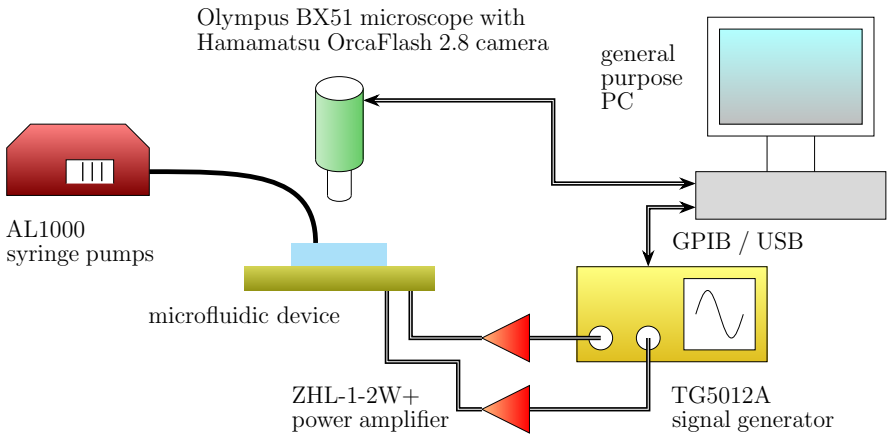

Figure 5.5: The experimental setup, comprising the microfluidic device, syringe pumps, signal generator and power amplifiers. The particle motion is observed through a regular microscope with bright field configuration, both the light source and camera are above the specimen

cannot be adjusted precisely, but a medium setting is usually adequate from 1-2 inches distance from the sample.

5.3 Experimental setup

The experimental setup (Fig. 5.5) comprised of the device mounted on printed circuit board, syringe pumps (World Precision Instruments, Sarasota, USA), a signal generator (TG5012A, Aim-TTi, UK) and power amplifiers (ZHL-1-2W+, Mini-Circuits, UK). The appropriate phase pattern and signal parameters were uploaded to the signal generator via a general-purpose interface bus (GPIB) connection using LabView (National Instruments, UK). The device was mounted on a microscope (Olympus BX51, Olympus, UK) and the particle trajectories were recorded with a camera (Orca Flash 2.8, Hamamatsu, UK) at a rate of 80 fps.

5.3.1 LabView optimization and porting

As the project was a continuation of a particle separation work carried out in a bulk device [195], I was provided with a LabView code that implemented the phase modulation in a direct fashion by updating the phase of one of the transducers step-by-step during the sorting process. However, the communication delay between the PC and the signal generator caused uneven phase modulation pattern with this on-the-fly approach. Therefore other possibilities of phase control were investigated

and a pre-programmed phase pattern applied to reduce communication delays. One period of the phase pattern was uploaded into the signal generator as an arbitrary signal and used as the source of internal phase modulation of one channel. During the actual sorting, only one instruction needs to be communicated with the signal generator: to switch on the phase modulation. To further minimise delay problems and ensure that enough time is given to record the process with the microscope, the phase pattern was uploaded reversed, first the resting period followed by the ramping period. A comparison of particle trajectories with the two approaches can be seen in Fig. 5.6, validating the superiority of the internal phase modulated approach, allowing for precise particle control.

As the standard configuration of the signal generator is equipped with a USB port, but not all models are fitted with a GPIB port, it is beneficial to ensure the code works on the simplest USB configuration (which appears as a virtual serial COM port on the PC). The LabView code was tested on the USB port and time-outs were observed for certain higher level function calls. As no direct control of timings within these functions is provided, to fix these, the functions needed to be implemented using low-level serial port instructions. As a consequence, at this point everything was provided to transfer the code into MATLAB or C#, where a considerably easier software design can be carried out, with additional error checks or status messages displayed. As C# offers a more flexible function calling and variable handling mechanism, it was chosen as the implementation tool for the final version of the control software. Modification to include the phase modulated or bandpass sorting techniques required couple of hours compared to the tedious LabView implementation.

5.4 Device characterization

5.4.1 Butterworth–van Dyke model of transducers

The usual lumped element Butterworth–van Dyke model [203,257–259] for a transducer (bulk or surface wave) around resonance is shown in Fig. 5.7. The elements with subscript m comprise the acoustic (mechanical) branch, while the parallel capacitor C_0 represents electrical processes. The additional R_s and L_s series elements correspond to parasitic losses as the transducers are soldered on an measured on a PCB. The

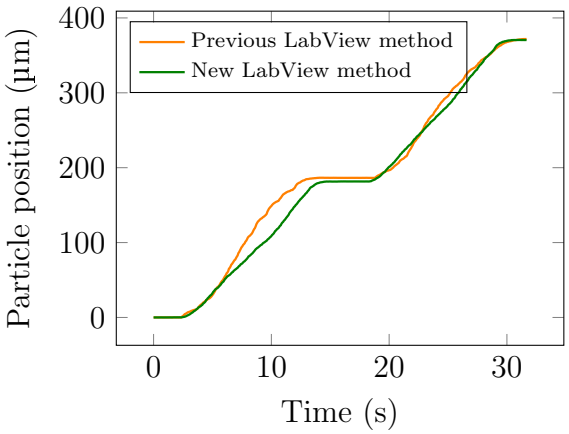

Figure 5.6: Comparison of 10 µm particle trajectories with the direct phase modulation and internal phase modulation approaches of signal generator control

admittance of the main transducer elements, the parallel components comprising the acoustic and electrical branches, can be written as

$$Y(\omega) = i\omega C_0 + \frac{1}{R_\mathrm{m} + i(\omega L_\mathrm{m} - 1/\omega C_\mathrm{m})} \tag{5.2}$$

Now denoting $\tau(\omega) = \omega L_\mathrm{m} - 1/\omega C_\mathrm{m}$ we have

$$Y(\omega) = \frac{R_\mathrm{m}}{R_\mathrm{m}^2 + \tau^2} + i\left(\omega C_0 - \frac{\tau}{R_\mathrm{m}^2 + \tau^2}\right) \tag{5.3}$$

and as at resonance, the real part of the admittance, at antiresonance the real part of the impedance has a maximum [258], the resonance and antiresonance frequencies can be expressed as

$$f_r = \frac{1}{2\pi\sqrt{L_\mathrm{m} C_\mathrm{m}}} \tag{5.4a}$$

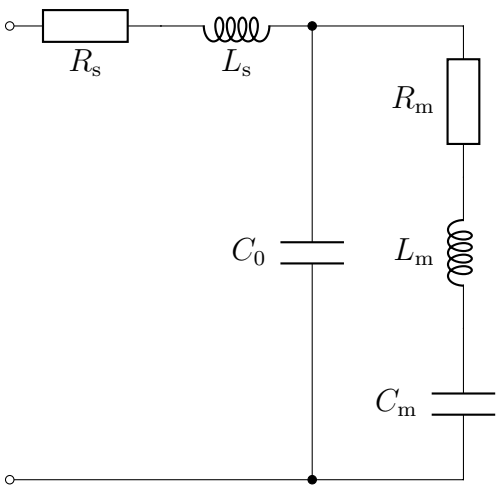

Figure 5.7: Butterworth–van Dyke lumped model of a transducer, the additional series elements represent parasitic losses due to the PCB mount

Variable	Fit performed on					
	$\lvert Z\rvert$	Re$[Z]$	Im$[Z]$	$\lvert Y\rvert$	Re$[Y]$	Im$[Y]$
R_m	89.54	109.2	90.64	89.46	101.3	101.5
L_m (×1e−5)	2.563	2.797	2.499	2.383	2.592	2.596
C_m (×1e−12)	5.89	5.393	6.057	6.341	5.819	5.810
r	18.25	18.66	17.75	17.22	17.91	17.92
C_0 (×1e−10)	107.49	100.63	107.51	109.19	104.22	104.12
R_s	20.88	19.27	20	22.73	20.79	20.75
L_s (×1e−8)	0.014	30	0.024	0.023	5.686	5.813
RMSE $\lvert Z\rvert$	6.3083	16.1143	6.2409	6.336	6.792	6.794
RMSE Re$[Z]$	6.3378	6.5958	6.3301	7.407	6.923	6.913
RMSE Im$[Z]$	6.2756	17.2821	6.2401	6.545	6.748	6.747
RMSE $\lvert Y\rvert$ (×1e−3)	0.375	1.380	0.343	0.316	0.340	0.341
RMSE Re$[Y]$ (×1e−3)	0.363	1.208	0.338	0.402	0.343	0.342
RMSE Im$[Y]$ (×1e−3)	0.376	1.090	0.344	0.335	0.344	0.344

Table 5.4: Obtained BVD model parameters and root mean square error for fit performed on absolute value, real part or imaginary part of admittance and impedance

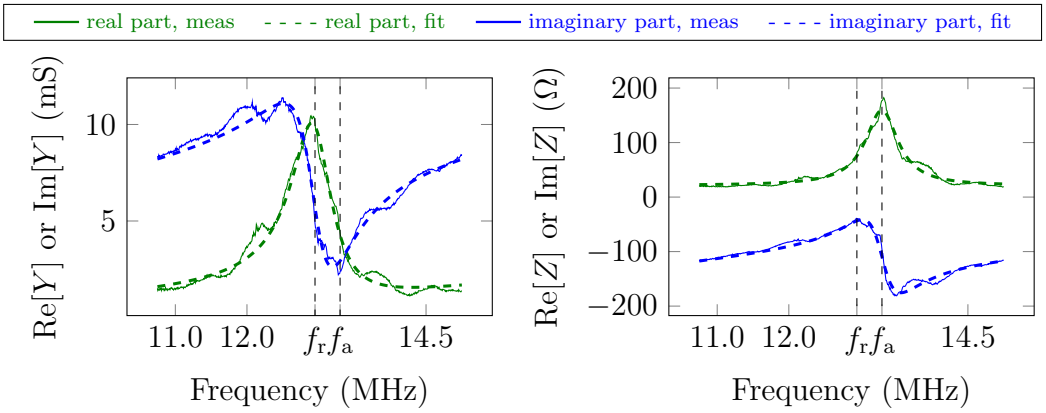

(a) Admittance, $Y(i\omega)$ (b) Impedance, $Z(i\omega)$

Figure 5.8: Measurement results of the transducers with the fitted curves using the lumped element BVD model. The resonance and antiresonance peaks are best visible in the admittance and impedance plots, respectively

$$f_a = f_r\sqrt{1+\frac{C_\mathrm{m}}{C_0}} \tag{5.4b}$$

and usually the capacitance ratio is denoted by $r = C_0/C_\mathrm{m}$. Of the two type of transducers the chirped IDT was investigated first as the fixed frequency IDT has a noisy response. The recorded S-parameters (using a vector network analyser N5225A, Agilent Technoligies, USA) were transformed to Z-parameters and Y-parameters (later referred to as impedance and admittance). The two transducers are characterised by Z_{11} and Z_{22}, while the cross-coupling coefficients Z_{12} and Z_{21} are now not investigated.

The BVD parameter fit can be performed on any of the six descriptive parameters

$|Z|$, Re$[Z]$, Im$[Z]$, $|Y|$, Re$[Y]$ or Im$[Y]$. Therefore first it was investigated how the choice of the target for the fit affects the overall fitting accuracy. The results are summarized in Table 5.4. This reveals a large root mean square error (RMSE) for a fit performed on Re$[Z]$ or $|Y|$. Moreover the lumped model parameters vary from fit to fit, except for the two last columns (fit for Re$[Y]$ and Im$[Y]$), and therefore the fit was chosen to be performed on the imaginary part of the admittance. An example transducer response and a corresponding fit can be seen in Fig. 5.8, where the maximum of admittance and the maximum of impedance align well with the resonance and antiresonance frequencies, respectively.

Next the transducer response at different temperatures was investigated. Data for fixed frequency and chirped transducers can be seen in Tables 5.5 and 5.6, respectively. The original measured frequency responses are also plotted in Fig. 5.9. It is clear that for all 4 transducers investigated, the frequency response has a negative temperature coefficient and shifts to the left with increasing temperature. Moreover, the response of the fixed frequency transducer is significantly more noisy than the chirped IDTs, while increase in resonance peak is only double. Therefore to achieve stable device operation, it is beneficial to use a chirped transducer, with small variance against frequency or temperature, and still high conductivity around resonance.

To further quantify the temperature dependence of the BVD parameters, they were plotted against temperature as shown in Fig. 5.10. Although some authors suggest a linear parameter dependence with temperature [260], this cannot be observed for these values. This is probably due to the low quality factor of these devices ($Q = \omega L_\mathrm{m}/R_\mathrm{m} \approx 20$ to 40) and a variation in fit.

However, the resulting resonance and antiresonance frequencies still follow a linear dependence as shown in Fig. 5.11. The fixed frequency device has a narrower response range and varies only between -916 to $-1094\,\mathrm{kHz\,°C^{-1}}$ in contrast to the variation of the chirped device between -745 to $-1157\,\mathrm{kHz\,°C^{-1}}$.

Final investigation was carried out for changing transducer aperture width. According to the literature [203], the lumped elements of the mechanical branch have the following width (W) and finger count (N) dependencies:

$$R_\mathrm{m} \propto \frac{1}{NW} \tag{5.5a}$$

$$L_\mathrm{m} \propto \frac{1}{NW} \tag{5.5b}$$

$$C_\mathrm{m} \propto NW \tag{5.5c}$$

Variable	$T = 3.3$℃		$T = 10.0$℃		$T = 19.9$℃		$T = 29.4$℃		$T = 38.9$℃		$T = 53.6$℃	
	Tr1	Tr2	Tr1	Tr2	Tr1	Tr2	Tr1	Tr2	Tr1	Tr2	Tr1	Tr2
R_m	57.94	41.24	57.45	40.62	56.06	39.40	55.59	39.46	55.69	39.01	55.69	37.13
L_m (×1e−5)	2.790	2.323	2.798	2.331	2.822	2.344	2.816	2.331	2.819	2.333	2.817	2.335
C_m (×1e−12)	5.388	6.433	5.389	6.413	5.351	6.390	5.373	6.437	5.374	6.446	5.392	6.450
r	18.69	18.75	18.59	18.79	18.40	18.69	18.40	18.70	18.32	18.52	18.28	18.60
C_0 (×1e−10)	100.70	120.60	100.20	120.50	98.44	119.40	98.86	120.40	98.44	119.40	98.55	120.00
R_s	13.90	26.71	15.82	26.47	18.96	27.21	18.31	26.90	19.12	27.18	20.77	28.64
L_s (×1e−8)	9.214	11.01	9.738	10.83	11.78	11.56	11.13	11.02	11.54	11.58	11.92	11.88
f_r (MHz)	12.965	13.019	12.961	13.017	12.952	13.004	12.939	12.993	12.931	12.978	12.914	12.969
f_a (MHz)	13.307	13.362	13.305	13.359	13.299	13.348	13.286	13.336	13.279	13.324	13.262	13.313

Table 5.5: BVD model parameters obtained for different temperatures. Two transducers tested, both follow the fixed 13.3 MHz design

Variable	$T = 11.5$℃		$T = 20.1$℃		$T = 30.0$℃		$T = 38.5$℃		$T = 49.6$℃	
	Tr1	Tr2	Tr1	Tr2	Tr1	Tr2	Tr1	Tr2	Tr1	Tr2
R_m	97.1	114.0	97.93	112.3	97.73	111.1	99.39	112.2	100.7	111.8
L_m (×1e−5)	2.374	2.939	2.376	2.93	2.392	2.917	2.419	2.909	2.43	2.901
C_m (×1e−12)	6.348	5.224	6.356	5.248	6.323	5.278	6.262	5.298	6.245	5.321
r	16.87	17.44	16.8	17.52	16.8	17.44	16.63	17.23	16.56	17.21
C_0 (×1e−10)	107.09	91.11	106.78	91.94	106.23	92.05	104.13	91.28	103.42	91.57
R_s	20.52	21.71	20.51	21.79	21.32	22.28	22.24	22.81	24.12	23.34
L_s (×1e−8)	3.746	28.79	4.301	28.4	4.603	28.17	5.997	28.79	7.239	29.06
f_r (MHz)	12.9647	12.8445	12.9510	12.8348	12.9413	12.8268	12.9314	12.8201	12.9197	12.8100
f_a (MHz)	13.3434	13.2077	13.3309	13.1960	13.3209	13.1894	13.3145	13.1869	13.3040	13.1769

Table 5.6: BVD model parameters obtained for different temperatures. Two transducers tested, both follow the chirped IDT design

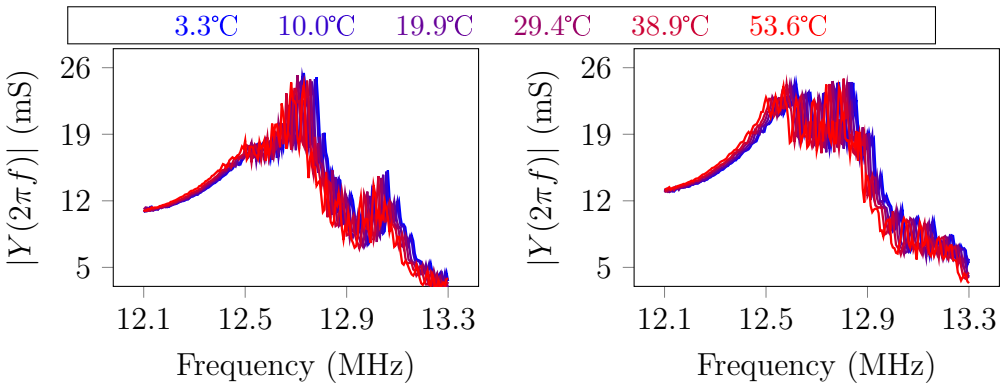

(a) Fixed frequency transducer 1

(b) Fixed frequency transducer 2

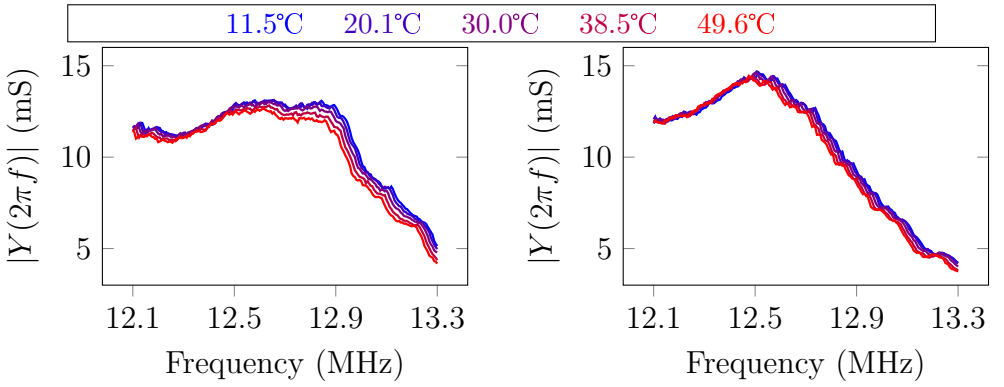

(c) Chirped transducer 1

(d) Chirped transducer 2

Figure 5.9: Plot of transducer response for various designs with changing temperature

The results obtained for fixed frequency (Table 5.7) and for chirped transducers (Table 5.8) show good tendency with aperture width, however, the ratio of the values for some parameters does not fall within the expected range. Moreover, as in both cases a 20 finger IDT design was used, the fixed frequency and chirped designs can be compared for the parameters: the L_{m} and C_{m} values are in good alignment for the two designs, for both widths, but an increase in R_{m} value is observed for the chirped IDT. As these type of transducers are essentially a broadband version of the fixed frequency IDTs, the same resonance and antiresonance frequencies are expected, but with lower peaks and higher R_{m} values due to the lower quality factor and higher bandwidth.

5.4.2 Force measurement methodology

To measure the primary acoustic radiation force acting on the particles and to obtain the acoustic energy density in the device, a modified version of the curve fitting method [133] is used. Firstly, the two IDTs are activated, and the particles

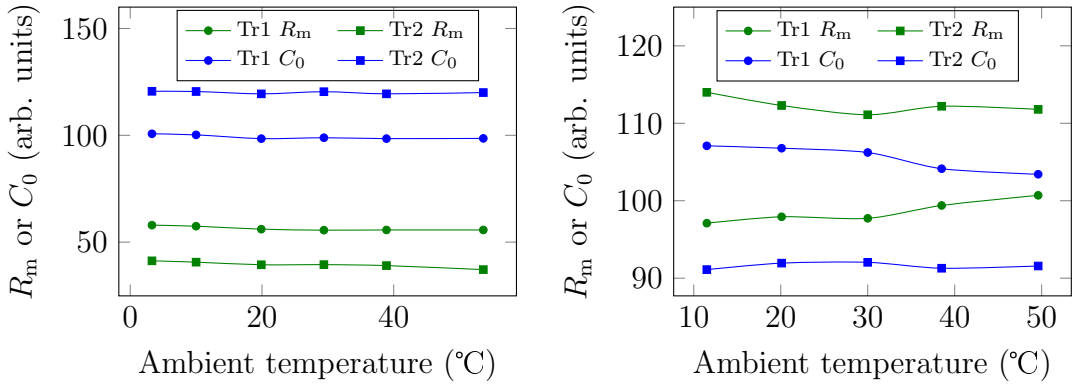

(a) Fixed frequency transducers (b) Chirped transducers

Figure 5.10: Various BVD model parameter dependence on temperature of a fixed frequency and a chirped IDT design

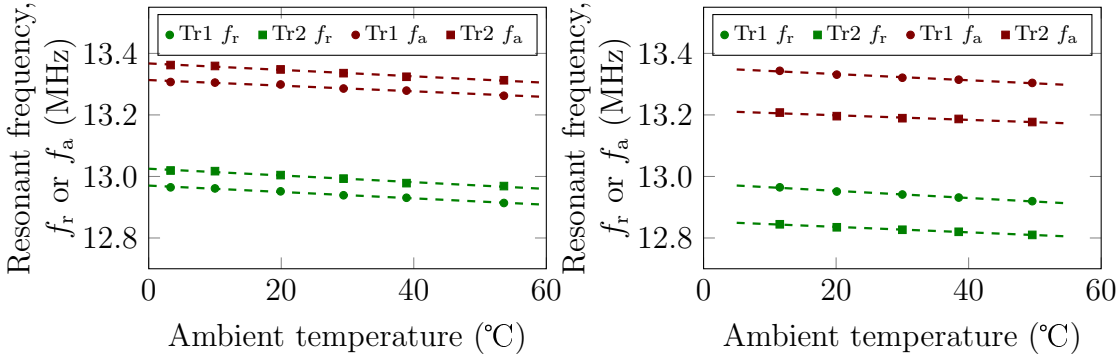

(a) Fixed frequency transducers (b) Chirped transducers

Figure 5.11: Resonance and antiresonance frequency dependence of a fixed frequency and a chirped IDT design on temperature

trapped at the pressure nodes. The phase of one IDT was suddenly changed by 130°, and the particles translated with the shifted node. A phase jump of 130° was used compared to the phase jump of 180° in [133] to avoid the unstable position of the particles at antinodes (Fig. 2.4). This jump of phase corresponds to $y_0 = 130°/360° \cdot \lambda/2 = 54.2\,\mu m$ initial position of the particles. The resulting trajectories follow Eq. 4.8 and this can be used to obtain the acoustic energy densities by a traditional curve fitting methodology to minimize root mean square error. However, this approach requires a relatively complex function (composed of tan() and ln() functions) to be fitted, requiring a complex analytical formula for the fit. With a simple preprocessing of the data, the fitting and acoustic energy estimation can be performed in a more deterministic way.

First note that from the force balance it is clear that the particle speed follows a

Variable	Long Tr		Short Tr		Parameter ratio		
	Tr1	Tr2	Tr1	Tr2	Min	Max	Nom
R_m	56.06	39.40	142.6	130.8	0.276	0.429	0.538
L_m (×1e-5)	2.822	2.344	5.337	5.388	0.435	0.529	0.538
C_m (×1e-12)	5.351	6.390	2.874	2.847	1.862	2.244	1.857
r	18.40	18.69	20.07	19.97	-	-	-
C_0 (×1e-10)	98.44	119.4	57.68	56.85	1.707	2.100	1.857
R_s	18.96	27.21	0	0	-	-	-
L_s (×1e-8)	11.78	11.56	25.67	27.88	-	-	-
f_r (MHz)	12.952	13.004	12.851	12.850	1.008	1.012	1.0
f_a (MHz)	13.299	13.348	13.167	13.168	1.010	1.014	1.0

Table 5.7: BVD parameters for a 1300 µm wide and 700 µm wide fixed frequency IDT with $N = 20$ fingers

Variable	Long Tr		Short Tr		Parameter ratio		
	Tr1	Tr2	Tr1	Tr2	Min	Max	Nom
R_m	97.93	112.3	191.7	204.9	0.478	0.586	0.538
L_m (×1e-5)	2.376	2.93	4.363	4.380	0.542	0.672	0.538
C_m (×1e-12)	6.356	5.248	3.475	3.465	1.510	1.834	1.857
r	16.8	17.52	19.36	18.47	-	-	-
C_0 (×1e-10)	106.78	91.94	67.276	63.999	1.367	1.668	1.857
R_s	20.51	21.79	20	20	-	-	-
L_s (×1e-8)	4.301	28.4	1.56e-13	15.86	-	-	-
f_r (MHz)	12.9510	12.8348	12.9256	12.9191	0.993	1.002	1.0
f_a (MHz)	13.3309	13.1960	13.2552	13.2642	0.995	1.006	1.0

Table 5.8: BVD parameters for a 1300 µm wide and 700 µm wide chirped IDT with $N = 20$ fingers

sinusoidal dependence as well:

$$c_{\text{ac}} \sin(2k_y y) = c_{\text{visc}} \dot{y} \implies \dot{y} = \frac{c_{\text{ac}}}{c_{\text{visc}}} \sin(2k_y y) \tag{5.6a}$$

$$= A \sin(2k_y y) \tag{5.6b}$$

which can be utilised in a much simpler way to obtain acoustic energy density fitting. Instead of plotting and fitting for the t–$y(t)$ curves (Fig. 5.12a) the numerical derivative can be obtained and the fit can be performed on the $y(t)$–$\dot{y}(t)$ graph (Fig. 5.12b). The numerical derivative is calculated as the central finite difference quotient $\dot{y}_i = (y_{i+1} - y_{i-1})/(t_{i+1} - t_{i-1})$ at each point of the trajectory. The only fitting parameter is the amplitude A that can be approximated by minimizing the overall squared error sum (SE):

$$\text{SE} = \sum_i \left(\dot{y}_i - A \sin(2k_y y_i)\right)^2 \tag{5.7a}$$

$$\frac{\partial \mathrm{SE}}{\partial A} = \frac{\partial}{\partial A} \sum_i \left(\dot{y}_i - A\sin(2k_y y_i)\right)^2 \tag{5.7b}$$

$$= \sum_i 2\left(\dot{y}_i - A\sin(2k_y y_i)\right)\left(-\sin(2k_y y_i)\right) \tag{5.7c}$$

and as the derivative must be equal to zero since we are looking at the minimum of the squared error, rearranging of Eq. 5.7c yields

$$A = \frac{\sum_i \dot{y}_i \sin(2k_y y_i)}{\sum_i \sin^2(2k_y y_i)} \tag{5.8}$$

From this approximated maximum speed A, the acoustic energy density can be simply obtained by

$$A = \frac{c_{\mathrm{ac}}}{c_{\mathrm{visc}}} = \frac{V_{\mathrm{p}} k_y E_{\mathrm{ac}} \Phi_{\mathrm{ac}}}{6\pi\eta_0 a} \implies E_{\mathrm{ac}} = \frac{9\eta_0 A}{2k_y \Phi_{\mathrm{ac}} a^2} \tag{5.9a}$$

where a is the radius of the particle, k_y is the apparent wave number in the y direction, Φ_{ac} is the acoustic contrast factor and η_0 is the dynamic viscosity of the medium. Furthermore, the pressure amplitude within the cavity is given by rearranging Eq. 2.4:

$$p_0 = \sqrt{\frac{4E_{\mathrm{ac}}}{\kappa_0}} \tag{5.10a}$$

Note here the definition of pressure amplitude: it is given for the total pressure field, not for a single travelling wave of the field.

This methodology is used to characterize the device by using 10 and 15 µm polystyrene particles. The two particle types were used to reduce the required number of experiments needed to be performed as the two particle types each result in an approximate energy density value. In total 5 experiments were performed for each voltage resulting in 10 energy density values for each voltage. The mean and standard deviation of these are shown in Fig. 5.13, along with a quadratic fit of $1.31\,\mathrm{mPa/V^2}$ on the average.

5.5 Chapter summary

The most commonly used transducer designs were introducing the chapter, discussing their advantages such as large feature sizes and ease of fabrication and disadvantages such as bidirectionality or reflectivity. It was argued that acoustofluidic applications do not require stringent transducer design, and therefore a simple $\lambda/4$ IDT and a chirped wideband design were chosen to be used. Description of the manufacturing

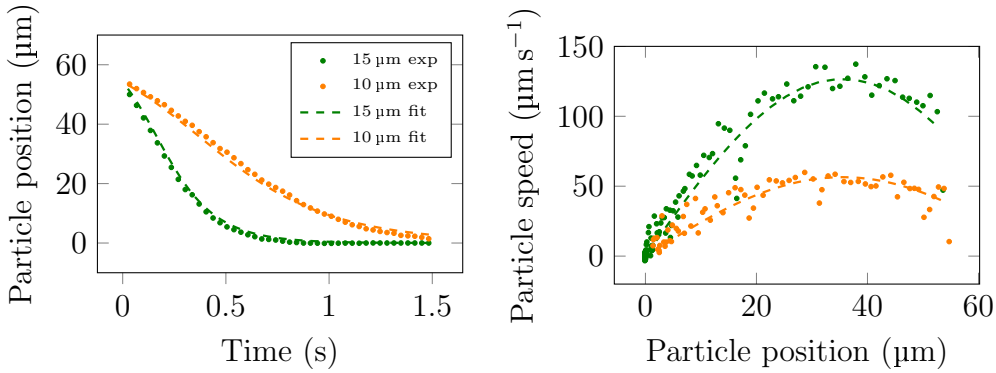

(a) Fit performed on the position-time plot

(b) Fit performed on the speed-position plot

Figure 5.12: Comparison of acoustic energy density approximation methods by fitting least mean square error curves of various characteristic plots of particle motion. The experimental results obtained for 24 $V_{p\text{-}p}$ transducer voltage

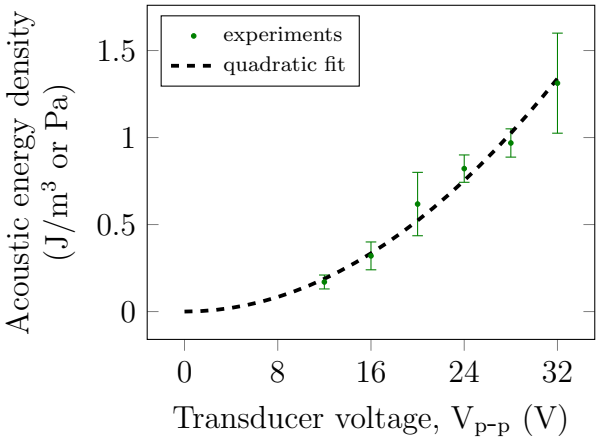

Figure 5.13: Acoustic energy density vs input peak-to-peak transducer voltage. As the theory predicts, the acoustic energy density depends on the square of the input voltage

process focused on the two main steps of device fabrication: transducer metal deposition and PDMS channel moulding, stressing the most complex and critical step being the bonding of the two parts. The section on experimental setup discusses how the phase and frequency modulation can be applied in a robust manner in real devices, and discusses different approaches of implementation such as high-level LabView or low-level function calls in MATLAB or C#. The transducers were characterised using Butterworth–van Dyke lumped element model, and scaling of the model parameters with device size or differences between narrow-band and wide-band operation were validated. Although the resonant frequency shift of both the simple and chirped designs were seen to be around $-1\,\mathrm{kHz\,°C^{-1}}$, the chirped design exhibits much smoother frequency response leading to a stabilised operation compared to

the large swings of the simple design. Finally, a simple acoustic radiation force measurement methodology was introduced and the final device was characterized to have 1.31 $\mathrm{mPa/V^2}$ energy density with changing input voltage.

Chapter 6

Simulation models

6.1 For fluid flow and particle focusing

As the sample mixture of particles need to be focused at the bottom or top pressure node based on the direction of sorting (see Section 4.3), a numerical simulation was developed to validate this focusing capability by changing the sheath inflows on the two sides. COMSOL Multiphysics was used to investigate how the flow rates can be used to achieve the appropriate focusing and what effect the asymmetric inlet design has on the focusing. The analysis consisted of two parts: first, a creeping flow CFD module was used to compute the velocity field in the channel. Secondly, this velocity field was utilised in the transport of diluted species module to visualize the mixing of fluids from the different inlets that approximates the particle distribution.

To reduce the computational domain size, only the upper half of the channel was simulated and applied the appropriate symmetry boundary condition on the bottom surface, both in the CFD and chemical transport modules. At the inlets mass inflow boundary condition was applied, as $\dot{m} = \rho Q_{\text{half}}$, where ρ is the density of medium,

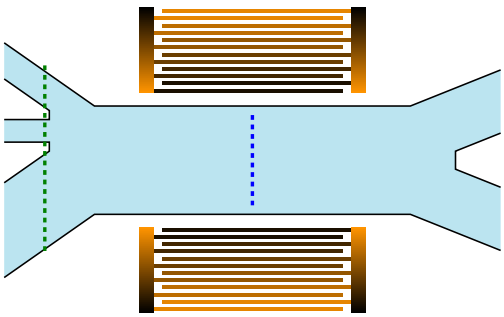

Figure 6.1: Schematic of the device with dashed green and blue lines indicating the locations for flow speed investigation in Fig. 6.2

here water at $\rho = 998\,\mathrm{kg/m^3}$, and Q_{half} is half of the volumetric flow rate at that inlet due to the symmetry condition. At the outlet, a zero pressure boundary was used. All other boundaries were modelled using the usual no-slip boundary condition. The channel was drawn in 2D and extruded to half the channel height.

During the initial particle separation experiments the total flow rate was between 1.0 to $2.0\,\mu\mathrm{l\,min^{-1}}$, with the particle flow accounting for 10–20% of that. The simulations were therefore carried out at a total flow rate of $1.5\,\mu\mathrm{l\,min^{-1}}$, and particle flow accounting for 15% of that. To verify the COMSOL model, the theoretical velocity profile in the rectangular channel is also plotted. All curves correspond to half of the channel height along the longer centreline of the cross-section. For the theoretical model for the velocity at the inlets, the equations given in Section 3.2 are used for the first three terms of $n = \{1, 3, 5\}$.

Figure 6.2 shows the velocity profiles for various flow rates and the resulting particle distributions, and the location of these plots within the device is illustrated in Fig. 6.1. To facilitate alignment and comparison with the channel structure, the graphs are rotated, i.e. position is plotted against velocity. Excellent agreement can be observed between theoretical velocity profiles (dashed lines) and simulation results (solid lines). For the symmetrical case where top and bottom sheath flows are the same (Fig. 6.2a-b), the distribution is also symmetric, as expected. As the main channel is much wider than high, low velocity regions at the sides can be neglected, and a uniform flow can be assumed in the main channel as verified by the blue curves [30]. Therefore, one can assume that each inflow occupies a region in the main channel with width proportional to the volumetric flow rate. Denoting the cross sectional areas occupied by each inflow by A_i, and the respective volumetric flow rates by Q_i, the relation

$$\frac{A_1}{Q_1} \approx \frac{A_2}{Q_2} \approx \frac{A_3}{Q_3} \tag{6.1}$$

can be used to estimate the focusing region of particles [261]. Dashed curves in the right hand side graphs of Fig. 6.2 show the edges of these regions, and for the symmetric case, this aligns perfectly with the simulation result. When the bottom sheath flow to top sheath flow ratio is increased to 85:15, the particles are pushed towards the top of the channel (Fig. 6.2c-d). In this case the theoretical approximation of occupied regions is less accurate but gives nevertheless a good approximation. Similarly, for a bottom sheath to top sheath ratio of 15:85, particles

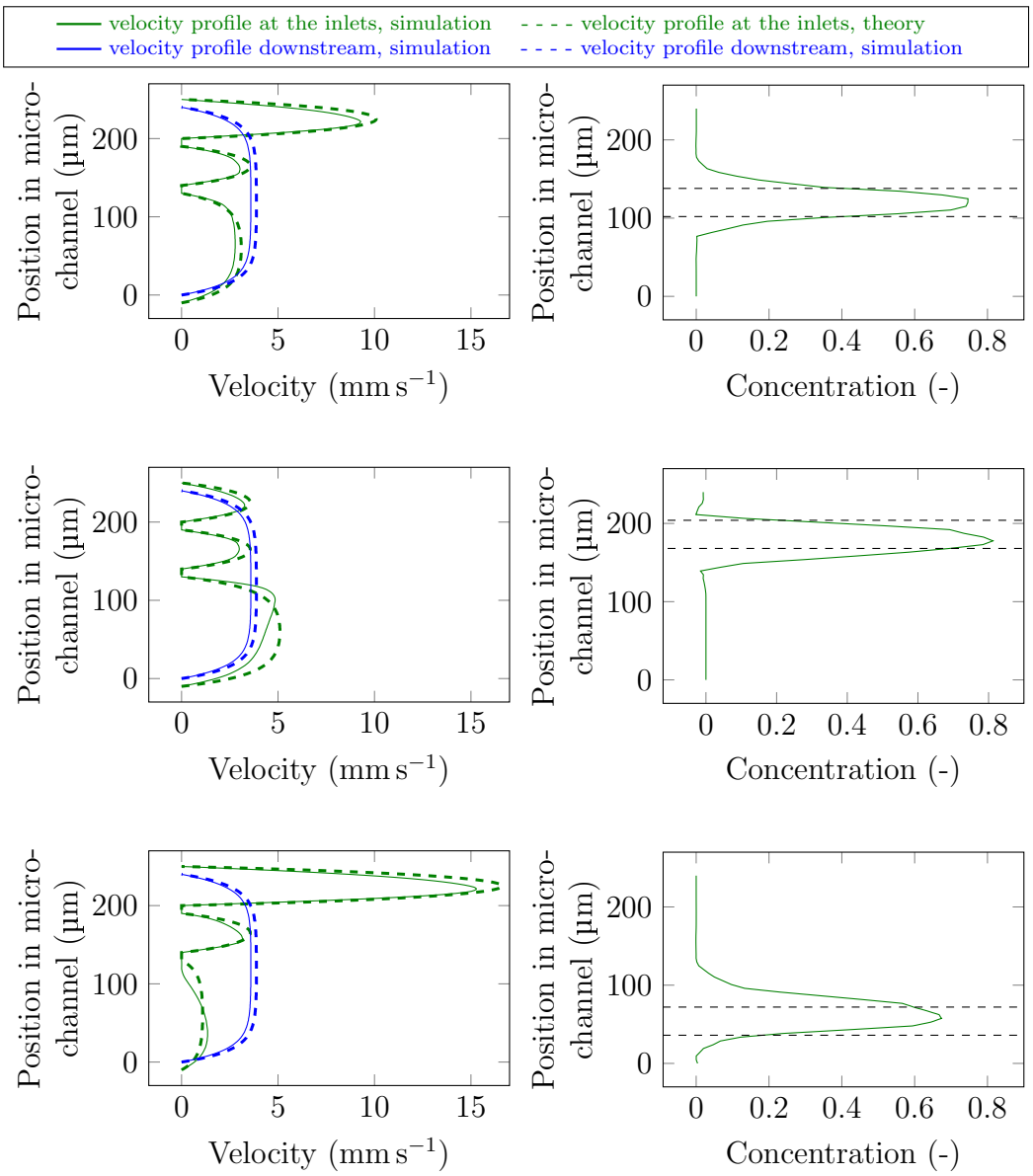

Figure 6.2: Velocity distributions at the inlets and in the main channel (left column) and particle distributions in the main channel (right column) for (a-b) equal sheath flows, (c-d) higher bottom sheath flow and (e-f) higher top sheath flow

are focused towards the bottom of the channel, with again a good agreement with the prediction (Fig. 6.2f). These results show that changing the location of particles is possible by solely changing the flow rates. The inlet geometry has a smaller effect and only results in a larger spread and smaller peak when focusing is performed towards the bottom. Therefore, it is expected to observe similar performance for the two sorting methods, with better results when the focusing is performed at the top and target particles are pushed towards the bottom.

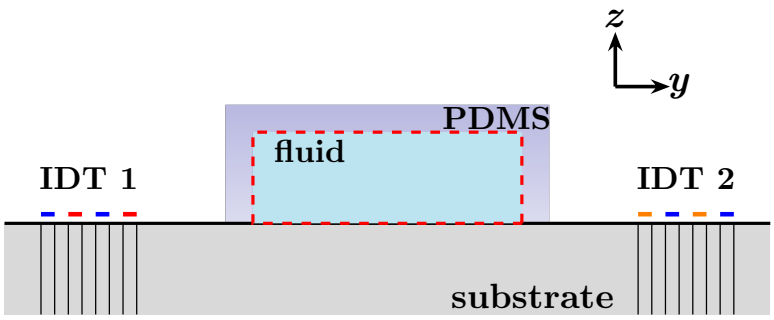

Figure 6.3: The full piezoelectric, acoustic, structural mechanic finite element model

6.2 Full piezoelectric/pressure acoustics simulation

The straightforward modelling of the problem requires coupling of piezoelectric, electric, acoustic and solid mechanics physical interfaces with the appropriate boundary conditions. Although the structure exhibits translational symmetry as the cross-section does not change along the channel axis and could be modelled in a 2D space, the special cut of the substrate requires a rotated coordinate system to be applied to its piezoelectric material property matrix. To allow flexibility of the model by changing the substrate material or rotation, the material matrix is evaluated on demand using the rotated coordinate system instead of being pre-computed. Nevertheless, the structure itself can be drawn in a 2D workplane and extruded into a 3D structure due to the aforementioned transversal symmetry. This workplane is schematically shown in Fig. 6.3 with the structural elements and boundary conditions emphasized. All dimensions are defined by parameters to allow for easy adjustment of the model. The workplane was extruded by 50 µm to obtain the final 3D model.

The Acoustic–Piezoelectric Interaction multiphysics interface is used in the model. The fluid within the channel is selected as pressure acoustics domain, the substrate as piezoelectric material domain, and finally, the PDMS as linear elastic material domain. As a result, the Acoustic–Structure Boundary is updated to be the edges of the fluid domain, as illustrated by the red dashed lines in Fig. 6.3. To aid applying the voltage excitation on the substrate, vertical lines were used to dissect the substrate domain as shown in Fig. 6.3. Top surfaces indicated in blue are the grounded transducers (potential zero), the orange surfaces of transducer 2 are fixed to V_0 while the red transducers on the left side are the phase shifted transducers, with applied potential $V_0 \exp(i\pi\Delta\varphi/180°)$, where $\Delta\varphi$ is the phase difference between

the transducers, given in degrees for convenience. Ideally the model would be meshed to allow for a minimum of 6 to 8 nodes within one wavelength for appropriate resolution of the solution in frequency domain study [262, 263]. However, a uniform mesh with this constraint would have resulted in more than half a million degrees of freedom (DOF), with solution time of order of tens of minutes on a general purpose PC equipped with 8 GB RAM. Therefore the mesh was fine-tuned to have better resolution towards the substrate top and coarser discretisation towards the channel bottom, successfully reducing the DOFs to around 350,000 to 450,000. The simulation time did not change significantly and remained in the same order of tens of minutes.

To reduce edge effects (see below anechoic corner in Section 6.3.2) and be able to simulate a typical pressure distribution within the device, the width was increased to 400 µm compared to the typical 240 µm in an experimental device. Otherwise all simulation parameters are explicitly given by material properties or are the same as of experiments ($f = 13.3\,\mathrm{MHz}$). The typical horizontal separation distance between nodes or antinodes is $(143.5 \pm 4.5)\,\mu\mathrm{m}$, in good agreement with the theoretical half-lambda separation distance ($\lambda/2 = 150\,\mu\mathrm{m}$). The results show a shift in the pressure distribution towards the right ($+y$) with increasing phase difference, as expected since the transducer on the left hand side is being phase shifted, moving the pressure pattern away from it. A complete $\lambda/2$ pattern shift occurs over 360° phase difference, as expected by theory.

However this model fully incorporates all physical processes during surface acoustic wave and fluidic interactions, its large computational demand prevents it from being used for trajectory calculations that require many frequency domain simulations for a single trajectory (see Section 6.3 below). Therefore alternative models were developed to assess streaming and generate particle trajectories in a more economical fashion while preserving accuracy in capturing the underlying physics.

6.3 Simplified models for particle trajectory generation

To obtain particle trajectories in the phase modulated sorting method, two approaches were developed detailed in the following two subsections. Both utilise a pressure

acoustics frequency domain simulation to obtain the pressure and velocity fields, that are used for primary acoustic radiation force calculation. As the continuous phase modulation cannot be implemented directly, a ten step discretisation is used: from 18° to 342° by 36° steps for the ramping period, followed by a simulation for 360° for the resting period. The opposing drag force in the simpler case is assumed to be the viscous drag force (neglecting streaming), while in the more realistic application an additional laminar flow module is used to incorporate streaming effects. In both models the two forces are passed to a time domain simulation study for particle trajectory generation. Further simplification in both cases is obtained by assuming the channel length is much larger than any cross sectional dimension, and a 2D model was applied.

6.3.1 Neglecting streaming effects

The model used in the simple case was a direct extension of the one used to validate the primary radiation force in surface acoustic wave devices in Section 3.4.2. As a quick overview, the model, with a typical pressure distribution is shown in Fig. 6.4.

The simulation domain comprised a rectangular fluid domain, surrounded by a perfectly matched layer, as shown in Fig. 6.4. The width was λ_y, so two pressure nodes were present in the device in the y direction, and the height was λ_0 to allow for more pressure nodes in the vertical direction. Both of these dimensions are greater than in a real device to ensure edge effects can be safely neglected. The thickness of the perfectly matched layer (PML) was tenth of the wavelength in the fluid domain ($\lambda_0/10$). The only boundary conditions were hard wall boundaries at the outer PML edges. The pressure fields were directly applied by background pressure fields, with propagation wave vectors $k_1 = k_y\hat{\mathbf{y}} + k_z\hat{\mathbf{z}}$ and $k_2 = -k_y\hat{\mathbf{y}} + k_z\hat{\mathbf{z}}$. Once the pressure and velocity fields are available, these are passed onto the Particle Tracing module for time domain simulation.

An example comparison with theoretical particle trajectories can be seen in Fig. 6.5. As this model is a direct implementation of the theoretical equations with no secondary or adverse effects, the agreement is excellent, as expected. The same 10 and 14.5 µm PS particles are used as for Fig. 4.2.

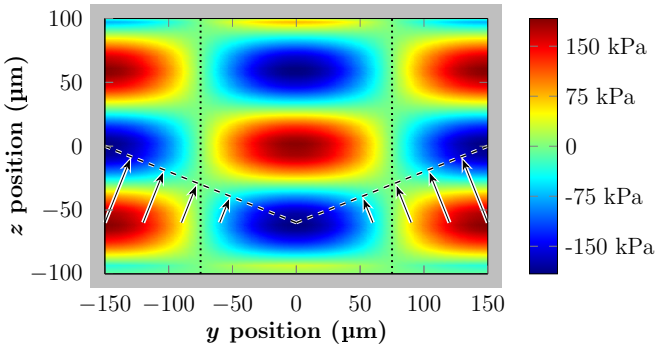

Figure 6.4: The simple 2D COMSOL model with the pressure distribution within the microchannel. The grey edges symbolize the perfectly matched layer domain. Slanted dashed lines denote the wavefronts of the two travelling BAW waves, with constant phase. The travelling waves have 22° angle with the z axis. The particles with positive contrast trap at the pressure nodes, denoted by vertical dotted lines

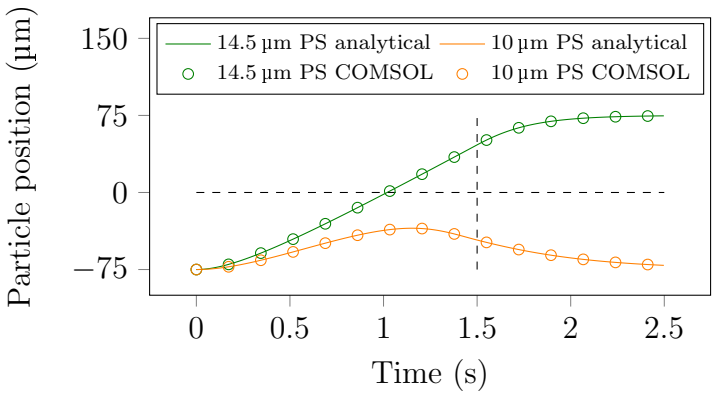

Figure 6.5: Trajectories obtained by the analytical trajectory equation (solid lines) and the COMSOL simulation (circles). Green and orange colour corresponds to 14.5 and 10 µm particles, respectively

6.3.2 Incorporating streaming effects

The excessive computational demand of the 3D fully coupled COMSOL simulation model for the piezoelectric–microfluidic device can be reduced by using an approximate model, only for the fluid domain enclosed by the PDMS walls and lithium niobate substrate [232, 233, 264]. As the surface waves can be fully characterized by their velocity field, and the thickness of the PDMS walls (greater than attenuation length) allows for representing these with appropriate boundary conditions. For the two sides and the top of the channel, the PDMS is modelled as a normal impedance BC of characteristic impedance $Z = \rho_{\mathrm{PDMS}} c_{\mathrm{PDMS}}$, which is the product of density and bulk sound speed. The surface waves travelling in opposite directions on the lithium niobate substrate are applied as velocity BCs at the bottom of the microchannel. As the surface acoustic waves follow an elliptical motion, the x and y velocity

components are 90° out of phase with respect to each other and the sign of the y component should agree with the travelling direction of the wave [233]. Two changes are necessary to these equations to be able to model our device and sorting method: the phase difference of the two transducers should be added, and, as the microchannel is not exactly an integer multiple of half the wavelength, an additional phase shift is required to have the adequate reference frame used in COMSOL. As COMSOL uses a time harmonic of $\exp(i\omega t)$ a rightward propagating wave from the left transducer is described by terms as $\exp(-iky)$ and the phase shift should be combined to these. Therefore, the velocity boundary condition in the y and z directions have the following form:

$$\begin{aligned} u_y(y,t) =& \zeta d_0 \omega \Bigg[e^{-C_\mathrm{d}\left(\frac{W}{2}-y\right)} e^{-i\left[k_\mathrm{sub}\left(\frac{W}{2}-y\right)\right]} \\ &+ e^{-C_\mathrm{d}\left(\frac{W}{2}+y\right)} e^{i\left[k_\mathrm{sub}\left(\frac{W}{2}-y\right)+\varphi_0+\Delta\varphi\right]} \Bigg] \end{aligned} \tag{6.2a}$$

$$\begin{aligned} u_z(y,t) =& -d_0 \omega \Bigg[e^{-C_\mathrm{d}\left(\frac{W}{2}-y\right)} e^{i\left[-k_\mathrm{sub}\left(\frac{W}{2}-y\right)-\frac{\pi}{2}\right]} \\ &- e^{-C_\mathrm{d}\left(\frac{W}{2}+y\right)} e^{i\left[k_\mathrm{sub}\left(\frac{W}{2}-y\right)-\frac{\pi}{2}+\varphi_0+\Delta\varphi\right]} \Bigg] \end{aligned} \tag{6.2b}$$

where ζ is the ratio of displacement amplitude in the y and z directions, d_0 is the y-displacement amplitude of the travelling wave, ω is the angular frequency, C_d is the attenuation coefficient, W is the width of the channel and k_sub is the wave number of the surface wave. The phase values φ_0 and $\Delta\varphi$ correspond to the shift of the reference frame and the phase difference between transducers, respectively. A positive phase difference results in a rightwards movement of the pressure distribution. The values of these parameters and material properties used in the simulation are listed in Table 6.1.

To be able to obtain the second-order streaming field, perturbation theory is applied to the pressure and velocity fields

$$p = p_0 + \epsilon p_1 + \epsilon^2 p_2 \tag{6.3a}$$

$$\rho = \rho_0 + \epsilon \rho_1 + \epsilon^2 \rho_2 \tag{6.3b}$$

$$\mathbf{u} = \mathbf{u}_0 + \epsilon \mathbf{u}_1 + \epsilon^2 \mathbf{u}_2 \tag{6.3c}$$

where index 0 corresponds to steady state, index 1 the first order acoustic variables, and index 2 the second order streaming effects. As the first order variations are known, and the streaming field has a much larger time-scale than the first order

Symbol	Description	Value
f	Frequency	13.3 MHz
ω	Angular frequency ($= 2\pi f$)	83.57 Mrad s^{-1}
λ_{sub}	Wavelength on the substrate ($= c_{\text{sub}}/f$)	300 µm
ρ_{sub}	Density of the substrate	4.7 g/cm^3
c_{sub}	Surface wave speed on lithium niobate substrate	3990 m s^{-1}
W	Width of microchannel	240 µm
H	Height of microchannel	50 µm
k_{sub}	Wave number ($= 2\pi/\lambda_{\text{sub}}$)	20 944 m^{-1}
ρ_{PDMS}	Density of the PDMS	1.03 g/cm^3
c_{PDMS}	Bulk speed of sound in PDMS	1076 m s^{-1}
ζ	Ratio of displacement amplitude	0.86
C_{d}	Attenuation coefficient	2063 m^{-1}
ρ_{PS}	Density of polystyrene	1.05 g/cm^3
c_{f}	Bulk speed of sound in water	1497 m s^{-1}
φ_0	Phase shift to achieve zero reference in COMSOL ($= k_{\text{sub}}(\lambda_{\text{sub}} - W)$)	1.26 rad

Table 6.1: Simulation parameters used in the 2D thermoviscous acoustics model incorporating streaming effects

ultrasonic frequency fields, the time-average of the above equations can be taken and substituted into the Navier-Stokes equation and the mass conservation to obtain the equations describing the second order fields [264]:

$$\rho_0 \boldsymbol{\nabla} \cdot \langle \mathbf{u}_2 \rangle = -\boldsymbol{\nabla} \cdot \langle \rho_1 \mathbf{u}_1 \rangle \tag{6.4a}$$

$$\eta \nabla^2 \langle \mathbf{u}_2 \rangle + \beta \eta \boldsymbol{\nabla}(\boldsymbol{\nabla} \cdot \langle \mathbf{u}_2 \rangle) - \langle \boldsymbol{\nabla} p_2 \rangle = \langle \rho_1 \frac{\partial \mathbf{u}_1}{\partial t} \rangle + \rho_0 \langle (\mathbf{u}_1 \cdot \boldsymbol{\nabla}) \mathbf{u}_1 \rangle \tag{6.4b}$$

which can be interpreted as the first order fields (right hand side) being the source terms for the second order fields.

The model comprised two physics interfaces to capture first and second order fields. A Thermoviscous Acoustics module was applied to obtain the first order pressure and velocity, which were passed to a Laminar Flow module to calculate the second order fields. The Thermoviscous Acoustics physics module was utilized with P2+P3 discretisation (second order elements for pressure and third order elements for velocity) to be able to capture small variations in the pressure and velocity fields accurately. The laminar flow physics used a stick wall boundary condition. To obtain the drag force, the built-in force feature inherent to COMSOL was used, which directly implements Eq. 4.1b using the streaming velocity fields from the laminar flow simulations, and an explicit equation for the acoustic force was given,

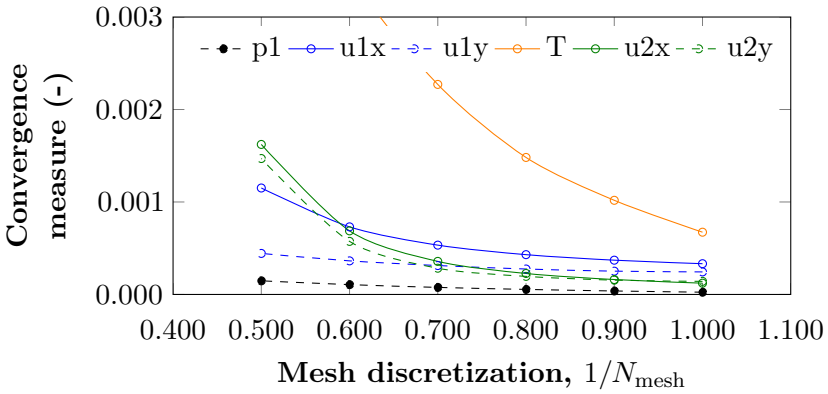

Figure 6.6: Mesh convergence analysis vs N_{mesh}. As for $N_{\mathrm{mesh}} = 1.5$ all pressure and velocity terms converge already well below the measure 0.002, and the temperature convergence is only slightly above this limit, $N_{\mathrm{mesh}} = 1.5$ was chosen as an adequate trade-off between computational cost and accuracy

as detailed in [264] and given by Eq. 3.16. In order to capture the thermoviscous effects while avoiding a high computational demand, a non-uniform mesh was applied. First, the viscous boundary layer thickness was computed $\delta_{\mathrm{v}} = \sqrt{2\eta/\rho\omega} \approx 0.15\,\mu\mathrm{m}$, and was used with a scaling parameter N_{mesh} to define the mesh at the boundaries and in the bulk of the fluid. At the boundaries, the maximum element size was set for $N_{\mathrm{mesh}}\delta_{\mathrm{v}}$, while in the bulk of the fluid, the minimum element size was $N_{\mathrm{mesh}}\delta_{\mathrm{v}}$ and the maximum element size $2\,\mu\mathrm{m}$. A mesh convergence analysis was carried out to determine the appropriate N_{mesh} value, resulting in precise solutions whilst minimizing the required number of degrees of freedom and therefore computational time. The method is described by Nama *et al.* [232]: simulations are run for various mesh sizes (controlled by the N_{mesh} value) and compared with an extremely fine mesh solution (where $N_{\mathrm{mesh}} = 0.8$) using the mean-square error as a measure (Fig. 6.6):

$$C(g) = \sqrt{\frac{\int (g - g_{\mathrm{ref}})^2 \, dx\, dy}{\int g_{\mathrm{ref}}^2 \, dx\, dy}} \tag{6.5}$$

where g is any of the characteristic variables pressure, velocity or temperature and g_{ref} corresponds to the results with the finest mesh. This analysis revealed that the mesh size $N_{\mathrm{mesh}} = 1.5$ is adequate, resulting in 35,890 domain elements and 2,820 boundary elements and a total number of degrees of freedom of under a million for both the acoustics and flow modules. This resolution was applied for all following investigations. Note that although the number of degrees of freedom is larger than for the complete 3D model, the simulation time in the simpler model was still below a minute. The relationship between the peak pressure amplitude and the SAW

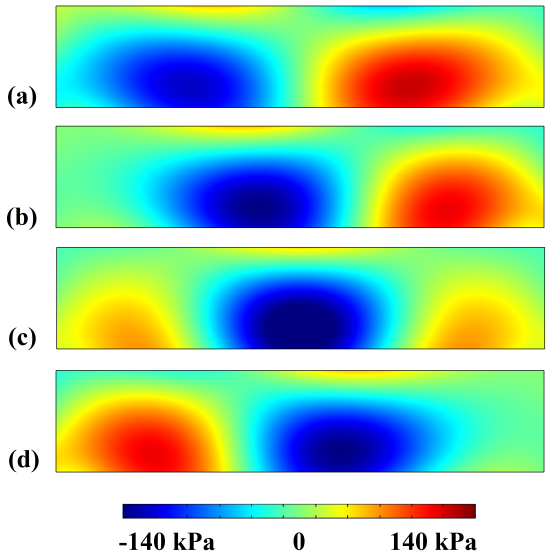

Figure 6.7: Pressure distribution within the microchannel for different phase differences between the two transducers: (a) 0° (b) 90° (c) 180° (d) 270°. The colors from blue through green to red correspond to −140 kPa to 140 kPa

amplitude was studied in order to use an excitation parameter that corresponds to the experiments. Simulations from 0.05 nm to 0.5 nm surface displacement amplitude were carried out and the recorded pressure maxima showed a linear relationship as $p_0 = 241.2 d_0$ where the pressure is in kPa and the displacement amplitude in nm.

Pressure distribution within the microchannel at various phase differences can be seen in Fig. 6.7. For 0° phase, the pressure distribution is symmetric, with a pressure node along the centerline of the channel. As the phase difference between the right and left transducers increases, the pressure pattern moves rightwards as expected. For 180° phase difference, the pressure distribution is again symmetric with a pressure antinode at the centreline of the channel.

As a next step the critical particle size was investigated [223, 232], above which acoustic streaming effects governing the behaviour of small size particles are dominated by the primary radiation force. This limit was identified by running simulations for particles with diameter ranging from 1 µm to 15 µm, originally dispersed in a 3 by 8 grid within the microchannel. The final particle locations after 2 s and trajectories can be seen in Fig. 6.8. For particle sizes of range 1 to 3 µm, movement is dominated by streaming, as the particles are not trapped at well-defined spatial positions but follow the vortices of the streaming velocity field. Above 5 µm, the particles behave in the usual manner by trapping at the nodes of the pressure field. Between 3 and 5 µm particle size, streaming and radiation force effects are of similar magnitude and

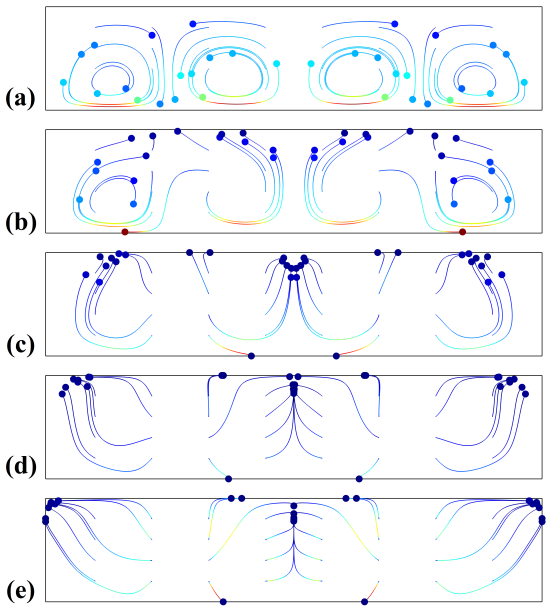

Figure 6.8: Analysis of the effect of particle size on trapping efficiency and identification of critical particle diameter. Simulation results of particle trajectories and final particle positions including primary acoustic radiation force and streaming induced drag force after 2 s for zero phase difference between transducers for (a) 1 µm (b) 3 µm (c) 5 µm (d) 7 µm and (e) 10 µm diameter polystyrene particles. For particle sizes below 3 µm, streaming induced effects dominate, while above 5 µm size particles are mainly trapped by the primary radiation force

particles neither follow streaming vortices nor are trapped at the pressure nodes.

To further investigate the effect of phase difference between the transducers on the trapping of the particles, a similar investigation, as presented in Fig. 6.8, was carried out, with fixed particle size (10 µm polystyrene) and by changing phase difference. The results of this analysis can be seen in Fig. 6.9: for zero phase difference, the particles are trapped at the middle of the channel. As the phase is gradually increased, this trapping location moves to the right. For 180° phase difference, where the pressure antinode is aligned with the centreline of the channel, the particles are pushed away from this position towards the two pressure nodes located symmetrically on the two sides (Fig. 6.9c). A comparison with Fig. 6.7 further validates this effect: the zero pressure nodes in Fig. 6.7 coincide well with the trapping positions of the particles in Fig. 6.9.

As a final verification, the model was compared with analytical separation results for 10 and 14.5 µm polystyrene particles. The results in Fig. 6.10 show good agreement between the analytical and the trajectories, however, differ in separation distance between the particles by 20%. This is attributed to the presence of an anechoic corner (illustrated in Fig. 6.11). As the surface waves radiate diagonally

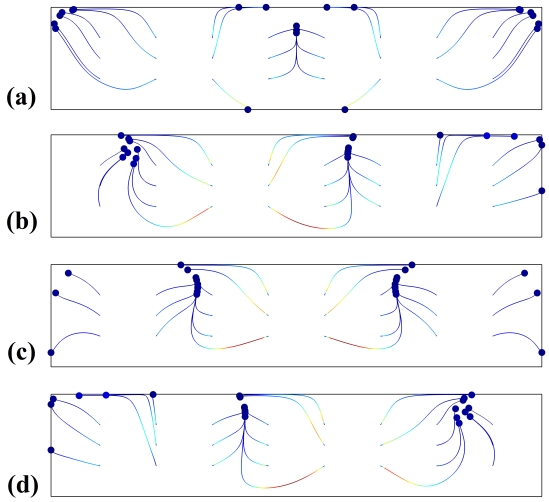

Figure 6.9: Illustration of trapping of a 10 µm polystyrene particle within the microchannel for various phase difference values between the two transducers: (a) 0° (b) 90° (c) 180° (d) 270°

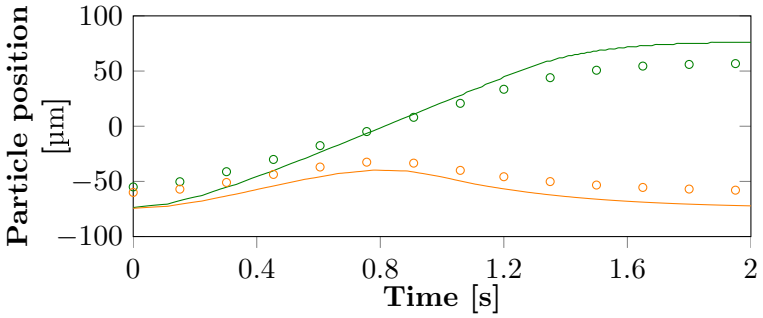

Figure 6.10: Analytical (solid lines) and numerical (circles) particle trajectories for separation of 10 µm (orange) and 14.5 µm (green) polystyrene particles

from the bottom surface of the channel, by the sides of the PDMS walls there is a region where comparably smaller pressure amplitudes are observed compared to the bulk of the fluid. This changes the location of the pressure nodes as well, and since in this case the width of the device is comparable to the acoustic wavelength, the effect is pronounced.

6.4 Secondary radiation force modelling

The secondary acoustic radiation force acting on a small probe particle has been determined by two types of FEM simulations. The first one, presented in the following subsection, uses a 2D axisymmetric FEM model to simulate the first order acoustic pressure and velocity distribution in the neighbourhood of a scatterer particle. These fields are substituted in the Gorkov expression to find the radiation force on a small

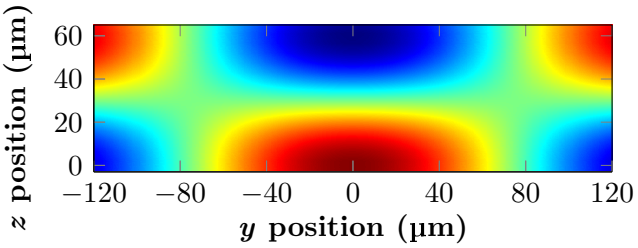

(a) Pressure distribution assuming perfect boundaries with no attenuation in the PDMS

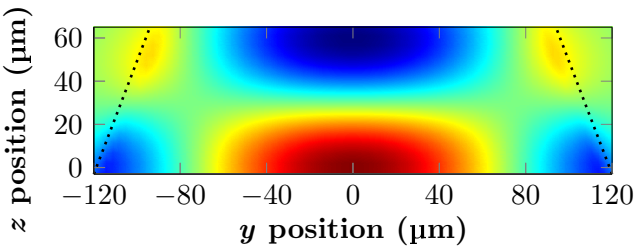

(b) Pressure distribution due to attenuation in PDMS

Figure 6.11: Illustration of the anechoic corner or shadow zone. Dashed lines indicate the approximate edges of the anechoic corner

probe particle, as detailed in Section 3.4.1. The second strategy combines a 3D FEM model and a tensor integral approach to calculate the radiation force on the probe particle, as detailed in Section 3.4.1. This strategy, presented in Section 6.4.2, considers re-scattering events between the particles as well. Both types of simulations have been implemented in the FEM software COMSOL Multiphysics (COMSOL AB, Stockholm, Sweden). In both cases a spherical coordinate system is used in the notation usual for physics (the polar angle is θ) as illustrated in Fig. 6.12.

6.4.1 Simplified 2D model

The scatterer sphere is located at the origin of the coordinate system (Fig. 6.12) and interest is in determining the secondary force on a small probe particle, located at the position $\mathbf{r} = z\hat{\mathbf{z}} + \varrho\hat{\boldsymbol{\varrho}}$ due to an external plane standing wave field. Attributable to the rotational symmetry of the problem, the model was set up as a 2D axisymmetric problem. In addition, the probe particle is neglected in the simulations, and only the incident fields are calculated at its location (see Section 3.4.1 for the force calculation method).

In the acoustics module of COMSOL Multiphysics, the external incident field is introduced as a background pressure field and the model is used to calculate the acoustic pressure and the velocity distribution caused by the superposition of the

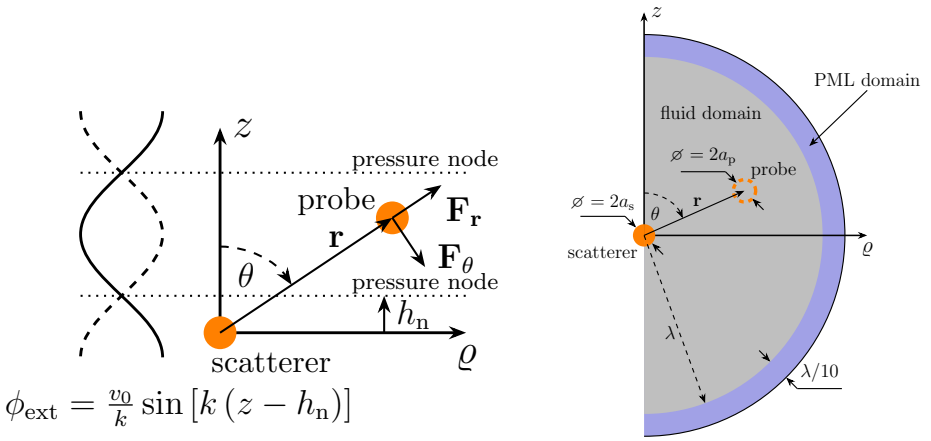

(a) Notations used for parameters and components of force

(b) The COMSOL model with its characteristic dimensions

Figure 6.12: Two small particles in a plane standing wave field. The total acoustic radiation force on the probe particle is the result of a primary radiation force and a secondary force. The model, based on the Gorkov expression, is used to calculate the incident acoustic pressure and velocity fields at the probe particle located at $\mathbf{r} = z\hat{\mathbf{z}} + \varrho\hat{\boldsymbol{\varrho}}$

external field with the scattered field from the scatterer particle. As shown in Fig. 6.12, a perfectly matched layer (PML) is used for absorption of the acoustic waves at the edge of the fluid domain.

After simulation, the secondary force potential and radiation force are obtained as

$$U_{\text{sec}} = U_{\text{tot}} - U_{\text{primary}} \tag{6.6a}$$

$$\mathbf{F}_{\text{sec}} = -\boldsymbol{\nabla} U_{\text{sec}} \tag{6.6b}$$

and the primary force potential is given theoretically (Section 3.4.1). For mesh convergence analysis refer to [**Simon2018MM**].

6.4.2 Full 3D model with re-scattering events

Both the theoretical and the previous simulation approach neglect the re-scattering effects between particles. Therefore, to assess the importance of these events the following 3D model was implemented in COMSOL. As the FEM simulation is a direct numerical solution of the Helmholtz equation with appropriate boundary conditions at the surfaces, re-scattering effects are directly included when the solutions are obtained [265]. To allow this, a second particle must be included at the probe location, that will act as a second scatterer. First, the pressure field is simulated including both the scatterer and the probe particles, followed by the evaluation of

the force using the tensor integral method (Section 3.4.1).

Using this method and subtracting the theoretical primary radiation force, one should arrive at the secondary radiation force. However, in some cases, slow convergence and numerical problems could be observed. The reason behind is the inadequately spaced mesh on the surface of the probe particle, as opposed to the multipole scattering methods [220, 221], where the quadrature is a well-spaced Gauss–Langrangian quadrature. Carrying out the integral of the total force, and then changing the material of the scatterer to the fluid, the exact same mesh is utilized in both cases, significantly reducing computational errors and increasing convergence speed. As a result, one simulation is required to obtain the total force on all particles, followed by one simulation for each particle to obtain the primary radiation force, resulting in a total number of $M + 1$ simulations for M particles.

6.4.3 Results of secondary radiation force simulations

To support the versatility of the models, two distinctly different cases were investigated for the secondary radiation force: particle in air and particle in water. As the range of the interaction force is significantly different for these, both the secondary potential and force were normalized by their primary counterpart to allow for direct comparison of the two cases by the relative values. The primary radiation force (given by Eq. 3.16) amplitude is $0.5V_iE_0\Phi_{\mathrm{ac}}k$. Using this value as normalization, the relative strength of the different cases to follow can be compared with ease.

As a first case, the polystyrene particles in air case was investigated with the parameters shown in the Appendix. The selected 10 kHz frequency is of the same order of that found in acoustic levitation devices [266], and results in wavelength of 34.3 mm in air. Both the scatterer and probe particles are 1.715 mm in diameter, as they were chosen to have diameter $\lambda/20$ for direct comparison with the case detailed in the next subsection. For polystyrene particles in air, the density of the particle is much larger than the density of the surrounding air ($\rho_{\mathrm{PS}} = 1050\,\mathrm{kg/m^3} \gg 1.225\,\mathrm{kg/m^3} = \rho_{\mathrm{AIR}}$), and according to Eq. 3.17d the dipole scattering factor is approximately unity $f_1 \approx 1$. Similarly, the adiabatic compressibility of the air is much larger than the compressibility of the polystyrene particle ($\kappa_{\mathrm{PS}} = 172\,\mathrm{TPa^{-1}} \ll 694\,\mathrm{MPa^{-1}} = \kappa_{\mathrm{AIR}}$), and therefore the particle can be taken as rigid in this case, with monopole scattering coefficient close to unity ($f_0 \approx 1$), according to Eqs. 3.17d and 3.34. To observe

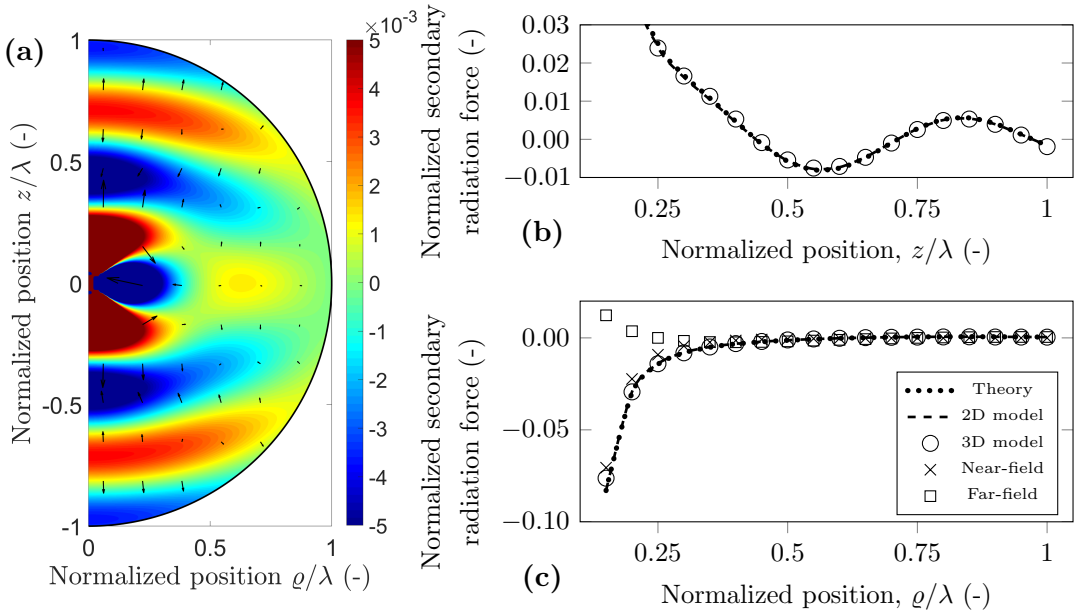

Figure 6.13: Simulation results for a polystyrene particle in air, when the nodal line aligns with the scatterer position ($h_\mathrm{n} = 0$). (a) Normalized secondary acoustic potential, and radiation force (arrows) (b) Normalized secondary radiation force along direction z. (c) Normalized secondary radiation force along direction ϱ

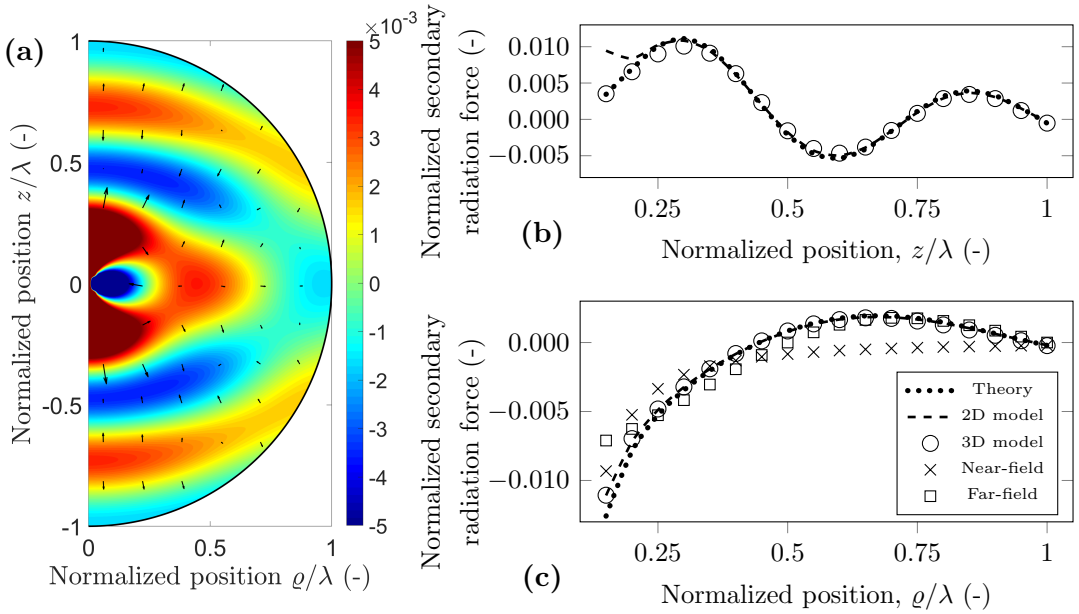

Figure 6.14: Simulation results for a polystyrene particle air, when the antinodal line aligns with the scatterer position ($h_\mathrm{n} = \lambda/4$). (a) Normalized secondary acoustic potential, and radiation force (arrows) (b) Normalized secondary radiation force along direction z. (c) Normalized secondary radiation force along direction ϱ

the effect of monopole and dipole coefficients, the normalized potential and force values are shown both at the nodal line ($h_\mathrm{n} = 0$) in Fig. 6.13 and in Fig. 6.14 for the antinodal case ($h_\mathrm{n} = \lambda/4$). The monopole scattering dominates the secondary force near the antinode, while the dipole scattering dominates near the node [211]. The potential maps in Fig. 6.13 and Fig. 6.14 were plotted using Eq. 3.34, and the arrows show the direction of the force, which points away from the minima, towards the maxima, as the particles have positive contrast factor Φ_AC. The force was obtained by numerical differentiation, and a logarithmic scaling was used for plotting. In the two cases, the normalized potential map has a similar pattern and magnitude. This is due to both the monopole and dipole scattering coefficients being approximately unity for a polystyrene particle in air, which can be considered rigid. The normalized secondary radiation force follows similar behaviour along the z direction and r direction for the nodal and antinodal cases, the only significant difference observed for the near-field of the z direction. Moreover, it shows some directivity as in the z direction being a magnitude stronger than along the radial direction.

Good agreement between theory, 2D model and 3D model can be observed for both nodal and antinodal cases, in both directions, however, the 2D model fails to capture the magnitude of the interaction force in the vicinity of the antinodal line, along z direction (Fig. 6.14). The three results (theory, 2D and 3D) include different approximations and therefore differences are expected. The theoretical results consider only monopole and dipole scattering mechanisms, however quadrupole or higher order scattering are important as well [220]. The 2D model does not put a limitation on the number of multipoles but neglects re-scattering effects. Finally, the 3D model, captures arbitrary number of poles (depending on the fineness of discretisation) and also accounts for re-scattering. For the radial direction, near the antinodal line, the error between the near field approximation and the theoretical values is below 50% for normalized distances of less than 0.3. The far field approximation converges much faster towards the theoretical solution: less than 12% error for normalized distances above 0.65. For the nodal line, the error between the near field approximation and theoretical values is less than 20% for normalized distances below 0.3. The error of far field approximation goes below 10% when the normalized distance is larger than 0.65.

The secondary radiation force along the radial direction can be large enough

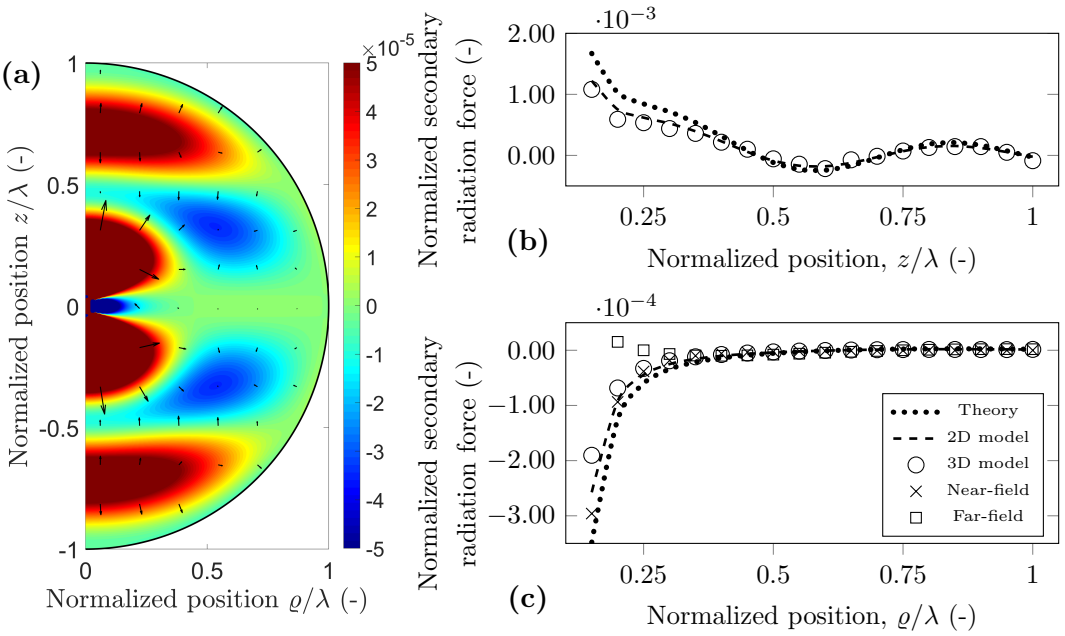

Figure 6.15: Simulation results for a polystyrene particle in water, when the nodal line aligns with the scatterer position ($h_\mathrm{n} = 0$). (a) Normalized secondary acoustic potential, and radiation force (arrows) (b) Normalized secondary radiation force along direction z. (c) Normalized secondary radiation force along direction ϱ

to influence the relative position of the particles. It has a crossover point around 0.63λ separation distance along the nodal line; particles closer than this exhibit an attractive (negative) force, while above the crossover point, the force is repulsive (positive). Due to this sign distribution of the force, the 0.63λ point is an unstable equilibrium, particles are always forced to move away from it.

As a summary, for the rigid particle in air, the two simulation results are in good agreement with the theory, except for forces along the z direction near an antinodal line. However, as the particles naturally agglomerate at the nodes, the secondary radiation force can be safely obtained using a simplified model and neglecting re-scattering effects.

A different investigation can be carried out when placing the polystyrene particle in water. As the main goal of microfluidic lab-on-chip devices is miniaturization, the operating frequency has to be increased, therefore the chosen 10 MHz reflects this typical average value [134, 267]. For further parameters, refer to the Appendix. The resulting wavelength is 148 µm, and the particle diameter 7.4 µm. More interesting to note the change in the scattering coefficients: the similarity in compressibilities of the particle and water ($\kappa_\mathrm{PS} = 172\,\mathrm{TPa}^{-1}$, $\kappa_\mathrm{Water} = 456\,\mathrm{TPa}^{-1}$) results in $f_0 = 0.623$. More significant is the drop in the dipole scattering coefficient: due to the similarity

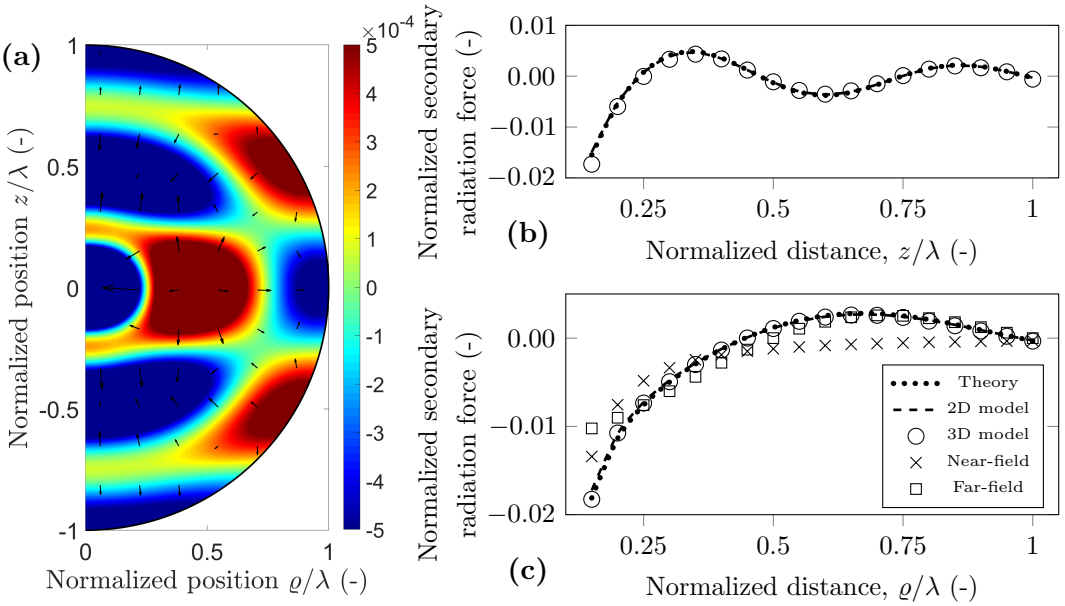

Figure 6.16: Simulation results for a polystyrene particle in water, when the antinodal line aligns with the scatterer position ($h_\mathrm{n} = \lambda/4$). (a) Normalized secondary acoustic potential, and radiation force (arrows) (b) Normalized secondary radiation force along direction z. (c) Normalized secondary radiation force along direction ϱ

of the densities (998 and 1050 kg/m^3), $f_1 \approx 0.03 \ll 1$. The potential maps in Fig. 6.15 and Fig. 6.16 were again plotted using Eq. 3.34, and the arrows show the direction of the force, again pointing away from the minima towards the maxima, as the particles have positive contrast factor Φ_AC.

For the polystyrene particle in water, the potential map around the node and the antinode has a significantly different shape and magnitude. This is due to the difference in monopole and dipole scattering coefficient [211]. Referring to Eq. 3.34, each term of the potential has either a dipole coefficient, f_1, or a $\sin(kh_\mathrm{n})$ expression. At the nodes $\sin(kh_\mathrm{n})$ is zero, and the dipole coefficient is much less than unity, as mentioned before, leading to the potential an order of magnitude smaller near the nodes compared to the antinodes. This difference is even more pronounced for the force along the radial direction: here the difference exceeds two orders of magnitude. Along z direction, the force is repulsive for the nodes, attractive for the antinodes, but again as its magnitude is much smaller than the primary force, no effect on particles is expected. For the antinodal case excellent agreement between theory and the two types of simulations can be observed. This shows that the theoretically assumed monopole and dipole approximation already successfully captures the secondary radiation force with small error. Furthermore, the good agreement between 2D and 3D models suggest that in this case, the re-scattering effects also contribute

only slightly to the secondary radiation force. For the radial direction, the near field approximation shows similar performance as for polystyrene in air, the error goes below 50% only when the normalized distances are less than 0.3. The far-field approximation shows slower convergence in this case: the error is 40% even at 0.85 distance.

However, for the nodal case, the three results can be different up to 50% error. The magnitude of the theoretical values is the largest, followed by the 2D model and the 3D model, seemingly the re-scattering events decrease the secondary force, as also noted by Doinikov for a bubble in water case [220]. The near-field and far-field approximations shown good agreement with the various models and the theory (Fig. 6.15).

Although, the particles both in air and water agglomerate at the nodal lines ($\Phi_{AC} > 0$), it is important to investigate the secondary radiation force for other cases. In a continuous flow microfluidic device the particles enter at random positions and can be near an antinodal line when they first experience the acoustic field. And as Fig. 6.16 suggests, in this case the attractive secondary force (which is two orders of magnitude higher than around the nodal line) can trap particles together, negatively affecting device performance [268].

6.5 Chapter summary

In this Chapter various simulation models were presented to aid device design, validate device behaviour or quantify secondary effects. A coupled Laminar Flow and Diluted Species model was used to simulate particle focusing and flow speeds within the microchannel. A complete piezoelectric–acoustic–mechanic model was employed to fully capture physical processes in the device and generate pressure distribution within the microchannel for various phase differences between the transducers. Although this model is the most accurate for device simulation, due to its high computational demand it was replaced by simpler approaches to be able to obtain particle separation trajectories. A basic model, only using background pressure fields and fully neglecting any reflection or streaming effects was first applied to see excellent agreement with analytical particle trajectories. To incorporate streaming effects and channel walls, a Thermoviscous Acoustic physics was applied for the fluid domain, with velocity and impedance boundary conditions, accounting for the

substrate and the PDMS. The particle trajectories are still in good agreement with the analytical model, however, 20% difference in final position can be observed, which is attributed to the so-called anechoic corner and small device width. Interparticle scattering gives rise to secondary radiation force that can cluster particles negatively affecting device performance. An axisymmetric 2D, and a more complex 3D model were developed utilising the tensor integral force calculation approach for simple interparticle force simulation. The models offer fast convergence and computational times, are applicable to arbitrary shaped and sized particles and arbitrary incident acoustic fields.

Chapter 7

Experimental results with synthetic particles

To assess the different sorting methods for efficiency or purity and thus compare them, synthetic particles were used that closely mimic the properties of biological cells. Therefore experiments can be carried out with relative ease without the need for culturing cells and maintaining expensive biological setup.

The sizes of biological cells can vary from a few microns to a few tens of microns for usual circulating and tissue cells. For example, disk-shaped red blood cells have a diameter of 6.2 to 8.2 µm and typical thickness of 1 to 2.5 µm [269]. Spheroid white blood cells are of 12 to 17 µm typical diameter, three times as big as RBCs [270]. Circulating tumour cells can be even larger, up to 30 µm [271]. The density of typical cells range from 1.048 to 1.054 $\mathrm{g/cm^3}$, since they are mainly composed of water [272, 273]. The compressibility is more difficult to characterise, but ranges 331 to 422 $\mathrm{TPa^{-1}}$ [274–276].

Synthetic polystyrene particles have identical density 1.05 $\mathrm{g/cm^3}$ to biological cells, while its compressibility is comparable to those of cells [232, 277]. I note here that different authors take PS compressibility different, from the simplest isentropic fluid particle approximation yielding 172 $\mathrm{TPa^{-1}}$ [125, 278], to the complete solid model, taking into account shear wave propagation and thus yielding 249 $\mathrm{TPa^{-1}}$ [232, 264]. Different values can also be found in the literature, such as 216 $\mathrm{TPa^{-1}}$ [274] or 330 $\mathrm{TPa^{-1}}$ [128, 277]. Furthermore, PS particles are available with high monodispersity ranging from a few microns to a few hundreds of microns in diameter—thus making it a perfect candidate for cell surrogate.

7.1 Comparison of sorting methods

To experimentally carry out sorting, three methods are available as presented within the theoretical and simulation Chapters 4 and 6: continuous linear phase modulation, linear phase modulation with a jump (non-continuous modulation) and frequency modulation. As discussed, continuous PM offers the most intuitive way of sorting by shifting the standing wave pattern directly. As theory suggests, the FM technique is essentially the same, in an indirect fashion, but requiring less work with the control software and the signal generator can be simply switched between two frequencies instead of the more complex phase ramping pattern. Finally, the jump modulation requires the most complex control software, but in turn offers the possibility of fastest sorting by making the large particles move linearly while displacing the smaller particles by a smaller amount compared to other methods. The required phase control signal and the resulting particle trajectories are shown in Fig. 7.1, a montage of figures from Chapter 4.

To illustrate sorting, first simple separation experiments were carried out for 10 and 14.5 µm PS particles as shown in Figs. 7.2 and 7.3 for the upwards and downwards direction, respectively. In both cases, the large particles to be separated are denoted by green circles, while the non-target particles are orange. Dashed lines are pressure nodes, dotted line is a pressure antinode. For both cases, after the ramping cycle, the two particle sets locate on different sides of the pressure antinode (see middle row of images in Figs. 7.2 and 7.3) and relax towards different pressure nodes during the resting cycle thus achieving sorting. The left column corresponds to continuous phase modulation experiments, while the right column shows jump PM experiments. As expected, in both cases the large particles travel more with the jump modulation, compared to the continuous modulation, while the opposite can be observed for the small particles, therefore achieving better separation. The adequate slope time for the jump modulation was calculated from typical acoustic pressure variation and particle properties to be $t_{\text{slope}} = 1.1\,\text{s}$, and the same ramping time used for the continuous method.

For rigorous analysis and comparison of the methods, multiple experiments were carried out with the surface acoustic wave device to extract at least 10 particle trajectories for each particle and for each modulation method. Afterwards these were averaged, and analytical plots fitted using pressure amplitude as the only fitting

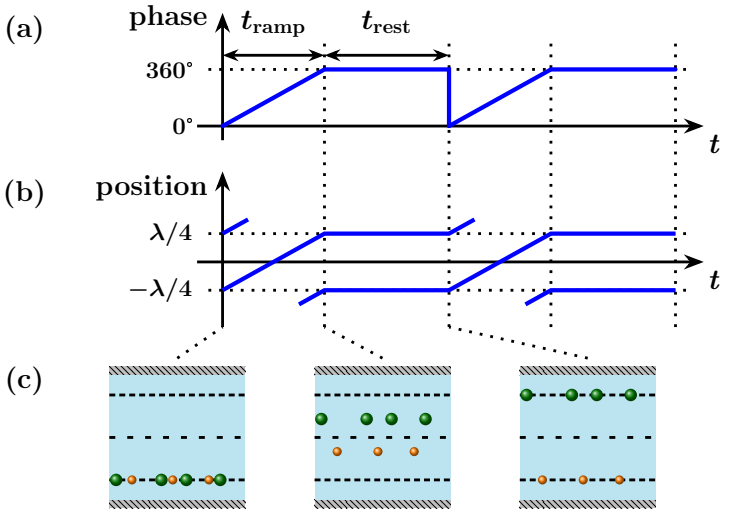

(a) Illustration of the phase modulated sorting method

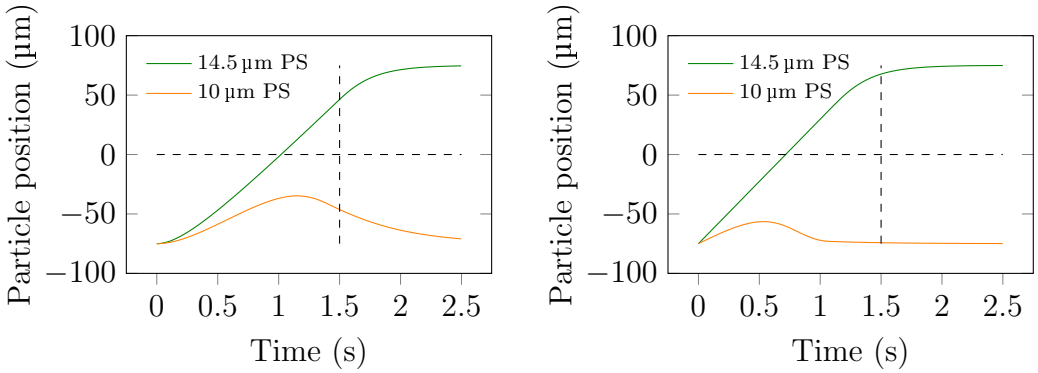

(b) Continuous phase modulation or frequency modulation particle trajectories

(c) Jump phase modulation particle trajectories

Figure 7.1: Recap of the available single direction sorting methods and anticipated particle trajectories

parameter ($p_0 = 103\,\mathrm{kPa}$ in this case). Note that only the upwards jump method had been fitted, all other modulations are adjusted using the timing parameters, and the opposite direction is simply taken as the inverse of the curves. The separation trajectories can be seen in Figs. 7.4 and 7.5 for the upwards and downwards direction, respectively. Error bars correspond to the standard deviation of experimental results.

Comparing the two directions, a clear difference between the curves is visible, indicating an asymmetric device operation. The most probable reason is the difference between the frequency response of the two transducers due to manufacturing errors and thus the difference of the delivered acoustic energy at the two sides of the channel. Other reason might be the different PDMS channel wall thickness and attenuation (as it is cut by hand). Therefore after manufacturing, an exhaustive device testing is necessary if dual operation is required to ensure the symmetry.

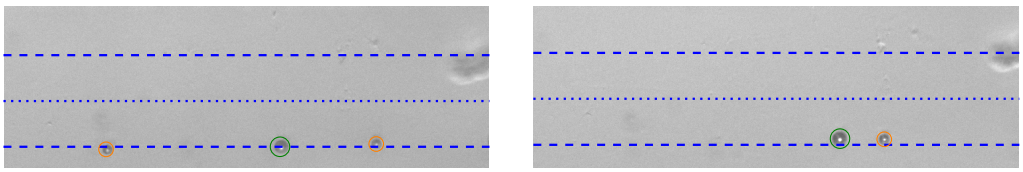

(a) Before sorting the small and large particles locate at the bottom pressure node where they are trapped by the primary acoustic radiation force

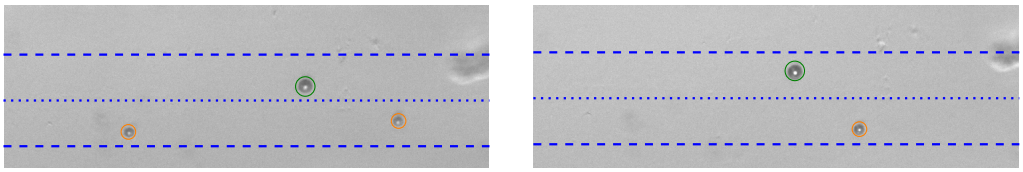

(b) After the ramping cycle, the large spheres locate on the top side of the pressure antinode

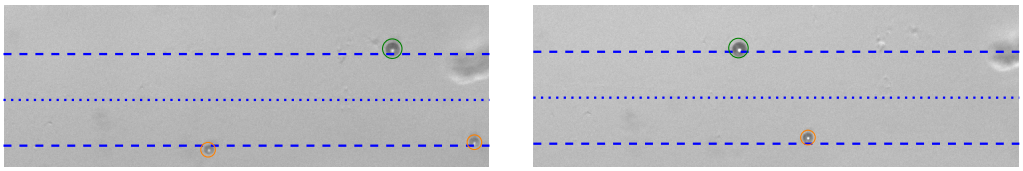

(c) After the full ramping/resting cycle, the largest spheres trap at the top pressure node, while the small particles are relaxed at the bottom pressure node

Figure 7.2: Upwards sorting of 10 (orange circles) and 14.5 µm (green circles) PS particles. Dashed lines indicate the position of the pressure nodes where particles trap, dotted line is the pressure antinode. The main phases of the sorting are shown as subfigures. Left column corresponds to continuous phase modulation, right column corresponds to jump phase modulation

When comparing the three methods within a directionality group, no significant difference is visible, especially for the downwards case. Here the frequency and continuous phase modulation techniques almost fully overlap, with the jump method below the large particle trajectory and above the small particle trajectory, as expected. For the upwards direction, the overlap of the FM and continuous PM methods is close, but not perfect, however, the jump modulation is clearly well above the large particle trajectory and below the small particle trajectory.

This investigation helps choosing a modulation method for the further experiments that can be used as a basis for exhaustive investigations, including various particle sets, scaling laws or the transition zones between sorting and non-sorting parameters. As the agreement between the FM and continuous PM methods is excellent, but the former offers much easier control, the continuous PM method was excluded from further investigations. For similar reasons, coupled with the inherent size difference limitation of the jump method (see Chapter 4), this non-continuous phase modulation was also put aside for future experiments. For a numerical comparison of sorting

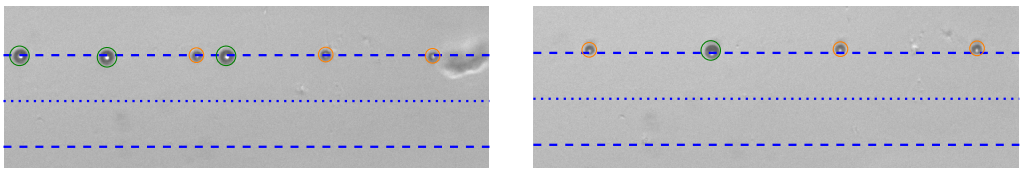

(a) Before sorting the small and large particles locate at the top pressure node where they are trapped by the primary acoustic radiation force

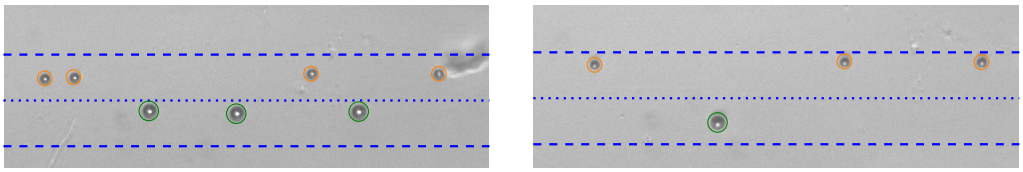

(b) After the ramping cycle, the large spheres locate on the bottom side of the pressure antinode

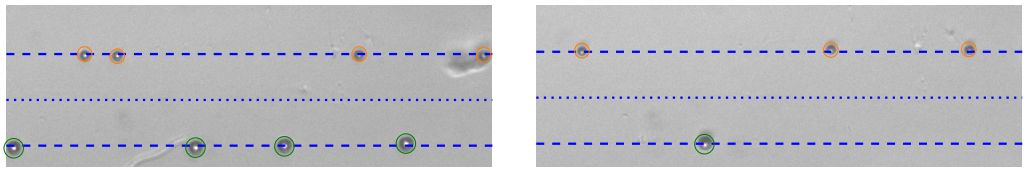

(c) After the full ramping/resting cycle, the largest spheres trap at the bottom pressure node, while the small particles are relaxed at the top pressure node

Figure 7.3: Downwards sorting of 10 (orange circles) and 14.5 µm (green circles) PS particles. Dashed lines indicate the position of the pressure nodes where particles trap, dotted line is the pressure antinode. The main phases of the sorting are shown as subfigures. Left column corresponds to continuous phase modulation, right column corresponds to jump phase modulation

efficiency between continuous and jump PM methods, please refer to Chapter 9.

7.2 Frequency modulated sorting

After choosing the frequency modulated method as the basis for further experiments, first it has been thoroughly analysed by varying frequency difference between the transducers. As shown in Chapter 4, the maximum particle speed is given as

$$v_{\max} = \dot{y}_{\max} = c_{\mathrm{ac}}/c_{\mathrm{visc}} \tag{7.1}$$

Any frequency difference that causes a nodal translational speed v_{p} less than $v_{\max}$, forces the particles to move linearly with a constant speed. However, if the nodal speed is greater than the maximum speed ($v_{\mathrm{p}} > v_{\max}$), the particles oscillate and shift at the same time, in a less deterministic manner [**Simon2018APL**].

Speed measurements were carried out to demonstrate this phenomenon. Particle trajectories were recorded to calculate average particle speeds. Results for 19 $V_{\mathrm{pk-pk}}$

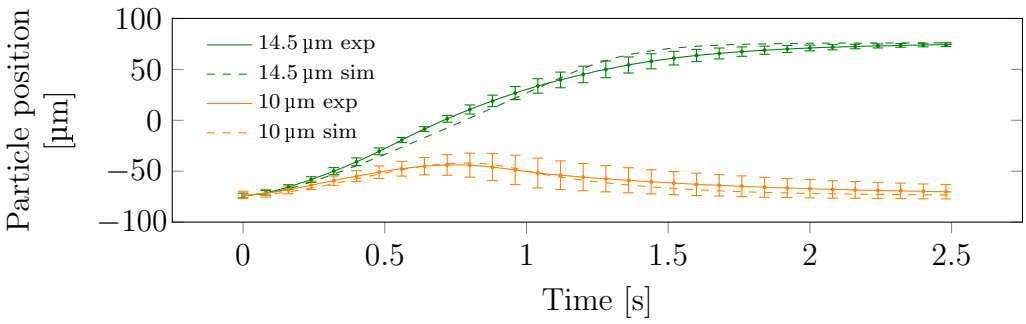

(a) Continuous phase modulation. Solid lines are experimental results, dashed lines correspond to simulation

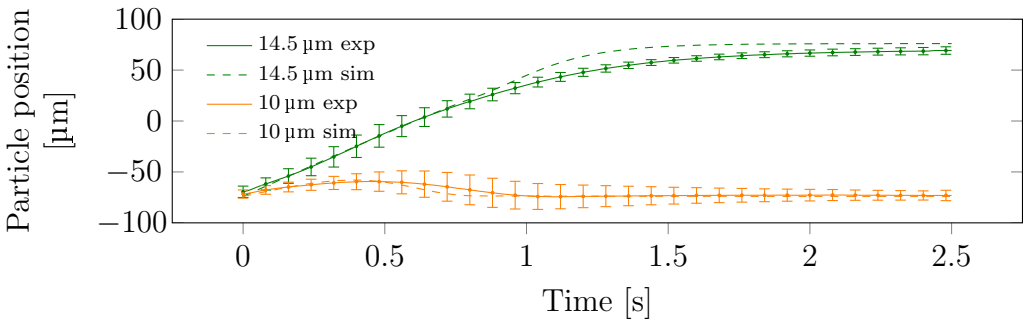

(b) Jump phase modulation. Solid lines are experimental results, dashed lines correspond to simulation

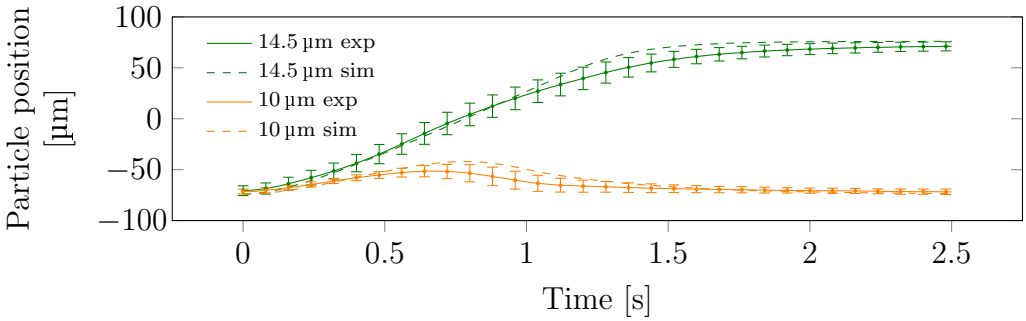

(c) Frequency modulation. Solid lines are experimental results, dashed lines correspond to simulation

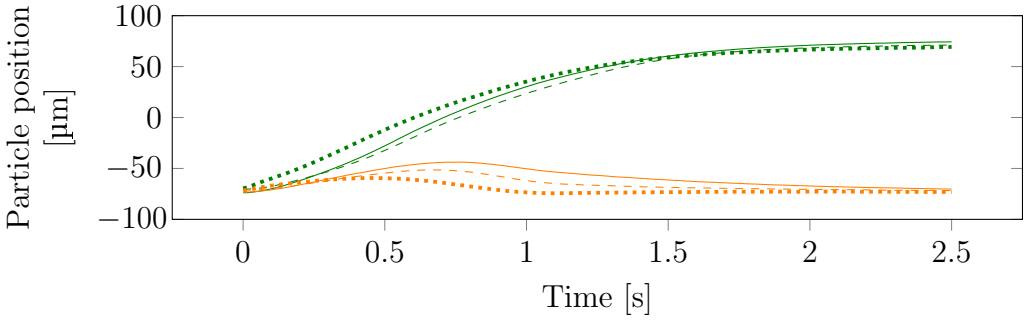

(d) Comparison of the continuous (solid line), jump phase (dashed line) and frequency modulation (dotted line) techniques. In this plot all curves indicate experimental results

Figure 7.4: Trajectories of upwards particle sorting experiments and analytical fit

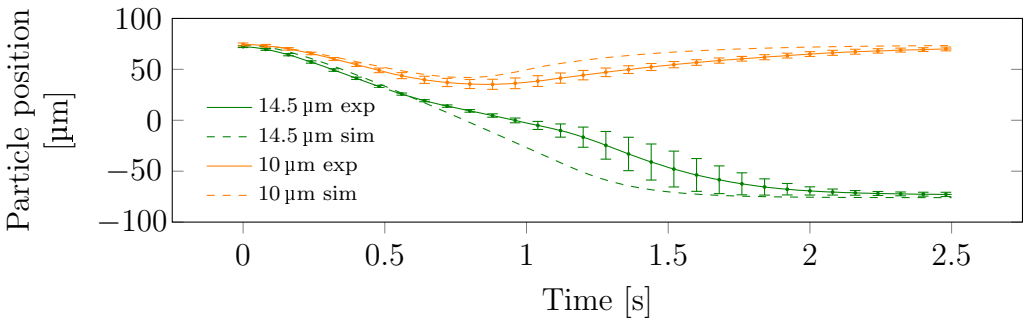

(a) Continuous phase modulation. Solid lines are experimental results, dashed lines correspond to simulation

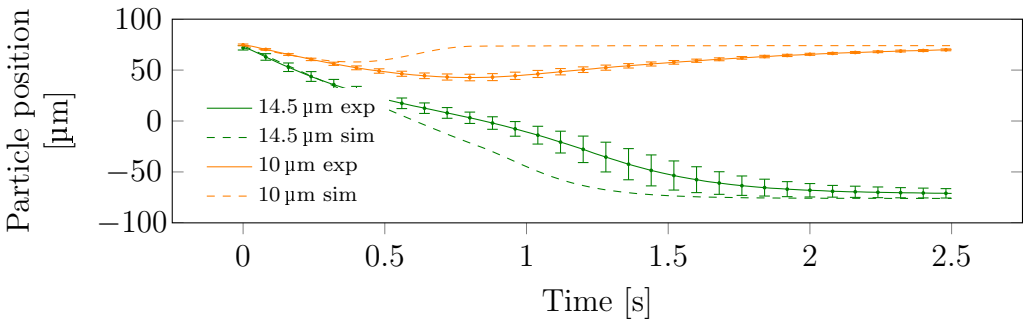

(b) Jump phase modulation. Solid lines are experimental results, dashed lines correspond to simulation

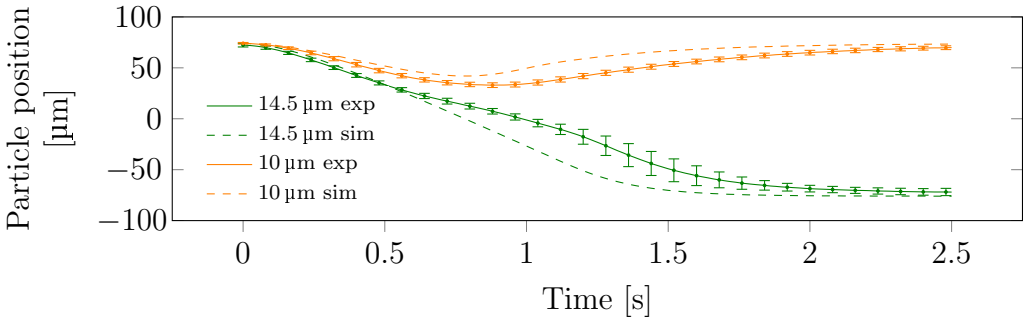

(c) Frequency modulation. Solid lines are experimental results, dashed lines correspond to simulation

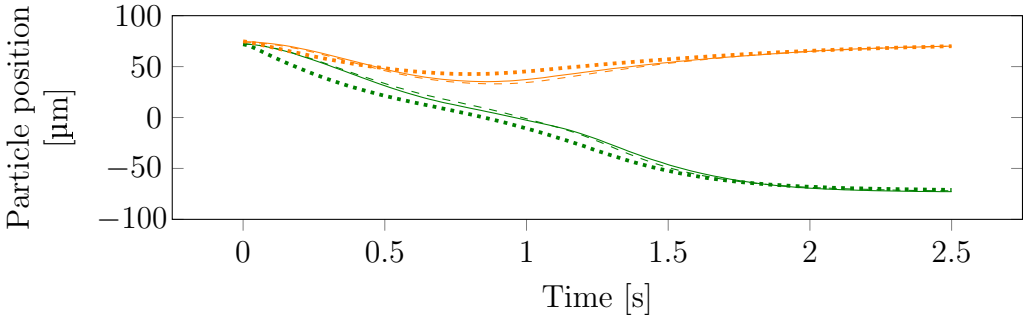

(d) Comparison of the continuous (solid line), jump phase (dashed line) and frequency modulation (dotted line) techniques. In this plot all curves indicate experimental results

Figure 7.5: Trajectories of downwards particle sorting experiments and analytical fit

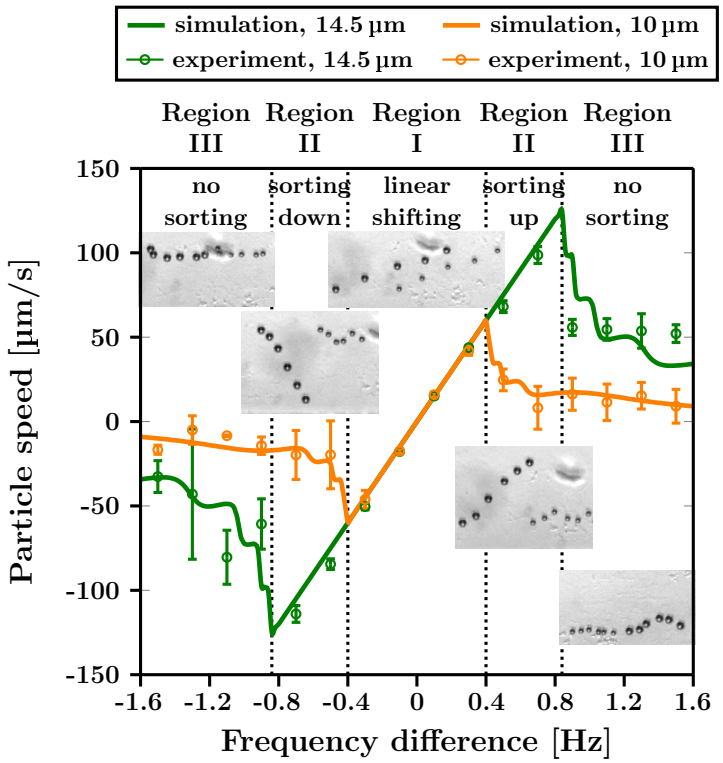

Figure 7.6: Experimental and theoretical average particle speed for various frequency difference values between transducers. Insets are overlay images of the corresponding videos, illustrating particle motion

transducer voltage for 10 and 14.5 µm particles are shown in Fig. 7.6. For frequency differences between -0.4 and 0.4 Hz (Fig. 7.6, Region I), both particles are below their respective speed limit $v_p < v_{max}$, so they both translate simultaneously, and no sorting can be achieved. When the frequency difference is less than -0.85 or greater than 0.85 Hz (Fig. 7.6, Regions III), as $v_p > v_{max}$, both particles only oscillate with small average speeds, which cannot be used for sorting. However, in regions between -0.85 to -0.4 and 0.4 to 0.85 Hz (Fig. 7.6, Regions II), the large particles are below their maximum speed and can be translated linearly, while the small particles oscillate and shift with a lower average speed. These regions are promising for sorting applications. The regions from -0.8 to -0.4 Hz and from 0.4 to 0.8 Hz are defined as the downwards and upwards regimes when target particles exit via the lower and upper outlet, respectively. Although the frequency difference between transducers is six orders of magnitude smaller than the centre frequency, speed measurements and separation experiments were highly reproducible showing good performance of the technique.

The fabricated microfluidic device presented an inhomogeneous pressure distribution along the SAW active area. The measured [**Simon2017Bio**]spatial variation in

particle mixture	dir*	flow rates ($\mu l\,min^{-1}$) top inlet	middle inlet	bottom inlet	Voltage (V_{p-p})	Δf (Hz)	off time (s)	efficiency (%)	purity (%)
14.5 and 10 µm PS	D	0.5	0.4	1.2	19	-1.3	2	94 ± 2	87 ± 4
	U	1.4	0.3	0.3	19	1.4	4	94 ± 2	81 ± 6
8 and 6 µm PS	D	0.25	0.15	0.6	19	-1.2	3.5	85 ± 4	83 ± 5
	U	0.9	0.16	0.2	19	1.15	4	84 ± 4	81 ± 7
6 and 5 µm PS	D	0.1	0.1	0.5	23	-1.5	3	71 ± 5	78 ± 6
	U	0.7	0.2	0.2	23	1.2	3.5	67 ± 9	73 ± 9
10 µm PS and FeO	D	1.1	0.4	0.3	23	-2.5	1.2	97 ± 4	93 ± 5
	U	0.3	0.4	1.1	23	2.5	1.2	98 ± 3	91 ± 5
10 µm PMMA and FeO	D	1.3	0.2	0.5	19	-2	2	85 ± 7	94 ± 3
		1.3	0.2	0.5	19	1	1.5	99 ± 1	71 ± 3
	U	0.5	0.15	1.6	19	-2	2	91 ± 8	86 ± 10
		0.5	0.15	1.6	19	1	1.5	97 ± 3	62 ± 9

Table 7.1: Experimental results for various particles and sorting scenarios. *Direction of sorting (dir): upwards (U) or downwards (D). PS: polystyrene, FeO: iron-oxide, PMMA: poly(methyl methacrylate)

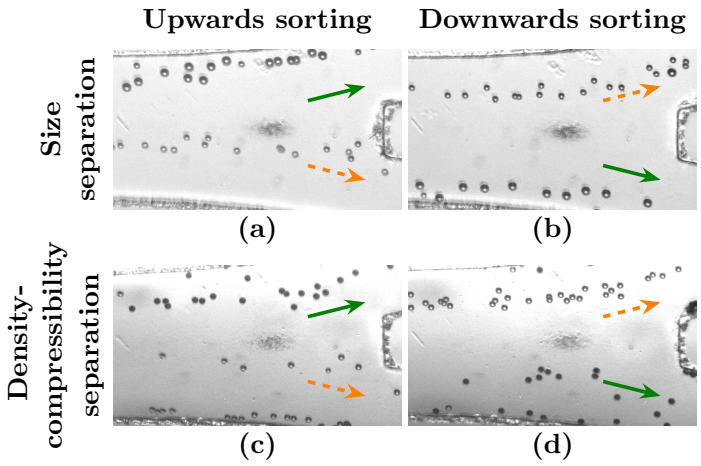

Figure 7.7: (a, b) Overlay images of size-based sorting for 10 and 14.5 µm PS particles in diameter. (c, d) Overlay images of density/compressibility particle sorting with PS (appearing with white centre) and iron-oxide particles (appearing as solid black), 10 µm in diameter. For sorting parameters refer to Table 7.1. Green solid and orange dashed arrows indicate target and waste particle flow, respectively

pressure was 30% higher at the sides of the active area than at the middle, where the average particle speed characterization experiments were carried out. Therefore, the frequency differences in the sorting experiments were increased by 40% compared to the values suggested by Fig. 7.6.

The experimental parameters and results are summarized in Table 7.1. For the size-based sorting experiments, the particles were suspended in polyethylene glycol solution (PEG, 0.1% w/v in DI water) to avoid stiction of particles to sidewalls. Particle concentration was at least $2 \cdot 10^6$ ml^{-1}, and at least 100 particles were counted to have accurate efficiency and purity values. Five counting periods were randomly chosen and averaged within a 10 minute timeframe when the experiment was running. The voltage used in the experiments was 19-23 $V_{\mathrm{pk-pk}}$, lower values did not provide high enough acoustic force to reliably trap and manipulate the particles; higher values result in heat generation that is unfavored for biological applications.

Since the acoustic radiation force depends also on the particle density and compressibility, separation experiments were carried out for 10 µm particles of polystyrene, PS ($\rho = 1.05\,\mathrm{g/cm^3}$, compressibility $\kappa = 250\,\mathrm{TPa^{-1}}$), iron-oxide, FeO ($\rho = 1.5\,\mathrm{g/cm^3}$, $\kappa < 15\,\mathrm{TPa^{-1}}$) and poly(methyl methacrylate), PMMA ($\rho = 1.2\,\mathrm{g/cm^3}$, $\kappa = 170\,\mathrm{TPa^{-1}}$) (calculated from parameters in [170]). To reduce sedimentation before entering the channel, these particles were suspended in 30% (w/v) iodixanol solution (from OptiPrep density gradient, Sigma-Aldrich, and DI water). The PS and iron-oxide particles showed excellent separability, as shown

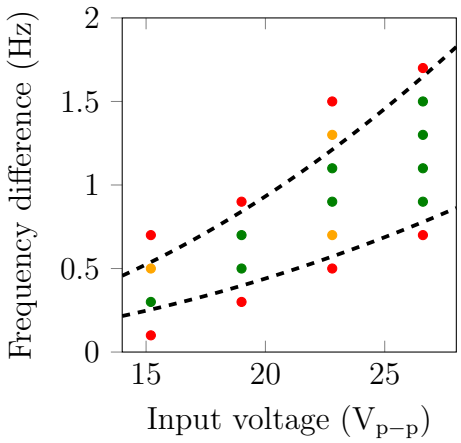

Figure 7.8: Comparison of experimental and theoretical limit for sorting. Sorting experiments have been carried out for 10 and 14.5 µm PS particles for various input voltages and frequency differences between transducers. The experiments were categorized as good (green, purity and efficiency >90%), bad (red, purity and efficiency <70%) and medium quality (yellow, purity and efficiency in between 70 and 90%). Excellent agreement with quadratic fit (dashed lines) can be observed

in Table 7.1, with >97% efficiency and >91% purity for both sorting directions. With the reduced difference in density for the PMMA and iron-oxide particles, high efficiency and purity were achieved by using two different frequency modulations: for 1 Hz, high efficiency (>97%), and for 2 Hz, high purity (>86%) were measured. For this sorting scenario both figures of merit are lower, and their variation is higher for the upwards sorting. Previous works [195, 235] also investigated sorting based on density and compressibility differences of particles. Although they showed higher efficiency values, they were carried out in the absence of flow. Therefore, no issues were present such as hydrodynamic focusing inaccuracies or the particles being subjected to the acoustic field for slightly different periods of time due to the parabolic flow profile and travel time though the device.

As detailed in the supplementary document of [**Simon2018APL**], different sorting scenarios are equivalent when the particles to be separated have the same size ratio. For particle size ratio greater than 1.3, high efficiency and purity, both for the upwards and downwards sorting were recorded. In all these cases, the efficiency was higher than 84% and the purity higher than 81%. The efficiency for both upwards and downwards sorting drops to around 70% with the purity being approximately 75% when the particles size ratio decreased to 1.2. As 70-75% efficiency and purity can be treated as minimum desirable values, the limit of this separation method and device is therefore found to be size ratio of 1.2. Overlay images illustrating the

sorting can be seen in Fig. 7.7.

According to the scaling laws presented theoretically in Chapter 4, $t_{\mathrm{ramp}}\gamma$ is equivalent to $\gamma/\Delta f$, and as $\gamma \propto V_{\mathrm{in}}^2$, it is expected to see a quadratic dependence of good quality sorting on input voltage. To validate this prediction, sorting experiments were carried out for various frequency differences and input voltages for the 10 and 14.5 µm particle mixture. To be able to see sorting solely due to the acoustic field, these were performed at the middle of the device in the absence of the flow. Results were categorized as sorting (>90% efficiency and purity), non-sorting (<70% efficiency or purity) and low efficiency sorting (for intermediate results). These results can be seen in Fig. 7.8 with the theoretical prediction.

7.3 Bandpass sorting

Again, a quick recap of the bandpass sorting method is provided with the aid of Fig. 7.9. When two distinct modulation cycles are used right after each other with different ramp times, sorting of medium-sized entities is possible from the heterogeneous mixture. The first cycle displaces the large and medium-sized particles towards the opposing pressure node. The second, slightly faster cycle is carried out in the negative direction, moving only the largest particles back to their original position, thus achieving bandpass sorting. As the Figure illustrates, by changing the sign of the cycles, sorting towards either of the two outlets is possible.

To carry out bandpass sorting, the frequency modulation was selected of the available three methods (continuous PM, jump PM, FM) as it offered the simplest control software to be written while its performance is similar to the other techniques as shown earlier in this Chapter. Furthermore, in this case there are two options for carrying out the second stage of sorting experimentally: either the voltage can be kept constant throughout the whole process and the frequency difference is adjusted for the two stages, or the frequency difference can be kept constant and the voltage adjusted. For brevity, these are referred to as CVBP sorting (constant voltage bandpass sorting) and CFDBP sorting (constant frequency difference bandpass sorting). The CVBP approach is more straightforward and easier to perform from the control software, however, the second approach allows for easier design in the future if a true lab-on-chip device is to be developed. Controlling the frequency precisely is usually much more difficult than controlling the voltage (especially here

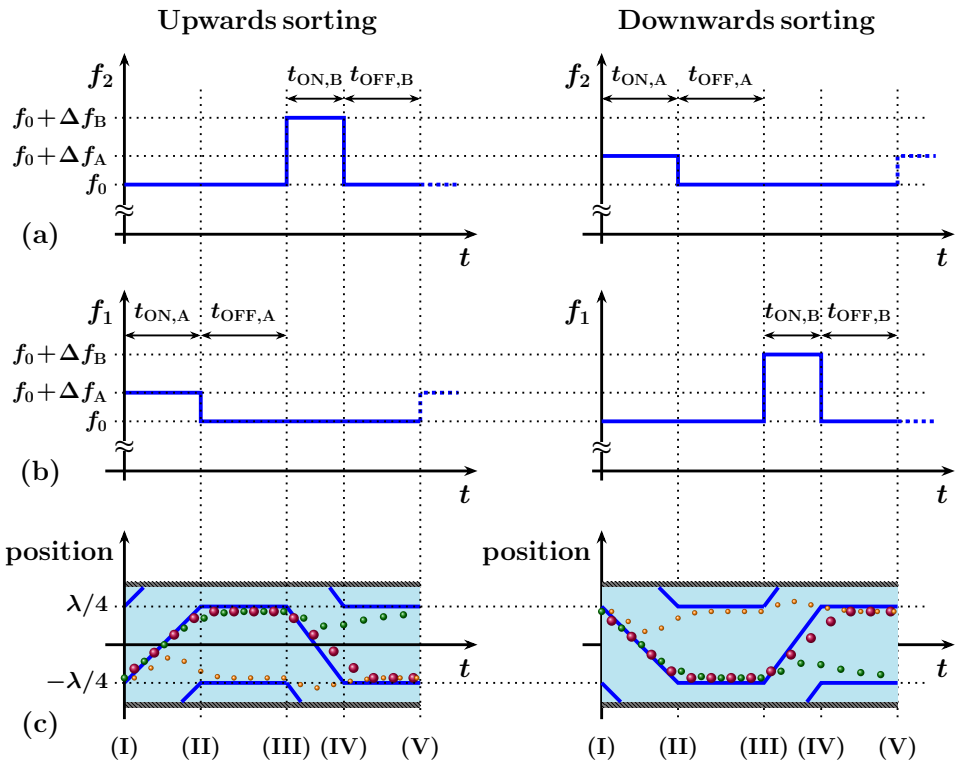

(a) Illustration of the bandpass sorting method

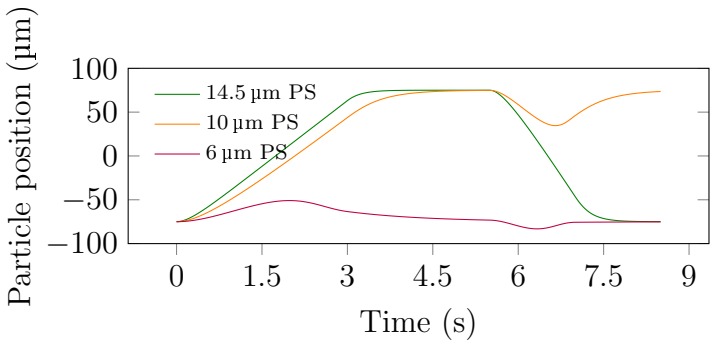

(b) Upwards bandpass sorting trajectories

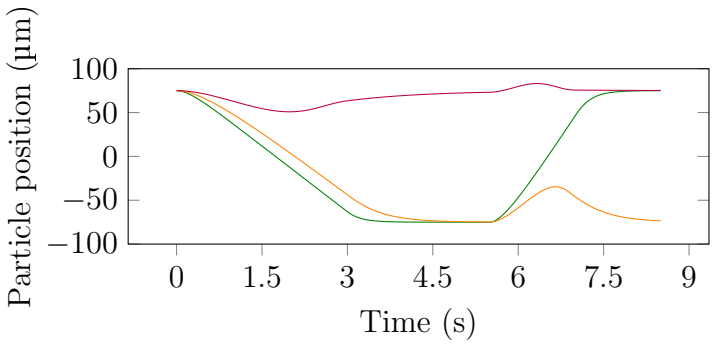

(c) Upwards bandpass sorting trajectories

Figure 7.9: Recap of the available bidirectional bandpass sorting methods and anticipated particle trajectories

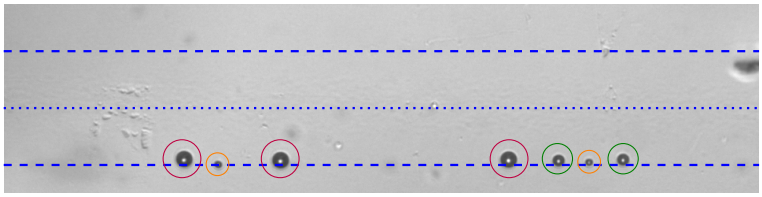

(a) Before sorting all three sized particles locate at the bottom pressure node where they are trapped by the primary acoustic radiation force

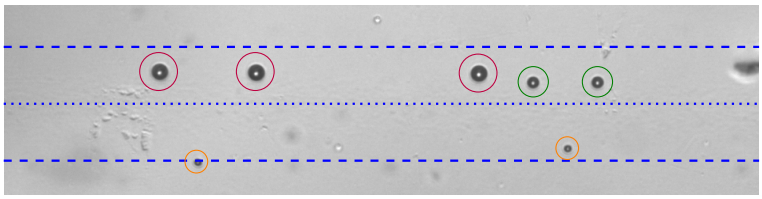

(b) After the first ramping cycle, the two larger-sized spheres (10 and 14.5 µm) locate on the top side of the pressure antinode

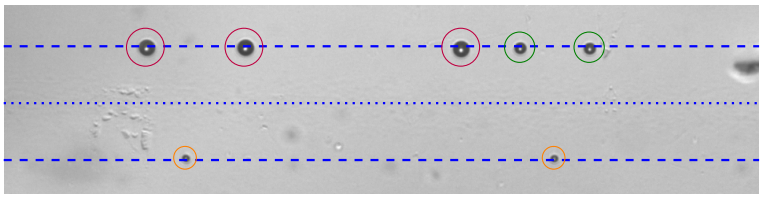

(c) After first full ramping/resting cycle, the two largest spheres trap at the top pressure node, while the small particles are relaxed at the bottom pressure node

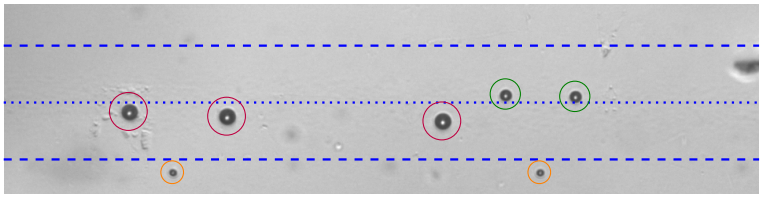

(d) After the second ramping cycle, the largest spheres are pushed back towards the bottom and cross the pressure antinode again, while the medium-sized spheres only get displaced by a smaller amount not allowing them to cross the antinodal line

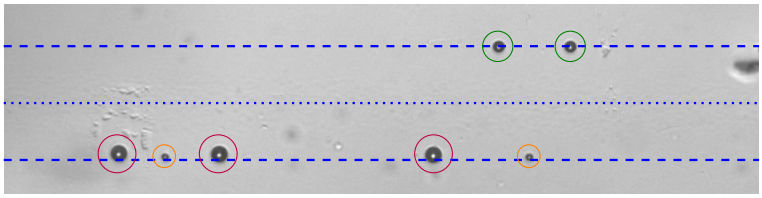

(e) After the full sorting cycle the smallest and largest spheres locate at the bottom pressure node, while the medium-sized 10 µm particles are sorted at the top pressure node

Figure 7.10: Upwards bandpass sorting of 6 (purple circles), 10 (orange circles) and 14.5 µm (green circles) PS particles. Dashed lines indicate the position of the pressure nodes where particles trap, dotted line is the pressure antinode. The main phases of the sorting are shown as subfigures

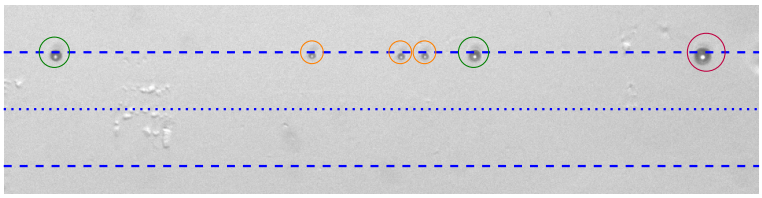

(a) Before sorting all three sized particles locate at the top pressure node where they are trapped by the primary acoustic radiation force

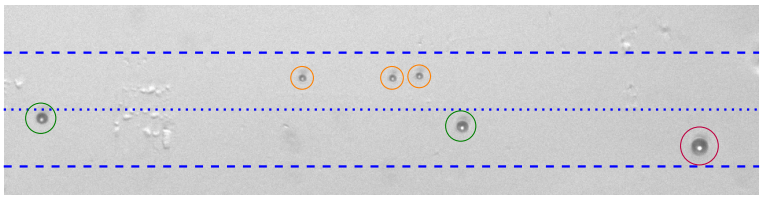

(b) After the first ramping cycle, the two larger-sized spheres (10 and 14.5 µm) locate on the bottom side of the pressure antinode

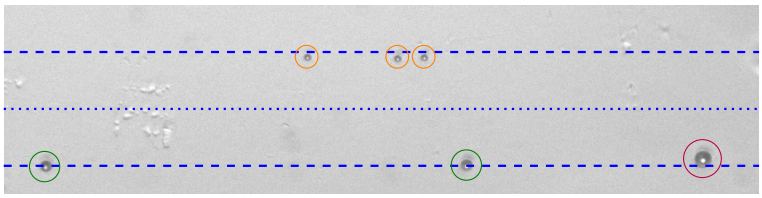

(c) After first full ramping/resting cycle, the two largest spheres trap at the bottom pressure node, while the small particles are relaxed at the top pressure node

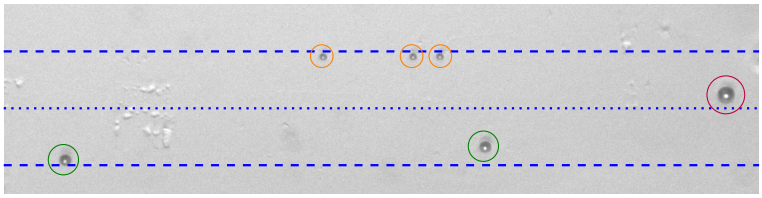

(d) After the second ramping cycle, the largest spheres are pushed back towards the top and cross the pressure antinode again, while the medium-sized spheres only get displaced by a small amount not allowing them to cross the antinodal line

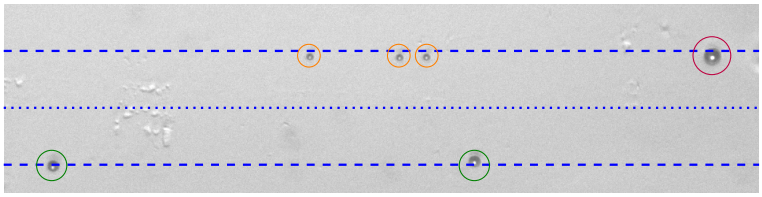

(e) After the full sorting cycle the smallest and largest spheres locate at the top pressure node, while the medium-sized 10 µm particles are sorted at the bottom pressure node

Figure 7.11: Downwards bandpass sorting of 6 (purple circles), 10 (orange circles) and 14.5 µm (green circles) PS particles. Dashed lines indicate the position of the pressure nodes where particles trap, dotted line is the pressure antinode. The main phases of the sorting are shown as subfigures

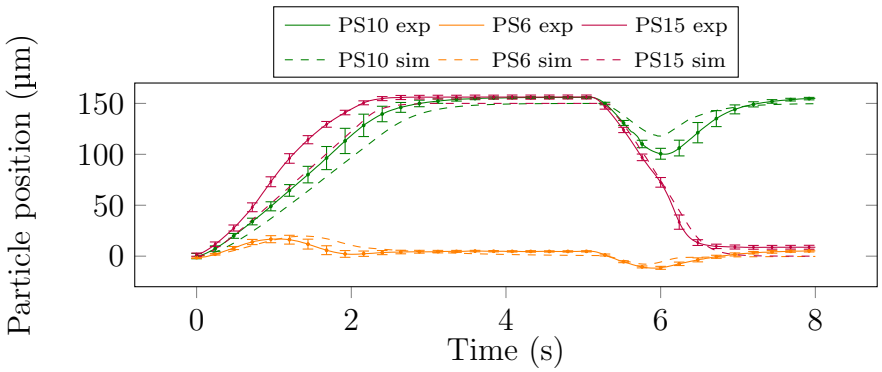

(a) Experimental and analytical sorting curves for fixed voltage sorting

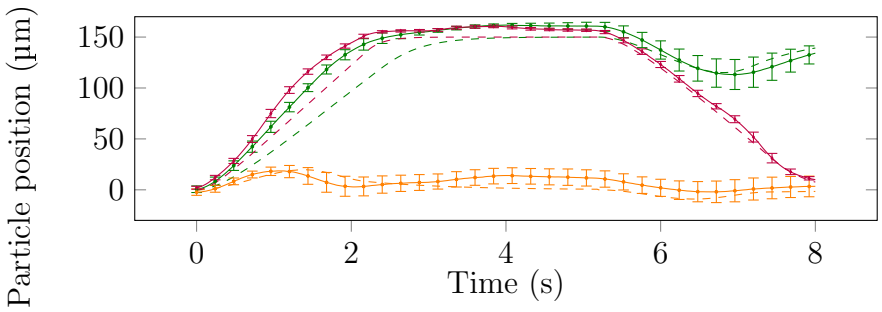

(b) Experimental and analytical sorting curves for fixed frequency difference sorting

Figure 7.12: Trajectories of upwards bandpass sorting

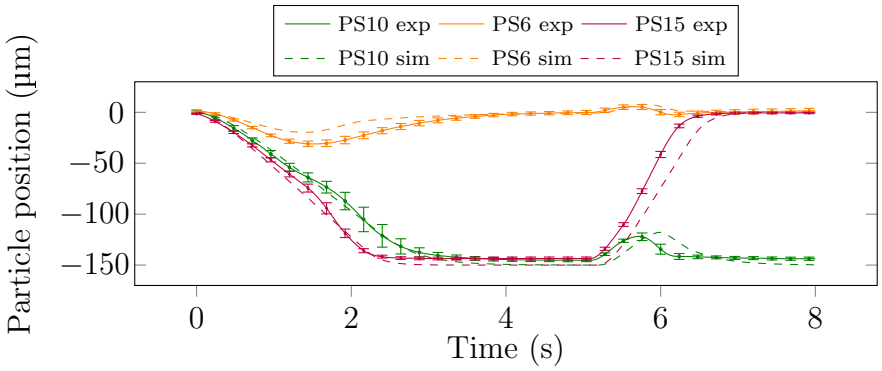

(a) Experimental and analytical sorting curves for fixed voltage sorting

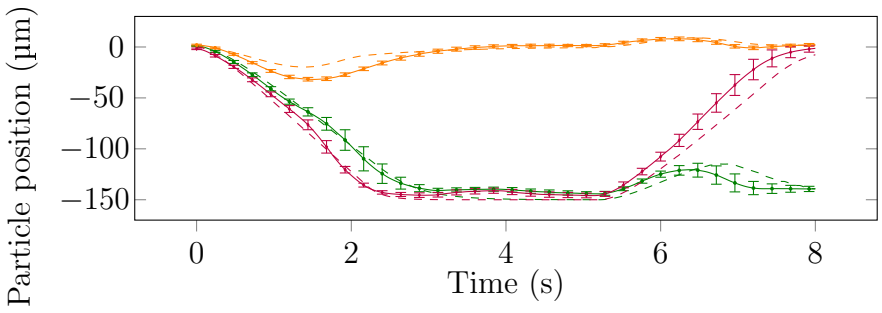

(b) Experimental and analytical sorting curves for fixed frequency difference sorting

Figure 7.13: Trajectories of downwards bandpass sorting

as 6 orders of magnitude precision is required). With the CFDBP approach, the device can operate at two frequencies that are precisely adjusted by the on-chip components, and the sorting is controlled by the voltage of the transducers and thus

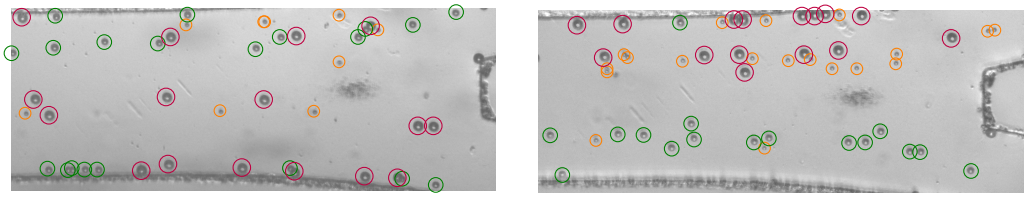

(a) Upwards sorting (b) Downwards sorting

Figure 7.14: Bandpass sorting of 6, 10 and 14.5 µm PS particles. Overlay images recorded at the device outlet

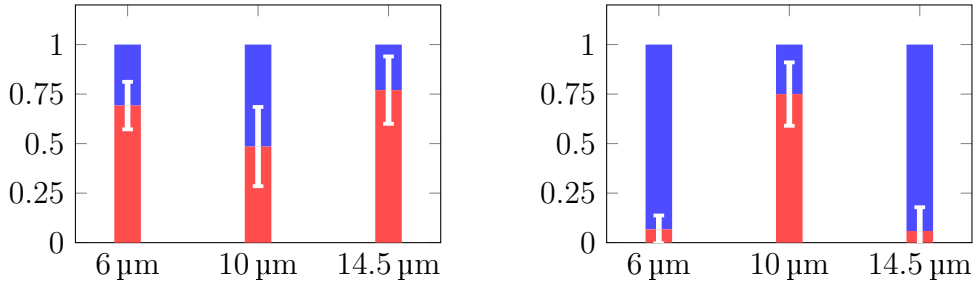

(a) Upwards sorting (b) Downwards sorting

Figure 7.15: Figures of merit of bandpass sorting of 6, 10 and 14.5 µm PS particles. Blue and red portions illustrate particles going to the top outlet and bottom outlet, respectively

the pressure amplitude within the cavity.

First, as with the other techniques, the feasibility of the method was tested in the absence of flow. Refer to Chapter 4 and Fig. 4.8 for theoretical overview as the basis of the comparison with experimental results. The upwards and downwards bandpass sorting of 6, 10 and 14.5 µm PS particles can be seen in Figs. 7.10 and 7.11, respectively. For both cases, the particles are color-coded similarly as before: the smallest particles are orange, the medium-size target particles green and the largest particles are purple. The pressure nodes are shown as blue dashed lines and the pressure antinode as a blue dotted line. Five subfigures are shown taken from the experimental video, corresponding to the key moments of sorting: (i) initial configuration, (ii) after first ramping, (iii) after first resting, (iv) after second ramping and (v) after second resting phase.

In the case of upwards bandpass sorting (Fig. 7.10) all particles are initially trapped at the bottom pressure node (Fig. 7.10a). During the first ramping stage, the two larger size particles are pulled across the antinodal line, while the smallest particles stay below (Fig. 7.10b). As a result, during the first resting stage, the small particles relax at the bottom pressure node, while the 10 and 14.5 µm particles relax towards the top pressure node (Fig. 7.10c). A faster second ramping cycle in

the opposite direction moves the largest particles back towards the bottom, forcing them to cross the antinodal line again (Fig. 7.10d). During the second resting stage, the 10 µm particles relax towards the top pressure node, while all other particles relax at the bottom pressure node, thus separating out the medium-size particles and achieving bandpass sorting (Fig. 7.10e).

In the case of the downwards sorting, all the stages are reversed, and can be followed by the aid of Fig. 7.11, showing separation of the 10 µm at the bottom pressure node after a complete cycle (Fig. 7.11e).

The separation trajectories of the fixed voltage sorting were recorded for $23\,V_{p-p}$ transducer voltage and 0.46 and 0.92 Hz frequency difference for the two stages. The resting time was 3 s in both cases. Multiple experiments were performed using the same experimental parameters to obtain at least 10 trajectories for each particle. These were averaged and are shown with standard deviation as errorbars in Figs. 7.12a and 7.13a. Using the scaling laws, the voltage required to achieve sorting in the second stage with the same 0.46 Hz frequency difference is $16.3\,V_{p-p}$ that was used in the experiments. The switching of the voltage occurs at the middle of the resting phase, small 'bumps' are visible where the voltage of the transducers is adjusted. As the two transducers are changed one after another, for a moment the two transducers have unbalanced voltages thus delivering non-uniform acoustic energy to the channel making the particles translate momentarily. Apart from this behaviour the two approaches (CVBP and CFDBP sorting) perform similarly.

By adding flow to the acoustic excitation, continuous flow bandpass sorting is possible as shown in Fig. 7.14. The ratio of particles going to the various outlets can be seen in Fig. 7.15. The average normalized efficiency is 51% and 75% for the upwards and downwards methods, respectively, while the average normalized purity is 49% and 85%, illustrating yet again the superiority of the downwards sorting direction.

7.4 Chapter summary

In this chapter first the continuous, jump phase modulation and frequency modulation techniques for particle sorting have been compared experimentally using synthetic particles as biological cell surrogates. The investigation revealed negligible difference between the three methods, and therefore the frequency modulation method have

been chosen as the subject for further experiments as it is the easier to implement in hardware. The technique has been thoroughly analysed, first, by adjusting the frequency difference and observing the various sorting and non-sorting zones. Separation experiments with fluid flow have been carried out next, for both sorting directions, for both size-based and physical properties based sorting, revealing good performance of the method from particle ratio of 1.2, and offering excellent efficiency and purity values (>85%) for size ratios over 1.5. Experimental investigation of scaling of sorting with input voltage is in good agreement with the theoretical quadratic dependence. Finally, bandpass sorting experiments of 6, 10 and 14.5 µm particles conclude the chapter. The downwards sorting direction outperforms the upwards direction for bandpass sorting experiments and shows an average normalized purity and efficiency of 85% and 75%, respectively.

Chapter 8

Experimental results with biological cells

After successful validation of the various sorting methods using cell-mimicking synthetic particles, experiments were carried out for biological cells. A wide variety of cell lines are used by other groups, such as tissue cells (mainly in the form of different cancer cell lines or circulating tumour cells) [137, 158, 162, 163, 279] or circulating blood cells [130, 167, 280]. The tissue cells are more difficult to work with as they stick to the cell culture flasks, requiring extra steps during sample preparation [137, 279], and they also tend to attach to the microfluidic channel and to each other (thus trying to form tissue [281]), risking blockage. Circulating tumour cells are delicate and require well-adjusted media to make sure adequate viability and survival [282]. This viability issue would require an extra thorough investigation step, to understand viability separately from the media and from the applied ultrasound. Therefore, to be able to carry out experiments with simple and fast sample preparation and high cell viability, Jurkat cells were chosen as the main target cells [283], while selecting RBCs as the non-target cells. Jurkat cells are an immortalized line of human peripheral blood T lymphocytes (further on referred to as either Jurkats or WBCs), their culture protocol is described below.

8.1 Jurkat cell culturing

8.1.1 Cell preparation protocol

As the circulating blood cells do not attach to the culturing flask (Corning 3814, 22.5 ml, Fischer Scientific UK) to form tissue, their culturing protocol does not require cell detachment and cell washing steps [102], but a small amount can be directly transferred to a new flask and media added. The Jurkat cells require Gibco RPMI 1640 medium (500 ml, Fischer Scientific UK) and an additional 10% fetal bovine serum (FBS or fetal calf serum – FCS, Gibco, Fischer Scientific UK) was added to promote cell growth. Moreover, to inhibit contamination and protect the cells, a mixture of penicillin and streptomycin (PenStrep) antibiotics were added to the media as well (Gibco Penicillin-Streptomycin 10,000 Uml^{-1}, Fischer Scientific UK).

Therefore, the composition of the cell culture media is:

- 500 ml Gibco RPMI 1640 medium
- 50 ml FBS
- 5 ml PenStrep

Every time the cells are split, they are counted according to the protocol described in the section below. The freshly prepared flask of cells always contained 10^5 cells per ml, this gives enough cells for experiments, but still would not allow them to become confluent in a few days and therefore damaged. Assume the count of the old batch resulted in $N \times 10^4$ cells per ml. To have Mml of cells in the new batch with the aforementioned 10^5 cells per ml density, one would need $\frac{10M}{N}$ml of the old cells and $M - \frac{10M}{N}$ml media, since

$$\frac{(N \times 10^4 \text{ ml}^{-1})\, \frac{10M}{N}\text{ml}}{M\text{ml}} = 10 \times 10^4 \text{ ml}^{-1} \tag{8.1}$$

The flask with cells was incubated at standard conditions at 37 °C and 5% CO_2.

8.1.2 Counting cells and doubling time

To precisely count the number of cells manually in the flask, a Neubauer improved hemocytometer with 0.0025 mm^2 minimum square size and 100 µm depth was used (Brand Blaubrand Neubauer Improved Counting Chambers, Fischer Scientific UK).

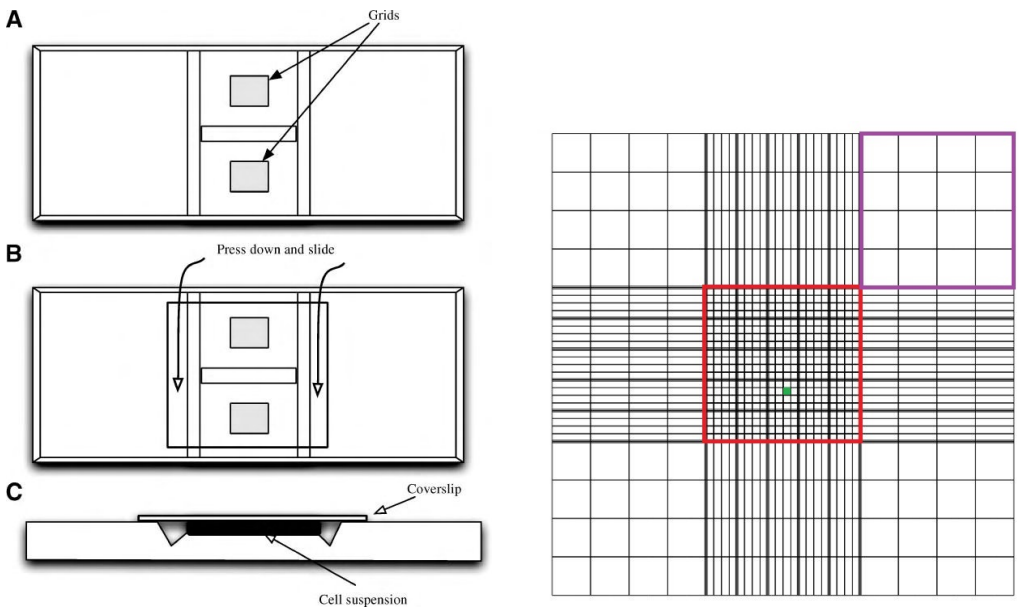

(a) (b)

Figure 8.1: Schematics of the Neubauer cell counting chamber. (a) Schematic of the device from different views. (b) The cell counting grid. Reproduced from [284] and [285]

The hemocytometer consists of a very thick microscope glass slide with a well in the middle that creates a chamber (refer to the left hand subfigures of Fig. 8.1). When placing another microscope slide on top (Fig. 8.1a middle), a precise amount of cell sample can be suspended in the gap (Fig. 8.1a bottom), and optically counted. As RBCs are much smaller than WBCs, the middle of the counting chamber has a finer grid engraved (red outline in Fig. 8.1b). The smallest square here is $0.0025\,\mathrm{mm}^2$, filled in green. Larger WBCs can be counted in the wider-spaced regions at the four corners of the grid (one of these outlined in purple in Fig. 8.1), that are 20 times larger in length than the finest square, and therefore 1 mm by 1 mm in size, or 100 nl in volume when the depth of the chamber is 100 µm. Counting N number of cells in one of these large regions gives a cell density of $N/100\,\mathrm{nl}$ or scaling up by a factor of 10^4 the more usual and convenient $N \times 10^4$ ml^{-1} count is available.

The cells in the flask are first pipetted up and down a couple of times to ensure a uniformly mixed sample. A few ml are then transferred to an Eppendorf tube for better accessibility. From the Eppendorf tube 50 µl is transferred to another tube where mixed with 50 µl Trypan blue solution (Trypan Blue Solution, 0.4%, ThermoFischer UK) to stain the dead cells through the damaged membrane [286]. Finally, the prepared sample is placed onto the hemocytometer for counting. Due to the 1:1 dilution with the Trypan blue dye, cell numbers in two of the large areas

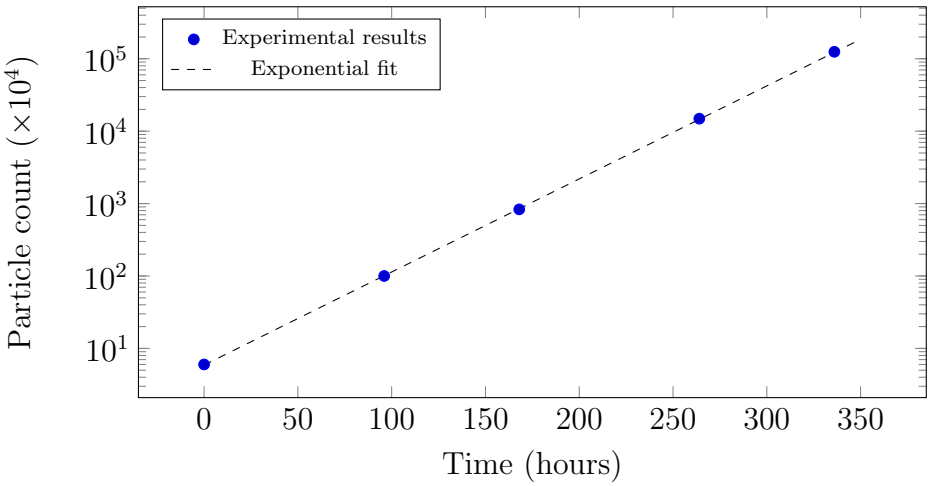

Figure 8.2: Cell counts versus incubation time, plotted on a semi-logarithmic scale. The experimental results follow an exponential fit well

have to be counted and added.

Thawed cells were cultured for at least a week to allow cell recovery. To quantify doubling time, observed for further two weeks with a few days between counting and splitting. Although the cells had to be split every few days not to allow them to be too confluent and suffocate, the splitting was carried out and the cell counts recorded correspond to the number of cells without the split. An example is shown in Fig. 8.2. As expected, the number of cells can be described by an exponential relationship [287]:

$$N(t) = N_0 2^{t/T_{\text{doubling}}} \tag{8.2}$$

where N_0 is the number of seed cells and T_{doubling} is the time required for the cells to double their number. This equation can be rearranged into a semi-logarithmic form to observe the linear fit:

$$\log_2 N(t) = \log_2 N_0 + t/T_{\text{doubling}} \tag{8.3}$$

and therefore the reciprocal of the slope is the doubling time. In the case shown in Fig. 8.2, the doubling time evaluates to $T_{\text{doubling}} = 23.4\,\text{h}$ or almost a day. Similar experiments were carried out multiple times to continuously monitor the cells, and the doubling time was observed to vary between 21.8 and 23.4 h.

The counting of cells allow for precise splitting and knowing the doubling time is used for one set of experiments when mitosis is to be inhibited using a specific drug.

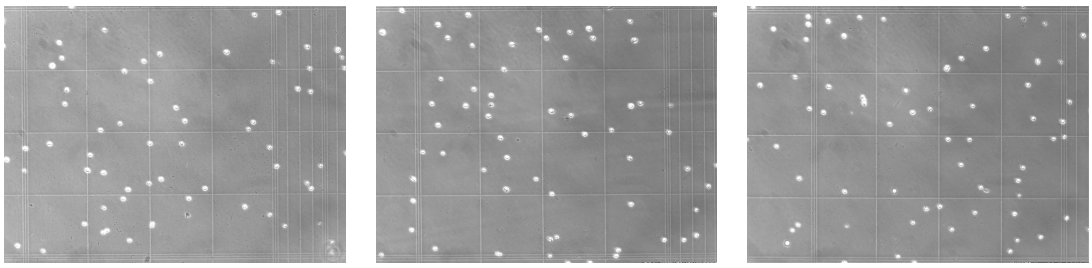

(a) NDC (b) 1 nM (c) 2 nM

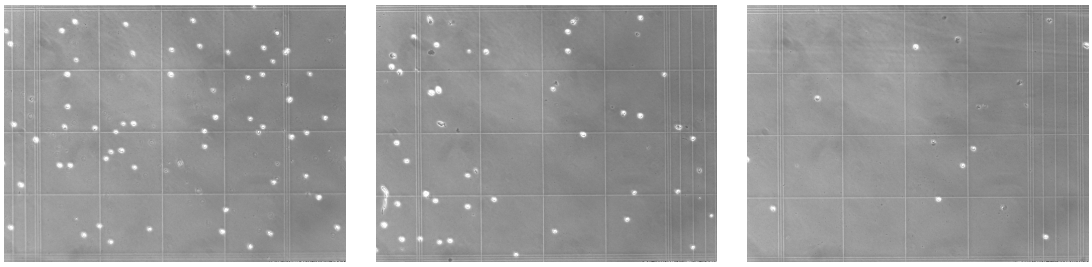

(d) 5 nM (e) 10 nM (f) 20 nM

Figure 8.3: Visual investigation of drug treated Jurkat cell samples

8.2 Planned experiments with biological cells

8.2.1 Size-based separation of RBCs and WBCs

As a verification of the modulated sorting method on biological samples, the most direct way is to carry out size-based separation. The two type of cells chosen are red blood cells and Jurkat white blood cells, as the rationale behind the choice is explained in the introduction. The size difference between these cells is threefold on average, providing sufficient difference for high quality sorting.

Furthermore, to illustrate bandpass sorting, 1 µm PS particles are mixed with the RBCs and WBCs and in this case the RBCs are the targets to be separated.

8.2.2 Size-based separation of Jurkat cells at different stages of the cell cycle

During mitosis of the cell cycle, there is a stage where chromosomes are already doubled yet a single cell with larger nucleus is present. This larger cell could be also used with regular cells to illustrate size-based sorting. Colchicine can be used to inhibit mitosis of cells by obstructing microtubule polymerisation [288]. The dose of the drug is usually of very low concentrations to allow for this effect without cell damage.

Concentration tests were therefore carried out in logarithmic steps from 1 nM to

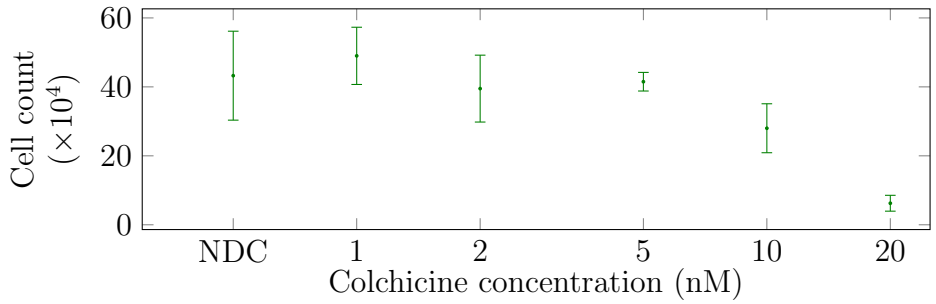

Figure 8.4: Dose test of colchicine treatment

1 mM in a 48-well assay. Cultured Jurkat cells were split to 10^5 ml^{-1} concentration and 1 ml pipetted in the two middle well of each column of the microplate (Corning 48-Well Clear Ultra Low Attachment Microplates, Fischer Scientific, UK). The cells were cultured for a day prior to adding the drug and cultured for a further day after applying colchicine. The adjacent two wells had the same concentration applied.

Visual examination of the cell samples revealed that concentrations higher than 20 nM resulted in necrosis and these cases are therefore excluded from the discussion. Microscope images taken of cell samples on a cell counting chamber can be seen in Fig. 8.3 for various drug concentrations and a no drug control (NDC). Two samples from each well were counted and therefore four results averaged for each concentration, shown in Fig. 8.4. Cell counts for colchicine concentrations lower than or equal to 5 nM were similar to the NDC count, illustrating no effect on the cell cycle. However, for 10 nM concentration the cell count is half of the reference, indicating that the cells did not go through mitosis and were inhibited by the drug. Further increasing the drug concentration the cell count is lower than the initial count, indicating necrosis. Therefore as literature shows [288], 10 nM colchicine concentration can be used to obtain cells with larger nuclei and size. Contrast factor measurements were carried out as discussed in the next section.

8.2.3 Compressibility-based separation of dead and live Jurkat cells

During tissue engineering, extracted cell samples are needed to be cultured in vitro and used later in vivo [289]. To allow for high quality tissue to grow, the dead cells has to be removed from the sample as they inhibit growth of neighbouring healthy cells [290, 291]. These live and dead cells are similar in size but differ in compressibility due to the collapsed membrane [274, 276, 292]. Although acoustic

methods are the least sensitive to such compressibility differences over size and density, the method might provide a solution for dead cell extraction. To investigate the feasibility, first the acoustic contrast factor of such live and dead cells is to be characterized and compared.

8.3 Jurkat cell phenotyping

8.3.1 Methodology using reference particles

To assess the acoustic contrast factor of the biological cells, either direct or indirect methods are available. Precise measurements of their density and compressibility, followed by calculation of the contrast factor, given by Eq. 2.5, gives the direct approach. Alternatively, reference particles can be used and the cell behaviour (trajectories) monitored while being subjected to an acoustic field, and thus obtaining the contrast factor indirectly [274, 276]. However, referring back to the force measurement technique proposed by fitting on the speed-position curves, it is clear that different particles or cells have different maximum speed that is proportional to their size and acoustic contrast factor:

$$v_{\max} = \frac{c_{\mathrm{ac}}}{c_{\mathrm{visc}}} \propto a^2 \Phi_{\mathrm{ac}} \tag{8.4}$$

Therefore, without too complex trajectory fitting, one can simply obtain the maximum slope of the trajectories (that gives maximum speed) and use it to calculate the unknown contrast factor after measuring particle and cell size:

$$\Phi_{\mathrm{ac}} = \frac{a_{\mathrm{ref}}^2}{a^2} \frac{v_{\max}}{v_{\max,\mathrm{ref}}} \Phi_{\mathrm{ac,ref}} \tag{8.5}$$

where subscript ref denotes the reference particle properties.

The advantages of this method compared to the trajectory fitting are the following: (i) no need to tediously fit trajectories one-by-one (ii) no need to calibrate for different acoustic pressure amplitude from experiment to experiment (iii) no need to calibrate for offset errors in the trajectories.

For all forthcoming characterisation experiments of Jurkat cells this method was used with 10 µm PS particles as reference particles.

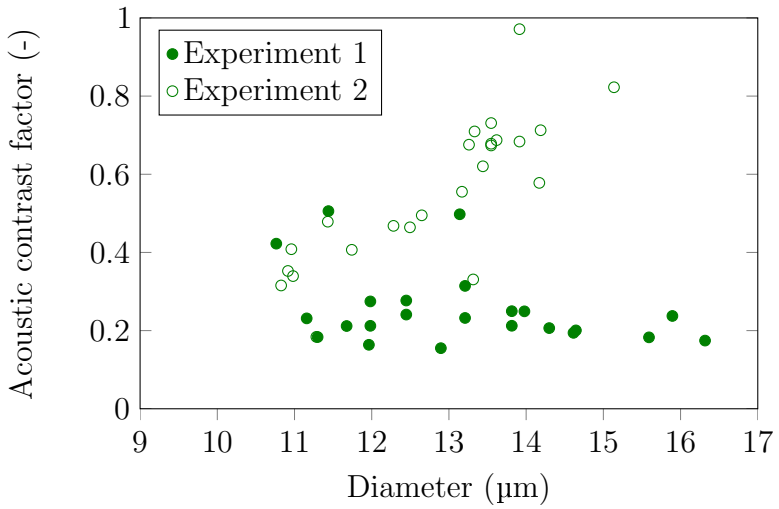

Figure 8.5: Acoustic contrast factor of live Jurkat cells versus diameter

8.3.2 Live Jurkat cell contrast factor measurements

For all characterisation experiments of live Jurkat cells the following protocol was used: the flask with cells was removed from the incubator, and 3 ml was prepared at 1 million cells per ml into a falcon tube. If the particle concentration was lower, they were spun down using 1400 rpm for 4 minutes. 50 µl particle suspension was added to the tube with the cells. The resulting sample roughly contained cells and particles in a 1:1 ratio. They were transferred to a pipette and immediately loaded into the surface wave device microchannel.

Results from two sets of cells can be seen in Fig. 8.5. Although the protocol was closely followed in all cases, due to lower level of experience in sample preparation and experimental setup it took significantly more time for cells in Experiment 1 to be tested, approximately 2-3 hours. Cells from Experiment 2 were recorded in less than an hour after removal from the incubator. It is suspected, that actually the cells from the first experiment suffered critical damage and were in a dead or dying state due to longer exposure to non-ideal conditions outside of the incubator. It is even more supported when compared in the next section to results of cells that were intentionally killed.

Therefore the contrast factor of live cells is taken as the spread of the empty circles in Fig. 8.5.

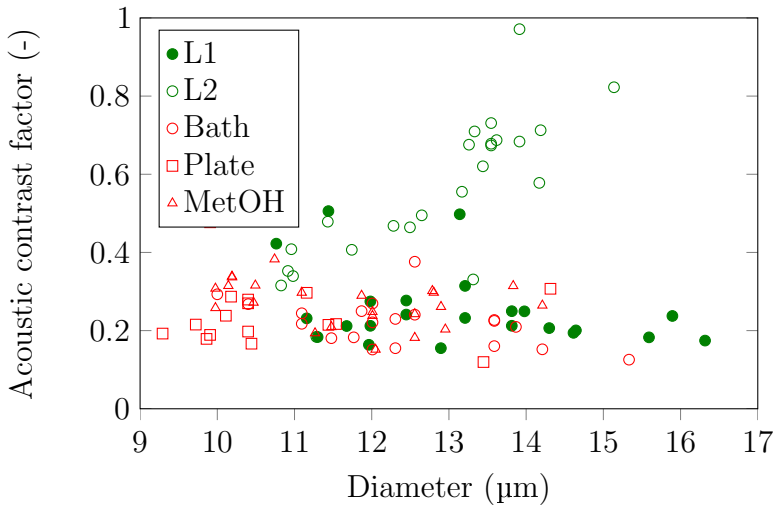

Figure 8.6: Acoustic contrast factor of live and dead Jurkat cells versus diameter. Dead cells are plotted in red. Bath: cells fixed in a hot bath; Plate: cells fixed on a hotplate; MetOH: cells fixed using methanol

8.3.3 Dead Jurkat cell contrast factor measurements

To prepare dead Jurkat cells that are similar in size and differ in acoustic contrast factor, various physical and chemical methods were used. As the cells cannot withstand temperatures higher than 65 °C, they were placed in a hot bath at this temperature and another batch on a hotplate for two hours. Afterwards the same preparation was carried out as for the live cells. To chemically induce cell death, first 70% methanol was used for 10 minutes.

The results of these tests can be seen in Fig. 8.6 where the two sets of live cell experiments are also shown. For all of these killing methods of cells, the size range has been moved down to 9 to 15 µm, while the acoustic contrast factor lies in the range of 0.1-0.4. Comparing with the cell sizes of live Jurkats (11 to 16 µm) a clear shrinking is observable. These methods, although alter the contrast factor compared to the 0.3-0.8 range of the live Jurkats, also induce a shrinkage that is too high. Finally compare the spread of filled green circles in Fig. 8.6 with any of the red markers to further validate the possibility of these cells actually being dead due to long processing delays.

Therefore an alternative way of fixing cells was tried using a formaldehyde treatment protocol [293]. By 1:9 dilution of formaldehyde (37% Formaldehyde solution, Sigma-Aldrich UK) in PBS (Phosphate buffered saline, pH 7.4, Sigma-Aldrich UK) a 4% formaldehyde solution was prepared and added to the pelleted cells. The suspension was incubated for 10 minutes when the cells were centrifuged

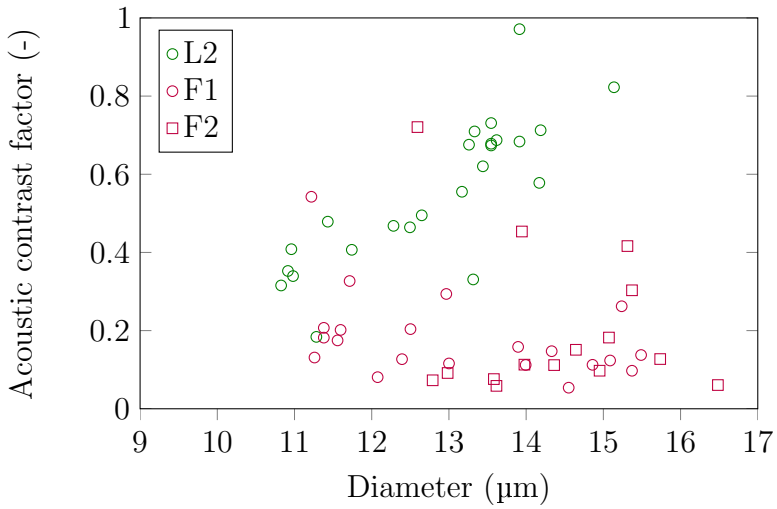

Figure 8.7: Acoustic contrast factor of live and formaldehyde fixed Jurkat cells versus diameter. Formaldehyde fixed cells are plotted in purple

and washed three times in PBS.

The results of two batches of cells fixed with formaldehyde can be seen in Fig. 8.7 where the live cells are again plotted as reference. These results provide a much better size spread compared to other fixing methods, as here the size range is very similar as that of the live cells. And although there is a clear difference in contrast factor, the regions cannot be separated well by a hyperbole as required for any sorting scenario and discussed in Chapter 4.

Therefore the feasibility of pure acoustic contrast-based separation of dead and live Jurkat cells was rejected and no separation experiments were carried out.

8.3.4 Acoustic contrast factor of colchicine treated cells

Colchicine treated cells using 10 nM drug concentration were prepared and used in cell contrast factor measurements. The results are plotted in Fig. 8.8. As the plot illustrates, the size distribution of the cells seem to shift again to 9 to 14 µm, lower than the live ones. Similarly, the acoustic contrast factor is within the range 0.15-0.4, as observed for dead cells, not the live ones. The shrinkage could be explained by the drug wearing off and allowing the cells to split, as these would be smaller in average size than a regular cell. However, the contrast factor cannot be explained by this, and it was suspected that either the drug treated cells react to the acoustics or the PDMS chamber in a different way compared to non-treated live ones. To validate this, another batch, using 5 nM was prepared, this concentration has no effect on cell cycle as shown in Fig. 8.4. However, the same behaviour was observed, a shift

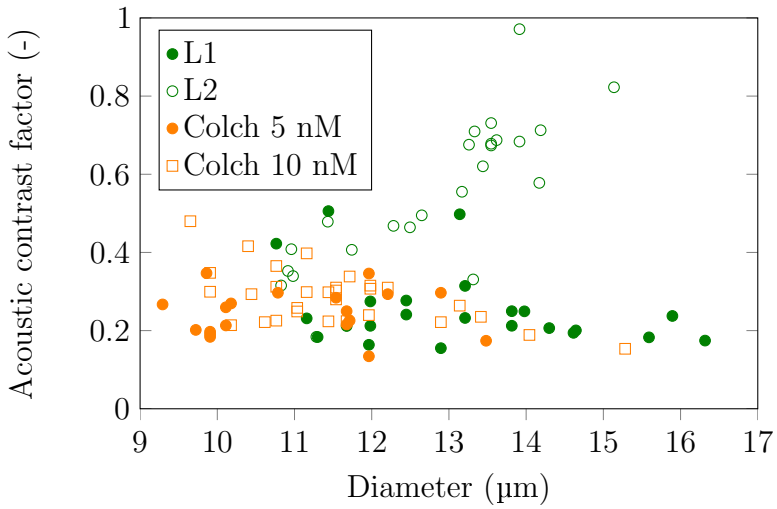

Figure 8.8: Acoustic contrast factor of live and colchicine treated Jurkat cells versus diameter. Treated cells are plotted in orange

in cell size. Therefore as this behaviour needs further thorough investigation, cell separation experiments were suspended for treated and non-treated Jurkat cells.

8.4 Cell viability of RBCs and Jurkat cells

8.4.1 Viability of RBCs

The effect of ultrasound on red blood cells can be investigated in relative ease as the cells are not spherical and any damage would result in the cell assuming a spherical shape due to the lack of cellular energy needed to sustain the irregular doughnut shape [269].

Stopping the fluid flow within the microchannel, the RBCs can be observed while subjected to ultrasound for longer times. An example of cell damage can be seen in Fig. 8.9 for 27 V_{p-p} input voltage. After a minute, the shape of the cells start to distort and in a couple of seconds they assume the minimum energy spherical shape.

The effect was investigated for various input voltages. For 19 V_{p-p}, no visual damage was observable up to 3 minutes; for 23 V_{p-p} visual damage on average after 2 minutes; for 27 V_{p-p} damage after 60 s and finally for 31 V_{p-p} damage after 40 s.

8.4.2 Viability of Jurkat cells

The viability of the Jurkat cells was investigated by collecting them after passing through the microfluidic device and culturing them for a few days. Tests were carried

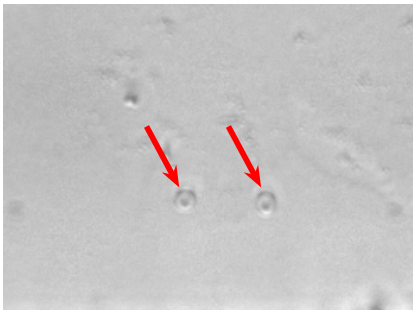

(a) At $t = 0$ when the ultrasound is applied. The RBCs are visibly intact, donut shaped with a dip in the middle

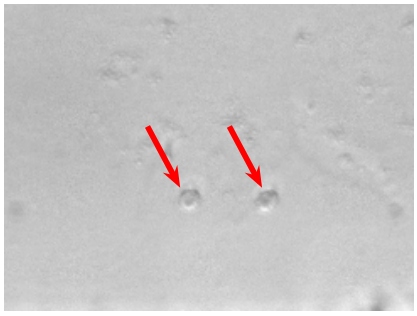

(b) At $t = 63\,\mathrm{s}$ the RBCs (especially the right one) start to deform

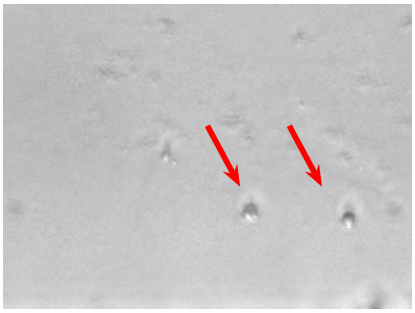

(c) After 66 s both RBCs lost their donut shape and appear spherical

Figure 8.9: The effect of ultrasound on the viability of the red blood cells. Applied input voltage is $27\,\mathrm{V_{p-p}}$

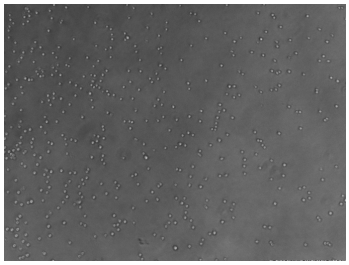

(a) Reference, start

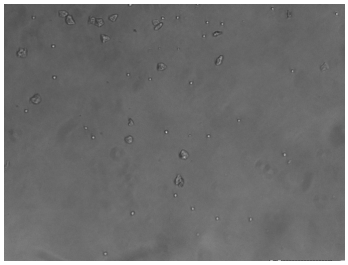

(b) No US, start

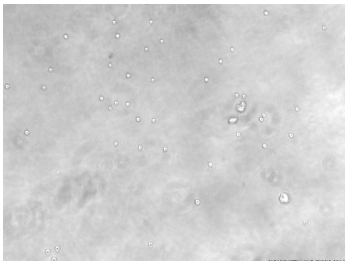

(c) With US, start

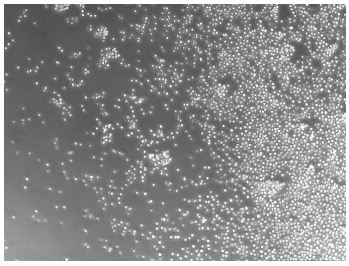

(d) Reference, end

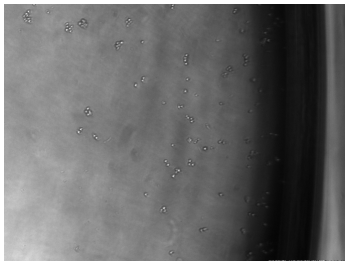

(e) No US, end

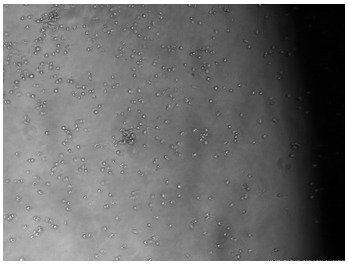

(f) With US, end

Figure 8.10: Visual investigation of viability of Jurkat cell samples

out both with and without ultrasound applied to differentiate any effect of the PDMS channel itself. For typical flow rates ($1.5\,\mu\mathrm{l\,min^{-1}}$) the amount of sample collected during minutes was of the order of microlitres, and therefore traditional cell counting

was not possible to carry out. Even when the density of the media was carefully adjusted using OptiPrep (Sigma-Aldrich) the cells sedimented in the channel after 15 minutes. Therefore, instead of cell counting, microscope images were taken of the cells in the culturing tray after collection and after a few days of incubation. The results are shown in Fig. 8.10. Both for the cells passing through the PDMS channel without applied ultrasound (Fig. 8.10b and e), and with ultrasound (c and f), there is a clear multiplication of the cells, indicating good viability. The irregular shaped fragments in these figures are pieces of the PDMS wall. Between the start and end micrographs the incubation time was 4 days and the applied ultrasound was 27 V_{p-p}.

8.5 Size-based separation of particles and cells

8.5.1 Separation trajectory of 5 micron PS particles and Jurkat cells

As a first step, the separation trajectories were to be recorded for the RBCs and Jurkat cells. This would have required keeping the ultrasound on and thus trapping the cells, while stopping the flow and waiting for it to completely stabilize in a stationary state. However, the flow stabilises quite slow, in the order of minutes, and the required ultrasound power to keep cells well trapped, overheated the RBCs. Therefore, they were substituted with 5 µm PS particles that have size and physical properties similar to RBCs. An example separation experiment for 27 V_{p-p} input voltage, 2.5 s ramping time and 2 s resting time can be seen in Fig. 8.11. Subfigure 'a' shows overlay images of the separation video, while subfigure 'b' illustrates the trajectories

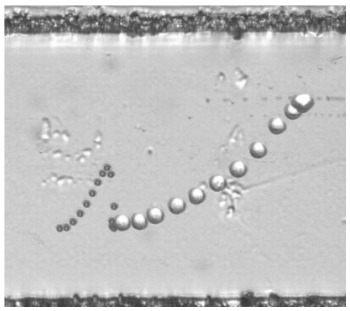

(a) Overlay image of a separation video of a 5 µm PS particle and a Jurkat cell

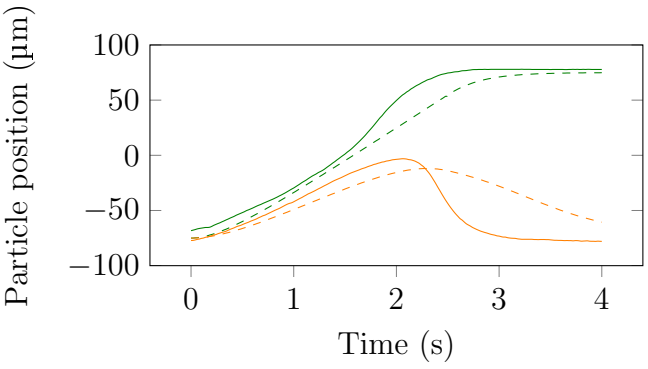

(b) Experimental trajectories and theoretical fit

Figure 8.11: Separation results of a 5 µm PS particle and a Jurkat cell

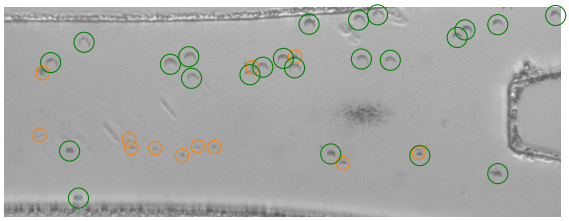

(a) Upwards

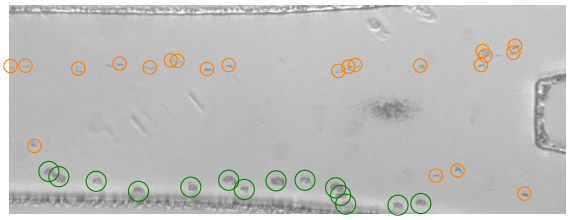

(b) Downwards

Figure 8.12: Separation of RBCs and Jurkats

	flow rate, µl min^{-1}						
	top	middle	bottom	t_{ramp} or Δf	t_{OFF}	efficiency	purity
U cont	0.62	0.08	0.17	1.7 s (0.59 Hz)	2.5 s	85 ± 6	83 ± 7
U jump	0.6	0.1	0.15	1.7 s (0.59 Hz)	2.5 s	83 ± 3	84 ± 5
U freq	0.8	0.25	0.2	0.8 Hz (1.25 s)	3 s	88 ± 3	93 ± 5
D cont	0.2	0.08	0.65	1.45 s (0.69 Hz)	2.7 s	97 ± 2	89 ± 6
D jump	0.2	0.1	0.65	1.75 s (0.57 Hz)	2.7 s	96 ± 4	86 ± 7
D freq	0.2	0.23	0.7	0.85 Hz (1.18 s)	3 s	94 ± 3	84 ± 6

Table 8.1: Separation experiments for RBCs and Jurkat cells

with analytical fit using $p_0 = 103\,\text{kPa}$ as pressure amplitude. The agreement between theory and experiment is good, however, there is a more pronounced difference for the resting phase of the PS particle. Similar behaviour was also observed in the particle experimental Chapter 7, here streaming effects might contribute as well due to the smaller particle size. Nevertheless these results illustrate the feasibility of the method well.

8.5.2 Separation experiments of RBCs and Jurkat cells

Separation experiments were carried out for RBCs and Jurkat cells with all three modulation methods (continuous, jump PM and FM). An example overlay of the separation videos recorded at the outlet can be seen in Fig. 8.12, illustrating both upwards and downwards sorting. As the cells are difficult to identify on steady images, they are colour coded using green for the target Jurkats and orange for the non-target RBCs. In a video the RBCs are recognizable as they rotate and change apparent diameter.

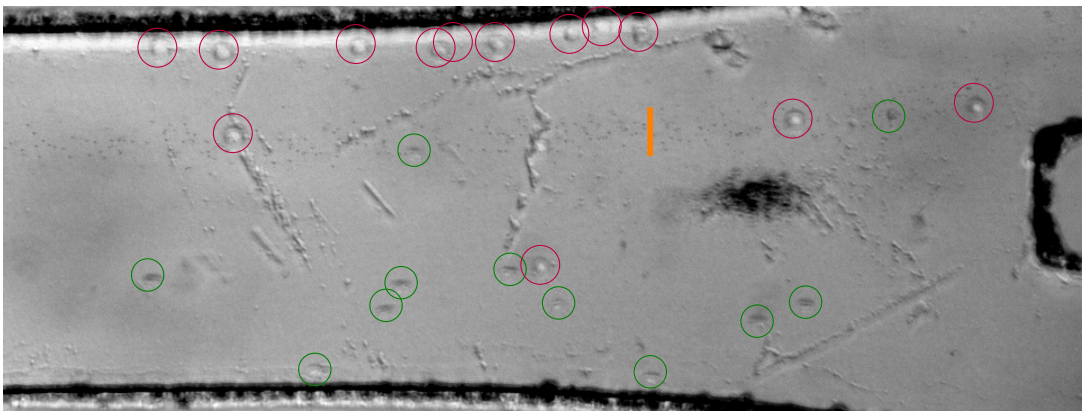

Figure 8.13: Bandpass separation of 1 µm PS particles (orange line indicating spread), RBCs (green circles) and Jurkat cells (purple circles)

The three type of experiments were also characterised by efficiency and purity by counting the cells exiting at the two outlets. For each experiment, cells from three videos were counted to obtain a total minimum of 100 cells. In all experiments, 27 V_{p-p} input voltage is used, other parameters are given in Table 8.1 along with the figures of merit values. This shows a similar behaviour as noticed for particle separation: (i) the three different techniques result in almost the same figures of merit values (ii) the downwards sorting performs better than the upwards sorting in efficiency by an average 10%.

8.6 Bandpass separation of cells

Bandpass separation experiments of particles showed an even more significant imbalance between downwards and upwards sorting than for single two-particle experiments. Therefore, for cell sorting the focus was placed solely on downwards bandpass sorting experiments. Moreover, as smallest entities, 1 µm PS particles were used, these can mimic platelets or small cell fragments (debris) in the experiments.

The same input voltage, 27 V_{p-p}, were applied on the transducers, with frequency modulation parameters 0.4 Hz and 0.6 Hz during the two cycles and 0.5 s and 1 s off times, respectively. The imbalance of the two transducers is even more visible with these experiments: the same frequency modulation is used to achieve translation of different entities in the two directions. Flow rates are 0.3 µl min^{-1}, 0.2 µl min^{-1} and 0.5 µl min^{-1} for the top, middle and bottom outlet, respectively. Overlay image of frames of separation video is shown in Fig. 8.13, where the target RBCs are circled in green and exit at the bottom outlet. The spread of non-target 1 µm PS particles

is indicated by an orange line, while the non-target Jurkat cells are circled in purple. The separation has an overall efficiency of $78 \pm 8\%$ efficiency and $74 \pm 6\%$ purity.

8.7 Chapter summary

In this Chapter experimental characterisation and separation of biological cells have been presented. First, the culturing protocol of Jurkat T-cells has been introduced, alongside with cell counting methodology and characterisation of cell doubling time. The three type of planned separation experiments have been discussed next, size-based separation of RBCs and Jurkats, size-based separation of Jurkat cells at different stages of cell cycle and finally dead and live Jurkat cells. To allow feasibility analysis of these planned experiments, Jurkat cell phenotyping has been carried out using a simple method introduced. Contrast factor measurements of live, dead and double nuclei Jurkat cells revealed various uncertainties and followed distributions that showed theoretically infeasible separation — the focus was therefore moved to size-based separation of RBCs and Jurkats. Sorting of RBCs and WBCs using frequency modulation shows higher than 90% efficiency while maintaining purity above 80% for the downwards sorting. The same figures of merit are above 80% for upwards sorting, highlighting an asymmetric device operation and superiority of downwards sorting. Bandpass sorting of 1 µm PS particles, RBCs and Jurkat cells shows around 75% efficiency and purity, while maintaining cell viability as it has been also demonstrated.

Chapter 9

Sensitivity analysis and Monte-Carlo simulation

9.1 The need for numerical sensitivity simulation

When the particle properties, such as size, density or compressibility, and the experimental parameters such as flow rate or pressure amplitude are of zero variance, it might be instinctive to assume that the sorting process operates at 100% efficiency and purity since all particles behave in the same manner. However, there are two properties of the phase modulated sorting method that might lead to lower figures of merit: the random particle arrival time, and the random lateral particle position within the inlet region. In the following subsections these two effects are investigated and later on in the chapter combined with non-uniform physical and experimental properties to compare the two phase modulated techniques and the time-of-flight acoustic particle sorting method for sensitivity. The time-of-flight method is used as a general term for the widely used standing wave sorting methods, where the principle of sorting is the different time scale of the various particles [130, 138, 147, 149]. It has been chosen as a basis for comparison due to its popularity.

9.1.1 Random initial time

Previously it was always assumed that the particles are subjected to the acoustic field at zero time and they are located precisely at the bottom pressure antinode:

$$y\left(t=0\right)=-\lambda/4 \tag{9.1}$$

However, in reality, the particles arrive at random relative time with respect to the start of the phase modulation period, and therefore not necessarily follow ideal trajectories for sorting as illustrated in Fig. 9.1. This figure uses exactly the same simulation parameters as Fig. 4.2a, but the arrival time is uniformly sampled over the interval (0, 2.5 s], that corresponds to a full modulation cycle with ramping and resting sections. The number of samples is 15. The 10 and 14.5 µm particle sets are denoted by shades of orange and green, respectively.

Two important conclusions can be drawn with the aid of the figure. Firstly, for certain arrival time (in this case approximately between 0.7 and 1.4 s), both the smaller and larger particles move downwards towards the $-y$ axis initially. If the device design places the inlet close to the bottom sidewall, the uneven pressure distribution due to the anechoic corner effect (Section 6.3.2) would drag particles to the wall and lower efficiency by trapping the larger particles at the bottom side and not letting them exit at the top outlet. The maximum negative displacement for large particles occurs for $t = 0.83$ s arrival time and is -27 µm.

Secondly, the large particles get shifted in two groups, as shown by the two green step-like curves in Fig. 9.1. The particles arriving before 0.7 s are transported immediately to the top pressure node and then further away with the next phase modulation cycle. However, particles arriving after 0.7 s first relax at the original pressure node after a transient behaviour, and only get shifted to the top pressure node during the second cycle. Therefore, the operating flow rate and device length cannot be designed for one phase modulation cycle: the sorting method inherently requires at least two phase modulation cycles to happen to the particles for high figure of merit sorting. Finally, particles getting pushed upwards multiple times, might stuck at the top channel sidewall and leave the device with a lower speed. This does not affect the figures of merit, but slows down the device operation.

9.1.2 Random particle position at inlet region

Precise focusing of the particle mixture at a given lateral position within the microchannel is challenging. Although small variation in position is possible by acoustic pre-focusing [138, 294], this stage requires additional substrate area and driving electronics. Usual hydrodynamic focusing methods result in moderate focusing region width [295]. To mimic the effect of the focusing, again the same sorting scenario

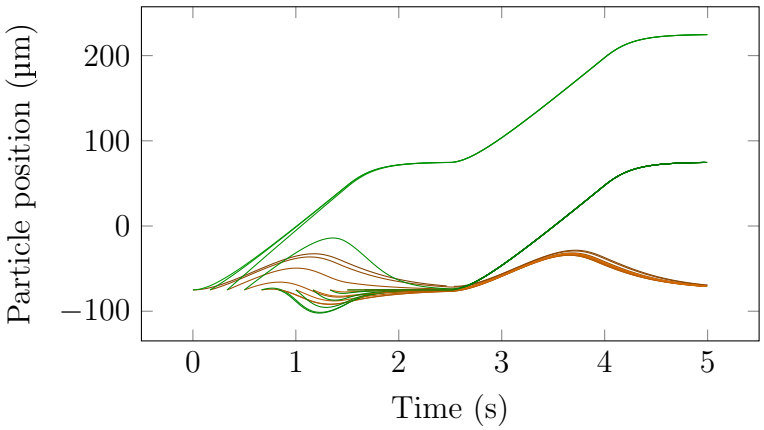

Figure 9.1: Particle trajectories for 10 and 14.5 µm PS particles with various start times with respect to the start of the ramping period. Shades of orange correspond to 10 µm particles, shades of green denote 14.5 µm particles

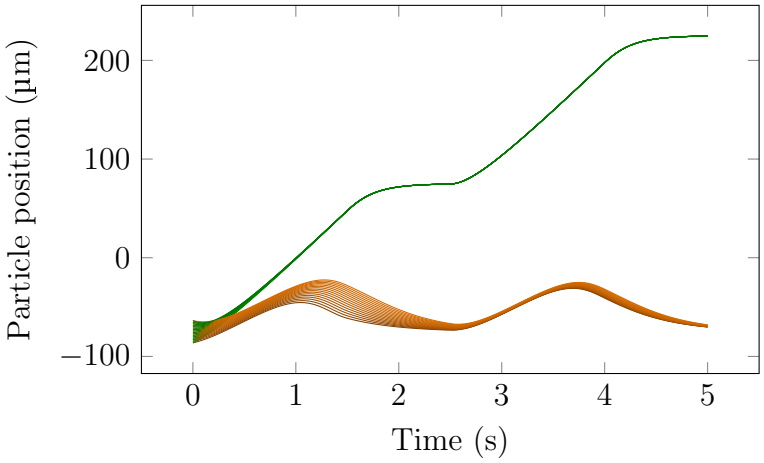

Figure 9.2: Particle trajectories for 10 and 14.5 µm PS particles with various initial y particle positions. Shades of orange correspond to 10 µm particles, shades of green denote 14.5 µm particles

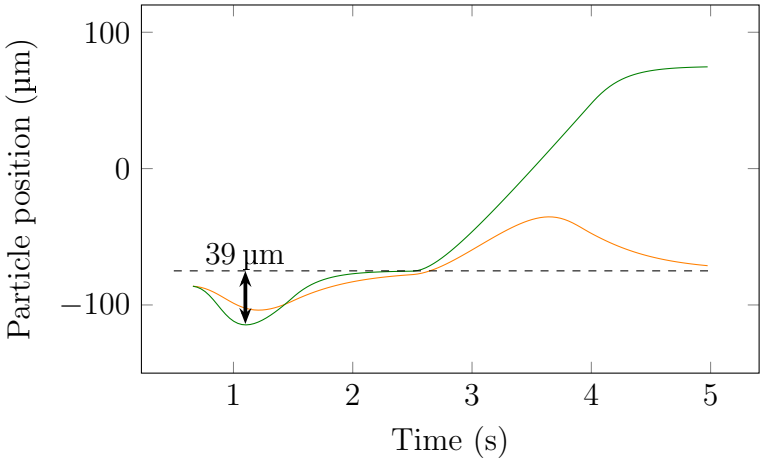

Figure 9.3: Particle trajectories for 10 (orange) and 14.5 µm (green) PS particles with $t = 0.66$ s start time and $y = -0.075\lambda/2$ initial particle position, resulting in the largest negative displacement of the large particles of −39 µm. Dashed line indicates a pressure node

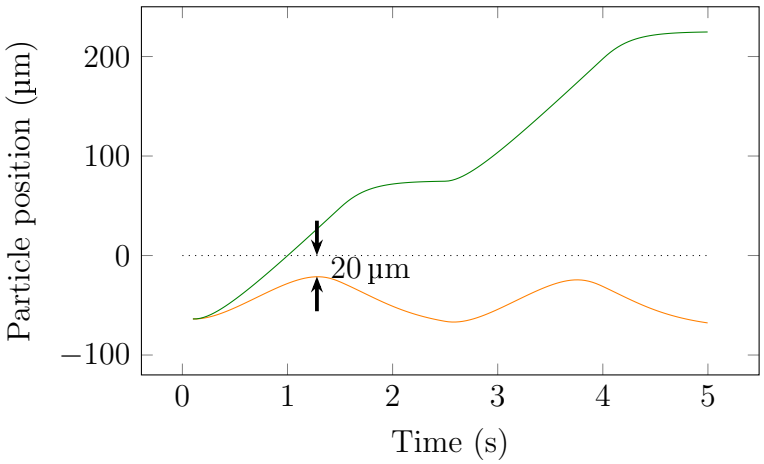

Figure 9.4: Particle trajectories for 10 (orange) and 14.5 µm (green) PS particles with $t = 0.1$ s start time and $y = 0.075\lambda/2$ initial particle position, resulting in the small particles locate closest to the antinode (dotted line) with 20 µm

is used as in Fig. 4.2a, but now the initial particle position is varied between -7.5 to 7.5% of half the wavelength. The results can be seen in Fig. 9.2, suggesting a larger particle trajectory spread for the smaller particles, for the worst case approaching the separation limit at the antinode ($y = 0$) by only 22 µm.

Combining the spatial and temporal variance, even higher displacement values can be observed towards the bottom wall for the large particles and towards the $y = 0$ limiting line for the small particles. In the above discussed case, for $t = 0.66$ s start time and $-0.075\lambda/2$ initial position the large particles gets displaced downwards by a maximum of -39 µm, which is 26% of the half wavelength separation distance between nodes (Fig. 9.3). The sensitivity of the small particle is much lower, even the largest displacement that occurs for these particles for the worst initial time and initial position approaches the antinodal line by an extra 2 µm only (Fig. 9.4) compared to the random position case.

As a summary, these results suggest that care must be taken when choosing the device dimensions. The length of the active separation area must accommodate two sorting cycles to allow transport of all large particles. Furthermore the width of the device and the inlet position must ensure that none of the large particles enters the anechoic corner even for the largest displacement towards $-y$.

Nominal diameter (µm)	Mean diameter (µm)	Standard deviation of diameter (µm)
4.5	4.52	0.15
5	4.97	0.06
6	5.9	0.29
10	10.1	0.7
15	15	1.05

Table 9.1: Mean particle diameter and standard deviation for numerical simulations

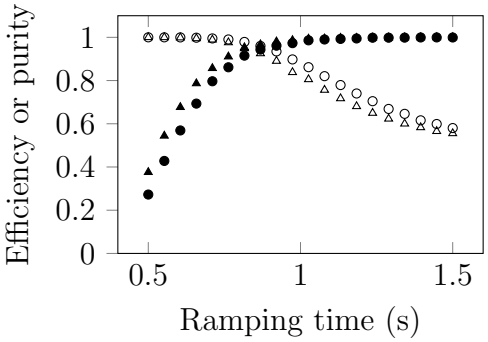

(a) 10 and 15 µm particle mixture

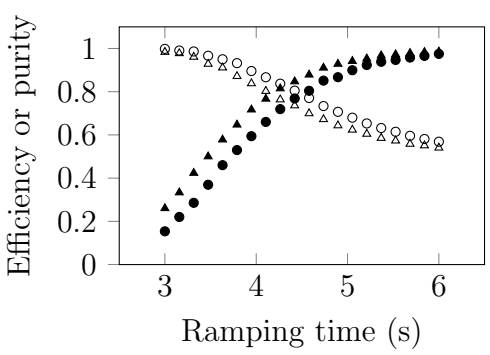

(b) 5 and 6 µm particle mixture

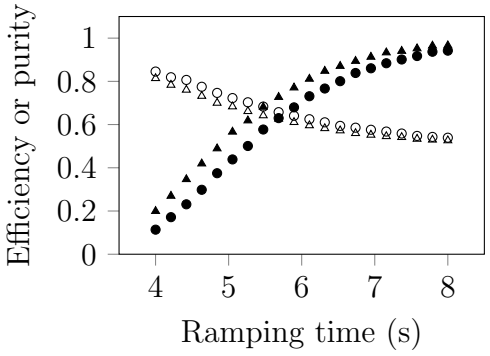

(c) 4.5 and 5 µm particle mixture

Figure 9.5: Efficiency (filled symbol) and purity (empty) values of continuous (disk shape) and jump (triangle shape) modulation sorting schemes for various ramping time and particle sets

9.2 Sensitivity of continuous and jump modulation methods

In the simplest case, the sensitivity analysis can be used in the absence of the fluid flow to compare the figures of merit and therefore performance of the continuous and jump modulation approaches. Making use of the analytical particle trajectory equations and their high computational speed, particle efficiency and purity in sorting applications can be investigated rapidly using Monte-Carlo simulations. These simulations attempt to describe real-life experiments in which the particle sizes are not all exactly equal to their nominal value. The particle mean sizes and

standard deviations are given in Table I as supplied by the manufacturer of these beads.

Based on the acoustic radiation force measurements for 23 V_{p-p} input voltage, the mean value of the acoustic pressure amplitude was found to be 96 kPa with a standard deviation of 10 kPa. The simulations were performed for 3 sets of polystyrene particles: 10-15, 5-6, and 4.5-5 µm with particle ratios of 1.5, 1.2, and 1.11, respectively. Ten thousand small and large particle trajectories were analysed for 20 different possible t_{ramp} values. Figure 9.5 shows that with increasing ramping time, generally efficiency increases, but purity decreases, which is due to an increased number of small particles being transported together with the large particles.

Comparing the 0° to 360° and -90° to 180° methods, for lower t_{ramp} times (faster sorting), the jump method offers up to 10% better sorting efficiency, with the purity being comparable. For higher t_{ramp} times (slower sorting), the linear phase modulation method offers up to 5% better purity while the efficiency remains similar for all particle mixtures. Generally, higher efficiency and faster sorting can be achieved using the -90° to 270° method while the linear phase modulation offers better purity. We can use the value of equal efficiency and purity as an overall figure of merit for establishing sorting. Both 10-15 and 5-6 µm sorting return high figures of merit, around 90% and 75%, respectively. Figure 9.5c shows that when the difference is less than 1 µm, the sorting becomes inefficient, as the purity drops significantly compared with the 5–6 µm mixture (Fig, 9.5b). The overall figure of merit in this case is 65%.

Furthermore, by these simulations the scaling laws presented theoretically in Section 4.1.2 are also validated. Taking the characteristic particle size for each case by the average of the two sizes, we obtain 12.5, 5.5 and 4.75 µm, respectively. The characteristic t_{ramp} time can be defined where purity and efficiency are equal, resulting in 0.87, 4.5 and 5.79 s, respectively. According to Eq. 4.11, γt_{ramp} is constant. Leaving out the experimental and material parameters (as they are the same for all particles), the equation simplifies to $a^2 t_{\text{ramp}}$. For the three cases it evaluates to 135.9, 136.1 and 130.6, verifying the scaling laws with less than 5% error.

9.3 Comparison of sensitivity of phase modulated and time-of-flight techniques

As a next step the sensitivity of the time-of-flight (ToF) and phase modulated (PM) methods are compared. First the investigated intrinsic and extrinsic parameters are presented, followed by a theoretical overview on the expected magnitude of sensitivity. Finally, Monte-Carlo simulations validate these theoretical predictions and emphasize the low variance of the figures of merit with extrinsic parameters using the phase modulated technique.

For a function f of several variables, x_1, ..., x_i, ..., x_n, the absolute sensitivity with respect to a single variable x_i is defined as [296]

$$\Delta f(x)_i = \frac{\partial f(x)}{\partial x_i} \Delta x_i \tag{9.2a}$$

$$\frac{\Delta f(x)_i}{f(x)} = \frac{\partial f(x)}{\partial x_i} \frac{x_i}{f(x)} \frac{\Delta x_i}{x_i} \tag{9.2b}$$

where the first equation was recast into a form that contains the relative error of the function f with respect to the relative error of variable x_i. Throughout the theoretical analysis of stability, the system is investigated one variable at a time and the above formula is used to obtain the relative error of particle trajectories given the partial derivative with respect to the variable in question and its relative error. This relative error of the final particle position is taken as an estimate of the sensitivity. To assess the quality of sorting, efficiency and purity are used as figures of merit as before.

9.3.1 Intrinsic parameters

The three intrinsic parameters investigated were the particle size (a), density (ρ_p) and compressibility (κ_p). During the manufacturing of microbeads, each of these vary randomly assuming nevertheless a Gaussian distribution, with well-defined mean and standard deviation [297].

As the ratio of the acoustic radiation and viscous drag forces is proportional to the square of the particle radius and proportional to the acoustic contrast factor (see Section 4.1.2 and in particular Eq. 4.11), a strong dependence on size and a moderate sensitivity to particle properties are expected. As the principle of sorting is similar in the time-of-flight (ToF) and phase modulated (PM) methods, no significant

difference in sensitivity on intrinsic particle properties is anticipated.

9.3.2 Extrinsic parameters

The three extrinsic parameters investigated were the flow rate (Q), acoustic energy density (E_{ac}) and focusing efficiency (or inlet width).

Increasing the flow rate results in particles exiting the device sooner and therefore being subjected to the acoustic field for a shorter time and being displaced by a smaller amount in the y-direction. Consequently, for the ToF method, we expect smaller number of target particles in the target region (reduced efficiency) and even smaller number of non-target particles (increased purity) with an increased flow rate. However, due to the periodic trapping of the PM method at the pressure nodes, and therefore stabilizing the position of the particles, we expect negligible dependence of any figure of merit on flow rate for the PM technique.

As the channel length has an equivalent effect on the sorting as changing the flow rate, the investigation of the channel length was excluded from the investigation.

The acoustic energy density has a similar effect to the flow rate: decreasing the energy density makes the particles travel less and consequently a drop in efficiency and increase in purity is observed. Due to the periodic forcing with the PM technique, again little influence of the energy density is expected. The acoustic radiation force has a direct dependence of energy density and quadratic dependence of pressure amplitude, and therefore it is worthwhile to investigate dependence of this parameter.

Finally, the focusing efficiency is expected to have a similar effect for both sorting methods: increasing the inlet width would lower purity and efficiency since the particles have a more dispersed initial position and would follow trajectories with a larger spread.

9.3.3 Analytical sensitivity of the time-of-flight method

To be able to assess sensitivity with respect to various parameters, the partial derivative of Eq. 2.7 is required with respect to all variables of interest:

$$\frac{\partial y(t)}{\partial t} = \frac{2c_{\mathrm{ac}} \tan(k_y y_0) \exp(\gamma t)}{c_{\mathrm{visc}} \left[\tan^2(k_y y_0) \exp^2(\gamma t) + 1\right]} \tag{9.3a}$$

$$\frac{\partial y(t)}{\partial \gamma} = \frac{t \tan(k_y y_0) \exp(\gamma t)}{k_y \left[\tan^2(k_y y_0) \exp^2(\gamma t) + 1\right]} \tag{9.3b}$$

$$\frac{\partial y(t)}{\partial c_{\mathrm{ac}}} = \frac{2t\tan(k_y y_0)\exp(\gamma t)}{c_{\mathrm{visc}}\left[\tan^2(k_y y_0)\exp^2(\gamma t)+1\right]} \tag{9.3c}$$

$$\frac{\partial y(t)}{\partial c_{\mathrm{visc}}} = -\frac{2c_{\mathrm{ac}}\tan(k_y y_0)\exp(\gamma t)}{c_{\mathrm{visc}}^2\left[\tan^2(k_y y_0)\exp^2(\gamma t)+1\right]} \tag{9.3d}$$

$$\frac{\partial y(t)}{\partial y_0} = \frac{\sec^2(k_y y_0\exp(\gamma t)}{\tan^2(k_y y_0)\exp^2(\gamma t)+1} \tag{9.3e}$$

where the last equation is the derivative with respect to the initial particle position.

To obtain numerical sensitivity values and be able to compare the effect of the different parameters, the same values that were applied in the simulation model were used as shown in Table 9.2. First, based on the energy density, frequency and particle properties, all variables are evaluated for the larger 10 µm sphere obtaining $c_{\mathrm{ac}} = 7.37\,\mathrm{nN}$ for the acoustic force constant, $c_{\mathrm{visc}} = 94.2\,\mu\mathrm{N}$ for the viscous force constant, $k_y = 20\,944\,\mathrm{m}^{-1}$ for the wave number on the surface. Using these, $\gamma = 3.28$, and assuming that the particle travels from the middle of the half inlet (0.0375λ) to the middle of the outlet (0.1875λ), the settling time evaluates to 0.7 s.

Firstly, the flow stability was investigated theoretically. Since the channel is more than twice wider than its height, and the flow speed is almost uniform towards the centreline of the channel [298], it was assumed that the flow variance can be directly approximated by time variance. First evaluating Eq. 9.3a we obtain $\partial y/\partial t = 55\,\mu\mathrm{m\,s}^{-1}$ and consequently $\Delta y/y = \partial y/\partial t{\cdot}\Delta t/t{\cdot}t/y = 0.69\Delta t/t$, or from the assumption that time variance is analogous to speed variance: $\Delta y/y = 0.69\Delta Q/Q$.

For stability against energy density, note that the acoustic force constant (c_{ac}) is directly proportional to the energy density. Therefore, stability against energy density is the same as against the acoustic force constant [296]. Using the same methodology as before, $\partial y/\partial c_{\mathrm{ac}} = 5.28\cdot 10^3\ \mathrm{m\,N}^{-1}$ and $\Delta y/y = \partial y/\partial c_{\mathrm{ac}}\cdot\Delta c_{\mathrm{ac}}/c_{\mathrm{ac}}\cdot c_{\mathrm{ac}}/y = 0.69\Delta c_{\mathrm{ac}}/c_{\mathrm{ac}}$, or $\Delta y/y = 0.69\Delta E_{\mathrm{ac}}/E_{\mathrm{ac}}$. This result is equivalent to the time (flow rate) dependence, which is expected, since t and c_{ac} appear equivalently in Eqs. 2.7, 9.3a and 9.3c.

For the final extrinsic parameter, the inlet focusing stability, direct substitution into Eq. 9.3e yields $\partial y/\partial y_0 = 1.56$, and therefore $\Delta y/y = \partial y/\partial y_0\cdot\Delta y_0/y_0\cdot y_0/y = 0.312\Delta y_0/y_0$.

For size dependence a similar technique as for the energy density can be used [296]. As γ is proportional to the square of the particle radius, $\partial\gamma/\partial a = 2\gamma/a$, and the size dependence can be obtained after calculating $\partial y/\partial\gamma = 1.19{\cdot}10^{-5}\mathrm{m\,s}$, and substituting into $\Delta y/y = \partial y/\partial\gamma\cdot\partial\gamma/\partial a\cdot a/y\cdot\Delta a/a = 1.38\Delta a/a$.

To approximate the density dependence, the derivative $\partial y/\partial \rho_\mathrm{p}$ should be calculated. Here we can simplify utilizing the proportionality between c_ac and Φ_AC. Therefore, in the chain rule $\partial y/\partial \rho_\mathrm{p} = \partial y/\partial c_\mathrm{ac} \cdot \partial c_\mathrm{ac}/\partial \Phi_\mathrm{AC} \cdot \partial \Phi_\mathrm{AC}/\partial \rho_\mathrm{p}$ the second term can be substituted by $c_\mathrm{ac}/\Phi_\mathrm{AC}$ [296] and as $\partial y/\partial c_\mathrm{ac}$ is known previously, only

$$\begin{aligned} \frac{\partial \Phi_\mathrm{AC}}{\partial \rho_\mathrm{p}} &= -\frac{3}{2}\cos 2\theta_\mathrm{r} \frac{6\rho_0}{(2\rho_\mathrm{p}+\rho_0)^2} \\ &\approx -6.74 \cdot 10^{-4}\ \mathrm{kg^3/m} \end{aligned} \tag{9.4}$$

needs to be derived. On substitution of the numerical values, one obtains $\partial y/\partial \rho_\mathrm{p} = -4.46 \cdot 10^{-8}\ \mathrm{m^4/kg}$ and $\Delta y/y = \partial y/\partial \rho_\mathrm{p} \cdot \rho_\mathrm{p}/y \cdot \Delta \rho_\mathrm{p}/\rho_\mathrm{p} = -0.833 \Delta \rho_\mathrm{p}/\rho_\mathrm{p}$.

A similar methodology applied for the compressibility dependence gives

$$\frac{\partial \Phi_\mathrm{AC}}{\partial \kappa_\mathrm{p}} = -\frac{1}{\kappa_0} \approx 2.2 \cdot 10^9\ \mathrm{Pa} \tag{9.5}$$

and consequently, applying the chain rule, $\partial y/\partial \kappa_\mathrm{p} = \partial y/\partial c_\mathrm{ac} \cdot c_\mathrm{ac}/\Phi_\mathrm{AC} \cdot \partial \Phi_\mathrm{AC}/\partial \kappa_\mathrm{p} = 1.46 \cdot 10^5\ \mathrm{N\,m^{-1}}$ and finally $\Delta y/y = \partial y/\partial \kappa_\mathrm{p} \cdot \kappa_\mathrm{p}/y \cdot \Delta \kappa_\mathrm{p}/\kappa_\mathrm{p} = 0.45 \Delta \kappa_\mathrm{p}/\kappa_\mathrm{p}$.

9.3.4 Simulation setup and parameters

Two such works were chosen as references for the techniques where the device dimensions and operating conditions were similar enough, that with minimal modifications, a direct comparison was possible. The time-of-flight method was implemented using the work from Jo and Guldiken [138], while for the phase modulation we relied on a work by Simon *et al.* [267,298]. Both references use 13.3 MHz operating frequency and a target outlet width that is half of the main channel width. There was a slight difference in channel height: 80 and 50 µm for the time-of-flight and for the phase modulated method, respectively. Therefore, in both models the average 65 µm was used. The inlet focusing is hydrodynamic with the PM and acoustic with the ToF technique; it was simply assumed that the sample inlet occupies 15% of the main channel width in both cases. Finally, the particles are considered to be perfectly suspended within the liquid and locate at the middle of the channel height.

For each simulation, 10,000 small 6 µm and 10,000 large 10 µm polystyrene particles were randomly dispersed within the inlet region. For the PM method, the particles entered the channel at a random time instant between 0 and t_ramp. The complete list of simulation parameters are shown in Table 9.2 for the two methods. The extrinsic parameters were simulated for 80% and 120% of their nominal values to

Symbol	Description	Value for ToF sorter	Value for PM sorter
f	Frequency	13.3 MHz	
c_s	Speed of sound on the lithium niobate surface	$3990\,\mathrm{m\,s^{-1}}$	
λ	Wavelength on the surface	300 µm	
	Width of channel	$\lambda/2 = 150\,\mu\mathrm{m}$	240 µm
	Height of channel	65 µm	
	Shadow zone width	39 µm	
	Length of active area	1.62 mm	3 mm
	Inlet width	22.5 µm	36 µm
	Inlet offset	0 µm	−55 µm
Q	Volumetric flow rate	$0.4\,\mu\mathrm{l\,min^{-1}} = 6.7\mathrm{e}{-12}\ \mathrm{m^3/s}$	
E_{ac}	Acoustic energy density	$1\,\mathrm{J/m^3}$	
t_{ramp}	Ramping time	-	1.7 s
t_{rest}	Resting time	-	1 s
ρ_0	Density of water	$998\,\mathrm{kg/m^3}$	
ρ_{PS}	Density of PS particle	$1050\,\mathrm{kg/m^3}$	
κ_0	Compressibility of water	$457\,\mathrm{TPa^{-1}}$	
κ_{PS}	Compressibility of PS particle	$172\,\mathrm{TPa^{-1}}$	
N	Number of simulations for each case	10000	
a_i	Particle radius	3 and 5 µm	

Table 9.2: Parameters used in the numerical simulation

obtain sensitivity for changes in both directions. For the intrinsic parameters, each of the 10,000 simulation steps used a physical property randomly selected following a Gaussian distribution with the nominal value as the mean and 20% of the nominal value as the standard deviation.

To take the anechoic corner effect (see Section 6.3.2) into consideration, the maximum width of the shadow zone was calculated, and with an additional 50% safety margin used as a freeze boundary condition in the simulations. This particle stop width in the channel in the simulations was 39 µm.

9.3.5 Results for the time-of-flight method

The simulation results for the time-of-flight method can be seen in Fig. 9.6a. As a quick summary of the analytical predictions, the relative error of the extrinsic parameters was estimated to have the following influence on sorting: 0.69, 0.69 and 0.312 for flow rate, energy density and inlet focusing, respectively. For the intrinsic parameters, the sensitivity values were 1.38, -0.833 and 0.45 for size, density and

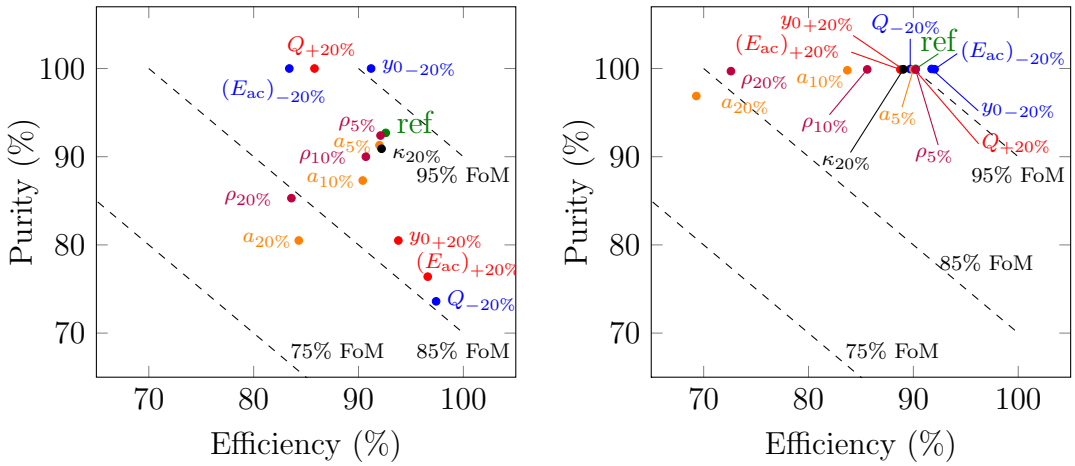

(a) Sensitivity of the time-of-flight method (b) Sensitivity of the phase modulated method

Figure 9.6: Sensitivity of the sorting efficiency and purity with variation of different extrinsic and intrinsic sorting parameters. Index: ref: reference simulation, Q: flow rate variation, E_{ac}: acoustic energy variation, y_0: inlet width variation. For these extrinsic simulations -20% denotes simulation runs with 80% of the nominal value, +20% denotes 120% of the nominal value. Furthermore, a: size variance, ρ: density variance, κ: compressibility variance

compressibility, respectively.

The simulation results are generally in good agreement with the predictions and expectations of Section 9.3.3 when considering the strength of the individual parameters. Increasing flow rate (point $Q_{+20\%}$ in Fig. 9.6a), decreasing energy density ($(E_{ac})_{-20\%}$) or inlet focusing ($(y_0)_{-20\%}$) all decrease efficiency and increase purity. For higher flow rate and lower energy density, the particles are not allowed to move enough in the y-direction, which explains this change. However, for reduced inlet width I believe the decrease in efficiency is explained by the antinode position near the particle initial position: the particles move slower towards the sidewalls and consequently efficiency drops. Change of these parameters in the opposite direction increases efficiency and drops purity. As shown in Fig. 9.6a, the change in purity is always more severe than the change in efficiency. Furthermore, the order of sensitivity of these parameters are in excellent agreement with the results of Section 9.3.3: highest sensitivity for flow rate and energy density, followed by a moderate sensitivity for inlet focusing.

Continuing with intrinsic parameters a more symmetric behaviour can be observed. All data points (a, ρ and κ) move towards the origin, and do not swing towards either the purity or efficiency side significantly. Again, excellent agreement with theoretical prediction can be seen: highest sensitivity is present for size change, followed by

density change and a negligible compressibility-dependence.

9.3.6 Results for the phase modulated method

Generally, the phase modulated method showed exceptional stability for most of the investigated parameters (Fig. 9.6b). As predicted, the method is virtually insensitive to changes in extrinsic parameters such as flow rate, acoustic energy density or inlet focusing, where the efficiency only changes by 3-4%. However, the method was more prone to changes in particle size or density, in both cases the efficiency lowers to about 70%. In these cases, the purity is still kept high, above 95%. Gao *et al.* argue that in microfluidic sorting devices, a higher purity is more important, as it allows direct detection of the sorted entities at the outlet without the need of post-processing [299].

9.4 Chapter summary

First in this chapter two factors have been introduced that can affect the phase modulated sorting method. As particles arrive at random times with respect to the modulation pattern, and they enter the channel with a spatial dispersion (i.e. at various y coordinates), they do not always follow the same trajectories. As a result, the device active length has to be long enough to accommodate two periods of the modulation signal for transporting all large particles to the target outlet. In certain cases large particles exhibit an initial negative displacement and therefore similar considerations shall be applied for the device width as it has to be large enough to ensure the particles avoiding the anechoic corner at the sides all times.

Secondly, the particle trajectory generation has been combined with pressure amplitude and particle size variation of Gaussian distribution to be able to estimate the purity and efficiency of the continuous and jump phase modulation techniques for various ramping time values. This investigation revealed superiority of the jump modulation when considering efficiency and superiority of the continuous method when considering purity as the more important figure of merit. Furthermore, the scaling law governing sorting and linking particle size and properties with t_{ramp} has been validated by the three different sorting scenarios.

Finally, the model has been extended to explicitly include the anechoic corner

using a freeze boundary condition within the region. Multiple intrinsic (size, density, compressibility) and extrinsic (flow rate, energy density, focusing efficiency) parameters have been taken into account for a final exhaustive comparison of the continuous phase modulation sorting technique and the time-of-flight approach. This investigation revealed excellent stability of the PM method against extrinsic parameters, but a better stability of efficiency for the time-of-flight method for intrinsic parameters.

Chapter 10

Summary and future work

In this thesis modulated ultrasound techniques have been investigated for particle and cell sorting applications in surface acoustic wave microfluidic devices. After a literature survey and an overview of the theoretical background of acoustic and fluidic phenomena, various phase and frequency modulated techniques have been suggested. Experimental and simulation validation of theoretical predictions, such as particle motion, scaling laws or differences in the proposed approaches, has been the principal motivation behind the work. Therefore, Chapters 4, 6, 7 and 8 strongly interconnect and support each other based on this trinity of theoretical, simulation and experimental work. Finally, Chapter 9 discusses uncertainties in experiments and models their effect on figures of merit using Monte-Carlo approach.

The main achievement of the thesis is development of a continuous flow acoustic sorter based on modulated ultrasonic signals that is highly reconfigurable for various particle and cell separations and can be made bidirectional as well allowing for bandpass sorting of medium-sized entities from a heterogeneous mixture. Representative sorting examples with their figures of merit are listed in Table 10.1 along with existing acoustic devices and techniques. This table reveals that for biological size-based separation, the modulated method offers better efficiency values and size discrimination at similar flow rates as others demonstrated [149], while slightly reducing purity. Density-based separation offers similar flow-rates and figures of merit as other works of the literature, however, in these publications an extremely high density contrast of particles or cells was used [138, 152].

Direct comparison of bandpass sorting with other works in challenging since these either use a multistage device [300] or travelling waves [170], where the particles

Sorting method / device type	Sorting parameters	Figures of merit
Frequency modulation, downwards, 14.5 and 10 µm PS	0.4 µl min^{-1}, 1.3 Hz frequency difference	Efficiency 94%, purity 87%
Frequency modulation, upwards, 14.5 and 10 µm PS	0.3 µl min^{-1}, 1.4 Hz frequency difference	Efficiency 94%, purity 81%
Frequency modulation, downwards, 6 and 5 µm PS	0.15 µl min^{-1}, 1.5 Hz frequency difference	Efficiency 71%, purity 78%
Frequency modulation, upwards, 6 and 5 µm PS	0.16 µl min^{-1}, 1.2 Hz frequency difference	Efficiency 67%, purity 73%
Frequency modulation, downwards, PS and FeO 10 µm	0.4 µl min^{-1}, 2.5 Hz frequency difference	Efficiency 97%, purity 93%
Frequency modulation, upwards, PS and FeO 10 µm PS	0.4 µl min^{-1}, 2.5 Hz frequency difference	Efficiency 98%, purity 91%
Frequency modulation, downwards, WBC/RBC	0.23 µl min^{-1}, 0.85 Hz frequency difference	Efficiency 94%, purity 84%
Frequency modulation, upwards, WBC/RBC	0.25 µl min^{-1}, 0.8 Hz frequency difference	Efficiency 88%, purity 93%
Standing surface wave, Nam *et al.* [149], platelet from blood	0.25 µl min^{-1} flow rate	Efficiency 74.1%, purity 99.9%
Standing surface wave, Nam *et al.* [152], alginate beads filled with cells (density-based)	8 µl min^{-1} sample flow rate	Efficiency: 97%, purity: 99%
Standing surface wave, Jo and Guldiken [138], 10 µm PS, melamine	up to 2 µl min^{-1}	Efficiency: 98.8%, purity: n/a

Table 10.1: Summary of the performance of acoustic sorting methods

exhibit strong frequency-dependent behaviour. In contrast, in my device a single transducer stage allows for tunable bandpass sorting, achieving 75% efficiency of 10 µm PS particle separation while removing 85% of 6 µm PS and 14.5 µm PS particles.

Simulation of secondary radiation force showed this force is generally 3-4 orders of magnitude smaller than the primary radiation force. However, in certain cases, for example when the positive contrast particles momentarily locate in the vicinity of the pressure antinode, this force can be a few percent of the primary radiation force, altering particle trajectories and in worst case causing particle clump formation. Care must be taken when the transient zones within a device are designed.

Monte-Carlo simulations of the modulated and the traditional time-of-flight methods were carried out to reveal sensitivity. This investigation revealed excellent stability of the modulated method against extrinsic parameters (flow rate, energy density, focusing efficiency), but a better stability of efficiency for the time-of-flight method for intrinsic parameters (size, density, compressibility). Purity variance of the modulated method was negligible, and the worst-case efficiency drop was of 20%.

Although the thesis forms a coherent unit with the achieved results, there is room for improvement or extension in various aspects. These have not been carried out mainly due to time limitations, therefore the proposed elements of future work should all be feasible to investigate with reasonable expansion of existing methods or models.

- The experiments were carried out in an asymmetric inlet configuration device with relatively narrow channel width. A wider channel with symmetric inlet configuration should in theory minimise the particle loss due to focussing problems and allow for higher figures of merit

- In addition, an acoustic pre-focussing stage could be used prior to sorting to even better localise the initial position of particles

- A wider channel with multiple outlets (more than the current 2) could be used to sort particle mixtures with even higher freedom to arbitrary outlet selection: instead of the currently used one or two modulation cycles, more cycles could provide greater flexibility

- The discussed simulation model for secondary radiation force could be verified by experiments both for spherical particles, or non-spherical entities, such as

red blood cells

- Investigation of a higher throughput device is essential for biological applications — this could either be feasible by a special surface wave device with multiple parallel channels and a single excitation, or by bulk devices using PMMA or similar materials

- The Monte-Carlo simulation models could be coupled with machine learning approaches for enhanced device design

Appendix A

Calculation of secondary radiation force potential

According to Gorkov's potential theory, the acoustic radiation potential of any arbitrary field, except a plane travelling wave, can be obtained as:

$$U(\mathbf{r}) = a_{\mathrm{p}}^3 \pi \rho_0 \left[\frac{f_{1,\mathrm{p}}}{3} k^2 \left| \phi_{\mathrm{total}}(\mathbf{r}) \right|^2 - \frac{f_{2,\mathrm{p}}}{2} k^2 \left| \nabla_{\mathrm{p}} \phi_{\mathrm{total}}(\mathbf{r}) \right|^2 \right] \tag{A.1}$$

Moreover, in our case, the total velocity potential is the sum of the velocity potential of the external field and the re-scattered field

$$\phi_{\mathrm{total}}(\mathbf{r}, t) = \phi_{\mathrm{ext}}(\mathbf{r}, t) + \phi_{\mathrm{sc}}(\mathbf{r}, t) \tag{A.2}$$

Neglecting time dependence, for complex fields

$$\begin{aligned} \left| \phi_{\mathrm{total}}(\mathbf{r}) \right|^2 &= \left| \phi_{\mathrm{ext}}(\mathbf{r}) + \phi_{\mathrm{sc}}(\mathbf{r}) \right|^2 = \left(\phi_{\mathrm{ext}}(\mathbf{r}) + \phi_{\mathrm{sc}}(\mathbf{r}) \right)^* \left(\phi_{\mathrm{ext}}(\mathbf{r}) + \phi_{\mathrm{sc}}(\mathbf{r}) \right) \\ &= \phi_{\mathrm{ext}}(\mathbf{r})^* \phi_{\mathrm{ext}}(\mathbf{r}) + \phi_{\mathrm{ext}}(\mathbf{r})^* \phi_{\mathrm{sc}}(\mathbf{r}) + \phi_{\mathrm{sc}}(\mathbf{r})^* \phi_{\mathrm{ext}}(\mathbf{r}) + \phi_{\mathrm{sc}}(\mathbf{r})^* \phi_{\mathrm{ext}}(\mathbf{r}) \end{aligned} \tag{A.3}$$

Here the first term corresponds to the primary radiation potential, the last term is small compared to the second and third. Moreover, generally

$$\mathrm{Re}[a^* b] = \mathrm{Re}[a b^*] \tag{A.4}$$

and therefore the second and third term can be contracted

$$\phi_{\mathrm{ext}}(\mathbf{r})^* \phi_{\mathrm{sc}}(\mathbf{r}) + \phi_{\mathrm{sc}}(\mathbf{r})^* \phi_{\mathrm{ext}}(\mathbf{r}) = 2\mathrm{Re}[\phi_{\mathrm{ext}}(\mathbf{r})^* \phi_{\mathrm{sc}}(\mathbf{r})] \tag{A.5}$$

and the potential of the secondary acoustic field can be approximated as

$$U_{\mathrm{sec}}(\mathbf{r}) = 2 a_{\mathrm{p}}^3 \pi \rho_0 \left[\frac{f_{1,\mathrm{p}}}{3} k^2 \mathrm{Re}[\phi_{\mathrm{ext}}(\mathbf{r})^* \phi_{\mathrm{sc}}(\mathbf{r})] - \frac{f_{2,\mathrm{p}}}{2} \mathrm{Re}[\nabla_{\mathrm{p}}^2 \phi_{\mathrm{ext}}(\mathbf{r})^* \phi_{\mathrm{sc}}(\mathbf{r})] \right] \tag{A.6}$$

or equivalently

$$U_{\mathrm{sec}}(\mathbf{r}) = \pi k^2 a_{\mathrm{p}}^3 \rho_0 \mathrm{Re}\left[\frac{2f_{1,\mathrm{p}}}{3}\phi_{\mathrm{ext}}(\mathbf{r})^*\phi_{\mathrm{sc}}(\mathbf{r}) - f_{2,\mathrm{p}}\frac{1}{k}\nabla_{\mathrm{p}}\phi_{\mathrm{ext}}(\mathbf{r})^*\frac{1}{k}\nabla_{\mathrm{p}}\phi_{\mathrm{sc}}(\mathbf{r})\right]$$
$$= U_{\mathrm{sec,A}} - U_{\mathrm{sec,B}} \tag{A.7}$$

The scattered velocity potential is given generally as

$$\phi_{\mathrm{sc}}(\mathbf{r}_{\mathrm{p}}|\mathbf{r}_{\mathrm{s}}) = i f_{1,\mathrm{s}}\frac{a_{\mathrm{s}}^3\omega}{3\rho_0}\frac{\rho_{\mathrm{in}}(\mathbf{r}_{\mathrm{s}})e^{ikR_{\mathrm{ps}}}}{R_{\mathrm{ps}}} - f_{2,\mathrm{s}}\frac{a_{\mathrm{s}}^3}{2}\boldsymbol{\nabla}_{\mathrm{p}}\cdot\left[\frac{\mathbf{u}_{\mathrm{in}}(\mathbf{r}_{\mathrm{s}})e^{ikR_{\mathrm{ps}}}}{R_{\mathrm{ps}}}\right] + O\left[\frac{(ka_{\mathrm{s}})^5}{(kR_{\mathrm{ps}})^3}\right] \tag{A.8a}$$

$$\phi_{\mathrm{sc}}(\mathbf{r}_{\mathrm{p}}|\mathbf{r}_{\mathrm{s}}) = \phi_{\mathrm{sc},1}(\mathbf{r}_{\mathrm{p}}|\mathbf{0}) - \phi_{\mathrm{sc},2}(\mathbf{r}_{\mathrm{p}}|\mathbf{0}) = \phi_{\mathrm{sc},1} - \phi_{\mathrm{sc},2} \tag{A.8b}$$

where ρ_{in} and $\mathbf{u}_{\mathrm{in}}$ are the acoustic density and velocity of the external field. Since the velocity potential of the external field is pure real, its complex conjugate is itself

$$\phi_{\mathrm{in}}^* = \phi_{\mathrm{in}} = \frac{u_0}{k}\sin\left[k\left(r\cos\theta - h_{\mathrm{n}}\right)\right] \tag{A.9}$$

and therefore its gradient

$$\mathbf{u}_{\mathrm{in}} = \boldsymbol{\nabla}_{\mathrm{p}}\phi_{\mathrm{in}} = \boldsymbol{\nabla}_{\mathrm{p}}\phi_{\mathrm{in}}^* = u_0\cos\left[k\left(r\cos\theta - h_{\mathrm{n}}\right)\right]\left\{\cos\theta\hat{\mathbf{r}} - \sin\theta\hat{\boldsymbol{\theta}}\right\} \tag{A.10}$$

Furthermore the acoustic density is

$$\rho_{\mathrm{in}} = \frac{i\omega\rho_0}{c_0^2}\frac{u_0}{k}\sin\left[k\left(r\cos\theta - h_{\mathrm{n}}\right)\right] \tag{A.11}$$

So the first term of Eq. A.8 at the origin (where the scatterer is) with its real part:

$$\phi_{\mathrm{sc},1} = i f_{1,\mathrm{s}}\frac{a_{\mathrm{s}}^3\omega}{3\rho_0}\frac{\rho_{\mathrm{in}}(\mathbf{r}_{\mathrm{s}})e^{ikR_{\mathrm{ps}}}}{R_{\mathrm{ps}}} = f_{1,\mathrm{s}}\frac{a_{\mathrm{s}}^3k^2}{3}\frac{u_0\sin(kh_{\mathrm{n}})e^{ikR_{\mathrm{ps}}}}{R_{\mathrm{ps}}} \tag{A.12a}$$

$$\mathrm{Re}\left\{\phi_{\mathrm{sc},1}\right\} = f_{1,\mathrm{s}}\frac{a_{\mathrm{s}}^3k^2}{3}\frac{u_0\sin(kh_{\mathrm{n}})\cos(kR_{\mathrm{ps}})}{R_{\mathrm{ps}}} \tag{A.12b}$$

For the second term of Eq. A.8 first

$$\boldsymbol{\nabla}\cdot\left[\frac{\mathbf{u}_{\mathrm{in}}(\mathbf{r}_{\mathrm{s}})e^{ikR_{\mathrm{ps}}}}{R_{\mathrm{ps}}}\right] = u_0\cos\theta\cos(kh_{\mathrm{n}})\left[\frac{1}{R_{\mathrm{ps}}^2} + \frac{ik}{R_{\mathrm{ps}}}\right]e^{ikR_{\mathrm{ps}}} - \frac{2u_0\cos\theta\cos(kh_{\mathrm{n}})}{R_{\mathrm{ps}}^2}e^{ikR_{\mathrm{ps}}}$$
$$= u_0\cos\theta\cos(kh_{\mathrm{n}})\left[\frac{ik}{R_{\mathrm{ps}}} - \frac{1}{R_{\mathrm{ps}}^2}\right]e^{ikR_{\mathrm{ps}}} \tag{A.13}$$

has to be obtained to arrive at the second term of Eq. A.8

$$\phi_{\mathrm{sc},2} = f_{2,\mathrm{s}}\frac{a_{\mathrm{s}}^3}{2}u_0\cos\theta\cos(kh_{\mathrm{n}})\left[\frac{ik}{R_{\mathrm{ps}}} - \frac{1}{R_{\mathrm{ps}}^2}\right]e^{ikR_{\mathrm{ps}}} \tag{A.14a}$$

$$\mathrm{Re}\left\{\phi_{\mathrm{sc},2}\right\} = -f_{2,\mathrm{s}}\frac{a_\mathrm{s}^3}{2}k^2u_0\cos\theta\cos(kh_\mathrm{n})\left[\frac{\sin(kR_\mathrm{ps})}{kR_\mathrm{ps}}+\frac{\cos(kR_\mathrm{ps})}{(kR_\mathrm{ps})^2}\right] \tag{A.14b}$$

As the first term of the secondary radiation potential, Eq. A.7, depends on the velocity potential of the external field, which is real, and the real parts of the scattered velocity potential are given by Eqs. A.12b and A.14b, $U_{\mathrm{sec,A}}$ can be obtained:

$$\begin{aligned}
U_{\mathrm{sec,A}} &= \pi k^2 a_\mathrm{p}^3\rho_0\mathrm{Re}\left[\frac{2f_{1,\mathrm{p}}}{3}\phi_\mathrm{ext}^*\phi_\mathrm{sc}\right] = \pi k^2 a_\mathrm{p}^3\rho_0\frac{2f_{1,\mathrm{p}}}{3}\phi_\mathrm{ext}^*\mathrm{Re}\left[\phi_{\mathrm{sc},1}-\phi_{\mathrm{sc},2}\right]\\
&= \pi k^2 a_\mathrm{p}^3\rho_0\frac{2f_{1,\mathrm{p}}}{3}\frac{u_0}{k}\sin\left[k(r\cos\theta-h_\mathrm{n})\right]\left\{f_{1,\mathrm{s}}\frac{a_\mathrm{s}^3k^2}{3}\frac{u_0\sin(kh_\mathrm{n})\cos(kR_\mathrm{ps})}{kR_\mathrm{ps}}\right.\\
&\left.+\, f_{2,\mathrm{s}}\frac{a_\mathrm{s}^3}{2}k^2u_0\cos\theta\cos(kh_\mathrm{n})\left(\frac{\sin(kR_\mathrm{ps})}{kR_\mathrm{ps}}+\frac{\cos(kR_\mathrm{ps})}{(kR_\mathrm{ps})^2}\right)\right\}\\
&= \frac{1}{2}\pi k^3 a_\mathrm{p}^3 a_\mathrm{s}^3\rho_0 u_0^2\frac{2f_{1,\mathrm{p}}}{3}\sin\left[k(r\cos\theta-h_\mathrm{n})\right]\left\{\frac{2}{3}f_{1,\mathrm{s}}\frac{\sin(kh_\mathrm{n})\cos(kR_\mathrm{ps})}{kR_\mathrm{ps}}\right.\\
&\left.+\, f_{2,\mathrm{s}}\cos\theta\cos(kh_\mathrm{n})\left(\frac{\sin(kR_\mathrm{ps})}{kR_\mathrm{ps}}+\frac{\cos(kR_\mathrm{ps})}{(kR_\mathrm{ps})^2}\right)\right\}
\end{aligned} \tag{A.15}$$

The second term of the secondary potential Eq. A.7 can be obtained on splitting the scattered potential for convenience:

$$U_{\mathrm{sec,B}} = \pi a_\mathrm{p}^3\rho_0 f_{2,\mathrm{p}}\mathrm{Re}\left[\boldsymbol{\nabla}_\mathrm{p}\phi_\mathrm{ext}^*(\mathbf{r}_\mathrm{p})\cdot\boldsymbol{\nabla}_\mathrm{p}\phi_\mathrm{sc}(\mathbf{r}_\mathrm{p})\right] \tag{A.16a}$$

$$\begin{aligned}
\mathrm{Re}\left[\boldsymbol{\nabla}_\mathrm{p}\phi_\mathrm{ext}^*(\mathbf{r}_\mathrm{p})\cdot\boldsymbol{\nabla}_\mathrm{p}\phi_\mathrm{sc}(\mathbf{r}_\mathrm{p})\right] &= \mathrm{Re}\left[\boldsymbol{\nabla}_\mathrm{p}\phi_\mathrm{ext}^*(\mathbf{r}_\mathrm{p})\cdot\boldsymbol{\nabla}_\mathrm{p}\phi_{\mathrm{sc,A}}(\mathbf{r}_\mathrm{p})\right]-\\
&\mathrm{Re}\left[\boldsymbol{\nabla}_\mathrm{p}\phi_\mathrm{ext}^*(\mathbf{r}_\mathrm{p})\cdot\boldsymbol{\nabla}_\mathrm{p}\phi_{\mathrm{sc,B}}(\mathbf{r}_\mathrm{p})\right]
\end{aligned} \tag{A.16b}$$

Equation A.16, requires the calculation of some auxiliary terms (the gradient of the scattered velocity potential for both terms)

$$\boldsymbol{\nabla}_\mathrm{p}\phi_{\mathrm{sc,A}}(\mathbf{r}_\mathrm{p}) = f_{1,\mathrm{s}}\frac{a_\mathrm{s}^3}{3}v_0\sin(kh_\mathrm{n})\left[\frac{ikR_\mathrm{ps}-1}{R_\mathrm{ps}^2}\right]e^{ikR_\mathrm{ps}}\hat{\mathbf{r}} \tag{A.17a}$$

$$\begin{aligned}
\boldsymbol{\nabla}_\mathrm{p}\phi_{\mathrm{sc,B}}(\mathbf{r}_\mathrm{p}) =& f_{2,\mathrm{s}}\frac{a_\mathrm{s}^3}{2}v_0\cos(kh_\mathrm{n})\frac{e^{ikR_\mathrm{ps}}}{R_\mathrm{ps}^3}\left\{-\cos\theta\left((kR_\mathrm{ps})^2+2ikR_\mathrm{ps}-2\right)\hat{\mathbf{r}}\right.\\
&\left.-\sin\theta\left(ikR_\mathrm{ps}-1\right)\hat{\boldsymbol{\theta}}\right\}
\end{aligned} \tag{A.17b}$$

And consequently, the first term of Eq. A.16 with its real part

$$\begin{aligned}
&\boldsymbol{\nabla}_\mathrm{p}\phi_\mathrm{ext}^*(\mathbf{r}_\mathrm{p})\cdot\boldsymbol{\nabla}_\mathrm{p}\phi_{\mathrm{sc,A}}(\mathbf{r}_\mathrm{p})\\
&\qquad = u_0\cos\theta\cos\left[k(r\cos\theta-h_\mathrm{n})\right]f_{1,\mathrm{s}}\frac{a_\mathrm{s}^3k}{3}u_0\sin(kh_\mathrm{n})\left[\frac{ikR_\mathrm{ps}-1}{R_\mathrm{ps}^2}\right]e^{ikR_\mathrm{ps}}
\end{aligned} \tag{A.18a}$$

$$\begin{aligned}
&\mathrm{Re}\left[\boldsymbol{\nabla}_\mathrm{p}\phi_\mathrm{ext}^*(\mathbf{r}_\mathrm{p})\cdot\boldsymbol{\nabla}_\mathrm{p}\phi_{\mathrm{sc,A}}(\mathbf{r}_\mathrm{p})\right]\\
&\qquad = -u_0^2 f_{1,\mathrm{s}}\frac{a_\mathrm{s}^3k}{3}\cos\theta\sin(kh_\mathrm{n})\left\{\frac{\sin kr}{kr}+\frac{\cos kr}{(kr)^2}\right\}
\end{aligned} \tag{A.18b}$$

and the second term of Eq. A.16 with its real part

$$\boldsymbol{\nabla}_{\mathrm{p}}\phi^{*}_{\mathrm{ext}}(\mathbf{r}_{\mathrm{p}})\cdot\boldsymbol{\nabla}_{\mathrm{p}}\phi_{\mathrm{sc,B}}(\mathbf{r}_{\mathrm{p}}) = u_0\cos\left[k(r\cos\theta-h_{\mathrm{n}})\right]f_{2,\mathrm{s}}\frac{a_{\mathrm{s}}^3k}{2}u_0 \cos(kh_{\mathrm{n}})\frac{e^{ikR_{\mathrm{ps}}}}{R_{\mathrm{ps}}^3}\left\{-\cos\theta\left((kR_{\mathrm{ps}})^2+2ikR_{\mathrm{ps}}-2\right)\hat{\mathbf{r}}\right\} \tag{A.19a}$$

$$\begin{aligned}\mathrm{Re}\left[\boldsymbol{\nabla}_{\mathrm{p}}\phi^{*}_{\mathrm{ext}}(\mathbf{r}_{\mathrm{p}})\cdot\boldsymbol{\nabla}_{\mathrm{p}}\phi_{\mathrm{sc,B}}(\mathbf{r}_{\mathrm{p}})\right] = u_0\cos\left[k(r\cos\theta-h_{\mathrm{n}})\right]f_{2,\mathrm{s}}\frac{a_{\mathrm{s}}^3}{2}u_0\cos(kh_{\mathrm{n}})\\ \left\{-\frac{\cos^2\theta\cos kr}{r^3}\left((kr)^2-2\right)-\frac{\sin^2\theta\cos kr}{r^3}\right.\\ \left.+\frac{2kr\sin kr\cos^2\theta}{r^3}-\frac{kr\sin^2\theta\sin kr}{r^3}\right\}\end{aligned} \tag{A.19b}$$

After simplification and using

$$2\cos^2\theta-\sin^2\theta=\frac{1+3\cos 2\theta}{2} \tag{A.20}$$

The real part Eq. A.19b can be written as

$$\begin{aligned}\mathrm{Re}\left[\boldsymbol{\nabla}_{\mathrm{p}}\phi^{*}_{\mathrm{ext}}(\mathbf{r}_{\mathrm{p}})\cdot\boldsymbol{\nabla}_{\mathrm{p}}\phi_{\mathrm{sc,B}}(\mathbf{r}_{\mathrm{p}})\right] =& u_0^2f_{2,\mathrm{s}}\frac{a_{\mathrm{s}}^3}{4}\cos\left[k(r\cos\theta-h_{\mathrm{n}})\right]\cos(kh_{\mathrm{n}})\\ &\left\{\frac{\cos kr}{(kr)^3}(1+3\cos 2\theta)-\frac{2\cos^2\theta\cos kr}{kr}\right.\\ &\left.+\frac{\sin kr}{(kr)^2}(1+3\cos 2\theta)\right\}\end{aligned} \tag{A.21}$$

At this point everything is known to obtain $U_{\mathrm{sec,B}}$ by Eqs. A.18b and A.21:

$$\begin{aligned}U_{\mathrm{sec,B}} =& -u_0^2\pi a_{\mathrm{p}}^3a_{\mathrm{s}}^3\rho_0f_{2,\mathrm{p}}k^3\cos\left[k(r\cos\theta-h_{\mathrm{n}})\right]\\ &\left[\frac{f_{1,\mathrm{s}}}{3}\cos\theta\sin(kh_{\mathrm{n}})\left\{\frac{\sin kr}{kr}+\frac{\cos kr}{(kr)^2}\right\}+\frac{f_{2,\mathrm{s}}}{4}\cos(kh_{\mathrm{n}})\right.\\ &\left.\left\{\frac{\cos kr}{(kr)^3}(1+3\cos 2\theta)-\frac{2\cos^2\theta\cos kr}{kr}+\frac{\sin kr}{(kr)^2}(1+3\cos 2\theta)\right\}\right]\end{aligned} \tag{A.22}$$

Finally Eqs. A.15 and A.22 yield the secondary radiation potential:

$$\begin{aligned}U_{\mathrm{sec}}(r,\theta) =& \pi E_0k^3a_{\mathrm{p}}^3a_{\mathrm{s}}^3\left(\cos\left[k(r\cos\theta-h_{\mathrm{n}})\right]\frac{f_{2,\mathrm{p}}}{2}\left\{f_{1,\mathrm{s}}\cos(kh_{\mathrm{n}})(1+3\cos 2\theta)\frac{\cos kr}{(kr)^3}\right.\right.\\ &+\left[\frac{4}{3}f_{1,\mathrm{s}}\sin(kh_{\mathrm{n}})\cos\theta\cos kr+f_{2,\mathrm{s}}\cos(kh_{\mathrm{n}})(1+3\cos 2\theta)\sin kr\right]\frac{1}{(kr)^2}\\ &\left.-\left[f_{2,\mathrm{s}}\cos(kh_{\mathrm{n}})(1+\cos 2\theta)\cos kr-\frac{4}{3}f_{1,\mathrm{s}}\sin(kh_{\mathrm{n}})\cos\theta\sin kr\right]\frac{1}{kr}\right\}\\ &+\sin\left[k(r\cos\theta-h_{\mathrm{n}})\right]\frac{2f_{1,\mathrm{p}}}{3}\left\{f_{2,\mathrm{s}}\cos(kh_{\mathrm{n}})\cos\theta\frac{\cos kr}{(kr)^2}\right.\\ &\left.\left.+\left[\frac{2}{3}f_{1,\mathrm{s}}\sin(kh_{\mathrm{n}})\cos kr+f_{2,\mathrm{s}}\cos(kh_{\mathrm{n}})\cos\theta\sin kr\right]\frac{1}{kr}\right\}\right)\end{aligned} \tag{A.23}$$

In the above derivation R_{ps} is equivalent to r as the scatterer is at the origin.

Appendix B

Radial and tangential components of the secondary radiation force

First, Eq. 3.34 has to be expanded and regrouped in order to facilitate calculating partial derivatives of r and θ.

B.1 Radial direction

The partials of different terms containing r are the following (for shorthand notation the argument $k\left(r\cos\theta - h_n\right)$ is omitted):

$$\frac{\partial}{\partial r}\left(\frac{\cos kr}{(kr)^3}\cos[\,]\right) = -\frac{3k\cos kr}{(kr)^4}\cos[\,] - \frac{k\sin kr}{(kr)^3}\cos[\,] - \frac{k\cos\theta\cos kr}{(kr)^3}\sin[\,] \tag{B.1a}$$

$$\frac{\partial}{\partial r}\left(\frac{\cos kr}{(kr)^2}\cos[\,]\right) = -\frac{2k\cos kr}{(kr)^3}\cos[\,] - \frac{k\sin kr}{(kr)^2}\cos[\,] - \frac{k\cos\theta\cos kr}{(kr)^2}\sin[\,] \tag{B.1b}$$

$$\frac{\partial}{\partial r}\left(\frac{\sin kr}{(kr)^2}\cos[\,]\right) = -\frac{2k\sin kr}{(kr)^3}\cos[\,] + \frac{k\cos kr}{(kr)^2}\cos[\,] - \frac{k\cos\theta\sin kr}{(kr)^2}\sin[\,] \tag{B.1c}$$

$$\frac{\partial}{\partial r}\left(\frac{\cos kr}{kr}\cos[\,]\right) = -\frac{k\cos kr}{(kr)^2}\cos[\,] - \frac{k\sin kr}{kr}\cos[\,] - \frac{k\cos\theta\cos kr}{kr}\sin[\,] \tag{B.1d}$$

$$\frac{\partial}{\partial r}\left(\frac{\sin kr}{kr}\cos[\,]\right) = -\frac{k\sin kr}{(kr)^2}\cos[\,] + \frac{k\cos kr}{kr}\cos[\,] - \frac{k\cos\theta\sin kr}{kr}\sin[\,] \tag{B.1e}$$

$$\frac{\partial}{\partial r}\left(\frac{\cos kr}{(kr)^2}\sin[\,]\right) = -\frac{2k\cos kr}{(kr)^3}\sin[\,] - \frac{k\sin kr}{(kr)^2}\sin[\,] + \frac{k\cos\theta\cos kr}{(kr)^2}\cos[\,] \tag{B.1f}$$

$$\frac{\partial}{\partial r}\left(\frac{\cos kr}{kr}\sin[\,]\right) = -\frac{k\cos kr}{(kr)^2}\sin[\,] - \frac{k\sin kr}{kr}\sin[\,] + \frac{k\cos\theta\cos kr}{kr}\cos[\,] \tag{B.1g}$$

$$\frac{\partial}{\partial r}\left(\frac{\sin kr}{kr}\sin[\,]\right) = -\frac{k\sin kr}{(kr)^2}\sin[\,] + \frac{k\cos kr}{kr}\sin[\,] + \frac{k\cos\theta\sin kr}{kr}\cos[\,] \tag{B.1h}$$

From these the radiation force in the radial direction is

$$\begin{aligned}
F_r = \pi E_0 k^3 a_p^3 a_s^3 \Bigg\{ & \frac{f_{1,p}}{2}\cos\left[k\left(r\cos\theta - h_n\right)\right]\Bigg\{ f_{1,s}\cos kh_n\left(1+3\cos 2\theta\right)\left[\frac{3k\cos kr}{(kr)^4}\right. \\
& \left. + \frac{3k\sin kr}{(kr)^3} - \frac{k\cos kr}{(kr)^2}\right] + \frac{4}{3}f_{0,s}\sin kh_n\cos\theta\left[\frac{2k\cos kr}{(kr)^3} + \frac{2k\sin kr}{(kr)^2} - \frac{k\cos kr}{kr}\right] \\
& - f_{1,s}\cos kh_n\left(1+\cos 2\theta\right)\left[\frac{k\cos kr}{(kr)^2} + \frac{k\sin kr}{kr}\right]\Bigg\} + \frac{2f_{0,p}}{3}\cos\left[k\left(r\cos\theta - h_n\right)\right]\Bigg\{ \\
& f_{1,s}\cos kh_n\cos\theta\left[-\frac{k\cos\theta\cos kr}{(kr)^2} - \frac{k\cos\theta\sin kr}{kr}\right] + \frac{2}{3}f_{0,s}\sin kh_n\left[-\frac{k\cos\theta\cos kr}{kr}\right]\Bigg\} \\
& + \frac{f_{1,p}}{2}\sin\left[k\left(r\cos\theta - h_n\right)\right]\Bigg\{ f_{1,s}\cos kh_n\left(1+3\cos 2\theta\right)\left[\frac{k\cos\theta\cos kr}{(kr)^3}\right. \\
& \left. + \frac{k\cos\theta\cos kr}{(kr)^2}\right] + \frac{4}{3}f_{0,s}\sin kh_n\cos\theta\left[\frac{k\cos\theta\cos kr}{(kr)^2} + \frac{k\cos\theta\sin kr}{kr}\right] \\
& - f_{1,s}\cos kh_n\left(1+\cos 2\theta\right)\left[\frac{k\cos\theta\cos kr}{kr}\right]\Bigg\} + \frac{2f_{0,p}}{3}\sin\left[k\left(r\cos\theta - h_n\right)\right]\Bigg\{ \\
& f_{1,s}\cos kh_n\cos\theta\left[\frac{2k\cos kr}{(kr)^3} + \frac{2k\sin kr}{(kr)^2} - \frac{k\cos kr}{kr}\right] \\
& + \frac{2}{3}f_{0,s}\sin kh_n\left[\frac{k\cos kr}{(kr)^2} + \frac{k\sin kr}{kr}\right]\Bigg\}\Bigg\}
\end{aligned} \tag{B.2}$$

To obtain the radiation force in the transversal plane, $\theta = \pi/2$ can be substituted in the previous equation. First use that $\cos(\pi/2) = 0$ and $1 + \cos(\pi) = 0$ in the above to simplify to

$$\begin{aligned}
F_r = \pi E_0 k^3 a_p^3 a_s^3 \Bigg\{ & \frac{f_{1,p}}{2}\cos\left[k\left(r\cos\theta - h_n\right)\right]\Bigg\{ \\
& f_{1,s}\cos kh_n\left(1+3\cos 2\theta\right)\left[\frac{3k\cos kr}{(kr)^4} + \frac{3k\sin kr}{(kr)^3} - \frac{k\cos kr}{(kr)^2}\right]\Bigg\} + \\
& \frac{2f_{0,p}}{3}\sin\left[k\left(r\cos\theta - h_n\right)\right]\left\{\frac{2}{3}f_{0,s}\sin kh_n\left[\frac{k\cos kr}{(kr)^2} + \frac{k\sin kr}{kr}\right]\right\}\Bigg\}
\end{aligned} \tag{B.3}$$

and now we can further simplify by $1+3\cos\pi = -2$, $\cos\left[k\left(r\cos\pi/2 - h_n\right)\right] = \cos kh_n$ and $\sin\left[k\left(r\cos\pi/2 - h_n\right)\right] = -\sin kh_n$ to arrive at

$$F_r = \pi E_0 k^3 a_p^3 a_s^3 \Bigg\{ f_{1,p} f_{1,s} \cos^2 kh_n \left[-\frac{3k\cos kr}{(kr)^4} - \frac{3k\sin kr}{(kr)^3} + \frac{k\cos kr}{(kr)^2} \right] - \frac{4}{9} f_{0,p} f_{0,s} \sin^2 kh_n \left[\frac{k\cos kr}{(kr)^2} + \frac{k\sin kr}{kr} \right] \Bigg\} \quad \text{(B.4)}$$

which is the same result as obtained by Silva and Bruus.

Along the z direction ($\theta = 0$), the simplification is not this pronounced, $\cos 0 = 1$, $1 + 3\cos 0 = 4$ and $1 + \cos 0 = 2$ and therefore

$$\begin{aligned} F_z = \pi E_0 k^3 a_p^3 a_s^3 \Bigg\{ & \frac{f_{1,p}}{2} \cos\left[k\left(z - h_n\right)\right] \Bigg\{ 4 f_{1,s} \cos kh_n \left[\frac{3k\cos kz}{(kz)^4} + \frac{3k\sin kz}{(kz)^3} - \frac{k\cos kz}{(kz)^2} \right] + \frac{4}{3} f_{0,s} \sin kh_n \left[\frac{2k\cos kz}{(kz)^3} + \frac{2k\sin kz}{(kz)^2} - \frac{k\cos kz}{kz} \right] \\ & - 2 f_{1,s} \cos kh_n \left[\frac{k\cos kz}{(kz)^2} + \frac{k\sin kz}{kz} \right] \Bigg\} + \frac{2 f_{0,p}}{3} \cos\left[k\left(z - h_n\right)\right] \Bigg\{ \\ & f_{1,s} \cos kh_n \left[-\frac{k\cos kz}{(kz)^2} - \frac{k\sin kz}{kz} \right] + \frac{2}{3} f_{0,s} \sin kh_n \left[-\frac{k\cos kz}{kz} \right] \Bigg\} \\ & + \frac{f_{1,p}}{2} \sin\left[k\left(z - h_n\right)\right] \Bigg\{ 4 f_{1,s} \cos kh_n \left[\frac{k\cos kz}{(kz)^3} + \frac{k\cos kz}{(kz)^2} \right] + \frac{4}{3} f_{0,s} \sin kh_n \left[\frac{k\cos kz}{(kz)^2} + \frac{k\sin kz}{kz} \right] \\ & - 2 f_{1,s} \cos kh_n \left[\frac{k\cos kz}{kz} \right] \Bigg\} + \frac{2 f_{0,p}}{3} \sin\left[k\left(z - h_n\right)\right] \Bigg\{ \\ & f_{1,s} \cos kh_n \left[\frac{2k\cos kz}{(kz)^3} + \frac{2k\sin kz}{(kz)^2} - \frac{k\cos kz}{kz} \right] \\ & + \frac{2}{3} f_{0,s} \sin kh_n \left[\frac{k\cos kz}{(kz)^2} + \frac{k\sin kz}{kz} \right] \Bigg\} \Bigg\} \end{aligned} \quad \text{(B.5)}$$

which simplifies to

$$\begin{aligned} F_z &= \pi E_0 k^3 a_p^3 a_s^3 f_{1,s} \Bigg\{ \frac{f_{1,p}}{2} \cos[kz] \Bigg\{ 4 \left[\frac{3k\cos kz}{(kz)^4} + \frac{3k\sin kz}{(kz)^3} - \frac{k\cos kz}{(kz)^2} \right] - 2 \left[\frac{k\cos kz}{(kz)^2} + \frac{k\sin kz}{kz} \right] \Bigg\} + \frac{2 f_{0,p}}{3} \cos[kz] \left\{ \left[-\frac{k\cos kz}{(kz)^2} - \frac{k\sin kz}{kz} \right] \right\} \\ &\quad + \frac{f_{1,p}}{2} \sin[kz] \left\{ 4 \left[\frac{k\cos kz}{(kz)^3} + \frac{k\sin kz}{(kz)^2} \right] - 2 \left[\frac{k\cos kz}{kz} \right] \right\} \\ &\quad + \frac{2 f_{0,p}}{3} \sin[kz] \left\{ \left[\frac{2k\cos kz}{(kz)^3} + \frac{2k\sin kz}{(kz)^2} - \frac{k\cos kz}{kz} \right] \right\} \Bigg\} \\ &= \pi E_0 k^4 a_p^3 a_s^3 f_{1,s} \Bigg\{ f_{1,p} \cos kz \left[\frac{6\cos kz}{(kz)^4} + \frac{6\sin kz}{(kz)^3} - \frac{3\cos kz}{(kz)^2} - \frac{\sin kz}{kz} \right] - \frac{2 f_{0,p}}{3} \cos kz \left[\frac{\cos kz}{(kz)^2} + \frac{\sin kz}{kz} \right] \\ &\quad + \left(f_{1,p} + \frac{2 f_{0,p}}{3} \right) \sin kz \left[\frac{2\cos kz}{(kz)^3} + \frac{2\sin kz}{(kz)^2} - \frac{\cos kz}{kz} \right] \Bigg\} \end{aligned} \quad \text{(B.6)}$$

when the nodes are aligned with the scatterer particle ($h = 0$), and $\sin kh_n = 0$,

$\cos kh_n = 1$.

Similarly, when the antinodes are aligned with the scatterer particle ($h = \lambda/4$), and $\sin kh_n = 1$, $\cos kh_n = 0$, $\sin = 0$, $\cos\left[k\left(r - h_n\right)\right] = \cos\left[kr - \pi/2\right] = \sin kr$ and $\sin\left[k\left(r - h_n\right)\right] = \sin\left[kr - \pi/2\right] = -\cos kr$ and therefore:

$$\begin{aligned}
F_z = \pi E_0 k^3 a_p^3 a_s^3 f_{0,s} \Bigg\{ & \frac{f_{1,p}}{2} \sin kr \left\{ \frac{4}{3} \left[\frac{2k\cos kz}{(kz)^3} + \frac{2k\sin kz}{(kz)^2} - \frac{k\cos kz}{kz} \right] \right\} \\
& + \frac{2f_{0,p}}{3} \sin kz \left\{ \frac{2}{3} \left[-\frac{k\cos kz}{kz} \right] \right\} - \frac{f_{1,p}}{2} \cos kz \left\{ \frac{4}{3} \left[\frac{k\cos kz}{(kz)^2} + \frac{k\sin kz}{kz} \right] \right\} \\
& - \frac{2f_{0,p}}{3} \cos kz \left\{ \frac{2}{3} \left[\frac{k\cos kz}{(kz)^2} + \frac{k\sin kz}{kz} \right] \right\} \Bigg\} \\
= \pi E_0 k^4 a_p^3 a_s^3 f_{0,s} \Bigg\{ & \frac{4}{3} f_{1,p} \sin kr \left[\frac{\cos kz}{(kz)^3} + \frac{\sin kz}{(kz)^2} \right] - \left(\frac{2f_{1,p}}{3} + \frac{4f_{0,p}}{9} \right) \sin kz \left[\frac{\cos kz}{kz} \right] \\
& - \left(\frac{2f_{1,p}}{3} + \frac{4f_{0,p}}{9} \right) \cos kr \left[\frac{\cos kz}{(kz)^2} + \frac{\sin kz}{kz} \right] \Bigg\} \qquad \text{(B.7)}
\end{aligned}$$

Note that this force is directly proportional to the monopole scattering coefficient of the scatterer particle.

B.2 Tangential direction

The derivatives of the various terms containing θ:

$$\frac{\partial}{\partial\theta}\left(\left(1 + 3\cos 2\theta\right)\cos[\,]\right) = -6\sin 2\theta\cos[\,] + kr\sin\theta\left(1 + 3\cos 2\theta\right)\sin[\,] \qquad \text{(B.8a)}$$

$$\frac{\partial}{\partial\theta}\left(\cos\theta\cos[\,]\right) = -\sin\theta\cos[\,] + kr\sin\theta\cos\theta\sin[\,] \qquad \text{(B.8b)}$$

$$\frac{\partial}{\partial\theta}\left(\left(1 + \cos 2\theta\right)\cos[\,]\right) = -2\sin 2\theta\cos[\,] + kr\sin\theta\left(1 + \cos 2\theta\right)\sin[\,] \qquad \text{(B.8c)}$$

$$\frac{\partial}{\partial\theta}\left(\cos\theta\sin[\,]\right) = -kr\sin\theta\cos\theta\cos[\,] - \sin\theta\sin[\,] \qquad \text{(B.8d)}$$

$$\frac{\partial}{\partial\theta}\left(\sin[\,]\right) = -kr\sin\theta\cos[\,] \qquad \text{(B.8e)}$$

And on substitution into Eq. 3.34:

$$\begin{aligned}
F_\theta = \frac{\pi E_0 k^3 a_p^3 a_s^3}{r} \Bigg\{ & \frac{f_{1,p}}{2} \cos\left[k\left(z - h_n\right)\right] \Bigg\{ f_{1,s}\cos kh_n \frac{\cos kr}{(kr)^3} \left[6\sin 2\theta\right] \\
& + \frac{4}{3} f_{0,s}\sin kh_n \frac{\cos kr}{(kr)^2} \left[\sin\theta\right] + f_{1,s}\cos kh_n \frac{\sin kr}{(kr)^2} \left[6\sin 2\theta\right] \\
& - f_{1,s}\cos kh_n \frac{\cos kr}{kr} \left[2\sin 2\theta\right] + \frac{4}{3} f_{0,s}\sin kh_n \frac{\sin kr}{kr} \left[\sin\theta\right] \Bigg\} \\
& + \frac{2f_{0,p}}{3} \cos\left[k\left(z - h_n\right)\right] \Bigg\{ f_{1,s}\cos kh_n \frac{\cos kr}{(kr)^2} \left[kr\sin\theta\cos\theta\right]
\end{aligned}$$

$$+\frac{2}{3}f_{0,s}\sin kh_n\frac{\cos kr}{kr}\left[kr\sin\theta\right]+f_{1,s}\cos kh_n\frac{\sin kr}{kr}\left[kr\sin\theta\cos\theta\right]\Bigg\}$$
$$+\frac{f_{1,p}}{2}\sin\left[k\left(z-h_n\right)\right]\Bigg\{f_{1,s}\cos kh_n\frac{\cos kr}{(kr)^3}\left[-kr\sin\theta(1+3\cos 2\theta)\right]$$
$$+\frac{4}{3}f_{0,s}\sin kh_n\frac{\cos kr}{(kr)^2}[-kr\sin\theta\cos\theta]+f_{1,s}\cos kh_n\frac{\sin kr}{(kr)^2}\left[-kr\sin\theta(1+3\cos 2\theta)\right]$$
$$-f_{1,s}\cos kh_n\frac{\cos kr}{kr}[-kr\sin\theta(1+\cos 2\theta)]+\frac{4}{3}f_{0,s}\sin kh_n\frac{\sin kr}{kr}[-kr\sin\theta\cos\theta]\Bigg\}$$
$$+\frac{2f_{0,p}}{3}\sin\left[k\left(z-h_n\right)\right]\Bigg\{f_{1,s}\cos kh_n\frac{\cos kr}{(kr)^2}\sin\theta+f_{1,s}\cos kh_n\frac{\sin kr}{kr}\sin\theta\Bigg\}\Bigg\} \quad \text{(B.9)}$$

As all terms contain $\sin\theta$ or $\sin 2\theta$, the above force goes to zero when $\theta = 0$ as expected for an axisymmetric arrangement perpendicular to the symmetry axis.

However, when $\theta = \pi/2$, only terms $\cos\theta$, $\sin 2\theta$ or $1+\cos 2\theta$ disappear, leaving

$$F_\theta = \frac{\pi E_0 k^3 a_p^3 a_s^3}{r}\Bigg\{\frac{f_{1,p}}{2}\cos\left[k\left(z-h_n\right)\right]\Bigg\{\frac{4}{3}f_{0,s}\sin kh_n\frac{\cos kr}{(kr)^2}\left[\sin\theta\right]$$
$$+\frac{4}{3}f_{0,s}\sin kh_n\frac{\sin kr}{kr}\left[\sin\theta\right]\Bigg\}$$
$$+\frac{2f_{0,p}}{3}\cos\left[k\left(z-h_n\right)\right]\Bigg\{\frac{2}{3}f_{0,s}\sin kh_n\frac{\cos kr}{kr}\left[kr\sin\theta\right]\Bigg\}$$
$$+\frac{f_{1,p}}{2}\sin\left[k\left(z-h_n\right)\right]\Bigg\{f_{1,s}\cos kh_n\frac{\cos kr}{(kr)^3}\left[-kr\sin\theta(1+3\cos 2\theta)\right]$$
$$+f_{1,s}\cos kh_n\frac{\sin kr}{(kr)^2}\left[-kr\sin\theta(1+3\cos 2\theta)\right]\Bigg\}$$
$$+\frac{2f_{0,p}}{3}\sin\left[k\left(z-h_n\right)\right]\Bigg\{f_{1,s}\cos kh_n\frac{\cos kr}{(kr)^2}\sin\theta+f_{1,s}\cos kh_n\frac{\sin kr}{kr}\sin\theta\Bigg\}\Bigg\} \quad \text{(B.10)}$$

now evaluating the remaining terms, and simplifying:

$$\cos[k(r\cos\theta-h_n)]=\cos kh_n\sin[k(r\cos\theta-h_n)] \qquad =-\sin kh_n \qquad \text{(B.11)}$$

$$F_\theta = \frac{\pi E_0 k^3 a_p^3 a_s^3}{r}\sin 2kh_n\Bigg\{\frac{f_{1,p}f_{0,s}}{3}\Bigg\{\frac{\cos kr}{(kr)^2}+\frac{\sin kr}{kr}\Bigg\}+\frac{2f_{0,p}f_{0,s}}{9}\cos kr$$
$$-\frac{f_{1,p}f_{1,s}}{2}\Bigg\{\frac{\cos kr}{(kr)^2}+\frac{\sin kr}{kr}\Bigg\}-\frac{f_{0,p}f_{1,s}}{3}\Bigg\{\frac{\cos kr}{(kr)^2}+\frac{\sin kr}{kr}\Bigg\}\Bigg\}$$
$$=\pi E_0 k^4 a_p^3 a_s^3\frac{\sin 2kh_n}{18}\Bigg[(6f_{1,p}f_{0,s}-9f_{1,p}f_{1,s}-6f_{0,p}f_{1,s})$$
$$\Bigg\{\frac{\cos kr}{(kr)^3}+\frac{\sin kr}{(kr)^2}\Bigg\}+4f_{0,p}f_{0,s}\frac{\cos kr}{kr}\Bigg] \quad \text{(B.12)}$$

which is only zero at either the nodes or antinodes, where $\sin 2kh_n = 0$.

Bibliography

[1] O. Jakobsson, C. Grenvall, M. Nordin, M. Evander, and T. Laurell, "Acoustic actuated fluorescence activated sorting of microparticles," *Lab Chip*, vol. 14, no. 11, pp. 1943–50, 2014.

[2] Z. Ma, Y. Zhou, D. J. Collins, and Y. Ai, "Fluorescence activated cell sorting via a focused traveling surface acoustic beam," *Lab Chip*, vol. 17, no. 18, pp. 3176–3185, 2017.

[3] K. Takahashi, A. Hattori, I. Suzuki, T. Ichiki, and K. Yasuda, "Non-destructive on-chip cell sorting system with real-time microscopic image processing," *Journal of Nanobiotechnology*, vol. 2, no. 5, 2004.

[4] L. Wang, L. A. Flanagan, E. Monuki, N. L. Jeon, and A. P. Lee, "Dielectrophoresis switching with vertical sidewall electrodes for microfluidic flow cytometry," *Lab Chip*, vol. 7, no. 9, pp. 1114–20, 2007.

[5] J. D. Adams, U. Kim, and H. T. Soh, "Multitarget magnetic activated cell sorter," *Proc Natl Acad Sci U S A*, vol. 105, no. 47, pp. 18165–70, 2008.

[6] L. Johansson, F. Nikolajeff, S. Johansson, and S. Thorslund, "On-chip fluorescence-activated cell sorting by an integrated miniaturized ultrasonic transducer," *Anal Chem*, vol. 81, pp. 5188–5196, 2009.

[7] L. Ren, Y. Chen, P. Li, Z. Mao, P. H. Huang, J. Rufo, F. Guo, L. Wang, J. P. McCoy, S. J. Levine, and T. J. Huang, "A high-throughput acoustic cell sorter," *Lab Chip*, vol. 15, no. 19, pp. 3870–9, 2015.

[8] H. M. Ji, V. Samper, Y. Chen, C. K. Heng, T. M. Lim, and L. Yobas, "Silicon-based microfilters for whole blood cell separation," *Biomed Microdevices*, vol. 10, no. 2, pp. 251–7, 2008.

[9] J. P. Brody, T. D. Osborn, F. K. Forster, and P. Yager, "A planar microfabricated fluid filter," *Sensors and Actuators A: Physical*, vol. 54, no. 1-3, pp. 704–708, 1996.

[10] T. A. Crowley and V. Pizziconi, "Isolation of plasma from whole blood using planar microfilters for lab-on-a-chip applications," *Lab Chip*, vol. 5, no. 9, pp. 922–9, 2005.

[11] H. Mohamed, J. N. Turner, and M. Caggana, "Biochip for separating fetal cells from maternal circulation," *J Chromatogr A*, vol. 1162, no. 2, pp. 187–92, 2007.

[12] J. H. Son, S. H. Lee, S. Hong, S. M. Park, J. Lee, A. M. Dickey, and L. P. Lee, "Hemolysis-free blood plasma separation," *Lab Chip*, vol. 14, no. 13, pp. 2287–92, 2014.

[13] Y. Cheng, X. Ye, Z. Ma, S. Xie, and W. Wang, "High-throughput and clogging-free microfluidic filtration platform for on-chip cell separation from undiluted whole blood," *Biomicrofluidics*, vol. 10, no. 1, p. 014118, 2016.

[14] T. Huang, C. P. Jia, Y. Jun, W. J. Sun, W. T. Wang, H. L. Zhang, H. Cong, F. X. Jing, H. J. Mao, Q. H. Jin, Z. Zhang, Y. J. Chen, G. Li, G. X. Mao, and J. L. Zhao, "Highly sensitive enumeration of circulating tumor cells in lung cancer patients using a size-based filtration microfluidic chip," *Biosens Bioelectron*, vol. 51, pp. 213–8, 2014.

[15] A. Meunier, J. A. Hernandez-Castro, K. Turner, K. Li, T. Veres, and D. Juncker, "Combination of mechanical and molecular filtration for enhanced enrichment of circulating tumor cells," *Anal Chem*, vol. 88, no. 17, pp. 8510–7, 2016.

[16] A. Cheer, S. Cheung, T. C. Hung, R. H. Piedrahita, and S. L. Sanderson, "Computational fluid dynamics of fish gill rakers during crossflow filtration," *Bull Math Biol*, vol. 74, no. 4, pp. 981–1000, 2012.

[17] V. VanDelinder and A. Groisman, "Separation of plasma from whole human blood in a continuous cross-flow in a molded microfluidic device," *Anal Chem*, vol. 78, no. 11, pp. 3765–71, 2006.

[18] Z. Geng, Z. Xu, W. Wang, W. Su, and Z. Li, "Separation of blood on a chip utilizing spiral micorchannel with fence and cofferdam as filtration structures," 2010.

[19] Z. Geng, Y. Ju, W. Wang, and Z. Li, "Continuous blood separation utilizing spiral filtration microchannel with gradually varied width and micro-pillar array," *Sensors and Actuators B: Chemical*, vol. 180, pp. 122–129, 2013.

[20] T. G. Kang, Y.-J. Yoon, H. Ji, P. Y. Lim, and Y. Chen, "A continuous flow micro filtration device for plasma/blood separation using submicron vertical pillar gap structures," *Journal of Micromechanics and Microengineering*, vol. 24, no. 8, p. 087001, 2014.

[21] V. VanDelinder and A. Groisman, "Perfusion in microfluidic cross-flow: separation of white blood cells from whole blood and exchange of medium in a continuous flow," *Anal Chem*, vol. 79, no. 5, pp. 2023–30, 2007.

[22] X. Chen, D. Cui, C. Liu, and H. Li, "Microfluidic chip for blood cell separation and collection based on crossflow filtration," *Sensors and Actuators B: Chemical*, vol. 130, no. 1, pp. 216–221, 2008.

[23] X. Li, W. Chen, G. Liu, W. Lu, and J. Fu, "Continuous-flow microfluidic blood cell sorting for unprocessed whole blood using surface-micromachined microfiltration membranes," *Lab Chip*, vol. 14, no. 14, pp. 2565–75, 2014.

[24] X. Chen, D. Cui, C. Liu, H. Li, and J. Chen, "Continuous flow microfluidic device for cell separation, cell lysis and dna purification," *Anal Chim Acta*, vol. 584, no. 2, pp. 237–43, 2007.

[25] E. Ledung, P. O. Eriksson, and S. Oscarsson, "A strategic crossflow filtration methodology for the initial purification of promegapoietin from inclusion bodies," *J Biotechnol*, vol. 141, no. 1-2, pp. 64–72, 2009.

[26] C. B. Raub, C. Lee, and E. Kartalov, "Sequestration of bacteria from whole blood by optimized microfluidic cross-flow filtration for rapid antimicrobial susceptibility testing," *Sensors and Actuators B: Chemical*, vol. 210, pp. 120–123, 2015.

[27] R. T. Davies, J. Kim, S. C. Jang, E. J. Choi, Y. S. Gho, and J. Park, "Microfluidic filtration system to isolate extracellular vesicles from blood," *Lab Chip*, vol. 12, no. 24, pp. 5202–10, 2012.

[28] S. W. Lee, K. A. Hyun, S. I. Kim, J. Y. Kang, and H. I. Jung, "Continuous enrichment of circulating tumor cells using a microfluidic lateral flow filtration chip," *J Chromatogr A*, vol. 1377, pp. 100–5, 2015.

[29] K. Aran, A. Fok, L. A. Sasso, N. Kamdar, Y. Guan, Q. Sun, A. Undar, and J. D. Zahn, "Microfiltration platform for continuous blood plasma protein extraction from whole blood during cardiac surgery," *Lab Chip*, vol. 11, no. 17, pp. 2858–68, 2011.

[30] H. Bruus, *Theoretical Microfluidics*. Oxford University Press, 2008.

[31] L. R. Huang, E. C. Cox, R. H. Austin, and J. C. Sturm, "Continuous particle separation through deterministic lateral displacement," *Science*, vol. 304, no. 5673, pp. 987–90, 2004.

[32] J. McGrath, M. Jimenez, and H. Bridle, "Deterministic lateral displacement for particle separation: a review," *Lab Chip*, vol. 14, no. 21, pp. 4139–58, 2014.

[33] D. W. Inglis, J. A. Davis, R. H. Austin, and J. C. Sturm, "Critical particle size for fractionation by deterministic lateral displacement," *Lab Chip*, vol. 6, no. 5, pp. 655–8, 2006.

[34] R. Huang, T. A. Barber, M. A. Schmidt, R. G. Tompkins, M. Toner, D. W. Bianchi, R. Kapur, and W. L. Flejter, "A microfluidics approach for the isolation of nucleated red blood cells (nrbcs) from the peripheral blood of pregnant women," *Prenat Diagn*, vol. 28, no. 10, pp. 892–9, 2008.

[35] S. H. Holm, J. P. Beech, M. P. Barrett, and J. O. Tegenfeldt, "Separation of parasites from human blood using deterministic lateral displacement," *Lab Chip*, vol. 11, no. 7, pp. 1326–32, 2011.

[36] K. K. Zeming, S. Ranjan, and Y. Zhang, "Rotational separation of non-spherical bioparticles using i-shaped pillar arrays in a microfluidic device," *Nat Commun*, vol. 4, p. 1625, 2013.

[37] J. P. Beech, S. H. Holm, K. Adolfsson, and J. O. Tegenfeldt, "Sorting cells by size, shape and deformability," *Lab Chip*, vol. 12, no. 6, pp. 1048–51, 2012.

[38] D. Holmes, G. Whyte, J. Bailey, N. Vergara-Irigaray, A. Ekpenyong, J. Guck, and T. Duke, "Separation of blood cells with differing deformability using deterministic lateral displacement(dagger)," *Interface Focus*, vol. 4, no. 6, p. 20140011, 2014.

[39] Z. Zhang, E. Henry, G. Gompper, and D. A. Fedosov, "Behavior of rigid and deformable particles in deterministic lateral displacement devices with different post shapes," *J Chem Phys*, vol. 143, no. 24, p. 243145, 2015.

[40] H. Okano, T. Konishi, T. Suzuki, T. Suzuki, S. Ariyasu, S. Aoki, R. Abe, and M. Hayase, "Enrichment of circulating tumor cells in tumor-bearing mouse blood by a deterministic lateral displacement microfluidic device," *Biomed Microdevices*, vol. 17, no. 3, p. 9964, 2015.

[41] F. Khodaee, S. Movahed, N. Fatouraee, and F. Daneshmand, "Numerical simulation of separation of circulating tumor cells from blood stream in deterministic lateral displacement (dld) microfluidic channel," *Journal of Mechanics*, vol. 32, no. 04, pp. 463–471, 2015.

[42] A. J. Laki, L. Botzheim, K. Iván, V. Tamási, and P. Civera, "Separation of microvesicles from serological samples using deterministic lateral displacement effect," *BioNanoScience*, vol. 5, no. 1, pp. 48–54, 2014.

[43] N. Tottori, T. Nisisako, J. Park, Y. Yanagida, and T. Hatsuzawa, "Separation of viable and nonviable mammalian cells using a deterministic lateral displacement microfluidic device," *Biomicrofluidics*, vol. 10, no. 1, p. 014125, 2016.

[44] M. Yamada, M. Nakashima, and M. Seki, "Pinched flow fractionation: continuous size separation of particles utilizing a laminar flow profile in a pinched microchannel," *Anal Chem*, vol. 76, no. 18, pp. 5465–71, 2004.

[45] J. Takagi, M. Yamada, M. Yasuda, and M. Seki, "Continuous particle separation in a microchannel having asymmetrically arranged multiple branches," *Lab Chip*, vol. 5, no. 7, pp. 778–84, 2005.

[46] Z. Wu, B. Willing, J. Bjerketorp, J. K. Jansson, and K. Hjort, "Soft inertial microfluidics for high throughput separation of bacteria from human blood cells," *Lab Chip*, vol. 9, no. 9, pp. 1193–9, 2009.

[47] H. W. Nho and T. H. Yoon, "Enhanced separation of colloidal particles in an aspff device with a tilted sidewall and vertical focusing channels (t-aspff-v)," *Lab Chip*, vol. 13, no. 5, pp. 773–6, 2013.

[48] H. W. Nho, N. Yang, J. Song, J. S. Park, and T. H. Yoon, "Separations of spherical and disc-shaped polystyrene particles and blood components (red blood cells and platelets) using pinched flow fractionation device with a tilted sidewall and vertical focusing channels (t-pff-v)," *Sensors and Actuators B: Chemical*, vol. 249, pp. 131–141, 2017.

[49] H. W. Nho, J. S. Park, and T. H. Yoon, "Redesigned t-pff-v device fabricated with one-step anisotropic chemical wet etching process: enhanced separation efficiency for colloidal particles in continuous-mode," *Journal of Micromechanics and Microengineering*, vol. 27, no. 5, p. 055009, 2017.

[50] M. Podenphant, N. Ashley, K. Koprowska, K. U. Mir, M. Zalkovskij, B. Bilenberg, W. Bodmer, A. Kristensen, and R. Marie, "Separation of cancer cells from white blood cells by pinched flow fractionation," *Lab Chip*, vol. 15, no. 24, pp. 4598–606, 2015.

[51] J. F. Ashley, C. N. Bowman, and R. H. Davis, "Hydrodynamic separation of particles using pinched-flow fractionation," *AIChE Journal*, vol. 59, no. 9, pp. 3444–3457, 2013.

[52] M. Yamada, K. Kano, Y. Tsuda, J. Kobayashi, M. Yamato, M. Seki, and T. Okano, "Microfluidic devices for size-dependent separation of liver cells," *Biomed Microdevices*, vol. 9, no. 5, pp. 637–45, 2007.

[53] S. Sugaya, M. Yamada, and M. Seki, "Observation of nonspherical particle behaviors for continuous shape-based separation using hydrodynamic filtration," *Biomicrofluidics*, vol. 5, no. 2, p. 24103, 2011.

[54] H. Wei Hou, H. Y. Gan, A. A. Bhagat, L. D. Li, C. T. Lim, and J. Han, "A microfluidics approach towards high-throughput pathogen removal from blood using margination," *Biomicrofluidics*, vol. 6, no. 2, pp. 24115–2411513, 2012.

[55] D. Di Carlo, "Inertial microfluidics," *Lab Chip*, vol. 9, no. 21, pp. 3038–46, 2009.

[56] D. Di Carlo, D. Irimia, R. G. Tompkins, and M. Toner, "Continuous inertial focusing, ordering, and separation of particles in microchannels," *Proc Natl Acad Sci U S A*, vol. 104, no. 48, pp. 18892–7, 2007.

[57] D. Di Carlo, J. F. Edd, D. Irimia, R. G. Tompkins, and M. Toner, "Equilibrium separation and filtration of particles using differential inertial focusing," *Anal Chem*, vol. 80, no. 6, pp. 2204–11, 2008.

[58] S. S. Kuntaegowdanahalli, A. A. Bhagat, G. Kumar, and I. Papautsky, "Inertial microfluidics for continuous particle separation in spiral microchannels," *Lab Chip*, vol. 9, no. 20, pp. 2973–80, 2009.

[59] M. Jimenez, B. Miller, and H. L. Bridle, "Efficient separation of small microparticles at high flowrates using spiral channels: Application to waterborne pathogens," *Chemical Engineering Science*, vol. 157, pp. 247–254, 2017.

[60] A. J. Mach and D. Di Carlo, "Continuous scalable blood filtration device using inertial microfluidics," *Biotechnol Bioeng*, vol. 107, no. 2, pp. 302–11, 2010.

[61] T. Tanaka, T. Ishikawa, K. Numayama-Tsuruta, Y. Imai, H. Ueno, N. Matsuki, and T. Yamaguchi, "Separation of cancer cells from a red blood cell suspension using inertial force," *Lab Chip*, vol. 12, no. 21, pp. 4336–43, 2012.

[62] K. Goda, A. Ayazi, D. R. Gossett, J. Sadasivam, C. K. Lonappan, E. Sollier, A. M. Fard, S. C. Hur, J. Adam, C. Murray, C. Wang, N. Brackbill, D. Di Carlo, and B. Jalali, "High-throughput single-microparticle imaging flow analyzer," *Proc Natl Acad Sci U S A*, vol. 109, no. 29, pp. 11630–5, 2012.

[63] E. Ozkumur, A. M. Shah, J. C. Ciciliano, B. L. Emmink, D. T. Miyamoto, E. Brachtel, M. Yu, P. I. Chen, B. Morgan, J. Trautwein, A. Kimura, S. Sengupta, S. L. Stott, N. M. Karabacak, T. A. Barber, J. R. Walsh, K. Smith, P. S. Spuhler, J. P. Sullivan, R. J. Lee, D. T. Ting, X. Luo, A. T. Shaw, A. Bardia, L. V. Sequist, D. N. Louis, S. Maheswaran, R. Kapur, D. A. Haber, and M. Toner, "Inertial focusing for tumor antigen-dependent and

-independent sorting of rare circulating tumor cells," *Sci Transl Med*, vol. 5, no. 179, p. 179ra47, 2013.

[64] L. Min, S. Chen, X. Xie, H. Dong, H. Pan, Z. Sheng, H. Wang, F. Wu, M. Wang, and X. Hou, "Development and application of bio-inspired microfluidics," *International Journal of Modern Physics B*, vol. 32, no. 18, p. 1840013, 2017.

[65] S. Yang, A. Undar, and J. D. Zahn, "A microfluidic device for continuous, real time blood plasma separation," *Lab Chip*, vol. 6, no. 7, pp. 871–80, 2006.

[66] S. S. Shevkoplyas, T. Yoshida, L. L. Munn, and M. W. Bitensky, "Biomimetic autoseparation of leukocytes from whole blood in a microfluidic device," *Anal Chem*, vol. 77, no. 3, pp. 933–7, 2005.

[67] A. Tripathi, A. Bhattacharya, and A. C. Balazs, "Size selectivity in artificial cilia-particle interactions: mimicking the behavior of suspension feeders," *Langmuir*, vol. 29, no. 14, pp. 4616–21, 2013.

[68] A. C. Balazs, A. Bhattacharya, A. Tripathi, and H. Shum, "Designing bioinspired artificial cilia to regulate particle-surface interactions," *J Phys Chem Lett*, vol. 5, no. 10, pp. 1691–700, 2014.

[69] S. Sohrabi, J. Tan, D. E. Yunus, R. He, and Y. Liu, "Label-free sorting of soft microparticles using a bioinspired synthetic cilia array," *Biomicrofluidics*, vol. 12, no. 4, p. 042206, 2018.

[70] W. Zhao, C. H. Cui, S. Bose, D. Guo, C. Shen, W. P. Wong, K. Halvorsen, O. C. Farokhzad, G. S. Teo, J. A. Phillips, D. M. Dorfman, R. Karnik, and J. M. Karp, "Bioinspired multivalent dna network for capture and release of cells," *Proc Natl Acad Sci U S A*, vol. 109, no. 48, pp. 19626–31, 2012.

[71] E. M. Southern, "Detection of specific sequences among dna fragments separated by gel electrophoresis," *Journal of Molecular Biology*, vol. 98, no. 3, pp. 503–517, 1975.

[72] D. E. Raymond, A. Manz, and H. M. Widmer, "Continuous separation of high molecular weight compounds using a microliter volume free-flow electrophoresis microstructure," *Anal Chem*, vol. 68, no. 15, pp. 2515–22, 1996.

[73] P. Hoffmann, H. Ji, R. L. Moritz, L. M. Connolly, D. F. Frecklington, M. J. Layton, J. S. Eddes, and R. J. Simpson, "Continuous free-flow electrophoresis separation of cytosolic proteins from the human colon carcinoma cell line lim 1215: a non two-dimensional gel electrophoresis-based proteome analysis strategy," *Proteomics*, vol. 1, no. 7, pp. 807–18, 2001.

[74] R. Pethig, A. Menachery, S. Pells, and P. De Sousa, "Dielectrophoresis: a review of applications for stem cell research," *J Biomed Biotechnol*, vol. 2010, p. 182581, 2010.

[75] G. R. Ballantyne and P. N. Holtham, "Application of dielectrophoresis for the separation of minerals," *Minerals Engineering*, vol. 23, no. 4, pp. 350–358, 2010.

[76] P. R. Gascoyne, X. B. Wang, Y. Huang, and F. F. Becker, "Dielectrophoretic separation of cancer cells from blood," *IEEE Trans Ind Appl*, vol. 33, no. 3, pp. 670–678, 1997.

[77] P. R. Gascoyne and S. Shim, "Isolation of circulating tumor cells by dielectrophoresis," *Cancers (Basel)*, vol. 6, no. 1, pp. 545–79, 2014.

[78] M. Li and R. K. Anand, "High-throughput selective capture of single circulating tumor cells by dielectrophoresis at a wireless electrode array," *J Am Chem Soc*, vol. 139, no. 26, pp. 8950–8959, 2017.

[79] A. Morimoto, T. Mogami, M. Watanabe, K. Iijima, Y. Akiyama, K. Katayama, T. Futami, N. Yamamoto, T. Sawada, F. Koizumi, and Y. Koh, "High-density dielectrophoretic microwell array for detection, capture, and single-cell analysis of rare tumor cells in peripheral blood," *PLoS One*, vol. 10, no. 6, p. e0130418, 2015.

[80] W. S. Low and N. A. Kadri, "Computational analysis of enhanced circulating tumour cell (ctc) separation in a microfluidic system with an integrated dielectrophoretic-magnetophorectic (dep-map) technique," *Chemosensors*, vol. 4, no. 3, 2016.

[81] Y. Nakashima, S. Hata, and T. Yasuda, "Blood plasma separation and extraction from a minute amount of blood using dielectrophoretic and capillary forces," *Sensors and Actuators B-Chemical*, vol. 145, no. 1, pp. 561–569, 2010.

[82] S. Yan, J. Zhang, G. Alici, H. Du, Y. Zhu, and W. Li, "Isolating plasma from blood using a dielectrophoresis-active hydrophoretic device," *Lab Chip*, vol. 14, no. 16, pp. 2993–3003, 2014.

[83] C. Szydzik, K. Khoshmanesh, A. Mitchell, and C. Karnutsch, "Microfluidic platform for separation and extraction of plasma from whole blood using dielectrophoresis," *Biomicrofluidics*, vol. 9, no. 6, p. 064120, 2015.

[84] F. Yang, Y. Zhang, X. Cui, Y. Fan, Y. Xue, H. Miao, and G. Li, "Extraction of cell-free whole blood plasma using a dielectrophoresis-based microfluidic device," *Biotechnol J*, p. e1800181, 2018.

[85] N. Piacentini, G. Mernier, R. Tornay, and P. Renaud, "Separation of platelets from other blood cells in continuous-flow by dielectrophoresis field-flow-fractionation," *Biomicrofluidics*, vol. 5, no. 3, pp. 34122–341228, 2011.

[86] H. Imasato, T. Yamakawa, and M. Eguchi, "Separation of leukemia cells from blood by employing dielectrophoresis," *Intelligent Automation and Soft Computing*, vol. 18, no. 2, pp. 139–152, 2012.

[87] H. W. Hou, A. A. S. Bhagat, W. C. Lee, S. Huang, J. Han, and C. T. Lim, "Microfluidic devices for blood fractionation," *Micromachines*, vol. 2, no. 4, pp. 319–343, 2011.

[88] D. Melville, F. Paul, and S. Roath, "Direct magnetic separation of red cells from whole blood," *Nature*, vol. 255, p. 706, 1975.

[89] K. H. Han and A. B. Frazier, "Paramagnetic capture mode magnetophoretic microseparator for high efficiency blood cell separations," *Lab Chip*, vol. 6, no. 2, pp. 265–73, 2006.

[90] E. P. Furlani, "Magnetophoretic separation of blood cells at the microscale," *Journal of Physics D-Applied Physics*, vol. 40, no. 5, pp. 1313–1319, 2007.

[91] Y. L. Zhou and X. C. Xuan, "Diamagnetic particle separation by shape in ferrofluids," *Applied Physics Letters*, vol. 109, no. 10, pp. 131–135, 2016.

[92] T. Zhu, R. Cheng, S. A. Lee, E. Rajaraman, M. A. Eiteman, T. D. Querec, E. R. Unger, and L. Mao, "Continuous-flow ferrohydrodynamic sorting of particles and cells in microfluidic devices," *Microfluid Nanofluidics*, vol. 13, no. 4, pp. 645–654, 2012.

[93] J. Zeng, Y. X. Deng, P. Vedantam, T. R. Tzeng, and X. C. Xuan, "Magnetic separation of particles and cells in ferrofluid flow through a straight microchannel using two offset magnets," *Journal of Magnetism and Magnetic Materials*, vol. 346, pp. 118–123, 2013.

[94] S. Miltenyi, W. Muller, W. Weichel, and A. Radbruch, "High gradient magnetic cell separation with macs," *Cytometry*, vol. 11, no. 2, pp. 231–8, 1990.

[95] D. Robert, N. Pamme, H. Conjeaud, F. Gazeau, A. Iles, and C. Wilhelm, "Cell sorting by endocytotic capacity in a microfluidic magnetophoresis device," *Lab Chip*, vol. 11, no. 11, pp. 1902–10, 2011.

[96] H. Abts, M. Emmerich, S. Miltenyi, A. Radbruch, and H. Tesch, "Cd20 positive human b lymphocytes separated with the magnetic cell sorter (macs) can be induced to proliferation and antibody secretion in vitro," *Journal of Immunological Methods*, vol. 125, no. 1, pp. 19–28, 1989.

[97] C. Kosmas, K. Stamatopoulos, N. Stavroyianni, N. Tsavaris, and T. Papadaki, "Anti-cd20-based therapy of b cell lymphoma: state of the art," *Leukemia*, vol. 16, no. 10, pp. 2004–15, 2002.

[98] M. Zborowski, C. B. Fuh, R. Green, L. Sun, and J. J. Chalmers, "Analytical magnetapheresis of ferritin-labeled lymphocytes," *Anal Chem*, vol. 67, no. 20, pp. 3702–12, 1995.

[99] M. Zborowski, L. P. Sun, L. R. Moore, P. S. Williams, and J. J. Chalmers, "Continuous cell separation using novel magnetic quadrupole flow sorter," *Journal of Magnetism and Magnetic Materials*, vol. 194, no. 1-3, pp. 224–230, 1999.

[100] A. Thiel, A. Scheffold, and A. Radbruch, "Immunomagnetic cell sorting–pushing the limits," *Immunotechnology*, vol. 4, no. 2, pp. 89–96, 1998.

[101] D. W. Inglis, R. Riehn, R. H. Austin, and J. C. Sturm, "Continuous microfluidic immunomagnetic cell separation," *Applied Physics Letters*, vol. 85, no. 21, pp. 5093–5095, 2004.

[102] V. I. Furdui and D. J. Harrison, "Immunomagnetic t cell capture from blood for pcr analysis using microfluidic systems," *Lab Chip*, vol. 4, no. 6, pp. 614–8, 2004.

[103] J. Darabi and C. Guo, "On-chip magnetophoretic isolation of cd4 + t cells from blood," *Biomicrofluidics*, vol. 7, no. 5, p. 54106, 2013.

[104] Y. L. Zheng, N. P. Carter, C. M. Price, S. M. Colman, P. J. Milton, G. A. Hackett, M. F. Greaves, and M. A. Ferguson-Smith, "Prenatal diagnosis from maternal blood: simultaneous immunophenotyping and fish of fetal nucleated erythrocytes isolated by negative magnetic cell sorting," *Journal of Medical Genetics*, vol. 30, no. 12, p. 1051, 1993.

[105] D. Ganshirt-Ahlert, R. BÖRjesson-Stoll, M. Burschyk, A. Dohr, H. S. P. Garritsen, E. Helmer, P. Miny, M. Velasco, C. Walde, D. Patterson, N. Teng, N. M. Bhat, M. M. Bieber, and W. Holzgreve, "Detection of fetal trisomies 21 and 18 from maternal blood using triple gradient and magnetic cell sorting," *American Journal of Reproductive Immunology*, vol. 30, no. 2-3, pp. 194–201, 1993.

[106] N. Xia, T. P. Hunt, B. T. Mayers, E. Alsberg, G. M. Whitesides, R. M. Westervelt, and D. E. Ingber, "Combined microfluidic-micromagnetic separation of living cells in continuous flow," *Biomed Microdevices*, vol. 8, no. 4, pp. 299–308, 2006.

[107] M. Yu, S. Stott, M. Toner, S. Maheswaran, and D. A. Haber, "Circulating tumor cells: approaches to isolation and characterization," *J Cell Biol*, vol. 192, no. 3, pp. 373–82, 2011.

[108] M. Antfolk, C. Antfolk, H. Lilja, T. Laurell, and P. Augustsson, "A single inlet two-stage acoustophoresis chip enabling tumor cell enrichment from white blood cells," *Lab Chip*, vol. 15, no. 9, pp. 2102–9, 2015.

[109] K. Hoshino, Y. Y. Huang, N. Lane, M. Huebschman, J. W. Uhr, E. P. Frenkel, and X. Zhang, "Microchip-based immunomagnetic detection of circulating tumor cells," *Lab Chip*, vol. 11, no. 20, pp. 3449–57, 2011.

[110] K. Hoshino, P. Chen, Y. Y. Huang, and X. Zhang, "Computational analysis of microfluidic immunomagnetic rare cell separation from a particulate blood flow," *Anal Chem*, vol. 84, no. 10, pp. 4292–9, 2012.

[111] P. Chen, Y. Y. Huang, K. Hoshino, and J. X. Zhang, "Microscale magnetic field modulation for enhanced capture and distribution of rare circulating tumor cells," *Sci Rep*, vol. 5, p. 8745, 2015.

[112] J. H. Kang, S. Krause, H. Tobin, A. Mammoto, M. Kanapathipillai, and D. E. Ingber, "A combined micromagnetic-microfluidic device for rapid capture and culture of rare circulating tumor cells," *Lab Chip*, vol. 12, no. 12, pp. 2175–81, 2012.

[113] N. M. Karabacak, P. S. Spuhler, F. Fachin, E. J. Lim, V. Pai, E. Ozkumur, J. M. Martel, N. Kojic, K. Smith, P.-i. Chen, J. Yang, H. Hwang, B. Morgan, J. Trautwein, T. A. Barber, S. L. Stott, S. Maheswaran, R. Kapur, D. A. Haber, and M. Toner, "Microfluidic, marker-free isolation of circulating tumor cells from blood samples," *Nature Protocols*, vol. 9, p. 694, 2014.

[114] S. A. Khashan, S. Dagher, A. Alazzam, B. Mathew, and A. Hilal-Alnaqbi, "Microdevice for continuous flow magnetic separation for bioengineering applications," *Journal of Micromechanics and Microengineering*, vol. 27, no. 5, 2017.

[115] S. A. Khashan, A. Alazzam, and E. P. Furlani, "Computational analysis of enhanced magnetic bioseparation in microfluidic systems with flow-invasive magnetic elements," *Sci Rep*, vol. 4, p. 5299, 2014.

[116] S. A. Khashan and E. P. Furlani, "Scalability analysis of magnetic bead separation in a microchannel. with an array of soft magnetic elements in a uniform magnetic field," *Separation and Purification Technology*, vol. 125, pp. 311–318, 2014.

[117] M. Berger, J. Castelino, R. Huang, M. Shah, and R. H. Austin, "Design of a microfabricated magnetic cell separator," *Electrophoresis*, vol. 22, no. 18, pp. 3883–92, 2001.

[118] H. R. Hulett, W. A. Bonner, J. Barrett, and L. A. Herzenberg, "Cell sorting: Automated separation of mammalian cells as a function of intracellular fluorescence," *Science*, vol. 166, no. 3906, pp. 747–749, 1969.

[119] W. A. Bonner, H. R. Hulett, R. G. Sweet, and L. A. Herzenberg, "Fluorescence activated cell sorting," *Review of Scientific Instruments*, vol. 43, no. 3, pp. 404–409, 1972.

[120] B. Yao, G. A. Luo, X. Feng, W. Wang, L. X. Chen, and Y. M. Wang, "A microfluidic device based on gravity and electric force driving for flow cytometry and fluorescence activated cell sorting," *Lab Chip*, vol. 4, no. 6, pp. 603–7, 2004.

[121] J. C. Baret, O. J. Miller, V. Taly, M. Ryckelynck, A. El-Harrak, L. Frenz, C. Rick, M. L. Samuels, J. B. Hutchison, J. J. Agresti, D. R. Link, D. A. Weitz, and A. D. Griffiths, "Fluorescence-activated droplet sorting (fads): efficient microfluidic cell sorting based on enzymatic activity," *Lab Chip*, vol. 9, no. 13, pp. 1850–8, 2009.

[122] S. H. Cho, C. H. Chen, F. S. Tsai, J. M. Godin, and Y. H. Lo, "Human mammalian cell sorting using a highly integrated micro-fabricated fluorescence-activated cell sorter (microfacs)," *Lab Chip*, vol. 10, no. 12, pp. 1567–73, 2010.

[123] T. K. Chiu, W. P. Chou, S. B. Huang, H. M. Wang, Y. C. Lin, C. H. Hsieh, and M. H. Wu, "Application of optically-induced-dielectrophoresis in microfluidic system for purification of circulating tumour cells for gene expression analysis-cancer cell line model," *Sci Rep*, vol. 6, p. 32851, 2016.

[124] L. V. King, "On the acoustic radiation pressure on spheres," *Proceedings of the Royal Society of London. Series A - Mathematical and Physical Sciences*, vol. 147, no. 861, pp. 212–240, 1934.

[125] K. Yosioka and Y. Kawasima, "Acoustic radiation pressure on a compressible sphere," *Acta Acustica united with Acustica*, vol. 5, no. 3, pp. 167–173, 1955.

[126] L. P. Gorkov, "On the forces acting on a small particle in an acoustic field in an ideal fluid," *Soviet Physics Doklady*, vol. 6, no. 9, pp. 773–775, 1962.

[127] M. Settnes and H. Bruus, "Forces acting on a small particle in an acoustical field in a viscous fluid," *Phys Rev E Stat Nonlin Soft Matter Phys*, vol. 85, no. 1 Pt 2, p. 016327, 2012.

[128] H. Bruus, "Acoustofluidics 7: The acoustic radiation force on small particles," *Lab Chip*, vol. 12, no. 6, pp. 1014–21, 2012.

[129] J. Shi, H. Huang, Z. Stratton, Y. Huang, and T. J. Huang, "Continuous particle separation in a microfluidic channel via standing surface acoustic waves (ssaw)," *Lab Chip*, vol. 9, no. 23, pp. 3354–9, 2009.

[130] F. Petersson, A. Nilsson, C. Holm, H. Jönsson, and T. Laurell, "Continuous separation of lipid particles from erythrocytes by means of laminar flow and acoustic standing wave forces," *Lab Chip*, vol. 5, no. 1, pp. 20–22, 2005.

[131] F. Petersson, L. Åberg, A.-M. Swärd-Nilsson, and T. Laurell, "Free flow acoustophoresis: microfluidic-based mode of particle and cell separation," *Analytical Chemistry*, vol. 79, no. 14, pp. 5117–5123, 2007.

[132] M. Evander, A. Lenshof, T. Laurell, and J. Nilsson, "Acoustophoresis in wet-etched glass chips," *Anal Chem*, vol. 80, no. 13, pp. 5178–85, 2008.

[133] C. R. P. Courtney, C. K. Ong, B. W. Drinkwater, A. L. Bernassau, P. D. Wilcox, and D. R. S. Cumming, "Manipulation of particles in two dimensions using phase controllable ultrasonic standing waves," *Proceedings of the Royal Society A: Mathematical, Physical and Engineering Sciences*, vol. 468, no. 2138, pp. 337–360, 2011.

[134] A. L. Bernassau, C. R. P. Courtney, J. Beeley, B. W. Drinkwater, and D. R. S. Cumming, "Interactive manipulation of microparticles in an octagonal sonotweezer," *Applied Physics Letters*, vol. 102, no. 16, p. 164101, 2013.

[135] A. L. Bernassau, P. Glynne-Jones, F. Gesellchen, M. Riehle, M. Hill, and D. R. Cumming, "Controlling acoustic streaming in an ultrasonic heptagonal tweezers with application to cell manipulation," *Ultrasonics*, vol. 54, no. 1, pp. 268–74, 2014.

[136] H. Bruus, "Acoustofluidics 10: Scaling laws in acoustophoresis," *Lab Chip*, vol. 12, no. 9, pp. 1578–86, 2012.

[137] A. H. Yang and H. T. Soh, "Acoustophoretic sorting of viable mammalian cells in a microfluidic device," *Anal Chem*, vol. 84, no. 24, pp. 10756–62, 2012.

[138] M. C. Jo and R. Guldiken, "Active density-based separation using standing surface acoustic waves," *Sensors and Actuators A: Physical*, vol. 187, pp. 22–28, 2012.

[139] G. Destgeer, K. H. Lee, J. H. Jung, A. Alazzam, and H. J. Sung, "Continuous separation of particles in a pdms microfluidic channel via travelling surface acoustic waves (tsaw)," *Lab Chip*, vol. 13, no. 21, pp. 4210–6, 2013.

[140] G. Destgeer, B. H. Ha, J. H. Jung, and H. J. Sung, "Submicron separation of microspheres via travelling surface acoustic waves," *Lab Chip*, vol. 14, no. 24, pp. 4665–72, 2014.

[141] Z. Ma, D. J. Collins, and Y. Ai, "Detachable acoustofluidic system for particle separation via a traveling surface acoustic wave," *Anal Chem*, vol. 88, no. 10, pp. 5316–23, 2016.

[142] C. Devendran, N. R. Gunasekara, D. J. Collins, and A. Neild, "Batch process particle separation using surface acoustic waves (saw): integration of travelling and standing saw," *RSC Adv.*, vol. 6, no. 7, pp. 5856–5864, 2016.

[143] J. W. Ng, D. J. Collins, C. Devendran, Y. Ai, and A. Neild, "Flow-rate-insensitive deterministic particle sorting using a combination of travelling and standing surface acoustic waves," *Microfluidics and Nanofluidics*, vol. 20, no. 11, 2016.

[144] A. Dolatmoradi and B. El-Zahab, "Thermally-assisted ultrasonic separation of giant vesicles," *Lab Chip*, vol. 16, no. 18, pp. 3449–53, 2016.

[145] K. W. Cushing, M. E. Piyasena, N. J. Carroll, G. C. Maestas, B. A. Lopez, B. S. Edwards, S. W. Graves, and G. P. Lopez, "Elastomeric negative acoustic contrast particles for affinity capture assays," *Anal Chem*, vol. 85, no. 4, pp. 2208–15, 2013.

[146] A. Mueller, A. Lever, T. V. Nguyen, J. Comolli, and J. Fiering, "Continuous acoustic separation in a thermoplastic microchannel," *Journal of Micromechanics and Microengineering*, vol. 23, no. 12, p. 125006, 2013.

[147] Y. Chen, M. Wu, L. Ren, J. Liu, P. H. Whitley, L. Wang, and T. J. Huang, "High-throughput acoustic separation of platelets from whole blood," *Lab Chip*, vol. 16, no. 18, pp. 3466–72, 2016.

[148] Y. Wu, M. S. Kanna, C. Liu, Y. Zhou, and C. K. Chan, "Generation of autologous platelet-rich plasma by the ultrasonic standing waves," *IEEE Trans Biomed Eng*, vol. 63, no. 8, pp. 1642–52, 2016.

[149] J. Nam, H. Lim, D. Kim, and S. Shin, "Separation of platelets from whole blood using standing surface acoustic waves in a microchannel," *Lab Chip*, vol. 11, no. 19, pp. 3361–4, 2011.

[150] P. Bohec, J. Gachelin, V. Ollivier, T. Mutin, X. Télot, B. Ho-Tin-Noé, and S. Sanfilippo, "Acoustophoretic purification of platelets: Feasibility and impact on platelet activation and function," *Platelets*, pp. 1–7, 2017.

[151] Y. Ai, C. K. Sanders, and B. L. Marrone, "Separation of escherichia coli bacteria from peripheral blood mononuclear cells using standing surface acoustic waves," *Anal Chem*, vol. 85, no. 19, pp. 9126–34, 2013.

[152] J. Nam, H. Lim, C. Kim, J. Yoon Kang, and S. Shin, "Density-dependent separation of encapsulated cells in a microfluidic channel by using a standing surface acoustic wave," *Biomicrofluidics*, vol. 6, no. 2, pp. 024120–024120–10, 2012.

[153] K. Lee, H. Shao, R. Weissleder, and H. Lee, "Acoustic purification of extracellular microvesicles," *ACS Nano*, vol. 9, no. 3, pp. 2321–7, 2015.

[154] J. W. Park, S. J. Lee, S. Ren, S. Lee, S. Kim, and T. Laurell, "Acousto-microfluidics for screening of ssdna aptamer," *Sci Rep*, vol. 6, p. 27121, 2016.

[155] A. M. Soliman, M. A. Eldosoky, and T. E. Taha, "Modelling and simulation of microparticles separation using standing surface acoustic waves (ssaws) microfluidic devices for biomedical applications," *International Journal of Computer Applications*, vol. 129, no. 9, pp. 30–38, 2015.

[156] A. M. Soliman, M. A. Eldosoky, and T. E. Taha, "The separation of blood components using standing surface acoustic waves (ssaws) microfluidic devices: Analysis and simulation," *Bioengineering (Basel)*, vol. 4, no. 2, 2017.

[157] A. Shamloo and M. Boodaghi, "Design and simulation of a microfluidic device for acoustic cell separation," *Ultrasonics*, vol. 84, pp. 234–243, 2018.

[158] K. Wang, W. Zhou, Z. Lin, F. Cai, F. Li, J. Wu, L. Meng, L. Niu, and H. Zheng, "Sorting of tumour cells in a microfluidic device by multi-stage surface acoustic waves," *Sensors and Actuators B: Chemical*, vol. 258, pp. 1174–1183, 2018.

[159] V. Skowronek, R. W. Rambach, and T. Franke, "Surface acoustic wave controlled integrated band-pass filter," *Microfluidics and Nanofluidics*, vol. 19, no. 2, pp. 335–341, 2015.

[160] G. Destgeer, J. H. Jung, J. Park, H. Ahmed, K. Park, R. Ahmad, and H. J. Sung, "Acoustic impedance-based manipulation of elastic microspheres using travelling surface acoustic waves," *Rsc Advances*, vol. 7, no. 36, pp. 22524–22530, 2017.

[161] W. L. Ung, K. Mutafopulos, P. Spink, R. W. Rambach, T. Franke, and D. A. Weitz, "Enhanced surface acoustic wave cell sorting by 3d microfluidic-chip design," *Lab Chip*, vol. 17, no. 23, pp. 4059–4069, 2017.

[162] X. Y. Ding, Z. L. Peng, S. C. S. Lin, M. Geri, S. X. Li, P. Li, Y. C. Chen, M. Dao, S. Suresh, and T. J. Huang, "Cell separation using tilted-angle standing surface acoustic waves," *Proceedings of the National Academy of Sciences of the United States of America*, vol. 111, no. 36, pp. 12992–12997, 2014.

[163] P. Li, Z. Mao, Z. Peng, L. Zhou, Y. Chen, P. H. Huang, C. I. Truica, J. J. Drabick, W. S. El-Deiry, M. Dao, S. Suresh, and T. J. Huang, "Acoustic separation of circulating tumor cells," *Proceedings of the National Academy of Sciences of the United States of America*, vol. 112, no. 16, pp. 4970–5, 2015.

[164] S. Li, F. Ma, H. Bachman, C. E. Cameron, X. Zeng, and T. J. Huang, "Acoustofluidic bacteria separation," *J Micromech Microeng*, vol. 27, no. 1, 2017.

[165] M. Wu, Y. Ouyang, Z. Wang, R. Zhang, P. H. Huang, C. Chen, H. Li, P. Li, D. Quinn, M. Dao, S. Suresh, Y. Sadovsky, and T. J. Huang, "Isolation of exosomes from whole blood by integrating acoustics and microfluidics," *Proc Natl Acad Sci U S A*, vol. 114, no. 40, pp. 10584–10589, 2017.

[166] S. Li, L. Ren, P. H. Huang, X. Yao, R. A. Cuento, J. P. McCoy, C. E. Cameron, S. J. Levine, and T. J. Huang, "Acoustofluidic transfer of inflammatory cells from human sputum samples," *Anal Chem*, vol. 88, no. 11, pp. 5655–61, 2016.

[167] S. Li, X. Ding, Z. Mao, Y. Chen, N. Nama, F. Guo, P. Li, L. Wang, C. E. Cameron, and T. J. Huang, "Standing surface acoustic wave (ssaw)-based cell washing," *Lab Chip*, vol. 15, no. 1, pp. 331–8, 2015.

[168] B. Ayan, A. Ozcelik, H. Bachman, S. Y. Tang, Y. Xie, M. Wu, P. Li, and T. J. Huang, "Acoustofluidic coating of particles and cells," *Lab Chip*, vol. 16, no. 22, pp. 4366–4372, 2016.

[169] A. Fakhfouri, C. Devendran, D. J. Collins, Y. Ai, and A. Neild, "Virtual membrane for filtration of particles using surface acoustic waves (saw)," *Lab Chip*, vol. 16, no. 18, pp. 3515–23, 2016.

[170] Z. Ma, D. J. Collins, J. Guo, and Y. Ai, "Mechanical properties based particle separation via traveling surface acoustic wave," *Anal Chem*, vol. 88, no. 23, pp. 11844–11851, 2016.

[171] B. W. Drinkwater, "Dynamic-field devices for the ultrasonic manipulation of microparticles," *Lab Chip*, vol. 16, no. 13, pp. 2360–75, 2016.

[172] T. M. Llewellyn-Jones, B. W. Drinkwater, and R. S. Trask, "3d printed components with ultrasonically arranged microscale structure," *Smart Materials and Structures*, vol. 25, no. 2, p. 02LT01, 2016.

[173] T. Franke, A. R. Abate, D. A. Weitz, and A. Wixforth, "Surface acoustic wave (saw) directed droplet flow in microfluidics for pdms devices," *Lab Chip*, vol. 9, no. 18, pp. 2625–7, 2009.

[174] A. A. Nawaz, Y. Chen, N. Nama, R. H. Nissly, L. Ren, A. Ozcelik, L. Wang, J. P. McCoy, S. J. Levine, and T. J. Huang, "Acoustofluidic fluorescence activated cell sorter," *Anal Chem*, vol. 87, no. 24, pp. 12051–8, 2015.

[175] L. Schmid, D. A. Weitz, and T. Franke, "Sorting drops and cells with acoustics: acoustic microfluidic fluorescence-activated cell sorter," *Lab Chip*, vol. 14, no. 19, pp. 3710–8, 2014.

[176] T. Franke, S. Braunmuller, L. Schmid, A. Wixforth, and D. A. Weitz, "Surface acoustic wave actuated cell sorting (sawacs)," *Lab Chip*, vol. 10, no. 6, pp. 789–94, 2010.

[177] E. Benes, F. Hager, W. Bolek, and M. Groschl, "Separation of dispersed particles by drifting ultrasonic resonance fields," *Ultrasonics International 91*, pp. 167–170, 1991.

[178] S. Oberti, A. Neild, and J. Dual, "Manipulation of micrometer sized particles within a micromachined fluidic device to form two-dimensional patterns using ultrasound," *The Journal of the Acoustical Society of America*, vol. 121, no. 2, pp. 778–785, 2007.

[179] X. Ding, S. C. Lin, M. I. Lapsley, S. Li, X. Guo, C. Y. Chan, I. K. Chiang, L. Wang, J. P. McCoy, and T. J. Huang, "Standing surface acoustic wave (ssaw) based multichannel cell sorting," *Lab Chip*, vol. 12, no. 21, pp. 4228–31, 2012.

[180] S. Li, X. Ding, F. Guo, Y. Chen, M. I. Lapsley, S. C. Lin, L. Wang, J. P. McCoy, C. E. Cameron, and T. J. Huang, "An on-chip, multichannel droplet sorter using standing surface acoustic waves," *Anal Chem*, vol. 85, no. 11, pp. 5468–74, 2013.

[181] P. Glynne-Jones, R. J. Boltryk, N. R. Harris, A. W. Cranny, and M. Hill, "Mode-switching: a new technique for electronically varying the agglomeration position in an acoustic particle manipulator," *Ultrasonics*, vol. 50, no. 1, pp. 68–75, 2010.

[182] N. Harris, R. Boltryk, P. Glynne-Jones, and M. Hill, "A novel binary particle fractionation technique," *Physics Procedia*, vol. 3, no. 1, pp. 277–281, 2010.

[183] Y. Liu and K. M. Lim, "Particle separation in microfluidics using a switching ultrasonic field," *Lab Chip*, vol. 11, no. 18, pp. 3167–73, 2011.

[184] C. Schram, "Manipulation of particles," 1985.

[185] C. Schram, "Particle separation," 1987.

[186] G. Whitworth, M. A. Grundy, and W. T. Coakley, "Transport and harvesting of suspended particles using modulated ultrasound," *Ultrasonics*, vol. 29, no. 6, pp. 439–444, 1991.

[187] W. T. Coakley, G. Whitworth, M. A. Grundy, R. K. Gould, and R. Allman, "Ultrasonic manipulation of particles and cells. ultrasonic separation of cells," *Bioseparation*, vol. 4, no. 2, pp. 73–83, 1994.

[188] C. A. Miles, M. J. Morley, W. R. Hudson, and B. M. Mackey, "Principles of separating micro-organisms from suspensions using ultrasound," *Journal of Applied Bacteriology*, vol. 78, no. 1, pp. 47–54, 1995.

[189] T. Kozuka, T. Tuziuti, H. Mitome, and T. Fukuda, "Two-dimensional acoustic micromanipulation using a line-focused transducer," in *Mhs'97: Proceedings of 1997 International Symposium on Micromechatronics and Human Science*, pp. 161–168, 1997.

[190] T. Kozuka, T. Tuziuti, H. Mitome, F. Arai, and T. Fukuda, "Three-dimensional acoustic micromanipulation using four ultrasonic transducers," *Mhs 2000: Proceedings of the 2000 International Symposium on Micromechatronics and Human Science*, pp. 201–206, 2000.

[191] S. Peterson, G. Perkins, and C. Baker, "Development of an ultrasonic blood cell separator," 1986.

[192] J. Lee, C. Rhyou, B. Kang, and H. Lee, "Continuously phase-modulated standing surface acoustic waves for separation of particles and cells in microfluidic channels containing multiple pressure nodes," *Journal of Physics D: Applied Physics*, vol. 50, no. 16, p. 165401, 2017.

[193] A. L. Bernassau, C.-K. Ong, Y. Ma, P. G. A. MacPherson, C. R. P. Courtney, M. Riehle, B. W. Drinkwater, and D. R. S. Cumming, "Two-dimensional manipulation of micro particles by acoustic radiation pressure in a heptagon cell," *IEEE Trans Ultrason Ferroelectr Freq Control*, vol. 58, no. 10, pp. 2132–2138, 2011.

[194] A. L. Bernassau, P. G. Macpherson, J. Beeley, B. W. Drinkwater, and D. R. Cumming, "Patterning of microspheres and microbubbles in an acoustic tweezers," *Biomed Microdevices*, vol. 15, no. 2, pp. 289–97, 2013.

[195] G. D. Skotis, D. R. Cumming, J. N. Roberts, M. O. Riehle, and A. L. Bernassau, "Dynamic acoustic field activated cell separation (dafacs)," *Lab Chip*, vol. 15, no. 3, pp. 802–10, 2015.

[196] C. Pozrikidis, *Fluid Dynamics: Theory, Computation, and Numerical Simulation. [eBook].* Boston, MA : Springer US, 2009. 2., 2009.

[197] J. Dual and D. Moller, "Acoustofluidics 4: Piezoelectricity and application in the excitation of acoustic fields for ultrasonic particle manipulation," *Lab Chip*, vol. 12, no. 3, pp. 506–14, 2012.

[198] Q. Zhou, S. Lau, D. Wu, and K. K. Shung, "Piezoelectric films for high frequency ultrasonic transducers in biomedical applications," *Progress in materials science*, vol. 56, no. 2, pp. 139–174, 2011.

[199] S. Priya, R. Taneja, R. Myers, and R. Islam, *Piezoelectric Energy Harvesting using Bulk Transducers*, pp. 373–388. Boston, MA: Springer US, 2008.

[200] J. F. Tressler, S. Alkoy, and R. E. Newnham, "Piezoelectric sensors and sensor materials," *Journal of Electroceramics*, vol. 2, no. 4, pp. 257–272, 1998.

[201] T. R. Meeker, "Thickness mode piezoelectric transducers," *Ultrasonics*, vol. 10, no. 1, pp. 26–36, 1972.

[202] V. E. Granstaff and S. J. Martin, "Characterization of a thickness-shear mode quartz resonator with multiple nonpiezoelectric layers," *Journal of Applied Physics*, vol. 75, no. 3, pp. 1319–1329, 1994.

[203] S. Datta, *Surface acoustic wave devices*. Prentice-Hall, 1986.

[204] Y.-H. Kim and J.-W. Choi, *Sound visualization and manipulation. [eBook].* Singapore : Wiley, 2013., 2013.

[205] L. E. Kinsler, A. R. Frey, A. B. Coppens, and J. V. Sanders, *Fundamentals of Acoustics*. Wiley, 1999.

[206] G. T. Silva and H. Bruus, "Acoustic interaction forces between small particles in an ideal fluid," *Phys Rev E Stat Nonlin Soft Matter Phys*, vol. 90, no. 6, p. 063007, 2014.

[207] W. L. Nyborg, "Theoretical criterion for acoustic aggregation," *Ultrasound Med Biol*, vol. 15, no. 2, pp. 93–9, 1989.

[208] P. Glynne-Jones, P. P. Mishra, R. J. Boltryk, and M. Hill, "Efficient finite element modeling of radiation forces on elastic particles of arbitrary size and geometry," *J Acoust Soc Am*, vol. 133, no. 4, pp. 1885–93, 2013.

[209] T. Baasch and J. Dual, "Acoustofluidic particle dynamics: Beyond the rayleigh limit," *J Acoust Soc Am*, vol. 143, no. 1, p. 509, 2018.

[210] R. R. Collino, T. R. Ray, R. C. Fleming, C. H. Sasaki, H. Haj-Hariri, and M. R. Begley, "Acoustic field controlled patterning and assembly of anisotropic particles," *Extreme Mechanics Letters*, vol. 5, pp. 37–46, 2015.

[211] T. Baasch, I. Leibacher, and J. Dual, "Multibody dynamics in acoustophoresis," *J Acoust Soc Am*, vol. 141, no. 3, p. 1664, 2017.

[212] V. F. K. Bjerknes, *Fields of Force*. New York: Columbia University, 1906.

[213] L. A. Crum, "Bjerknes forces on bubbles in a stationary sound field," *The Journal of the Acoustical Society of America*, vol. 57, no. 6, pp. 1363–1370, 1975.

[214] N. A. Pelekasis, A. Gaki, A. Doinikov, and J. A. Tsamopoulos, "Secondary bjerknes forces between two bubbles and the phenomenon of acoustic streamers," *Journal of Fluid Mechanics*, vol. 500, pp. 313–347, 2004.

[215] N. A. Pelekasis and J. A. Tsamopoulos, "Bjerknes forces between two bubbles. part 1. response to a step change in pressure," *Journal of Fluid Mechanics*, vol. 254, no. -1, p. 467, 2006.

[216] N. A. Pelekasis and J. A. Tsamopoulos, "Bjerknes forces between two bubbles. part 2. response to an oscillatory pressure field," *Journal of Fluid Mechanics*, vol. 254, no. -1, p. 501, 2006.

[217] K. Yasui, Y. Iida, T. Tuziuti, T. Kozuka, and A. Towata, "Strongly interacting bubbles under an ultrasonic horn," *Phys Rev E Stat Nonlin Soft Matter Phys*, vol. 77, no. 1 Pt 2, p. 016609, 2008.

[218] A. P. Zhuk, "Hydrodynamic interaction of two spherical particles due to sound waves propagating perpendicularly to the center line," *Soviet Applied Mechanics*, vol. 21, no. 3, pp. 307–312, 1985.

[219] A. Garcia-Sabate, A. Castro, M. Hoyos, and R. Gonzalez-Cinca, "Experimental study on inter-particle acoustic forces," *J Acoust Soc Am*, vol. 135, no. 3, pp. 1056–63, 2014.

[220] A. A. Doinikov, "Acoustic radiation interparticle forces in a compressible fluid," *Journal of Fluid Mechanics*, vol. 444, 2001.

[221] S. Sepehrirahnama, K. M. Lim, and F. S. Chau, "Numerical study of interparticle radiation force acting on rigid spheres in a standing wave," *J Acoust Soc Am*, vol. 137, no. 5, pp. 2614–22, 2015.

[222] F. B. Wijaya, S. Sepehrirahnama, and K.-M. Lim, "Interparticle force and torque on rigid spheroidal particles in acoustophoresis," *Wave Motion*, vol. 81, pp. 28–45, 2018.

[223] M. Wiklund, R. Green, and M. Ohlin, "Acoustofluidics 14: Applications of acoustic streaming in microfluidic devices," *Lab Chip*, vol. 12, no. 14, pp. 2438–51, 2012.

[224] S. S. Sadhal, "Acoustofluidics 13: Analysis of acoustic streaming by perturbation methods," *Lab Chip*, vol. 12, no. 13, pp. 2292–300, 2012.

[225] H. M. Hertz, "Standing-wave acoustic trap for nonintrusive positioning of microparticles," *Journal of Applied Physics*, vol. 78, no. 8, pp. 4845–4849, 1995.

[226] N. Riley, "Acoustic streaming," *Theoretical and Computational Fluid Dynamics*, vol. 10, no. 1, pp. 349–356, 1998.

[227] C. Suri, K. Takenaka, H. Yanagida, Y. Kojima, and K. Koyama, "Chaotic mixing generated by acoustic streaming," *Ultrasonics*, vol. 40, no. 1, pp. 393–396, 2002.

[228] P. Hahn, I. Leibacher, T. Baasch, and J. Dual, "Numerical simulation of acoustofluidic manipulation by radiation forces and acoustic streaming for complex particles," *Lab Chip*, vol. 15, no. 22, pp. 4302–13, 2015.

[229] M. Ohlin, A. E. Christakou, T. Frisk, B. Önfelt, and M. Wiklund, "Influence of acoustic streaming on ultrasonic particle manipulation in a 100-well ring-transducer microplate," *Journal of Micromechanics and Microengineering*, vol. 23, no. 3, 2013.

[230] H. Zhang, Z. Tang, Z. Wang, S. Pan, Z. Han, C. Sun, M. Zhang, X. Duan, and W. Pang, "Acoustic streaming and microparticle enrichment within a microliter droplet using a lamb-wave resonator array," *Physical Review Applied*, vol. 9, no. 6, 2018.

[231] C. Devendran, I. Gralinski, and A. Neild, "Separation of particles using acoustic streaming and radiation forces in an open microfluidic channel," *Microfluidics and Nanofluidics*, vol. 17, no. 5, pp. 879–890, 2014.

[232] N. Nama, R. Barnkob, Z. Mao, C. J. Kahler, F. Costanzo, and T. J. Huang, "Numerical study of acoustophoretic motion of particles in a pdms microchannel driven by surface acoustic waves," *Lab Chip*, vol. 15, no. 12, pp. 2700–9, 2015.

[233] C. Devendran, T. Albrecht, J. Brenker, T. Alan, and A. Neild, "The importance of travelling wave components in standing surface acoustic wave (ssaw) systems," *Lab Chip*, vol. 16, no. 19, pp. 3756–3766, 2016.

[234] H. Dwight, *Tables of integrals and other mathematical data*. New York: The Macmillan Company, 1966.

[235] M. A. B. Andrade, G. D. Skotis, S. Ritchie, D. R. S. Cuming, M. O. Riehle, and A. L. Bernassau, "Contactless acoustic manipulation and sorting of particles by dynamic acoustic fields," *IEEE Trans Ultrason Ferroelectr Freq Control*, vol. 63, no. 10, pp. 1593–1600, 2016.

[236] A. A. Mohanan, R. Parthiban, and N. Ramakrishnan, "Shadow mask assisted direct growth of zno nanowires as a sensing medium for surface acoustic wave devices using a thermal evaporation method," *Journal of Micromechanics and Microengineering*, vol. 26, no. 2, 2016.

[237] G. A. Borrero, J. P. Bravo, S. F. Mora, S. Velásquez, and F. E. Segura-Quijano, "Design and fabrication of saw pressure, temperature and impedance sensors using novel multiphysics simulation models," *Sensors and Actuators A: Physical*, vol. 203, pp. 204–214, 2013.

[238] K. Y. Hashimoto, T. Omori, and M. Yamaguchi, "Design considerations on surface acoustic wave resonators with significant internal reflection in interdigital transducers," *IEEE Trans Ultrason Ferroelectr Freq Control*, vol. 51, no. 11, pp. 1394–403, 2004.

[239] A. Akther, A. Kafy, L. Zhai, H. C. Kim, M. D. I. R. Shishir, and J. Kim, "Ultrasonic wave propagation of flexible piezoelectric polymer for tactile actuator: simulation and experiment," *Smart Materials and Structures*, vol. 25, no. 11, 2016.

[240] A. A. M. Ralib, A. N. Nordin, and U. Hashim, "Equivalent circuit modeling of two-port al-doped zinc oxide cmos saw resonator using matlab™," in *2013 IEEE International Conference on Circuits and Systems (ICCAS)*, pp. 140–145.

[241] L. Johansson, J. Enlund, S. Johansson, I. Katardjiev, and V. Yantchev, "Surface acoustic wave induced particle manipulation in a pdms channel–principle concepts for continuous flow applications," *Biomed Microdevices*, vol. 14, no. 2, pp. 279–89, 2012.

[242] H. Oh, K. Lee, K. Eun, S. H. Choa, and S. S. Yang, "Development of a high-sensitivity strain measurement system based on a sh saw sensor," *Journal of Micromechanics and Microengineering*, vol. 22, no. 2, 2012.

[243] V. K. Varadan, V. V. Varadan, and H. Subramanian, "Fabrication, characterization and testing of wireless mems-idt based microaccelerometers," *Sensors and Actuators A: Physical*, vol. 90, no. 1, pp. 7–19, 2001.

[244] S. Lehtonen, V. P. Plessky, C. S. Hartmann, and M. M. Salomaa, "Spudt filters for the 2.45 ghz ism band," *IEEE Transactions on Ultrasonics, Ferroelectrics, and Frequency Control*, vol. 51, no. 12, pp. 1697–1703, 2004.

[245] X. Ding, S. C. Lin, B. Kiraly, H. Yue, S. Li, I. K. Chiang, J. Shi, S. J. Benkovic, and T. J. Huang, "On-chip manipulation of single microparticles, cells, and organisms using surface acoustic waves," *Proc Natl Acad Sci U S A*, vol. 109, no. 28, pp. 11105–9, 2012.

[246] X. Ding, J. Shi, S. C. Lin, S. Yazdi, B. Kiraly, and T. J. Huang, "Tunable patterning of microparticles and cells using standing surface acoustic waves," *Lab Chip*, vol. 12, no. 14, pp. 2491–7, 2012.

[247] W. Zhou, L. Niu, F. Cai, F. Li, C. Wang, X. Huang, J. Wang, J. Wu, L. Meng, and H. Zheng, "Spatial selective manipulation of microbubbles by tunable surface acoustic waves," *Biomicrofluidics*, vol. 10, no. 3, p. 034121, 2016.

[248] A. Fakhfouri, C. Devendran, T. Albrecht, D. J. Collins, A. Winkler, H. Schmidt, and A. Neild, "Surface acoustic wave diffraction driven mechanisms in microfluidic systems," *Lab Chip*, vol. 18, no. 15, pp. 2214–2224, 2018.

[249] C. Devendran, D. J. Collins, Y. Ai, and A. Neild, "Huygens-fresnel acoustic interference and the development of robust time-averaged patterns from traveling surface acoustic waves," *Phys Rev Lett*, vol. 118, no. 15, p. 154501, 2017.

[250] J. Paskauskas, R. Rimeika, and C. D., "Velocity and attenuation of surface acoustic waves in proton-exchanged 128 degrees -rotated y-cut linbo3," *J. Phys. D: Appl. Phys.*, vol. 28, no. 1, p. 1419, 1995.

[251] X. Ding, P. Li, S. C. Lin, Z. S. Stratton, N. Nama, F. Guo, D. Slotcavage, X. Mao, J. Shi, F. Costanzo, and T. J. Huang, "Surface acoustic wave microfluidics," *Lab Chip*, vol. 13, no. 18, pp. 3626–49, 2013.

[252] S. C. Lin, X. Mao, and T. J. Huang, "Surface acoustic wave (saw) acoustophoresis: now and beyond," *Lab Chip*, vol. 12, no. 16, pp. 2766–70, 2012.

[253] M. R. H. Sarker, H. Karim, R. Martinez, D. Delfin, R. Enriquez, M. A. I. Shuvo, N. Love, and Y. R. Lin, "Temperature measurements using a lithium niobate (linbo3) pyroelectric ceramic," *Measurement*, vol. 75, pp. 104–110, 2015.

[254] S. Bhowmick, M. Iodice, M. Gioffrè, G. Breglio, A. Irace, M. Riccio, G. Romano, S. Grilli, P. Ferraro, L. Mecozzi, S. Coppola, O. Gennari, R. Rega, and G. Coppola, "Investigation of pyroelectric fields generated by lithium niobate crystals through integrated microheaters," *Sensors and Actuators A: Physical*, vol. 261, pp. 140–150, 2017.

[255] MicroChem, "Su-8 3000 permanent epoxy negative photoresist," 2019.

[256] K. Haubert, T. Drier, and D. Beebe, "Pdms bonding by means of a portable, low-cost corona system," *Lab Chip*, vol. 6, no. 12, pp. 1548–9, 2006.

[257] S. J. Ippolito, A. Trinchi, D. A. Powell, and W. Wlodarski, *Acoustic Wave Gas and Vapor Sensors*, pp. 1–44. Boston, MA: Springer US, 2009.

[258] J. D. L. III, P. D. Bradley, S. Wartenberg, and R. C. Ruby, "Modified butterworth-van dyke circuit for fbar resonators and automated measurement system," 2000.

[259] S. Thomas, Z. Racz, M. Cole, and J. W. Gardner, "High-frequency one-port colpitts saw oscillator for chemical sensing," in *The Sixth International Conference on Advances in Circuits, Electronics and Micro-electronics*, pp. 13–17.

[260] L. Allies, B. E., H. M'Jahed, G. Prieur, and O. Elmazria, "Modeling of wireless saw temperature sensor and associated antenna," *Instrumentation*, vol. 1, no. 1, pp. 8–14, 2014.

[261] B. J. Kirby, *Micro- and Nanoscale Fluid Mechanics*. Cambridge University Press, 2010.

[262] A. Neild, S. Oberti, A. Haake, and J. Dual, "Finite element modeling of a microparticle manipulator," *Ultrasonics*, vol. 44 Suppl 1, pp. e455–60, 2006.

[263] R. Ciskowski, *Boundary element methods in acoustics*. Computational Mechanics Pubs., 1991.

[264] P. B. Muller, R. Barnkob, M. J. Jensen, and H. Bruus, "A numerical study of microparticle acoustophoresis driven by acoustic radiation forces and streaming-induced drag forces," *Lab Chip*, vol. 12, no. 22, pp. 4617–27, 2012.

[265] P. A. Martin, *Multiple Scattering: Interaction of Time-Harmonic Waves with N Obstacles*. Cambridge University Press, 2006.

[266] P. Zhang, T. Li, J. Zhu, X. Zhu, S. Yang, Y. Wang, X. Yin, and X. Zhang, "Generation of acoustic self-bending and bottle beams by phase engineering," *Nat Commun*, vol. 5, p. 4316, 2014.

[267] G. Simon, M. A. B. Andrade, J. Reboud, J. Marques-Hueso, M. P. Y. Desmulliez, J. M. Cooper, M. O. Riehle, and A. L. Bernassau, "Particle separation by phase modulated surface acoustic waves," *Biomicrofluidics*, vol. 11, no. 5, p. 054115, 2017.

[268] A. Lenshof, C. Magnusson, and T. Laurell, "Acoustofluidics 8: Applications of acoustophoresis in continuous flow microsystems," *Lab Chip*, vol. 12, no. 7, pp. 1210–23, 2012.

[269] M. Diez-Silva, M. Dao, J. Han, C. T. Lim, and S. Suresh, "Shape and biomechanical characteristics of human red blood cells in health and disease," *MRS Bull*, vol. 35, no. 5, pp. 382–388, 2010.

[270] J. Prinyakupt and C. Pluempitiwiriyawej, "Segmentation of white blood cells and comparison of cell morphology by linear and naive bayes classifiers," *Biomed Eng Online*, vol. 14, p. 63, 2015.

[271] S. J. Hao, Y. Wan, Y. Q. Xia, X. Zou, and S. Y. Zheng, "Size-based separation methods of circulating tumor cells," *Adv Drug Deliv Rev*, vol. 125, pp. 3–20, 2018.

[272] W. H. Grover, A. K. Bryan, M. Diez-Silva, S. Suresh, J. M. Higgins, and S. R. Manalis, "Measuring single-cell density," *Proc Natl Acad Sci U S A*, vol. 108, no. 27, pp. 10992–6, 2011.

[273] A. Zipursky, E. Bow, R. S. Seshadri, and E. J. Brown, "Leukocyte density and volume in normal subjects and in patients with acute lymphoblastic leukemia," *Blood*, vol. 48, no. 3, pp. 361–71, 1976.

[274] D. Hartono, Y. Liu, P. L. Tan, X. Y. Then, L. Y. Yung, and K. M. Lim, "On-chip measurements of cell compressibility via acoustic radiation," *Lab Chip*, vol. 11, no. 23, pp. 4072–80, 2011.

[275] L. A. G. Lin, A. Q. Liu, Y. F. Yu, C. Zhang, C. S. Lim, S. H. Ng, P. H. Yap, and H. J. Gao, "Cell compressibility studies utilizing noncontact hydrostatic pressure measurements on single living cells in a microchamber," *Applied Physics Letters*, vol. 92, no. 23, 2008.

[276] H. Wang, Z. Liu, D. M. Shin, Z. G. Chen, Y. Cho, Y. J. Kim, and A. Han, "A continuous-flow acoustofluidic cytometer for single-cell mechanotyping," *Lab Chip*, 2019.

[277] R. Barnkob, P. Augustsson, T. Laurell, and H. Bruus, "Measuring the local pressure amplitude in microchannel acoustophoresis," *Lab Chip*, vol. 10, no. 5, pp. 563–70, 2010.

[278] R. Barnkob, P. Augustsson, T. Laurell, and H. Bruus, "Acoustic radiation- and streaming-induced microparticle velocities determined by microparticle image velocimetry in an ultrasound symmetry plane," *Phys Rev E Stat Nonlin Soft Matter Phys*, vol. 86, no. 5 Pt 2, p. 056307, 2012.

[279] P. Augustsson, C. Magnusson, M. Nordin, H. Lilja, and T. Laurell, "Microfluidic, label-free enrichment of prostate cancer cells in blood based on acoustophoresis," *Anal Chem*, vol. 84, no. 18, pp. 7954–62, 2012.

[280] Y. Chen, S. Li, Y. Gu, P. Li, X. Ding, L. Wang, J. P. McCoy, S. J. Levine, and T. J. Huang, "Continuous enrichment of low-abundance cell samples using standing surface acoustic waves (ssaw)," *Lab Chip*, vol. 14, no. 5, pp. 924–30, 2014.

[281] S. Halldorsson, E. Lucumi, R. Gomez-Sjoberg, and R. M. T. Fleming, "Advantages and challenges of microfluidic cell culture in polydimethylsiloxane devices," *Biosens Bioelectron*, vol. 63, pp. 218–231, 2015.

[282] A. D. Hughes, J. Mattison, J. D. Powderly, B. T. Greene, and M. R. King, "Rapid isolation of viable circulating tumor cells from patient blood samples," *J Vis Exp*, no. 64, p. e4248, 2012.

[283] R. T. Abraham and A. Weiss, "Jurkat t cells and development of the t-cell receptor signalling paradigm," *Nature Reviews Immunology*, vol. 4, p. 301, 2004.

[284] L. R. Quinlan, *Phosphoinositides, Inositol Phosphates, and Phospholipase C in Embryonic Stem Cells*, pp. 127–149. Totowa, NJ: Humana Press, 2006.

[285] J. G. A. Barbedo, "Automatic object counting in neubauer chambers," 2013.

[286] W. Strober, "Trypan blue exclusion test of cell viability," *Current Protocols in Immunology*, vol. 21, no. 1, pp. A.3B.1–A.3B.2, 1997.

[287] H. R. Hirsch and J. Engelberg, "Determination of the cell doubling-time distribution from culture growth-rate data," *Journal of Theoretical Biology*, vol. 9, no. 2, pp. 297–302, 1965.

[288] S. K. Kim, S. M. Cho, H. Kim, H. Seok, S. O. Kim, T. K. Kwon, and J. S. Chang, "The colchicine derivative ct20126 shows a novel microtubule-modulating activity with apoptosis," *Exp Mol Med*, vol. 45, p. e19, 2013.

[289] D. Howard, L. D. Buttery, K. M. Shakesheff, and S. J. Roberts, "Tissue engineering: strategies, stem cells and scaffolds," *J Anat*, vol. 213, no. 1, pp. 66–72, 2008.

[290] M. J. Tomlinson, S. Tomlinson, X. B. Yang, and J. Kirkham, "Cell separation: Terminology and practical considerations," *J Tissue Eng*, vol. 4, p. 2041731412472690, 2013.

[291] S. W. O'Driscoll, B. Meisami, Y. Miura, and J. S. Fitzsimmons, "Viability of periosteal tissue obtained postmortem," *Cell Transplantation*, vol. 8, no. 6, pp. 611–616, 1999.

[292] M. M. Pasternak, E. M. Strohm, E. S. Berndl, and M. C. Kolios, "Properties of cells through life and death - an acoustic microscopy investigation," *Cell Cycle*, vol. 14, no. 18, pp. 2891–8, 2015.

[293] R. Thavarajah, V. K. Mudimbaimannar, J. Elizabeth, U. K. Rao, and K. Ranganathan, "Chemical and physical basics of routine formaldehyde fixation," *Journal of oral and maxillofacial pathology : JOMFP*, vol. 16, no. 3, pp. 400–405, 2012.

[294] R. Guldiken, M. C. Jo, N. D. Gallant, U. Demirci, and J. Zhe, "Sheathless size-based acoustic particle separation," *Sensors (Basel)*, vol. 12, no. 1, pp. 905–22, 2012.

[295] T. Yang, V. Vitali, and P. Minzioni, "Acoustofluidic separation: impact of microfluidic system design and of sample properties," *Microfluidics and Nanofluidics*, vol. 22, no. 4, 2018.

[296] P. Fornasini, *The Uncertainty in Physical Measurements*. Springer, 2008.

[297] A. K. Hipp, G. Storti, and M. Morbidelli, "Acoustic characterization of concentrated suspensions and emulsions. 2. experimental validation," *Langmuir*, vol. 18, no. 2, pp. 405–412, 2002.

[298] G. Simon, Y. Pailhas, M. A. B. Andrade, J. Reboud, J. Marques-Hueso, M. P. Y. Desmulliez, J. M. Cooper, M. O. Riehle, and A. L. Bernassau, "Particle separation in surface acoustic wave microfluidic devices using reprogrammable, pseudo-standing waves," *Applied Physics Letters*, vol. 113, no. 4, 2018.

[299] Y. Gao, W. Li, and D. Pappas, "Recent advances in microfluidic cell separations," *Analyst*, vol. 138, no. 17, pp. 4714–21, 2013.

[300] J. D. Adams and H. T. Soh, "Tunable acoustophoretic band-pass particle sorter," *Applied Physics Letters*, vol. 97, no. 6, p. 064103, 2010.